



HAL
open science

Evaporation in model porous media with transport of particles

Elisa Ghiringhelli

► **To cite this version:**

Elisa Ghiringhelli. Evaporation in model porous media with transport of particles. Fluids mechanics [physics.class-ph]. Université Paul Sabatier - Toulouse III, 2023. English. NNT : 2023TOU30147 . tel-04329675

HAL Id: tel-04329675

<https://theses.hal.science/tel-04329675>

Submitted on 7 Dec 2023

HAL is a multi-disciplinary open access archive for the deposit and dissemination of scientific research documents, whether they are published or not. The documents may come from teaching and research institutions in France or abroad, or from public or private research centers.

L'archive ouverte pluridisciplinaire **HAL**, est destinée au dépôt et à la diffusion de documents scientifiques de niveau recherche, publiés ou non, émanant des établissements d'enseignement et de recherche français ou étrangers, des laboratoires publics ou privés.



Université
de Toulouse

THÈSE

En vue de l'obtention du

DOCTORAT DE L'UNIVERSITÉ DE TOULOUSE

Délivré par : *l'Université Toulouse 3 Paul Sabatier (UT3 Paul Sabatier)*

Présentée et soutenue le (27/06/2023) par :

GHIRINGHELLI Elisa

**Evaporation in model porous media with transport of
particles**

EMMANUEL KEITA
MANUEL MARCOUX
MARC PRAT
SOPHIE ROMAN
JEAN-BAPTISTE SALMON
LOUNÈS TADRIST

JURY
UGE
UPS/IMFT
IMFT/CNRS
ISTO
LOF
AMU

Rapporteur
Directeur de thèse
Co-directeur de thèse
Examineur
Rapporteur
Examineur

École doctorale et spécialité :

MEGEP : Dynamique des fluides

Unité de Recherche :

Institut de mécanique des fluides Toulouse

Directeur(s) de Thèse :

Manuel Marcoux et Marc Prat

Rapporteurs :

Emmanuel Keita et Jean-Baptiste Salmon

Acknowledgments

First and foremost, I have to thank my thesis supervisor, Manuel Marcoux, for having given me this great opportunity and my co-supervisor, Marc Prat, for having guided me through this PhD. I would like to thank you for your assistance and involvement, without which this paper would have never been accomplished.

I would also like to warmly thank Sébastien Cazin, for always being available to help me solve my experimental and imaging problems, for sharing his wide knowledge and broad experience with me while always being supportive and encouraging. Concerning the technical side of the research, many thanks to Julien Lefort and Maëlle Ogier for tirelessly trying out different experimental set-ups.

I would also like to show gratitude to my committee, Lounès Tadrst for having presided the defense, the reviewers Emmanuel Keita and Jean-Baptiste Salmon, as well as Sophie Roman, for having accepted to review my work and for the interesting discussion during my defense.

Getting through my dissertation required more than academic support, and I have many, many people to thank for listening to and, at times, having to tolerate me over the past three years. Let me start with my colleagues, with whom I shared the journey through the porous media, Asma, Marion, Terence, Simon, David and all the others in the group, as well as Guillaume, Christos and Amin, thank you for lightening up these three years and half. Not less important, Bilal, thank you for always being there to encourage me and cheer me up.

Outside the lab, my gratitude goes to all those people from salsa that helped me disconnect and take a break. To finish, the most important thank you goes to Ana, who, even far away, was always there and here care, understand, support and friendship meant (and still mean) everything.

Most importantly, none of this could have happened without my parents, my brother and sister-in-law, thank you for providing me unfailing support and continuous encouragement throughout these years of study and through the process of researching and writing this thesis. Finally, to Clément, thank you for always being there, none of this would have never been possible without you.

Contents

Acknowledgments	i
List of Figures	xv
List of Tables	xvii
Abstract	xix
Resumé	xxi
Introduction	1
I State of the art and advances on drying	3
1 Evaporation at the pore-scale	3
1.1 The capillary circular tube	4
1.2 The effect of liquid films	6
2 Evaporation in a porous medium	8
3 Particles and deposit	10
3.1 Thin films and droplets	10
3.2 Confined geometries	11
3.3 The porous medium	15
4 The effect of wettability on evaporation	18
5 Motivation and objectives	20
5.1 The fuel cell and its water problematic	20
5.2 The hydrophobization of the Gas Diffusion Layer	22
II Evaporation in a single channel	27
1 Materials and Methods	28
1.1 The experimental material	28
1.2 The experimental protocol	30
1.3 The wettability of the materials	30
1.4 The numerical simulations	31
2 The phase distribution	32
2.1 Corner films and contact angles	33
3 The effect of particles	33
4 Evaporation kinetics in the pure water case	35
4.1 Image processing	35
4.2 The three phases	38
4.3 The evaporation rate	38

4.4	Surface Evolver simulations	39
5	Impact of particles on the evaporation kinetics	40
5.1	Image processing	41
5.2	The effects on the evaporation dynamic	41
6	The final deposit	43
7	The impact of corner film thickness on the evaporation rate	44
8	On the accumulation of particles in the films and the film thinning effect	46
8.1	Particle convective transport is dominant in the films	46
8.2	Accumulation of particles and particle compact packing in the corner films	48
8.3	Estimation of A_c	50
8.4	On the effect of particles on corner films	52
9	High concentration of particles	55
9.1	Liquid - gas distribution in the channel and final deposit	56
9.2	Evaporation kinetics	58
10	Conclusion	61
III Evaporation in a double channel		63
1	Introduction	63
2	Materials and Methods	63
3	Experiment with the SUEX system (pure water)	65
4	Experiment with the SUEX system (with particles)	69
5	Evaporation kinetics	70
5.1	The case of pure water	71
5.2	The impact of particles	72
6	The final deposit	73
7	Pre-test experiment with the Plexiglas system: the reversal of the main meniscus dynamic	75
8	Conclusions	78
IV Experiments with micromodel for pure water		79
1	Introduction	80
2	Methods and Materials	81
2.1	Model porous medium	81
2.2	The experimental protocol	82
2.3	Drying setup (no gravity effect, $P = P_{atm}$)	83
2.4	Drying setup with gravity effects ($P_g = P_{atm}$)	85
2.5	Drying setup with partial vacuum conditions (no gravity, $P = 0.1P_{atm}$)	85
2.6	Drying setup with partial vacuum conditions and gravity effects ($P = 0.1P_{atm}$)	87
3	Image treatment (phase distribution, evaluation of evaporation rate)	88
4	Drying patterns	90
4.1	Compariong levels of saturation	91
4.2	Impact of gravity	91
4.3	Impact of partial vacuum and temperature	93
5	Evaporation kinetics	96
5.1	Impact of partial vacuum and temperature (in the absence of gravity effects)	96

5.2	Impact of gravity effects	99
6	Conclusion	100
V	Experiments with micromodel in the presence of particles	103
1	Introduction	104
2	Methods and Materials	104
2.1	The experimental protocol	104
2.2	The plasma treatment	106
2.3	Experimental set up	108
2.4	Imaging the deposit: Particle deposit image processing	108
3	Impact of particles on drying patterns	110
3.1	$B = 0, P = P_{atm}, T = 22^{\circ}\text{C}$	110
3.2	$B > 0, P = P_{atm}, T = 22^{\circ}\text{C}$	110
3.3	$B = 0$ and $B > 0, P = 0.1P_{atm}, T = 22^{\circ}\text{C}$	112
3.4	$B = 0$ and $B > 0, P = 0.1P_{atm}, T = 50-60^{\circ}\text{C}$	114
4	Impact of particles on drying kinetics	115
4.1	$B = 0, P = P_{atm}, T = 22^{\circ}\text{C}$	115
4.2	$B > 0, P = P_{atm}, T = 22^{\circ}\text{C}$	116
4.3	$B = 0$ and $B > 0, P = 0.1P_{atm}, T = 22^{\circ}\text{C}$	116
4.4	$B = 0$ and $B > 0, P = 0.1P_{atm}, T = 50-60^{\circ}\text{C}$	119
5	Péclet number evaluation	120
6	Final deposit	121
6.1	Impact of drying conditions	121
6.2	Impact of the initial particle concentration	124
7	Impact of the plasma treatment	124
8	Attempt of final deposit statistical analysis	128
8.1	Statistical analysis by channels (procedure)	128
8.2	Correlation between mean brightness and area percentage	130
8.3	Comparison of the deposits	132
8.4	Evaporation time statistics	133
8.5	Conclusion on the "statistical" analysis	136
8.6	Conclusions	137
	Conclusion and future work	139
	A SUEX fabrication protocol	143
	B Evaporation time treatment	145
	Bibliographie	148

List of Figures

I.1	Schema of evaporation in a capillar tube	4
I.2	[Chauvet <i>et al.</i> , 2010] Sketch of the thick liquid films in a capillary tube of square cross section. The bulk meniscus position is denoted as z_0	7
I.3	Overview of drying and flooding problem [Chauvet, 2009], where Bo is the Bond number	8
I.4	Typical evolution of the drying rate from a porous medium highlighting the different characteristic stages [Mosthaf <i>et al.</i> , 2014]	9
I.5	[Bodiguel et Leng, 2010] Schematic view of the sessile droplet of colloidal suspension (nanoparticles + colloidal tracers) sitting on a glass substrate and undergoing evaporation. The data acquisition process consists in rapidly and repeatedly scanning the drop with a confocal microscope along the x-direction at a fixed z-position.	11
I.6	[Leng, 2010] Schematic view of the confined drying geometry where a droplet of a colloidal solution is squeezed in between two circular glass plates and let to dry up. A camera captures the image and is further processed for contour detection.	12
I.7	[Bodiguel <i>et al.</i> , 2009] Optical image of the capillary rise during a typical experiment. The cell thickness is 0.40 mm. On this image, horizontal patterns can be seen above the capillary rise.	13
I.8	[Doumenc et Guerrier, 2010] Sketch of the Problem Geometry.	14
I.9	[Dufresne <i>et al.</i> , 2003] Bright-field image of a drying suspension of silica nanoparticles. Inset: a schematic of the experimental geometry. Water evaporates from the drying edge, $y = 0$. The crack tips extend to y_C , just behind the compaction front, at y_F . The inner meniscus lies at y_M	14
I.10	[Pingulkar et Salmon, 2023] Confined directional drying of a colloidal dispersion. Capillary forces hold the air-water menisci (radius of curvature r) at the outlet of the cell.	15
I.11	[Sghaier et Prat, 2009] a) Schematic of the efflorescence pumping effect. The liquid (in dark grey) contained in the porous domain and in contact with the efflorescence is pumped by capillarity (solid arrows) through the efflorescence and evaporates at the efflorescence evolving external periphery. b) The efflorescence as porous barrier to vapor diffusion. Evaporation takes place within the porous medium. The vapor (dashed arrows) migrates from the menisci at the boundary of liquid clusters (in dark grey) to the surrounding air through the dry region of the porous domain and the efflorescence. Subflorescences may eventually appear in the disconnected clusters as a result of evaporation.	16

I.12	[Keita <i>et al.</i> , 2013] Drying through the upper free surface of a cylindrical (height (H) = 4 cm) porous medium made of glass beads initially filled with a colloidal suspension at 5% volume fraction in water. Drying occurs through the upper surface (right) with a steady dried air flow. MRI measurements were carried out every 2h over 4 days giving us access to (a) χ the distribution of particles in the pores at the end of the experiment [the black line corresponds to Eq. 3.3, (b) Ψ the distribution of colloids in the liquid phase, and (c) Φ the distribution of water as a function of sample height. For the two last panels the profiles displayed are separated by 10 h. Red thick lines represent the initial state.	17
I.13	[He <i>et al.</i> , 2022] Top view of the representative contact line moving. . .	18
I.14	[Shokri <i>et al.</i> , 2008] Images of sand columns used in evaporation experiments with blue color showing the saturated zone, gray color showing the unsaturated zone and dashed line showing the interface between hydrophobic (HO) and hydrophilic (HI) sand. (a) completely HI sand; (b) top layer (7 mm) of HO sand on top of HI sand; (c) 25 mm HO sand on top of HI sand; and (d) 7 mm HO sand layer placed 18 mm below HI sand surface.	19
I.15	[Shokri et Or, 2013] Surface of columns packed with (a) hydrophilic (HI) sand and (b) two hydraulically coupled vertical domains of hydrophobic (HO) and HI sand. The dash line indicates the vertical HI/HO interface. (a) Since evaporation occurs at surface, tracer is deposited there (b) capillary suction between HI and HO grains causes lateral liquid flow from HO to HI sand layer and subsequent evaporation and preferential dye deposition exclusively on HI surface.	20
I.16	Components and functioning of the fuel cell.	21
I.17	SEM image (upper) and corresponding EDS map of fluorine (F) (bottom) of cross-section of samples (a) CT1 (Toray 090 with air-dried PTFE), (b) CT2 (Toray 090 with vacuum-dried PTFE). (Images and caption from [Ito <i>et al.</i> , 2014])	23
I.18	Capillary pattern (a) and front pattern (b) in drying observed in a 2D micromodel [Prat, 2002]. Liquid region in black and gas region in white. The solid phase is not visible. Vapor escapes from top edge of micromodel. Other edges are sealed.	23
II.1	Composite SUEX -PDMS channel of rectangular cross section.	28
II.2	Contact angle variation on SUEX and PDMS layers during evaporation of a droplet in the fixed triple line regime	31
II.3	Typical fluid distribution in the channel during evaporation: a) top view of the channel in the experiment with pure water, b) quasi-static shape computed with Surface Evolver for $\theta_{SUEX} = 30^\circ$ and $\theta_{PDMS} = 104^\circ$, c) in the presence of particles (10^{-4})	32
II.4	Overlay of picture of the experiment with pure water with focus on the SUEX bottom wall and corresponding images obtained from Surface Evolver simulations (solid lines in color) for three values of contact angle.	33

II.5	Triple line shape on SUEX bottom plate for pure water and the three particle concentrations. The curve in red is the shape in the main meniscus region in the pure water experiment whereas the shape in yellow is the shape in the corner film upper region in the pure water experiment. The bright zones in the pictures with particles correspond to particle accumulation zones. The indicated times correspond to the time in Fig. II.14a	34
II.6	Corner film thickness at time $t = 90$ min evaluated at a distance of 0.3 mm from the channel entrance (this location corresponds to the horizontal orange line in the inset); I denotes the light intensity (expressed in grey level in the images). In the images with particles, the light intensity is maximum at the triple line. Note that the plots are over the half of the channel width.	35
II.7	Images of the evaporation experiment in the pure water case with focus at the bottom of the channel (SUEX); images are taken every 25 minutes.	36
II.8	From raw image to post processes in ImageJ, on the right the line for the Reslice plugin is drawn and measure 1716 pixels.	36
II.9	Result of the Reslice plugin and consequent binarization to be treated in Matlab, the image is 850×1716 , where 850 is the number of images and 1716 is the size of the channel from Fig. II.8.	37
II.10	Evolution of the triple line on SUEX and on PDMS resulting from the processing in Matlab of Fig. II.9	37
II.11	(a) Experiment: Evolution of triple line most advanced point on SUEX bottom surface (z_{bm1} in Figs. II.3 or II.6) and on PDMS top surface (z_{bm2} in Figs. II.3 or II.6) for pure water, (b) Experiment: Evolution of the difference in the triple line most advanced point positions between PDMS top wall and SUEX bottom wall (i.e. $z_{bm2} - z_{bm1}$)	38
II.12	(a) Surface Evolver simulation: variation of triple line most advanced point on SUEX bottom surface and on PDMS top surface as a fraction of the volume fraction of gas in the channel, (b) Surface Evolver simulation of the evolution of the difference in the triple line most advanced point positions between PDMS top wall and SUEX bottom wall (i.e. $z_{bm2} - z_{bm1}$).	40
II.13	Resulting image from the reslice plugin in ImageJ. The white pixels represent the accumulation of the particles, therefore the position of the two fronts.	41
II.14	(a) Evolution of triple line most advanced point on SUEX bottom surface (z_{bm1} in Fig. II.3), (b) and PDMS top surface (z_{bm2} in Fig. II.3). (c) Experiment: Evolution of the difference in the triple line most advanced point positions between PDMS top wall and SUEX bottom wall (i.e. $z_{bm2} - z_{bm1}$) for the various concentrations in particles.	42
II.15	Spatial distribution of deposited particles at the end of experiment after full evaporation. The preferential zones of particle deposition are in bright. The false color image on the right shows a more detailed information on the deposited particle distribution for the highest concentration tested.	44
II.16	Final liquid distribution in the composite channel as computed by Surface Evolver for two values of contact angle on the SUEX walls	45

II.17	Impact of film thickness on evaporation rate from the channel from numerical simulations. a) computational domain, b) computational domain in the channel (gas region), c) illustration of normalized vapor partial pressure field (dimensionless) in the channel, d) Variation of evaporation rate as a function of film thickness (in the inset the evaporation rate is normalized by the evaporation rate from the fully liquid saturated channel).	47
II.18	Size of a compact particle packing in the corner films made of all particles introduced in the channel. The inset shows the particle volume fraction in the corner films assuming a uniform distribution of all the particles in the corner films for $z_{bm1} = 1mm$.	49
II.19	Relationship between corner meniscus curvature radius, film thickness and contact angle.	50
II.20	Impact of suspension viscosity on film thickness variation along the channel; μ_{ref} is the dynamic viscosity for pure water, $w_{film-ref}$ is the film thickness when viscous effects are negligible.	54
II.21	a-g) Images every 25 minutes of the evaporation process with the highest concentration of particles, h) Final deposit distribution. The red arrows materialize the increase in the size of the particle deposit in the entrance region of the channel. The red line in Fig. II.21c corresponds to the triple line on the SUEX bottom wall in the pure water experiment.	57
II.22	(a) Evolution of triple line most advanced point on SUEX bottom surface (z_{bm1} in Fig. II.2), (b) and PDMS top surface (z_{bm2} in Fig. II.2). (c) Evolution of the difference in the triple line most advanced point positions between PDMS top wall and SUEX bottom wall (i.e. $z_{bm2} - z_{bm1}$) for the various concentrations in particles.	59
III.1	Sketch of SUEX – PDMS system of interconnected channels studied in this chapter.	64
III.2	The pure water experiment after 172 minutes. The red line represent the position where the corner film is characterized.	65
III.3	Typical fluid distribution in the channel during evaporation: a) top view of the double channel in the experiment with pure water after 95 minutes, b) quasi-static shape computed with Surface Evolver for $\theta_{SUEX} = 30^\circ$ and $\theta_{PDMS} = 104^\circ$.	66
III.4	Evolution of the evaporation process in the SUEX-PDMS double channel with images every 59 minutes.	67
III.5	Evolution of the liquid film triple line position at the position in the channel marked with the red line in Fig. III.2.	68
III.6	Comparison of the film triple line position at the entrance (red line in Fig. III.2) of the largest channel (top plot identical to Fig. III.5) and at the end of the largest channel a bit before the junction with the interconnecting channel (bottom plot).	69
III.7	Evolution of the evaporation process in the SUEX-PDMS double channel with the the 0.5×10^{-4} g/mL concentration of particles (bright spots). Images every 49 minutes.	70
III.8	Evolution of the film width, from border to triple line in blue. The distance between the two lines represents the evolution of the width of accumulated particles at the entrance of the channel.	71

III.9	Kinetics of drying in each channel of the chip, red lines refer to the position of meniscus triple line on the PDMS top wall, blue ones on the SUEX bottom wall; a) larger channel, b) interconnecting channel, c) smaller channel with occurrence of a second receding meniscus.	72
III.10	Kinetics of the drying in every channel of the chip in the presence of a particles concentration of 10^{-4} , the red lines refer to the position of the front on PDMS, blue ones on the SUEX walls; a) right larger channel, b) middle channel, c) left narrower channel with the apparition of a second receding front.	73
III.11	The preferential zones of particle accumulation are in bright; a. after 281 min of evaporation, i.e. 5 minutes before the complete evaporation of the corner films, b. spatial distribution of deposited particles at the end of experiment after full evaporation.	74
III.12	Spatial distribution of deposited particles at the end of experiment after full evaporation. During the image treatment the brightness was increased to highlight the minor presence of deposited particles along the corners of all the channels.	74
III.13	Evolution of the evaporation process in a Plexiglas double channel closed with PDMS with images every 53 minutes. The bright spots represent particles.	75
III.14	Time steps, of 8 minutes, of the evolution of the evaporation process in a plexiglas double channel of width 0.2 mm closed with PDMS. The bright spots represent the particles.	77
III.15	Final particle deposit in the Plexiglas-PDMS system.	78
IV.1	Top) Image of the micromodel with liquid (in black) in the channels. Bottom) Sketch of the cross section of the micromodel with the various layers, PDMS is colored in grey for illustration but is transparent in reality	81
IV.2	Schematic of the drying setup for experiment at the atmospheric pressure. The setup is composed of a balance, two boxes on the side for the salt solution used to control the relative humidity, a back light and a support for the micromodel. Everything is placed in a transparent box (see Fig. IV.3).	83
IV.3	Photo of the set up of the experiment at atmospheric pressure.	84
IV.4	Experimental setup for the case with gravity effect.	85
IV.5	Set up of the experiment under vacuum conditions.	85
IV.6	Photo of the set up of the experiment under vacuum conditions.	86
IV.7	The assembly used for the partial vacuum drying experiments.	87
IV.8	PDMS deformation created on a channel by compressing the micromodel assembly of SUEX, PDMS and glass between the two Plexiglass plates.	87
IV.9	Steps of the image treatment procedure to obtain the percentage area, from the raw image, through the splitting of the channels, to the binary image.	89
IV.10	Comparison of the evolution of the dimensionless mass of liquid in the micromodel between the data of the balance and the image processing data. Drying is performed at atmospheric pressure; micromodel horizontal on the left; micromodel vertical on the right	90

IV.11	Comparison of the saturation patterns for $S = 0.9, 0.7$ and 0.5 (from left to right) between the case without gravity effects and with gravity effects. Liquid phase in black and gas phase in white, vapor escapes through top edge of micromodel. B is the Bond number ($B = \frac{\Delta\rho g a^2}{\gamma \cos\theta}$, where a is the distance between two nodes of network) characterizing the competition between gravity and capillary effects.	92
IV.12	Time step $t = 50h$ of $B > 0$ at atmospheric pressure.	92
IV.13	Comparison of the saturation patterns for $S = 0.9, 0.7$ and 0.5 (from left to right) between the case at normal gas pressure and the case under partial vacuum conditions for two temperature in the absence of gravity effects. Liquid phase in black and gas phase in white, vapor escapes through top edge of micromodel. A gas bubble is visible in the red circle.	94
IV.14	Comparison of the saturation patterns for $S = 0.9, 0.7$ and 0.5 (from left to right) between the case at normal gas pressure and the case under partial vacuum conditions for two temperature with gravity effects. Liquid phase in black and gas phase in white, vapor escapes through top edge of micromodel. Gas bubbles are visible in the red circles	95
IV.15	Evaporation kinetics. Impact of partial vacuum and temperature in the absence of gravity effects. The insets show the drying kinetics using the dimensionless time defined in the text.	96
IV.16	. Evaporation kinetics. Impact of partial vacuum and temperature with gravity effects. The insets show the drying kinetics using the dimensionless time defined in the text.	99
IV.17	Dimensionless evaporation kinetics. Impact of gravity effects.	100
V.1	On the left, equilibrium contact angles on SUEX right after the plasma treatment, after 20 hours and after 48 hours. On the right, evolution of the contact angles of an evaporating droplet of water set on a layer of SUEX treated with plasma	107
V.2	Patter used for scanning the deposit in the channels of the pore network.	109
V.3	Illustration of Fiji's plugin for stitching the images of the deposit. The particles correspond to the bright spots	109
V.4	Example of final image of the deposit (in bright light grey) in the micromodel after completion of the stitching procedure.	110
V.5	Comparison of the drying patterns for $S = 0.9, 0.7$ and 0.5 (from left to right) without gravity effects at $P = P_{atm}$, $T = 22^\circ\text{C}$ in the absence of particles and with particles. Liquid phase in black and gas phase in white, vapor escapes through top edge of micromodel. The black region in the red circle for the high concentration corresponds to a deposit of particles.	111
V.6	Comparison of the drying patterns for $S = 0.9, 0.7$ and 0.5 (from left to right) with gravity effects at $P = P_{atm}$, $T = 22^\circ\text{C}$ in the absence of particles and with particles. Liquid phase in black and gas phase in white, vapor escapes through top edge of micromodel.	112

V.7	Comparison of the drying patterns for $S = 0.9, 0.7$ and 0.5 (from left to right) without gravity effects ($B = 0$) under partial vacuum conditions ($P = 0.1P_{atm}$) and $T = 22^\circ\text{C}$ in the absence of particles and with particles. Liquid phase in black and gas phase in white, vapor escapes through top edge of micromodel. The red circles indicate the presence of expanding bubbles.	113
V.8	Comparison of the drying patterns for $S = 0.9, 0.7$ and 0.5 (from left to right) with gravity effects ($B > 0$) under partial vacuum conditions ($P = 0.1P_{atm}$) and $T = 22^\circ\text{C}$ in the absence of particles and with particles. Liquid phase in black and gas phase in white, vapor escapes through top edge of micromodel.	113
V.9	Comparison of the drying patterns for $S = 0.9, 0.7$ and 0.5 (from left to right) without gravity effects ($B = 0$) under partial vacuum conditions ($P = 0.1P_{atm}$) and $T = 50\text{-}60^\circ\text{C}$ in the absence of particles and with particles. Liquid phase in black and gas phase in white, vapor escapes through top edge of micromodel. The red circle indicates the presence of an expanding bubble (visible in the movie but not in the selected images shown here)	114
V.10	Comparison of the drying patterns for $S = 0.9, 0.7$ and 0.5 (from left to right) with gravity effects ($B > 0$) under partial vacuum conditions ($P = 0.1P_{atm}$) and $T = 50\text{-}60^\circ\text{C}$ in the absence of particles and with particles. Liquid phase in black and gas phase in white, vapor escapes through top edge of micromodel.	115
V.11	Drying kinetics for various initial particle concentrations in the absence of gravity forces for $P = P_{atm}$, $T = 22^\circ\text{C}$	116
V.12	Drying patterns for $S = 0.9, 0.7$ and 0.5 (from left to right) without gravity effects at $P = P_{atm}$, $T = 22^\circ\text{C}$ for the higher concentration in particles (experiments #1 and #2). Liquid phase in black and gas phase in white, vapor escapes through top edge of micromodel. Deposit of particles (unfortunately in black as for the liquid phase) is present on top of the images.	117
V.13	Comparison of drying kinetics for pure water and the low concentration in particles in the presence of gravity forces for $P = P_{atm}$, $T = 22^\circ\text{C}$. .	118
V.14	Comparison of drying kinetics for pure water and the low concentration in particles in the absence and in the presence of gravity forces for $P = 0.1P_{atm}$, $T = 22^\circ\text{C}$	118
V.15	Formation of bubbles for the case of pure water and the low concentration in particles in the absence of gravity forces for $P = 0.1P_{atm}$ and $T = 22^\circ\text{C}$, images at $t = 11\text{min}$	119
V.16	Comparison of drying kinetics for pure water and the low concentration in particles in the absence and in the presence of gravity forces for $P = 0.1P_{atm}$, $T = 50\text{-}60^\circ\text{C}$	120

V.17	Final particle deposit (in bright light grey) in the micromodel for the various drying conditions and the low initial particle concentration (0.5×10^{-4} g/mL). Note that drying with expanding bubbles as observed for the conditions $B = 0$, $P = 0.1P_{atm}$, $T = 22^\circ\text{C}$, $T = 50\text{-}60^\circ\text{C}$. The white rectangles in the image for $B > 0$, $P = 0.1P_{atm}$ and $T = 22^\circ\text{C}$ represent areas for which the superposition of images could not be satisfactorily achieved with the image stitching procedure (see Section V.2.4 for details on this image recombination procedure)	122
V.18	Schematic of liquid trapped in corners in micromodel channels (the image with cubic blocks is adapted from [Geistlinger <i>et al.</i> , 2019])	123
V.19	Illustration of “corner deposit” (left) and “plugging deposit” (right). . .	123
V.20	Final particle deposit (in bright light whitish/grey) in the micromodel for the conditions $B=0$, $P = P_{atm}$, $T = 22^\circ\text{C}$ and the low and higher initial particle concentration.	125
V.21	Comparison of the drying patterns for $S = 0.9$, 0.7 and 0.5 (from left to right) for $B = 0$, $P = P_{atm}$, $T = 22^\circ\text{C}$ with low concentration in particles for the “right after” and “one month after” experiments. Liquid phase in black and gas phase in white, vapor escapes through top edge of micromodel.	126
V.22	Comparison of drying kinetics for the “right after” and “one month after” experiments. for the low concentration in particles in the absence of gravity forces for $P = P_{atm}$, $T = 22^\circ\text{C}$	126
V.23	Illustration of corner liquid films in a channel of square cross-section (from Chapter 1 in [Prat, 2023])	127
V.24	Final particle deposit (in bright light whitish/grey) in the micromodel for the conditions $B = 0$, $P = P_{atm}$, $T = 22^\circ\text{C}$ and the low initial particle concentration for the “right after” and “one month after” experiments. .	127
V.25	Enumeration of the channels, in black the horizontal ones and in red the vertical ones. Examples of ROIs in yellow.	129
V.26	On the left the final image of the deposit for the experiment with the horizontal chip at atmospheric pressure and with particle concentration 0.5×10^{-4} . On the right, the result after the binarization process, where the black pixels represent the deposited particles.	129
V.27	Division of the micromodel in horizontal slices.	130
V.28	Experiment for $B = 0$, $P = P_{atm}$, $T = 22^\circ\text{C}$, $C = 0.5 \times 10^{-4}$ g/mL: a. correlation between the sizes of the channels and their mean levels of grey, b. correlation between the sizes of the channels and the percentage area, c. difference in absolute value between the norms of the mean grey values and the area percentages, d. correlation between the area percentage and the brightness.	131
V.29	Experiment for $B > 0$, $P = P_{atm}$, $T = 22^\circ\text{C}$, $C = 0.5 \times 10^{-4}$ g/mL, a. correlation between the sizes of the channels and their mean levels of grey b. correlation between the sizes of the channels and their area percentage, c. difference in absolute value between the norms of the mean grey values and the area percentage, d. correlation between the area percentage and the brightness	132

V.30 Correlations between the channel size and the deposit mean level of grey for the different experiments and the low concentration in particles. The cases between the horizontal and vertical micromodel position are compared for the same pressure and temperature conditions on each horizontal row. The columns are for the same micromodel position (horizontal or vertical) but different temperatures (a. 20°, c. 20°, e. 50/60°) or pressures (b. P_{atm} , d. P_{atm} f. $P = 100mbar$.) 134

V.31 Individual channel “evaporation” starting times as function of channel size and localization in the network (color code) for the conditions ($B = 0$, $P = P_{atm}$, $T = 22^\circ C$, 1 month after plasma treatment). The final deposit (bright zones) is shown in the image on the right. 135

V.32 Deposit channel invasion sequence for the conditions ($B = 0$, $P = P_{atm}$, $T = 22^\circ C$, 1 month after plasma treatment). The final deposit corresponds to the bright zones. 136

B.1 In light blue the evolution of the liquid in two different channels, for the enumeration refer to Fig. V.25. The dashed lines are the different fitting function computed from different starting conditions while the yellow dots highlight the best fitting function. On the left the best fitting function is given by the starting conditions $a = 100$, $b = 800$, while on the right $a = 200$, $b = 700$ 146

B.2 The black dashed line is the best fitting function (yellow in Fig. B.1) and the red dot represent the computed starting point of the evaporation in this channel, through the gradient condition. The green point is the computed end time step of the evaporation, although you may notice that the drying is not properly finished, it may have stopped or liquid films are still present. 147

List of Tables

IV.1	The various drying conditions explored in the chapter.	80
V.1	The various drying conditions explored in the chapter for the low concentration in particles (0.5×10^{-4} g/mL). The red cells indicate an experiment with expanding bubbles.	105
V.2	Conditions for the two experiments performed with a high particle concentration (0.6×10^{-2} g/mL)	106

Abstract

Using a SUEX resin microchannel, we studied the effect of the presence of particles on the evaporation dynamics in a single channel. The experiments showed that the kinematics is slowed down by the presence of the particles due to their effect on the thickness of the corner films. They are thicker with pure water than in the presence of particles, at small concentrations, which results in smaller vapor partial pressure gradients in the channel entrance region. The work is extended considering a two-dimensional network of interconnected channels as model porous medium. To this end, an experimental set up was developed to study the effect of the particles presence in the model porous medium and their respective deposit. The constructed network is composed of interconnected throats of rectangular cross section. The drying process is analyzed from optical visualizations, while the deposit is observed under the microscope with confocal green light. Different parameters were varied in order to better understand the particles preferential regions of deposit and their relation with the drying pattern. For example, changing the wettability of the chip's material completely changes the localization of the deposit. The particles concentrate in the channels closest to the top edge of the network (open edge of network), while the concentration is decreasing further away in the network. Two other variables that were changed, was the total pressure and temperature. Using an oven to perform the drying under partial vacuum condition (100mbar) at ambient temperature and at 55°C , the invasion patterns are very different from the one obtained at the atmospheric pressure under diffusive evaporation condition and the deposits are more homogeneous throughout the micromodel. Furthermore we investigated the role of gravity on the evaporation rate, which was slowed down, and on the final deposit for which it is found out that particles do not tend to accumulate at the bottom of the network, instead the distribution is still homogeneous.

Resumé

Dans un premier temps, l'effet de la présence des particules sur la dynamique de l'évaporation est étudié dans un canal unique en résine SUEX. Les expériences montrent que la cinématique est ralentie en présence de particules du fait de leur influence sur l'épaisseur des films liquides dans les coins. Ces derniers sont plus épais avec de l'eau pure qu'avec une faible concentration de particules. Cela induit des gradients de pression partielle plus faibles dans la région de l'entrée du canal. Le travail est ensuite approfondi en considérant un réseau en deux dimensions de canaux de section rectangulaire et interconnectés comme un modèle d'un milieu poreux. Une installation expérimentale a été développée afin d'étudier l'effet de la présence de particules et leur dépôt dans un milieu poreux. Le processus de séchage est analysé par visualisation optique, alors que le dépôt est observé à l'aide d'un microscope confocal à lumière verte. Une sensibilité sur différents paramètres est effectuée pour une meilleure compréhension des régions préférentielles du dépôt des particules et de leur relation avec le chemin de séchage. Il est d'abord montré que changer la mouillabilité du milieu poreux modifie complètement la localisation de ce dépôt. Les particules se concentrent dans les canaux plus proches du côté supérieur (le côté ouvert du réseau), alors que la concentration diminue plus loin dans le réseau. Ensuite, l'effet de la pression totale et de la température est étudié en utilisant un four pour réaliser des expérimentations sous des conditions de vide partiel (100mbar), à température ambiante et à 55°C . On montre alors que le chemin d'invasion peut être affecté par la formation de bulles d'air sous vide partiel. Globalement, les dépôts sont plus homogènes dans le micromodèle. Enfin, l'impact de la gravité sur le taux de séchage et sur le dépôt final a aussi été investigué. On trouve alors que les particules n'ont pas tendance à s'accumuler dans le fond du réseau mais sont distribuées de façon assez homogène.

Introduction

Drying of colloidal dispersions has been the subject of many studies, e.g. [Dufresne *et al.*, 2003, Lidon et Salmon, 2014] and references therein, because it is both a fascinating phenomenon and of importance as a common industrial process, such as the fabrication of fuel cell components [Ito *et al.*, 2014], as well as for engineering innovative materials [Velev et Gupta, 2009]. As pointed out in [Keita *et al.*, 2013], drying of a suspension in a porous medium is also frequent in industry and nature in relation with the transport of pollutants through soils [Michel *et al.*, 2010], the evolutions of soil fertility [Alramahi *et al.*, 2010] the hydrophobization of porous components [Ito *et al.*, 2014] or the improvement of the thermal properties of electronic chips [Brunschwiler *et al.*, 2016], to name only a few. Nevertheless, the understanding and modeling of the effect of colloidal suspensions in a drying porous medium are less advanced than for the drying of suspensions, e.g. [Bacchin *et al.*, 2018] and references therein, but have significantly been improved in recent years thanks to new experimental and numerical studies, e.g. [Keita *et al.*, 2013, Keita *et al.*, 2016a, Keita, 2021, Qin *et al.*, 2019]. In [Qin *et al.*, 2019], the focus was on the formation of clogging structures induced by evaporation within a model porous medium from numerical simulations at the pore scale. In [Keita *et al.*, 2013] and [Keita, 2021], experimental results with granular medium columns showed that drying is slower in the presence of particles compared to pure water. The greater the particle concentration, the slower is the drying. As in the case of drying with a saline solution, e.g. [Huinink *et al.*, 2002, Eloukabi *et al.*, 2013], the particles are transported by advection up to the evaporative surface where they accumulate, deposit and reduce the porosity [Qin *et al.*, 2019]. This process leads to the formation of a region with deposited particles on top of the granular column [Keita *et al.*, 2013]. The gradual decrease of the evaporation rate was then explained by the formation of a receding evaporation front into the medium as a result of the deposit of particles in the top region of the column.

On the other hand, it has been shown that thick capillary liquid films, also referred to as corner liquid films, can have an important impact in drying, e.g. [Chauvet *et al.*, 2009, Yiotis *et al.*, 2004, Prat, 2007, Yiotis *et al.*, 2012]. These films formed in crevices or cor-

ners in the pore space are distinct from the thin films with thickness of the order of nanometers, e.g. [Zhao *et al.*, 2011]. Compared to that of thick capillary films, the contribution of thin films to the overall liquid flow in drying is considered as negligible [Yiotis *et al.*, 2004]. In the simple situation of evaporation in a capillary tube, drying is much faster in a square tube compared to drying in a circular tube due to the presence of capillary liquid films along the inner corners of the square tube. Such an enhanced evaporation effect was also reported in micromodel experiments [Laurindo et Prat, 1998] as well as in a packing of grains confined between two plates [Yiotis *et al.*, 2012]. Results on these aspects will be synthesised in Chapter I. Thus, the question arises as to whether a slower drying in the presence of particles can be attributed to the effect of particles on the capillary films.

In Chapter II, this question is addressed from evaporation experiments in a channel of almost square cross-section in conjunction with numerical simulations combining Surface Evolver [Brakke, 1992] simulations of the gas-liquid interface in the channel and computations of the evaporation rate using a commercial code, followed by a discussion on the possible mechanisms leading to the corner film thinning.

Chapter III is dedicated to the presentation of the experimental results and visualizations, through the presence of fluorescent particles, of the capillary pumping effect in a system of two interconnected channels of different widths [Javadi *et al.*, 2013]. First we present this effect where the meniscus in the largest channel recedes, while it stays stuck in the narrower. Afterwards, we show experiments with the opposite outcome.

The work is extended considering a two-dimensional network of interconnected channels as a model porous medium. To this end, in Chapter IV, an experimental set up was developed to study the evaporation in a two dimensional pore network. We studied the effects on the evaporation rate by modifying different parameters such as the vertical or horizontal position of the chip, the temperature and the pressure.

Finally, in Chapter V the same experiments are reproduced in the pore network with different concentrations of fluorescent particles with the subsequent study of the deposit in the channels. Here, the effect of changing the wettability of the material is investigated finding the same results as in [Shokri *et al.*, 2008].

Chapter I

State of the art and advances on drying

Contents

1	Evaporation at the pore-scale	3
1.1	The capillary circular tube	4
1.2	The effect of liquid films	6
2	Evaporation in a porous medium	8
3	Particles and deposit	10
3.1	Thin films and droplets	10
3.2	Confined geometries	11
3.3	The porous medium	15
4	The effect of wettability on evaporation	18
5	Motivation and objectives	20
5.1	The fuel cell and its water problematic	20
5.2	The hydrophobization of the Gas Diffusion Layer	22

1 Evaporation at the pore-scale

In this section we present a model to describe the physics of the evaporation phenomenon at the porous scale. Considering a circular cylinder it is possible to predict the reduction of the liquid's level using Stefan's law [Mitrovic, 2012] with inspiration from [Bird, 2002]. Nevertheless, by changing the shape of the tube's cross section, the formation of corner films is observed [Prat, 2007]. We report here some results concerning the effects of films in a squared capillary tube during evaporation [Chauvet, 2009] and, finally, the state of the art research about the capillary evaporation with particle and their deposit.

1.1 The capillary circular tube

Let us consider the simplest situation of a capillary tube with a circle section, one closed side and partially filled with volatile liquid, see Fig. I.1. The air around the system is kept dry so that the liquid can evaporate, then the vapor is transported thanks to the diffusion in the atmosphere from the liquid interface. The system is isothermal, since the cooling related to the change of phase is negligible. In these conditions it is possible to predict the position of the front thanks to the Stefan law [Mitrovic, 2012].

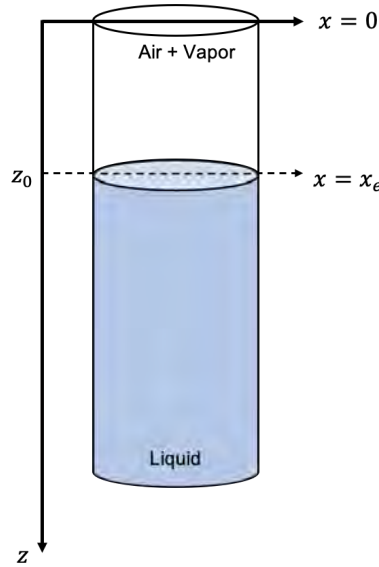


Figure I.1: Schema of evaporation in a capillary tube

Assuming that the process of evaporation is slow, we consider the system quasi-stationary. In addition we make the one dimensional hypothesis that the height of the cylinder ℓ is much bigger than its radius r , then the general diffusion equation of vapor in gas phase above the meniscus is:

$$n_v = x(n_v + n_a) - \xi D \frac{dx}{dz} \quad (1.1)$$

where z is the ordinate axis depicted in Fig. I.1, \vec{n}_v is the vapor molar flux, \vec{n}_a the air molar flux, x the vapor molar flux in the gaseous phase, ξ the molar density of the mixture and D the diffusion coefficient of the vapor in the air. On the other hand, the air can be consider stagnant, since it does not dissolve in the liquid and the system is quasi-stationary, then we can say $n_a = 0$ [Incropera et Incropera, 2007], so that Eq. 1.1 becomes:

$$n_v = \frac{\xi D}{1 - x} \frac{dx}{dz} \quad (1.2)$$

It is important to notice that, similarly to the presence of the molar fraction of the vapor gradient, it exists a molar fraction of air gradient x_a , indeed the air enters the capillary tube and it necessarily exits since it can mix with the liquid. Therefore, strictly speaking, the air cannot be considered as stagnant in every point of the cylinder.

By knowing that the only variable that depends on z is the molar fraction x , it is easily possible to integrate Eq. 1.2 between $x(z = 0) = 0$ and $x(z = z_0) = x_e$, where x_e is the vapor molar fraction at the equilibrium, then we can express the molar vapor flux as:

$$n_v = -\frac{\xi D}{z_0} \ln \left(\frac{1}{1 - x_e} \right) \quad (1.3)$$

Thanks to 1.3, we can predict the evaporation rate $E = M_v d^2 n_v$, where M_v is the vapor molar mass, when the front is at a distance z_0 from the top. It can be described as well by using the height of the liquid in time $E = -\rho_l d^2 \frac{dz_0}{dt}$, then by combining the two different formulas for the evaporation rate with (1.3), we obtain the evolution of z_0 :

$$z_0 = \sqrt{\frac{2M_v \xi D}{\rho_l} \ln \left(\frac{1}{1 - x_e} \right) (t - t_{start})} + z_{0,start} \quad (1.4)$$

where $z_{0,start}$ is the initial position of the air-liquid interface at the initial time t_{start} . This equation is known as Stefan's law and it may be noticed that it is independent of the diameter of the cylinder.

It has to be kept in mind that this law is valid under the hypothesis that the air is considered as stagnant, although, strictly speaking, there exists a circulation in the capillary. In fact, as a molar fraction of vapor exists along z , there exists also a molar fraction of air transported toward the interface and, since it cannot penetrate in the liquid, it has to leave the cylinder, creating a convective movement. Several works were conducted to estimate this effect on the evaporation rate and to correct Stefan's law. In [Heinzelmann *et al.*, 1965], they examined theoretically, by using the Taylor diffusion model, and experimentally the concentrations profiles in the tube with the conclusion that the radial concentration profile is effectively flat across the diffusion tube. While in [Meyer et Kostin, 1975] they found that, by coupling diffusion and Navier-Stokes equations, there is an effective circulation in the gaseous species, which, consequently, cannot be considered stagnant. More recently, by applying to the Stefan diffusion tube the theory of [Kerkhof et Geboers, 2005] for a two-dimensional fluid transport, in [Salcedo-Díaz *et al.*, 2008], they found that for narrow tubes shear effects dominate, while for larger the results are still comparable with Stefan's law.

1.2 The effect of liquid films

The mechanism of evaporation in a square capillary tube is radically different from the case of the circular one due to the presence of liquid films [Prat, 2007, Yiotis *et al.*, 2004]. On the other hand, [Camassel *et al.*, 2005] studied theoretically and experimentally evaporation in a square cross-section tube. The transport equation of vapor in the gas phase was numerically solved for different lengths and thicknesses of the films of a perfectly wettable liquid. The results show that the gaseous phase stays saturated in the tube, except close to the top of the films. This demonstrates that most of the liquid-gas interface does not contribute to evaporation, but only the top of the films is active, which is an indication of the films effect to "bring" the liquid to evaporate. Moreover, Camassel made some qualitative experiments thanks to which it could be established that evaporation in square cross section capillary tube is faster than in a circular one.

Starting from this results for which evaporation happens only at the top of the films, in [Prat, 2007], an analytical model of evaporation taking into consideration only capillary and viscous effects was developed. Two periods are identified, the first one, when the films are still attached to the top of the tube, is characterized by a constant evaporation rate. Then, the second period starts when the the curvature R of the top of the films tends to zero, which is when the films start to recede and an evolution in \sqrt{t} is expected for the position of the front.

Under the assumption of a quasi-stationary state, [Chauvet *et al.*, 2010], showed the importance of viscous effects by modeling the mass flow rate in the corners starting from the results presented in [Ransohoff et Radke, 1988], where they studied the effect of corner geometry, Fig. I.2, contact angle and surface shear viscosity on the laminar flow of a wetting liquid. Therefore the liquid flow rate in the liquid films is related to the liquid pressure gradient by a Poiseuille-like law corrected for gravity [Chauvet *et al.*, 2010]:

$$q(z) = -\rho_l \frac{A_c R^2}{\beta \mu_l} \left(\frac{dp_l}{dz} - \rho_l g \right) \quad \text{for } z_f < z < z_0 \quad (1.5)$$

where $A_c = \lambda R^2$ is the passage section of the liquid fingers, μ_l is the dynamic viscosity of the liquid and z_f is the position of the fingers top. Considering the law of Laplace for the liquid pressure and the experimental measure for the mass flow rate, they obtain an implicit formulation for the curvature of the film's top $R(z_f)$. At this point two cases are considered, the vertical capillary tube and the horizontal one. Their results show that, in the fist case, the detachment of the films is after a moment, on the other hand, when the tube is horizontal, they stay connected to the top of the tube. The slimming of

the films, when the tube is vertical is mainly due to gravity, when their thickness is still important, then when they get thinner, viscous friction becomes more significant until the detachment. After this moment, the rate of evaporation decreases, as well as viscous effects, and the films thickness is controlled by gravity. Instead, in the horizontal case, solely the viscous effects regulate the films thickness. In addition, the model presented to predict the slimming is conformed with experimental observations.

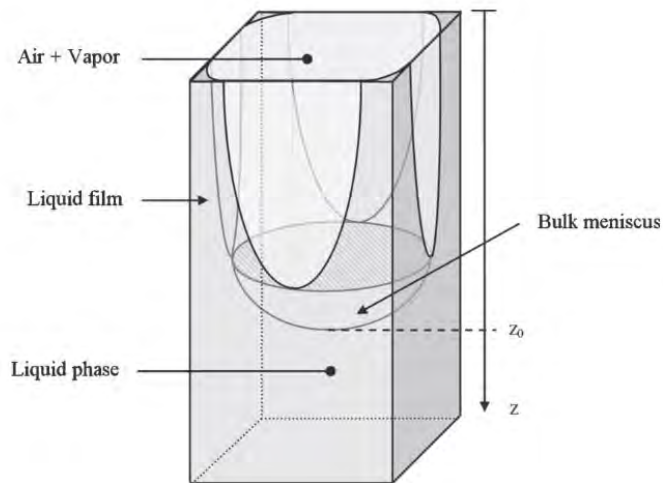


Figure I.2: [Chauvet *et al.*, 2010] Sketch of the thick liquid films in a capillary tube of square cross section. The bulk meniscus position is denoted as z_0

In his thesis, Chauvet explains, with different experiments, the cinematic of evaporation in capillary tubes with different sizes. This process can be divided in three phases, the CRP, constant rate period, the FRP, falling rate period, and the RFP, receding front period. During the first phase the liquid films are connected to the top of the tube and the rate of evaporation, see Fig. I.3, is high and it slowly decreases due to the slimming of the films under the effects of gravity and viscosity. On the other hand, during the second period, the films are no more connected to the top, but they move away causing a supplementary diffusive resistance for the transport of vapor. Thus, the rate of evaporation brutally falls. Finally, during the last period, the RFP, the internal diffusive resistance augments as the liquid evaporates, then we can distinguish two situations: if the effect of gravity is present or not. In the first case the length of the films tends to its hydrostatic equilibrium and the cinematic obeys to the law $z_0 \propto \sqrt{t}$ in the long times same as in the absence of gravity, but in this case the films stretch out indefinitely.

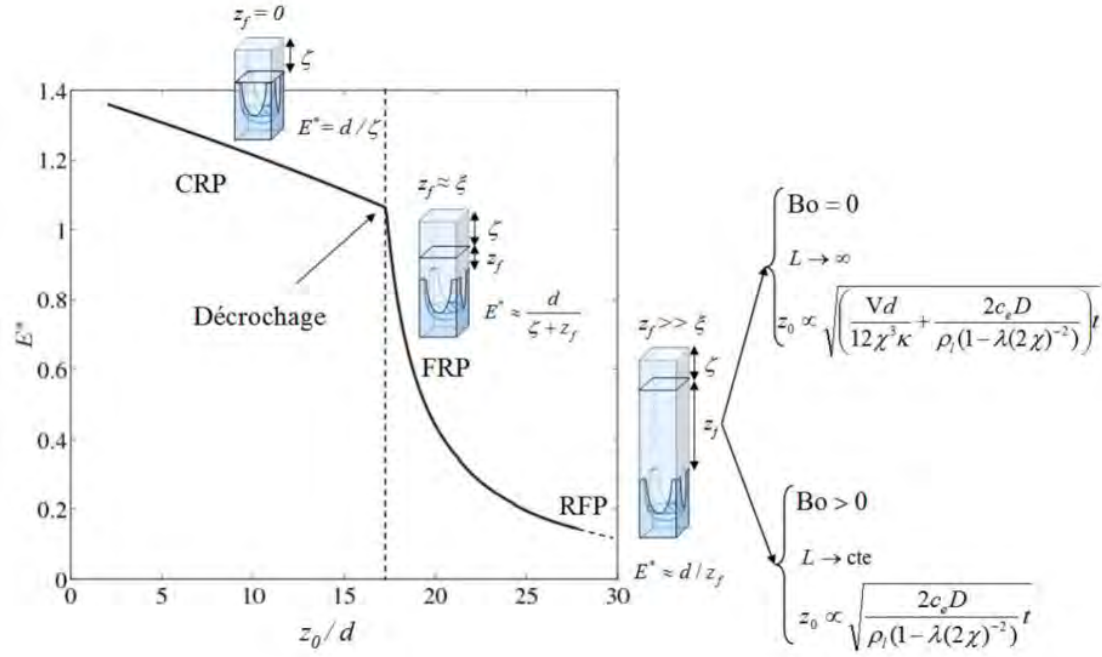


Figure I.3: Overview of drying and flooding problem [Chauvet, 2009], where Bo is the Bond number

2 Evaporation in a porous medium

Many studies have concentrated their attention on the evaporation phenomenon of a saturated porous medium. From an experimental perspective, the mostly used ways of reproducing a porous medium with known properties, are columns of sands [Shokri *et al.*, 2008, Zhang *et al.*, 2010] or glass beads [Hidri *et al.*, 2013], for a three dimensional investigation, or micro models to decrease complexity and have solely two dimensions [Laurindo et Prat, 1996, Laurindo et Prat, 1998]. These are models recreating porous media, for which the distribution of the pores, the shape and their sizes are determined, for example, [Roman *et al.*, 2016] etched silicon micro-models that represent natural complex porous media (e.g., sandstone). Moreover they can be produced with different materials, in this thesis SUEX is employed (see the next Chapters or Annex A on the protocol) although other resin materials can be employed in experimental studies, especially PDMS (polydimethylsiloxane) [Fujii, 2002, Friend et Yeo, 2010, Fantinel *et al.*, 2017, Zhang *et al.*, 2014].

Evaporation from a porous medium is the effect of the difference in the vapor partial pressure at its surface ($p_{v,s}$) with respect to the vapor pressure in the surrounding air ($p_{v,\infty}$), creating a transfer of the liquid molecules into the gaseous phase. Therefore the velocity of this process j can be estimated through $j \propto p_{v,s} - p_{v,\infty} = \frac{dm_e}{dt}$, where m_e is

the evaporated mass. Commonly, for experiments, this evolution is expressed through the registration of mass data thanks to a balance. This register the loss of the liquid in time which gives us the saturation of the porous media $S = \frac{m_l}{m_T}$, where m_l and m_T are respectively the liquid mass and the total initial mass. On the other hand, we can rewrite m_l as a function of the total mass as $m_l = m_T - m_e$, therefore, using the previous definition of the evaporation rate, it is possible to write it as a function of the liquid mass evolution or of the saturation $j = -\frac{dm_l}{dt} = -\frac{dS}{dt}$.

This process changes in function of the surrounding conditions such as the temperature, the absolute pressure or the boundary conditions, for example an air stream at the open face of the porous medium can be imposed, called the convective drying, for which introduces a turbulent region. Overall, the drying kinetics, similarly to the capillary tube case of Fig. I.2, can be characterized by two main stages, see Fig I.4

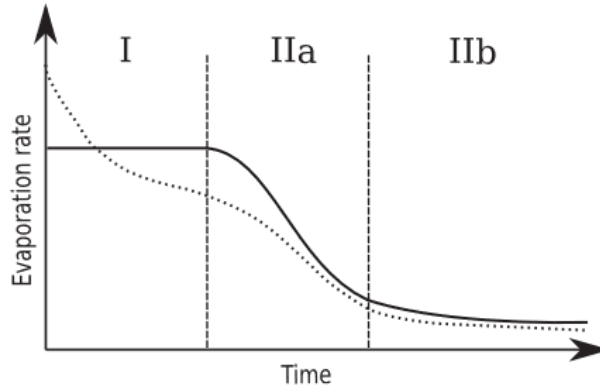


Figure I.4: Typical evolution of the drying rate from a porous medium highlighting the different characteristic stages [Mosthaf *et al.*, 2014]

During the first stage the evaporation is constant with high evaporation rate, also called CRP (constant rate period), this is caused by the capillary action transporting the water molecules up to the surface of the porous medium. Next, the evaporation enters the falling rate period, FRP or stage IIa in Fig. I.4, where the evaporation drops over time with capillary forces growing weaker, eventually, we observe a dried zone at the top of the porous medium. Lastly, the last period, IIb in Fig. I.4, is defined by the front receding in the porous medium no direct evaporation at the surface, this period is also called RFP that stands for receding front period.

3 Particles and deposit

In this section we report some recent research on the particles dynamics in different configurations of a drying liquid. First we look into evaporation of "free" shapes, such as drops or thin film, then the solvent is confined to different geometries, such as a capillary tube or two plates and finally we will talk about the deposit in a porous medium.

3.1 Thin films and droplets

The drying of a suspension or a solution is a common technique to realize the coating or covering of a solid surface. Though many studies have been devoted to the design of controlled patterned deposits, such as the evaporation in thin films and the following creation of line patterns [Vyawahare *et al.*, 2006], or the drying of a drop of water where the interaction of paramagnetic particles was possible thanks to the presence of an external magnetic field [Helseth et Fischer, 2003], a full understanding of the dominant phenomena is still lacking, as the process is governed by the coupling between hydrodynamics, heat and mass transfer, and physico-chemical properties of the solution and the substrate.

In [Bodiguel et Leng, 2010], it was possible to investigate from the inside the drying kinetics of a droplet through fast confocal microscopy, i.e. imaging several time- and space-dependent fields in a droplet of a colloidal suspension undergoing evaporation, see Fig. I.5. The technique permits to observe simultaneously the fluorescence due to the dispersed phase, and the one due to particles that act as tracers. They observed that in the case of an aqueous drop on glass, evaporation generates a three-dimensional flow due to a thermal Marangoni effect.

[Haw *et al.*, 2002] studied the effects of phase behavior on the evaporative drying of droplets of a suspension of hard sphere colloidal particles and nonadsorbing polymer. As drying (evaporation of solvent) progresses, the concentrations of both colloid and polymer increase, so that the droplet's average composition traces out a "drying line" across the composition diagram. They found that drying behavior can be broadly classified according to the initial composition of the suspension, into three regions on a "drying behavior diagram".

Furthermore, [Routh et Zimmerman, 2004] examined the distribution of particles during solvent evaporation from thin films, proposing an analysis based on the Peclet number defined as $Pe = \frac{6\pi\mu R_0 H \dot{E}}{kT}$, is the rate of particle convection divided by the rate of diffusion. Here μ is the solvent viscosity, R_0 is the particle radius, H the film thickness, \dot{E} the evaporation rate and kT the thermal energy. Notice that for colloidal particles the diffusion coefficient is defined as $D_0 = \frac{kT}{6\pi\mu R_0}$. The governing equation for evolution of

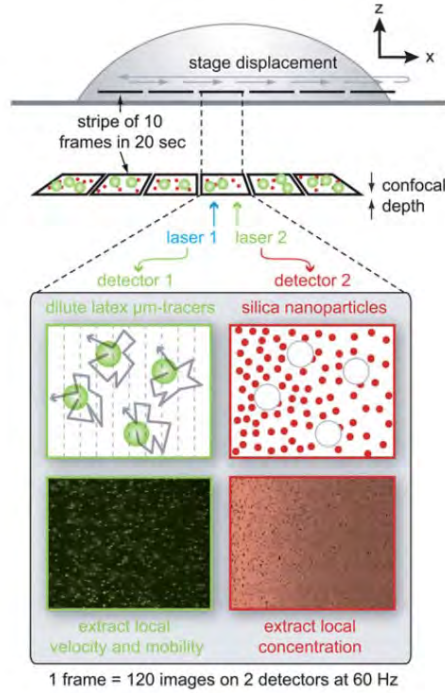


Figure I.5: [Bodiguel et Leng, 2010] Schematic view of the sessile droplet of colloidal suspension (nanoparticles + colloidal tracers) sitting on a glass substrate and undergoing evaporation. The data acquisition process consists in rapidly and repeatedly scanning the drop with a confocal microscope along the x-direction at a fixed z-position.

particle volume fraction ϕ is derived:

$$\frac{\partial \phi}{\partial t} = \frac{1}{Pe} \frac{\partial}{\partial y} \left[K(\phi) \frac{d}{d\phi} [\phi Z(\phi)] \frac{\partial \phi}{\partial y} \right] \quad (3.1)$$

where $Z(\phi)$ is the compressibility of the dispersion and $K(\phi)$ is the sedimentation coefficient. They used three distinct methods to examine the distribution of particles in an evaporating film. Direct numerical simulation gave a solution to the governing equation, although numerical problems were encountered as the Peclet number increased. This is because of the divergence of the compressibility in the packed region as the volume fraction approaches close packing.

3.2 Confined geometries

Recent works studied the evaporation phenomenon with colloidal suspension in confined geometries. For example, Leng's work, [Leng, 2010], is focused on a qualitative picture of the drying of a colloidal solution between two glass plates. They used two colloids sizes and different concentration and they observed that the particles tends to accumulate at the meniscus, where a crust is formed, see Fig I.6.

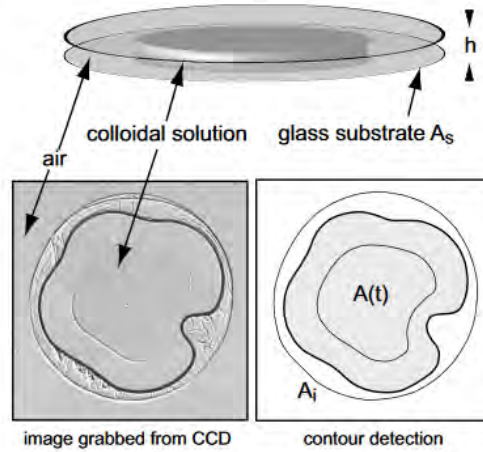


Figure I.6: [Leng, 2010] Schematic view of the confined drying geometry where a droplet of a colloidal solution is squeezed in between two circular glass plates and let to dry up. A camera captures the image and is further processed for contour detection.

More recently, [Loussert *et al.*, 2016] studied the same configuration of a drop, with a charged colloidal dispersion, between two glass plates, but covered with a thin layer of PDMS to avoid the pinning of the contact line. Through the imaging of fluorescent tracers, the drying of the drop is characterized by two regimes, first the flow is induced by buoyancy forces, then tracer trajectories reveal a gelation of the colloids that traps the tracers.

In [Bodiguel *et al.*, 2009], they studied the pattern formation during the drying of a colloidal suspension between two plates spaced by 0.4 to 1 mm. The deposition of particles is characterized by the velocity of evaporation. In fact, at high velocities the deposit is more homogeneous as the movement of the contact line is continuous, on the other hand, when the velocity is smaller, they observe the stick-slip phenomenon, leading to a patterned deposit, as illustrated in Fig. I.7. The critical velocity characterizing the transition, is shown that depends on the concentration of particles.

The same results were found in [Jing *et al.*, 2010] with a similar experiment, here the set up allows to control the velocity of the contact line thanks to a push-pull syringe that pumps out the liquid from the reservoir where the plates are immersed allowing a capillary rise. Almost the same configuration is used by [Doumenc et Guerrier, 2010], where they developed a model simulating the drying of a solution in a meniscus in contact with a moving substrate, and depending on this velocity it describes the way in which the evaporation flux and concentration profile take shape, the geometry is reported in Fig. I.8. The governing equations describing the liquid are the global mass conservation and

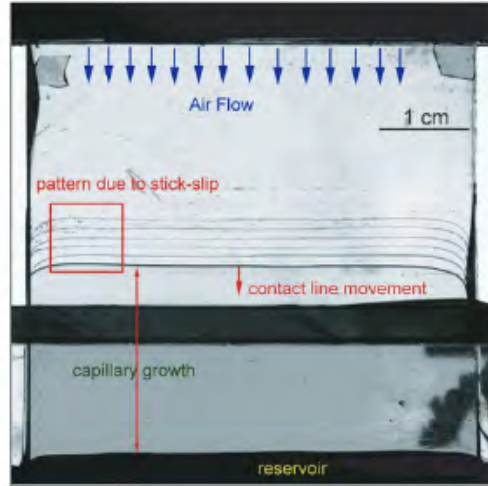


Figure I.7: [Bodiguel *et al.*, 2009] Optical image of the capillary rise during a typical experiment. The cell thickness is 0.40 mm. On this image, horizontal patterns can be seen above the capillary rise.

the nonvolatile solute mass conservation, respectively:

$$\begin{aligned} \frac{\partial h}{\partial t} + \frac{\partial Q}{\partial x} &= -\nu_{ev}(x, t) \\ \frac{\partial \phi h}{\partial t} + \frac{\partial \phi Q}{\partial x} &= \frac{\partial}{\partial x} \left(h D_{mut} \frac{\partial \phi}{\partial x} \right) \end{aligned} \quad (3.2)$$

where h is the liquid height, $Q(x, t)$ its volume flux, ν_{ev} is the local evaporation velocity, determined by solving a diffusion problem in the gas phase, ϕ is the solute volume fraction and D_{mut} is the mutual diffusion coefficient of the binary system. Their results showed that for a large substrate velocity, the classical Landau-Levich regime is obtained, for which if a plate is withdrawn out of a wetting bath at low capillary numbers, it deforms the very top of the liquid reservoir. At this place, a dynamic meniscus forms, whose shape and curvature select the thickness of the film entrained by the plate. For smaller velocities, a drying front appears that is characterized by a strong concentration gradient and a peak in the evaporation flux.

Instead of using two plates, in [Abkarian *et al.*, 2004], they studied the pattern created by the deposition of the particles in a cylinder. The results are similar to the ones previously described, the patterns are characterized by rings of different heights, which, along with the spacing between them, it changes in function of the concentration of beads and the velocity of evaporation. Indeed, as the concentration increases, the gap between the rings gets bigger.

Considering a glass capillary tube with rectangular cross section, [Dufresne *et al.*, 2003]

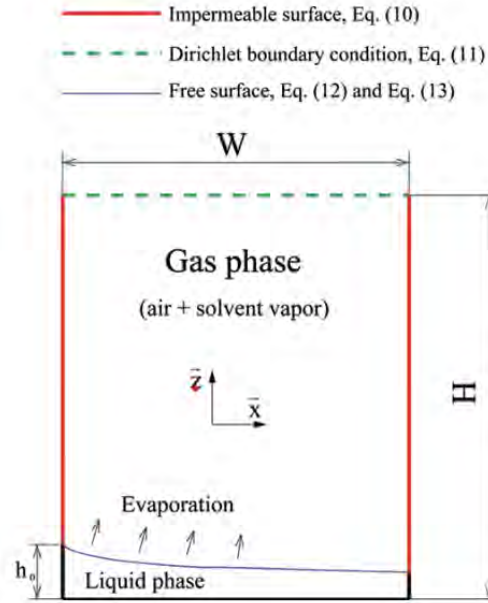


Figure I.8: [Doumenc et Guerrier, 2010] Sketch of the Problem Geometry.

investigated the drying dynamics of a solution of silica nanoparticles and the formation of cracks after a few minutes from the beginning of the experiment, see Fig. I.9. Evaporation takes place at $y = 0$ and the progression of a compaction front y_F is observed, as the liquid flows toward the top. The growth of this front gets slower in time, forming a porous media with a pore size of the order of the particle size (nm), and, as a consequence, the drying rate is reduced.

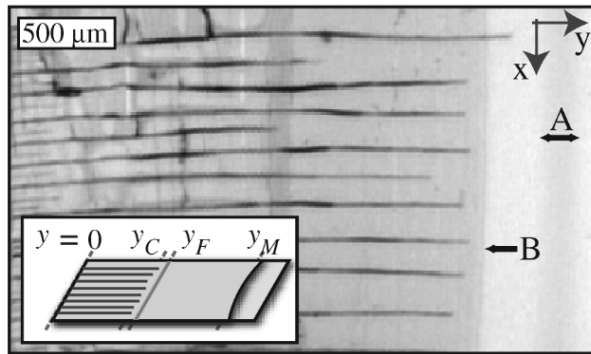


Figure I.9: [Dufresne *et al.*, 2003] Bright-field image of a drying suspension of silica nanoparticles. Inset: a schematic of the experimental geometry. Water evaporates from the drying edge, $y = 0$. The crack tips extend to y_C , just behind the compaction front, at y_F . The inner meniscus lies at y_M .

More recently, a similar problem is examined by [Pingulkar et Salmon, 2023]. In their paper they evaluate the different mechanisms of the particles effect during directional drying, such as in a capillary tube or in a Hele-Shaw cell. Their model is described by the water potential and the initial configuration is the one in Fig. I.10. As a result, the

slowing down of the evaporation rate to the square root of time finds its explication in, one, the Kelvin effect, and two, the recession of the evaporative interface (*capillary-limited regime*).

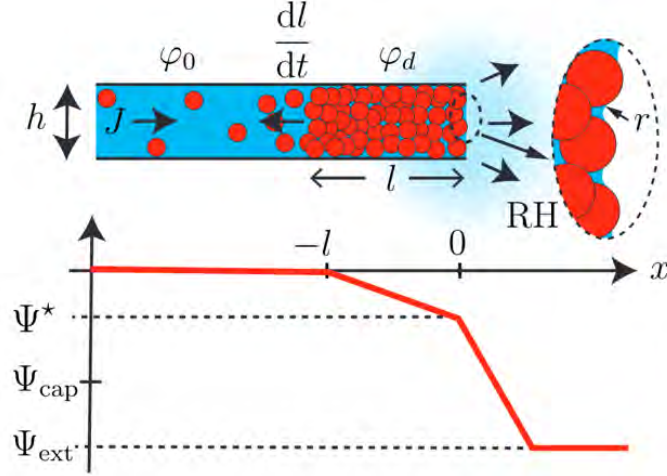


Figure I.10: [Pingulkar et Salmon, 2023] Confined directional drying of a colloidal dispersion. Capillary forces hold the air-water menisci (radius of curvature r) at the outlet of the cell.

3.3 The porous medium

The presence of particles, colloids or ions in a liquid drying in a porous medium, can drastically change the dynamic of the evaporation and even the characteristics of the medium itself. When ion salts are dissolved in water, if the flow toward the free surface due to the evaporation process overcome the ions diffusion, they concentrate and crystallize at the evaporative surface. In [Hidri *et al.*, 2013] they studied this process numerically and experimentally where the porous media consist in packings of approximately spherical glass beads of different sizes saturated with solutions of various concentrations of sodium chloride. The result was the so called coffee ring effect, since the salt concentration is higher where the evaporative flux is significant, the preferential region for the crystals formation is the one along the borders. Furthermore they found that the initial concentration of ions and the size of the beads strongly affect the first crystallization time.

On the other hand, in [Sghaier et Prat, 2009] they investigated the effect of efflorescence, the migration of a salt to the surface of a porous material, where it forms a coating, on the evaporation rate. As a result, first the drying rate is higher in the presence of ions with respect to the pure water case, while, on a second moment, it drastically reduces as the efflorescence dries out and works as a vapor diffusion barrier, a sketch of this phenomenon is reported in Fig. I.11 from [Sghaier et Prat, 2009].

Moving on from ions to colloidal particles, the same effect of advection toward the

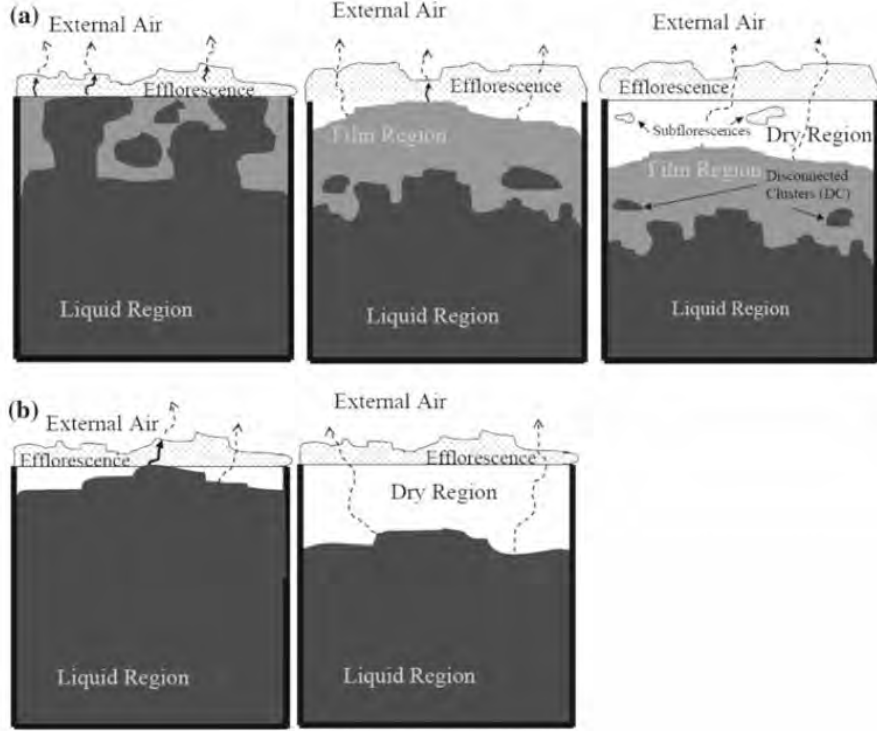


Figure I.11: [Sghaier et Prat, 2009] a) Schematic of the efflorescence pumping effect. The liquid (in dark grey) contained in the porous domain and in contact with the efflorescence is pumped by capillarity (solid arrows) through the efflorescence and evaporates at the efflorescence evolving external periphery. b) The efflorescence as porous barrier to vapor diffusion. Evaporation takes place within the porous medium. The vapor (dashed arrows) migrates from the menisci at the boundary of liquid clusters (in dark grey) to the surrounding air through the dry region of the porous domain and the efflorescence. Subflorescences may eventually appear in the disconnected clusters as a result of evaporation.

free surface is shown in [Keita *et al.*, 2013, Keita, 2021]. In the first reference, a MRI technique is employed to follow the evolution of air, water and colloids of 20nm diameter during evaporation. Then, from the experimental results, they developed a model that does not take diffusion into consideration, which can predict the distribution of particles and the drying rate. The final particle distribution $\chi_{final}(z)$ is given by:

$$\chi_{final}(z) = \psi_m (1 - z/H)^{(\psi_m - \psi_0)/\psi_0} \quad (3.3)$$

where they consider ψ the local volume fraction of colloidal particles in the liquid, which is given by $\psi = \chi/(\chi + \Phi)$, with χ the volume fraction of the colloids in the pores and Φ the local water saturation. Then ψ_0 is the initial concentration and ψ_m is the approximate maximum concentration of the colloids $\psi_m \approx 60\%$, z is the measured thickness of the compact front and H is the sample height.

Whereas, in reference [Keita, 2021], they carried out similar experiments, but focusing

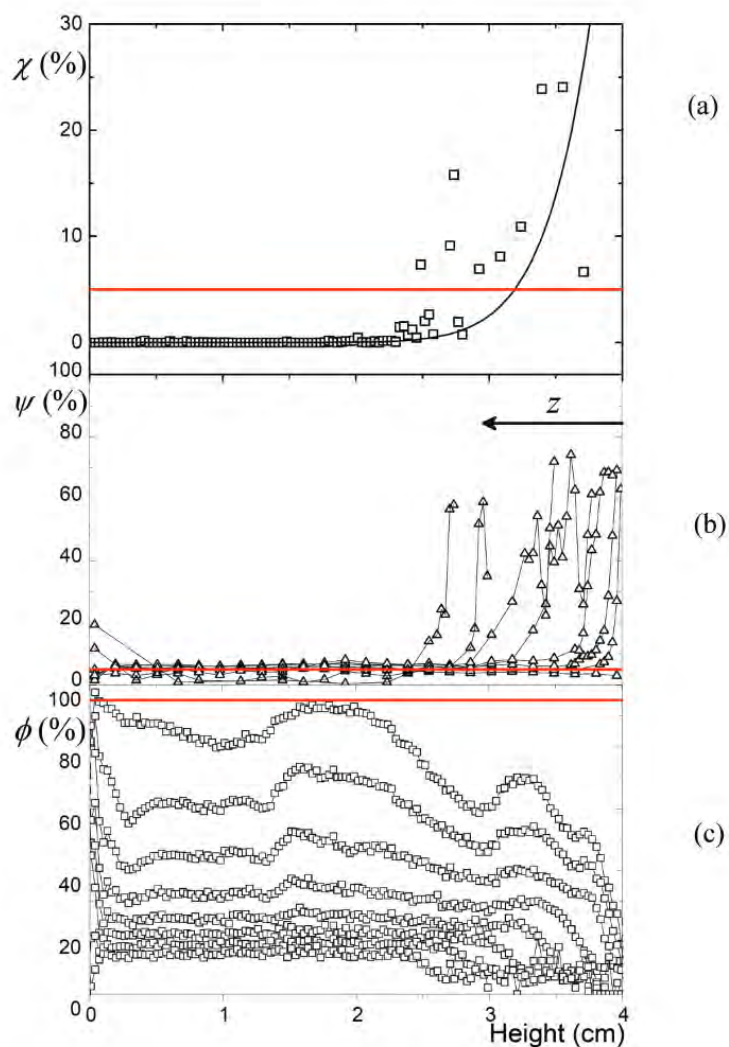


Figure I.12: [Keita *et al.*, 2013] Drying through the upper free surface of a cylindrical (height (H) = 4 cm) porous medium made of glass beads initially filled with a colloidal suspension at 5% volume fraction in water. Drying occurs through the upper surface (right) with a steady dried air flow. MRI measurements were carried out every 2h over 4 days giving us access to (a) χ the distribution of particles in the pores at the end of the experiment [the black line corresponds to Eq. 3.3, (b) Ψ the distribution of colloids in the liquid phase, and (c) Φ the distribution of water as a function of sample height. For the two last panels the profiles displayed are separated by 10 h. Red thick lines represent the initial state.

on the final deposit of the particles and studying it through SEM and X-ray microtomography. As the liquid dries out, particles are transported toward the surface and, in the end, they form a compact matrix resulting in the decrease of porosity of the porous medium and, consequently the permeability may be significantly affected as well, see Fig. I.12.

4 The effect of wettability on evaporation

The main complexity of predicting evaporation rates is due to its dependence on a variety of factors, such as humidity, air temperature, air velocity and characteristics of the porous medium, such as porosity, angularity, grain size and wettability. Many studies were conducted to understand the impact of hydrophilic surface with respect to a hydrophobic one. Starting at the micro-scale, in [Huber *et al.*, 2018] they used different wettability beads to build a pore, fill it with water and let it evaporate. They found that the droplet on the hydrophobic beads takes more time to dry out than the hydrophilic case and the contact angle stays constant, while on the other case it decreases. Similar results are found in [Kim et Kang, 2003], although evaporation occurs on the outside wall of horizontal tubes which are normally hydrophobic and treated with plasma to make them hydrophilic. The explanation for both articles is based on the presence of the liquid films for the hydrophilic surface, and, having a smaller thickness and greater evaporation area, yields to a higher evaporation rate. Likewise, the effect of the plasma treatment was investigated in [Takata *et al.*, 2004] for different materials, they let a water droplet dry and the results are equivalent to the previous ones. An interesting study is considering a drop of water evaporating on a chemically patterned surface, in [He *et al.*, 2022] hydrophilic squares on a hydrophobic surface, Fig. I.13, they investigated the four stages dynamic of evaporation and developed a numerical model that takes into account the stick-slip phenomenon. Meanwhile in [Wan *et al.*, 2015] they discovered that evaporation on a patterned surface is faster than any other with homogeneous wettability thanks to experiments and simulations.

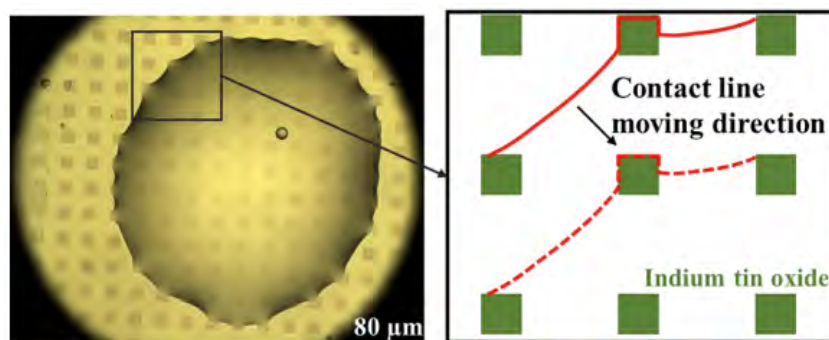


Figure I.13: [He *et al.*, 2022] Top view of the representative contact line moving.

Different wettability properties can largely affect the evaporation rate and the deposit of particles in a porous medium. By using two columns of glass beads with different wettability characteristics, in [Shahidzadeh-Bonn *et al.*, 2007] they studied the effects on the evaporation rate, considering as well the presence or absence of an air flow to investigate the role of vapor transport. The reported results showed that for the hydrophilic beads the drying rate stays constant most of the time and decreases for the late stage, for a dynamic mainly controlled by liquid films, while they found a strong dependence on the boundary conditions for the hydrophobic porous medium. Similarly, [Shokri *et al.*, 2008] investigated the effects on hydrophobic layers in a column of hydrophilic sand on the evaporation and the deposit of the blue dye, results are illustrated in Fig. I.14. The introduction of a hydrophobic sand layer results in remarkable reduction of cumulative evaporation, formation of a stationary vaporization plane, while the pattern of the blue dye varies as a function of the position of this plane defined by the hydrophilic/hydrophobic interface.

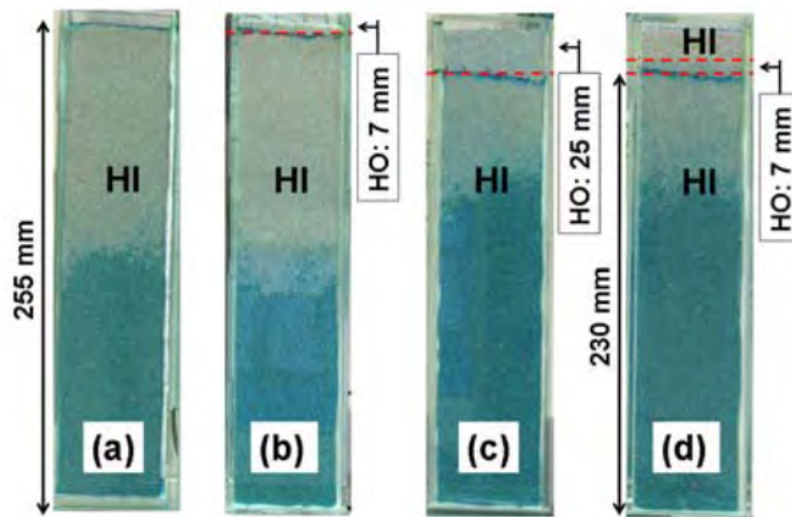


Figure I.14: [Shokri *et al.*, 2008] Images of sand columns used in evaporation experiments with blue color showing the saturated zone, gray color showing the unsaturated zone and dashed line showing the interface between hydrophobic (HO) and hydrophilic (HI) sand. (a) completely HI sand; (b) top layer (7 mm) of HO sand on top of HI sand; (c) 25 mm HO sand on top of HI sand; and (d) 7 mm HO sand layer placed 18 mm below HI sand surface.

Their research continued in [Shokri *et al.*, 2009], where they, experimentally and theoretically, examined the potential effects of wettability on capillary driving forces required for sustaining liquid flows in order to understand its consequences on the evaporation behavior in a granular porous medium. Furthermore, they investigated the effects on dye deposition in a porous medium containing sharp wettability discontinuities and explained the preferential drying front displacement in the hydrophobic domain and the

spatial extent of capillary flow supporting the vaporization plane using a physically-based model [Shokri et Or, 2013]. As a result the presence of vertical wettability interfaces, i.e. hydrophobic beads in the left column and hydrophilic in the right one in Fig. I.15b and resulted in preferential solute deposition at the surface of hydrophobic domain, see Fig. I.15

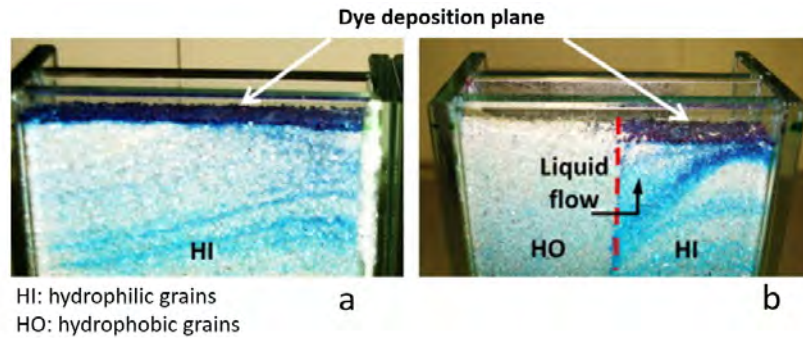


Figure I.15: [Shokri et Or, 2013] Surface of columns packed with (a) hydrophilic (HI) sand and (b) two hydraulically coupled vertical domains of hydrophobic (HO) and HI sand. The dash line indicates the vertical HI/HO interface. (a) Since evaporation occurs at surface, tracer is deposited there (b) capillary suction between HI and HO grains causes lateral liquid flow from HO to HI sand layer and subsequent evaporation and preferential dye deposition exclusively on HI surface.

5 Motivation and objectives

5.1 The fuel cell and its water problematic

A motivation for the present thesis stems from the problematic of water management related to the fuel cell which is an electrochemical cell that produces electricity from oxygen and hydrogen. Differently from other batteries, for which the substances producing electricity are already present in within, the fuel cell continuously needs the gases to be injected to sustain the chemical reaction. It is composed of two bipolar plates, the anode and the cathode, at the sides of the core component, called membrane electrode assembly (MEA), composed of a Gas Diffusion Layer (GDL) and a catalytic layer (CL) on both sides of an electrolyte, see Fig. I.16. This component allows ions, often positively charged hydrogen ions (protons), to move between the two sides of the fuel cell as sketched in Fig. I.16. There exists various type of fuel cells depending on what kind of electrolyte is employed, the most interesting, from a startup time point of view which is about 1 second, is the nafion Proton Exchange Membrane (PEM), which leads to a PEM Fuel Cell or PEMFC.

Hydrogen is injected at the anode side and, as it flows through to reach the cathodic

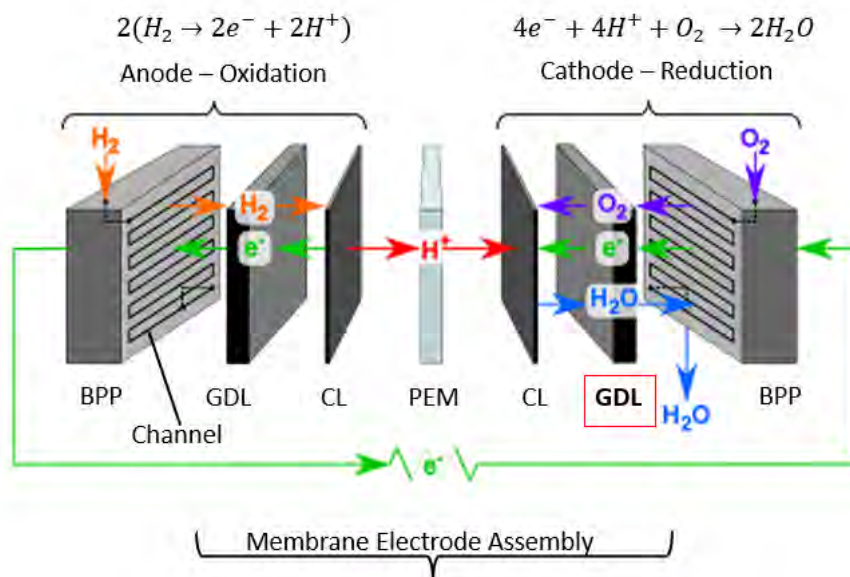


Figure I.16: Components and functioning of the fuel cell.

side, it dissociates in proton (H^+) and electrons thanks to a platinum catalyst. This reaction, $2(H_2 \rightarrow 2e^- + 2H^+)$, is called the anodic oxidation. As the membrane is electrically insulating, electrons will travel through an external circuit before getting back to cathode, while the PEM facilitates the passage to the cathodic side of hydrogen protons. Here, as oxygen is injected in the bipolar plate, the cathodic reduction, $4e^- + 4H^+ + O_2 \rightarrow 2H_2O$ takes place and water is produced. A diagram of the described process can be found in Fig. I.16.

While the fuel cell can be seen as technology of the future, thanks to the wide presence of used gases and to the clean production of electricity, there are still a few problems to solve to secure the best possible efficiency. For example, the cost of the cell is elevated, but researchers are working on keeping the same productivity while decreasing the amount of platinum; the reaction $2H_2 + O_2 \rightarrow 2H_2O$ produces a non negligible thermal load therefore the temperate has to be maintained constant. Moreover, for an optimal performance of the fuel cell, the water management issue is of great importance. In fact, on one hand, water has to evaporate slowly to maintain a proper level of hydration of the PEM and ensure a high proton conductivity, and not too fast or the membrane could crack, but, on the other hand, if it evaporates too slowly, the accumulation of liquid would flood the cell preventing the gases from passing through.

The cathodic Gas Diffusion Layer, a fibrous medium, plays a vital role in water management, hence optimizing its structure and properties and understanding the methods to achieve it, would help increase and stabilize the performance of these devices. There are different procedures to do so, [Chen *et al.*, 2004] studied the permeability of the GDL and

the performance of the cell by adding a water management layer, while [Voss *et al.*, 1995] found that water can be removed via the anode fuel stream by imparting a water gradient, but in this study we focus on the hydrophobization of the GDL thanks to the Polytetrafluoroethylene, or PTFE, such as in [Ito *et al.*, 2014], whose distribution needs to be as homogeneous as possible to help the expulsion of water.

5.2 The hydrophobization of the Gas Diffusion Layer

The starting point for the present thesis lies in the results reported in [Ito *et al.*, 2014] investigating different ways to hydrophobize the GDL. The samples are dipped for two minutes in solution with a 10%w/w concentration of PTFE and then it is let to dry in two different conditions. Both experiments were performed in an oven heated to 100°C during 1h. The heating was then turned off and the oven returned to room temperature in about 10h. The difference in the two experiments lies in the gas pressure in the oven. The pressure was 1 bar in the experiment referred to as the air-drying experiment whereas the experiment was performed under vacuum in the other experiment: the pressure in the oven was 0.1 kPa (1 mbar). Initially, the fibrous medium (305 μm in thickness) was saturated by a 10 wt % PTFE dispersion (D-201c, Daikin). The dispersion consists of water with PTFE particles (average size 200 nm) and surfactant. The main result is illustrated in Fig. I.17

The PTFE distribution, characterized by the fluorine distribution, in the medium (which was actually dried from both the sample bottom and top surfaces) is markedly different depending on the drying conditions. The distribution is much more uniform over the medium thickness in the case of the vacuum drying whereas the fluorine tends to localize in the top and bottom regions in the case of the air-drying. However, no physical explanation is provided in [Ito *et al.*, 2014] to explain the difference in the PTFE particles distribution depending on the drying conditions. Since the distribution of the PTFE affects the local wettability properties of the medium, it is important to better understand how one can tune the PTFE distribution via the drying process.

Since the PTFE particles are in the liquid phase initially, it can be conjectured that the difference in the distribution of the PTFE deposit on the fibers is due to a difference in the way the liquid distribution evolves in the medium during the drying process. The various patterns, i.e. fluid distributions, that can be expected in a drying process have been studied from both experiments and numerical simulations [Laurindo et Prat, 1998, Laurindo et Prat, 1996, Prat, 2002, Vorhauer *et al.*, 2018]. Based on the literature, one can distinguish the two patterns illustrated in Fig. I.18: the capillary pattern and the front pattern.

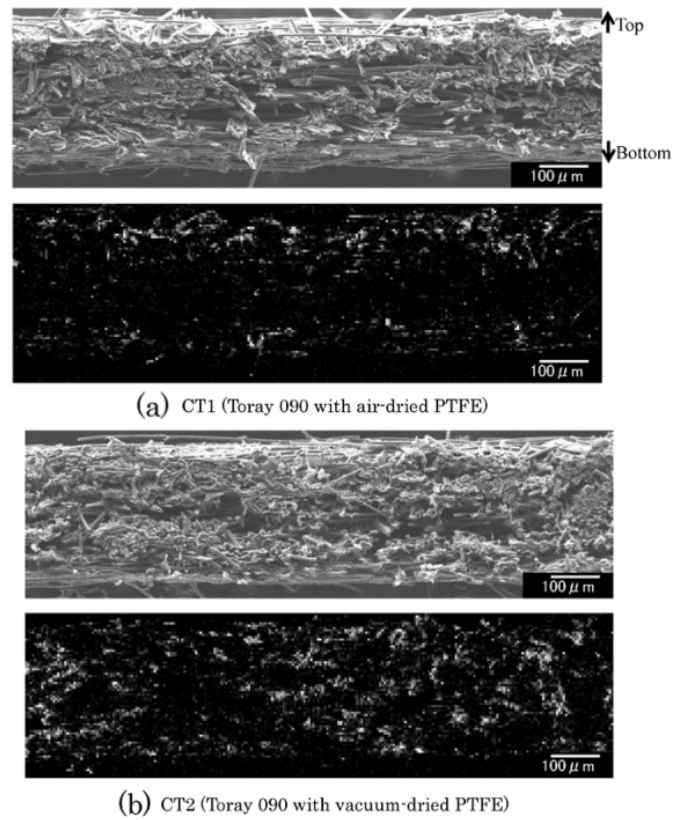


Figure I.17: SEM image (upper) and corresponding EDS map of fluorine (F) (bottom) of cross-section of samples (a) CT1 (Toray 090 with air-dried PTFE), (b) CT2 (Toray 090 with vacuum-dried PTFE). (Images and caption from [Ito *et al.*, 2014])

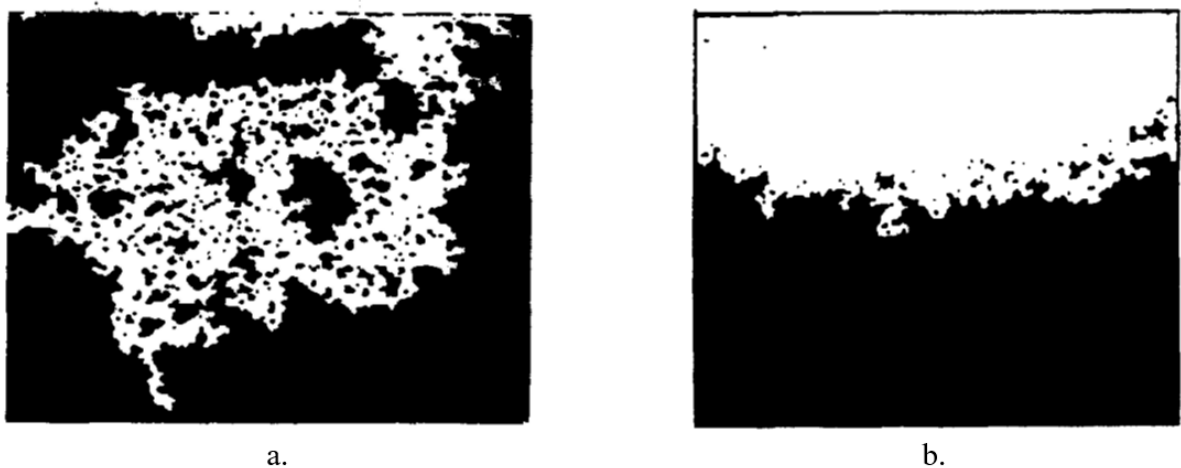


Figure I.18: Capillary pattern (a) and front pattern (b) in drying observed in a 2D micromodel [Prat, 2002]. Liquid region in black and gas region in white. The solid phase is not visible. Vapor escapes from top edge of micromodel. Other edges are sealed.

The capillary pattern is obtained when the capillary forces control the gas invasion in the pores resulting from evaporation. The corresponding invasion process can be described as an invasion percolation process [Wilkinson et Willemssen, 1983] according to a rule stating that the pores are invaded in a decreasing order of size. The front pattern shown in Fig.I.18b has been obtained when the micromodel was held vertically. In this case, the gravity effect is sufficient to stabilize the pattern which is characterized by a fully liquid zone at the bottom (black region in Fig.I.18b), a region fully invaded by the gas phase on top (white region in Fig.I.18b) and a traveling two-phase zone (thin in Fig.I.18b), referred to as the front, in between.

It is noteworthy that a front pattern can be also obtained when viscous effects in the liquid stabilizes the invasion [Shaw, 1987] or when drying occurs in a hydrophobic material [Chapuis et Prat, 2007]. In the case of the experiments illustrated in Fig. I.17, the medium is rendered hydrophobic as the result of the PTFE particle deposit on the fibers. However, it is likely that the drying process itself, i.e. the process leading to the PTFE particle deposit, can be considered as occurring in a hydrophilic medium (the fibers visible in Fig. I.17 are carbon fibers, the contact angle of water on carbon is expected to be on the order of 80° , whereas the contact angle on PTFE is on the order of $110-120^\circ$). Thus, it is hypothesized that the difference in the final PTFE distribution between the two drying conditions in Fig. I.17 is not due to a wettability effect.

It can be also noted that a surfactant is present in the PTFE dispersion. The impact of a surfactant on the drying process is not documented, at least from experiments similar to the ones illustrated in Fig.I.18. The surfactant is introduced to stabilize the dispersion, i.e. to avoid the formation of PTFE particle agglomerates. Here also, it is hypothesized that the presence of the surfactant is not the main reason for explaining the difference between the PTFE distributions in Fig.I.17.

Unfortunately, no information is given in [Ito *et al.*, 2014] as regards the drying process itself, such as for instance the drying kinetics. For instance, it is not indicated whether drying is faster or slower under vacuum. It seems that vacuum drying has not yet been investigated with micromodels, i.e. according to an approach allowing to visualize easily the pattern. Vacuum drying is in fact mainly used for the drying of food products, i.e. [Richter Reis, 2014], or wood [Espinoza et Bond, 2016] because it is typically faster than convective drying under ambient pressure and can be performed at ambient temperature, that is without altering the product. The works on vacuum drying, i.e. [Erriguible *et al.*, 2007] and references therein, typically deal with a situation where

the porous medium is heated on one side (a situation referred to as contact drying) and in contact with a dry air at low pressure on the opposite side. Also, the considered porous media are typically low permeability porous media, as wood for instance. Compared to classical convective drying, the studies on vacuum drying of wood point out two specific mechanisms: the formation of gas total pressure gradients in the medium inducing convective flows of both the gas phase and the liquid phase, the possible “boiling” of the liquid phase since the temperature in the medium can reach the saturation temperature depending on the evolution of the gas pressure (for instance the saturation temperature is about 20°C when the pressure is 2500 Pa). However, “boiling” does not mean the formation of many bubbles in the liquid phase as in a conventional pool boiling situation. “Boiling “ means that the total pressure of the gas phase at the liquid-gas interface in the medium is equal to the water vapor saturation pressure, the gas phase is therefore only composed of water vapor at the interface. Following Krischer [Krischer et Kröll, 2013], one can therefore distinguish the case where air is still present at the liquid-gas interface with the vapor from the situation where there is no air anymore and only water vapor. The former situation is referred to as “evaporation” whereas the latter is referred to as “vaporization” (which is more adequate than “boiling”). In a typical vacuum drying configuration, drying starts under evaporation conditions. Then, as the total pressure decreases and the temperature increases (the product is often heated up), the saturation conditions are reached and drying continues under “vaporization” condition. The case of interest for the present study, [Ito *et al.*, 2014] and Fig. I.17, is however somewhat different. The permeability of the medium is high (typically $k \sim 10^{-11}m^2$ [Gostick *et al.*, 2006]) compared to wood ($k \sim 10^{-16}m^2$ [Erriguible *et al.*, 2007]). The medium is thin (300 μm in Fig. I.17) compared to wood samples which are typically in the centimetric range in laboratory experiments [Erriguible *et al.*, 2007]. The pores sizes are much bigger ($\sim O(10\mu m)$) compared to wood (mostly in the submicronic range down to a few nanometers [Plötze et Niemz, 2011]). It can therefore be expected that the generation of gas total pressure gradients is much less a key mechanism compared to previous works on vacuum drying with wood samples. Also, in spite of the cooling effect due to evaporation or vaporization, considering the temperature over the medium as equal to the temperature in the vacuum chamber is probably acceptable in the case of the vacuum drying of a thin medium leading to the result illustrated in Fig. I.17.

To sum up, the main idea is to explore whether the difference in the PTFE distribution with the two drying modes in Fig. I.17 is due to a change in the drying pattern (Fig. I.18) from a capillary pattern in the case of the air-drying mode to a stabilized front pattern in the vacuum drying mode and, therefore, a change in the drying kinetics. To do so,

two drying set ups were developed. Firstly, evaporation is studied at the micro-scale in an almost square cross-section microchannel under a microscope, with pure water and different concentrations of colloidal particles that are fluorescent for a better visualization. Then, a pore network with the same materials is built and evaporation with and without particles is observed with a camera. In these cases, the effects of a different pressure, temperature and position of the porous media, i.e. horizontal or vertical, are investigated. To conclude, the same experiment with the same material, but a different wettability to understand the impact of the contact angle on the transport of particles, is carried out as well.

Chapter II

Evaporation in a single channel

Contents

1	Materials and Methods	28
1.1	The experimental material	28
1.2	The experimental protocol	30
1.3	The wettability of the materials	30
1.4	The numerical simulations	31
2	The phase distribution	32
2.1	Corner films and contact angles	33
3	The effect of particles	33
4	Evaporation kinetics in the pure water case	35
4.1	Image processing	35
4.2	The three phases	38
4.3	The evaporation rate	38
4.4	Surface Evolver simulations	39
5	Impact of particles on the evaporation kinetics	40
5.1	Image processing	41
5.2	The effects on the evaporation dynamic	41
6	The final deposit	43
7	The impact of corner film thickness on the evaporation rate	44
8	On the accumulation of particles in the films and the film thinning effect	46
8.1	Particle convective transport is dominant in the films	46
8.2	Accumulation of particles and particle compact packing in the corner films	48
8.3	Estimation of A_c	50
8.4	On the effect of particles on corner films	52
9	High concentration of particles	55

9.1	Liquid - gas distribution in the channel and final deposit	56
9.2	Evaporation kinetics	58
10	Conclusion	61

In this chapter we present the a first description of the phenomenology of evaporation in a single channel of almost squared section. Using different concentrations of particles, we put in advance the effect on the rate of evaporation and on the thickness of the films of the presence of particles with respect to experiments with pure water. Experimental results and data are compared with Surface Evolver [Brakke, 1992] simulations of the gas-liquid interface in the channel and computations of the evaporation rate using a commercial code.

1 Materials and Methods

Evaporation experiments are conducted in a single channel of rectangular cross section. The channel is 2.4 mm long, 0.8 mm large and with a depth of 1mm. As illustrated in Fig. II.1, it is a composite channel with four walls made in a hydrophilic material (SUEX), namely the end wall, the lateral walls and the bottom wall, whereas the top wall is hydrophobic (PDMS). To close the channel, the developed SUEX chip is covered with a thin layer of polydimethylsiloxane, (PDMS) (Fig. II.1) to ensure proper sealing, to avoid leaks and facilitating the observation of corner films, which, as it will be shown, develop along the two lower corners of the channel.

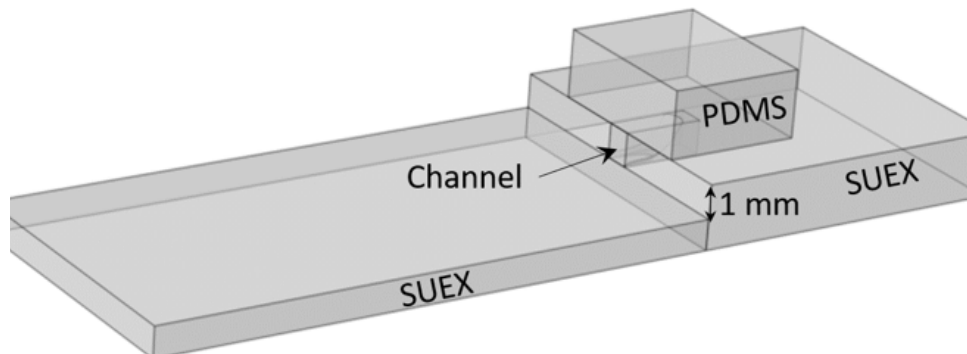


Figure II.1: Composite SUEX -PDMS channel of rectangular cross section.

1.1 The experimental material

1.1.1 The SUEX

SUEX are photo imageable epoxy sheets from Dj Microlaminates, Inc. that consist of a catatonically cured modified epoxy photoresist between two throw-away layers of protec-

tive polyester film (PET). The epoxy photoresist formulation contains an antimony-free photoacid generator and is prepared under a highly controlled solvent-less process, which provides uniform coatings. The solvent developed negative working photoresist is sensitive to UV radiation in the range of 350 – 395nm.

The microfabrication sequence is the following: a glass plate, used as support, is cleaned with acetone, ethanol and dried with compressed air. The SUEX sheet is set on a hot plate to be cut. Then, after removing the PET cover sheets, a first layer of SUEX is set on the glass plate. A second layer of SUEX is placed on top of it. This resin sheet assembly is put in the UV lamp, covered with the mask imposing the channel shape. To finish, the sheet is developed at room temperature with PGMEA (propylene glycol methyl ether acetate), face down with mild agitation and then cleaned with IPA (isopropyl alcohol) and dried in an oven several hours. This yields a 1 mm deep channel on top of the SUEX sheet assembly. The chip so obtained undergoes a final cleaning protocol. It is brushed with soap, rinsed with ethanol and dried with compressed air, in order to remove any residual deposited particles or dust. The detailed protocol for the fabrication of SUEX micro channels or networks is in Annex A

1.1.2 The PDMS

SYLGARD™184 Silicone Elastomers (Neyco) are supplied as two-part liquid component kits. When liquid components are thoroughly mixed, the mixture cures to a flexible elastomer, which is well suited for many different application. They require no post cure and can be placed in service immediately following the completion of the cure schedule. We used a 4% mixing ratio, to have the sheet more flexible and sticky. Then, we put the mixture in vacuum bell to degas it, pour the mixture in a clean plate and place it in the oven for two hours at a temperature of 80°C before gradually letting it cool down. The main reasons for the choice of this material are its high transparency, that allows easy imaging and easy inspection of the particles, the low price and the easy fabrication process.

1.1.3 Colloidal system

The particles we used, are carboxylate-modified fluorescent microspheres of 1 μm in diameter. Molecular Probes™ Fluo Spheres are manufactured using high-quality, ultraclean polystyrene microspheres and the employed method also ensures the narrow distribution of fluorescence intensity and size, moreover the dye have a negligible effect on the surface properties of the polystyrene beads. The final product is sold as a suspension in ultrapure

water with 2% (w/w) particles, in most cases containing 2 mM azide or 0.02% thimerosal as a preservative.

1.2 The experimental protocol

Experiments were carried out as follow. After cleaning the channel and closing it with PDMS, the liquid was injected manually with a syringe. Care was exercised for not flooding the channel so as to avoid any spreading of solution in excess in the outer region of channel. The result was that the channel was not fully filled when the experiment started. Then, the chip was placed under a microscope (Zeiss Axio Scope.A1 with a 5x/0.16Ph1 lens) equipped with a camera (LaVision Image sCMOS) and images of channel during evaporation were taken from the top at a frequency of 0.1 Hz. Positions of the triple line on the SUEX bottom wall or PDMS top wall were obtained after image processing using ImageJ and Matlab.

Four experiments, with pure water and three different particles concentrations (in g/mL), namely 10^{-5} , 0.5×10^{-4} and 10^{-4} , were performed. These concentrations were obtained by mixing a volume V_{part} of the 2% (g/mL) solution with a selected volume V_{H_2O} of pure water. This gives

$$C = \frac{V_{part}C_0}{V_{part} + V_{H_2O}} \quad (1.1)$$

where $C_0 = 0.02$ g/mL and C denotes the obtained concentration. Prior to each experiment, the conditions in the box around the microscope were measured and, if necessary, modified with the addition of a salty solution in order to impose the same relative humidity, $58\% \pm 2\%$ in each experiment. Since the relative humidity in the room was around 40%, we used the saturated salt/water solution with potassium chloride (KCl) to increase it. The room temperature was $T = 22^\circ \text{C} \pm 1^\circ \text{C}$. Both the temperature and relative humidity were recorded every 5 minutes.

1.3 The wettability of the materials

The wettability properties of the channel materials were characterized from contact angle measurements. These measurements were performed for pure water and the various concentrations in particles using the Drop Shape Analyzer Krüss based on the sessile drop technique. For both pure water and with particles the contact angle was found to be on the order $70^\circ - 75^\circ$ on a SUEX layer. These values correspond to measurements right after the droplet has reached an equilibrium on the SUEX, i.e. a short time after the drop is set on the SUEX plate surface. These values change during the gradual evaporation of

the droplet. As can be seen from Fig. II.2, the contact angle θ of a specific drop during evaporation decreases almost linearly as a function of time for both pure water and water with particles while the triple line remains pinned. The variation is quite significant with the contact angle reaching values less than 20° . While SUEX is a hydrophilic material ($\theta < 90^\circ$), contact angle measurements on PDMS led to a mean value of 104° , consistent with values in the literature [Mata *et al.*, 2005], with a limited effect of the particles. However, with the evaporation, the measured contact angle decreases and can become as low as $45^\circ - 50^\circ$ (Fig. II.2), in line with the results reported in [Mishra *et al.*, 2016].

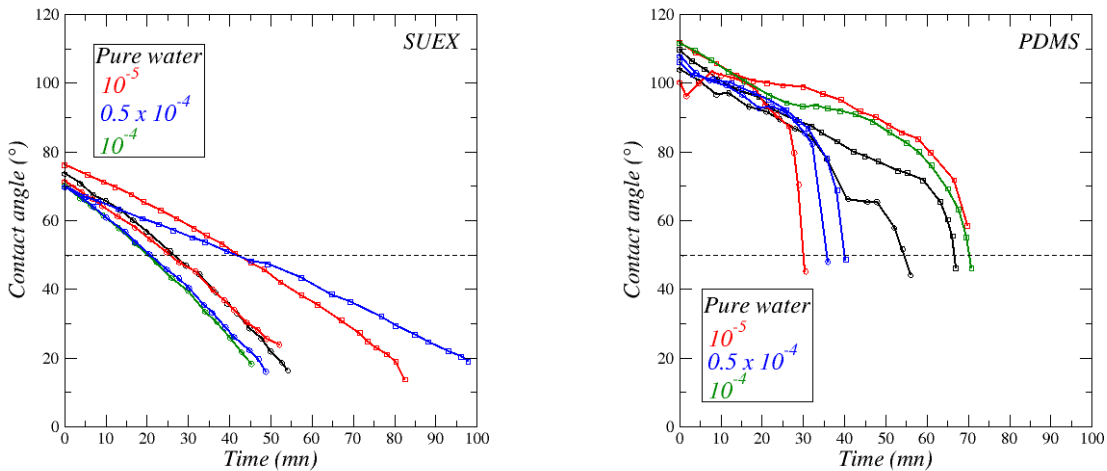


Figure II.2: Contact angle variation on SUEX and PDMS layers during evaporation of a droplet in the fixed triple line regime

Contact angle measurements were also attempted on particles forming a homogeneous deposit on a SUEX plate, obtained by letting dry a drop of concentration 2% (g/mL). Droplets on the particles deposit spread rapidly leading to the conclusion that the contact angle is close to zero. Hence, the particles are considered as hydrophilic, consistently with a previous work [Kim *et al.*, 2018], where a contact angle value of 34° is indicated for carboxylate modified polystyrene particles.

1.4 The numerical simulations

As indicated in the introduction, numerical simulations were also performed using the open-source software “Surface Evolver” [Brakke, 1992]. This software allows computing the quasi-static liquid-gas interface within the channel, i.e. the shape of the interface when capillary effects are dominant. The parameter which is varied in these simulations is the saturation. A given volume fraction S_l of liquid is set in the channel under the form of

a plug almost filling the channel from its end. Then the plug shape in the channel evolves in the simulation due to capillary effects until the equilibrium shape is reached. The next step is to gradually reduced the liquid volume (which is an imposed constraint in the Surface Evolver simulations). A new equilibrium shape is obtained for each considered liquid volume. Hence, by decreasing S_l (or equivalently by increasing the gas volume fraction S_g), the evolution of the liquid- gas distribution due to the evaporation process is mimicked. As explained in Section II.4, some of the liquid gas distributions computed with Surface Evolver were also used to compute the evaporation rate by importing the Surface Evolver computed interface shapes in the commercial code COMSOL Multiphysics.

2 The phase distribution

The typical liquid distribution in the composite channel during evaporation is illustrated in Fig. II.3a for pure water. A main meniscus, also referred to as the bulk meniscus, forms within the channel. This meniscus is attached to the top wall (in PDMS) and to the bottom wall (in SUEX). As can be seen, the difference in wettability between PDMS and SUEX introduces a distortion in the bulk meniscus shape. The triple line is more advanced within the channel on the top wall (PDMS) than on the bottom wall (SUEX). A major feature is also the development of corner liquid films in the lower corners of the channel corresponding to SUEX corners.

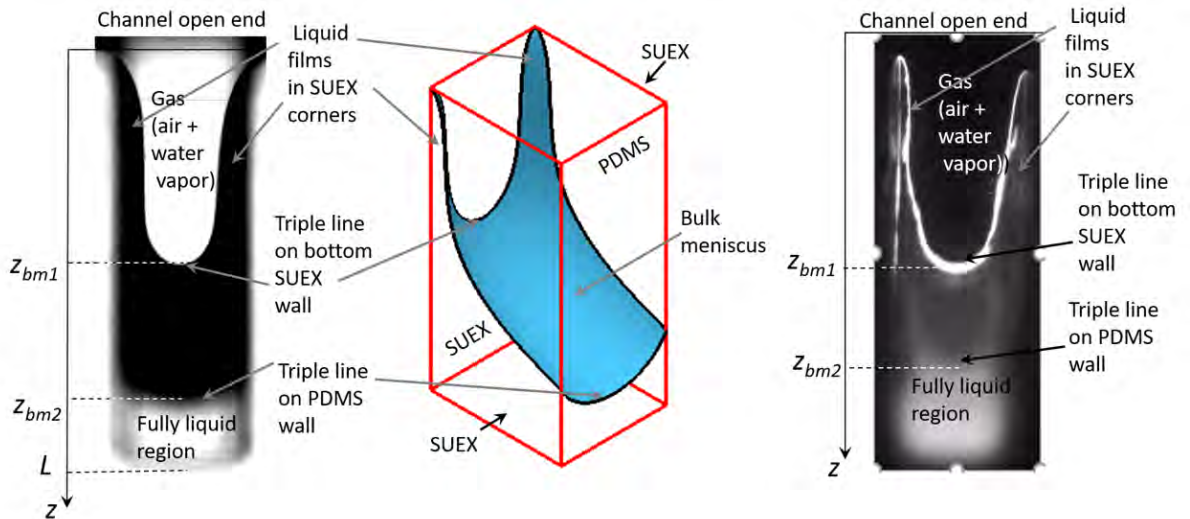


Figure II.3: Typical fluid distribution in the channel during evaporation: a) top view of the channel in the experiment with pure water, b) quasi-static shape computed with Surface Evolver for $\theta_{SUEX} = 30^\circ$ and $\theta_{PDMS} = 104^\circ$, c) in the presence of particles (10^{-4})

2.1 Corner films and contact angles

Corner films are a well identified feature of evaporation or drainage in tubes or channels of polygonal cross-section, e.g. [Chauvet *et al.*, 2009, Prat, 2007, Geoffroy *et al.*, 2006, Keita *et al.*, 2016b]. However, for such films to form, the contact angle must be lower than 45° in the case of a right corner geometry, e.g. [Prat, 2007, Concus et Finn, 1969]. The contact angle fresh value of 70° (Fig. II.2, time zero) is not compatible with the development of corner films. As in the case of the droplet evaporation where, as depicted in Fig. II.2, the contact angle decreases with time, the contact angle actually decreases and eventually becomes sufficiently small for the corner films to form. From the overlay of the experimental image with the corresponding images obtained from Surface Evolver simulations for various values of the contact angle on the SUEX walls, it is found that the contact angle in the experiment with pure water is $\theta_{SUEX} \simeq 30^\circ$ (Fig. II.4). This value gives a comparable film thickness and a comparable distance difference $z_{bm2} - z_{bm1}$ (Fig. II.3) between the triple line position on the top PDMS wall and SUEX bottom wall. It can be noted that contact angles below 45° on a SUEX plate are reached after about 30 min in the contact angle measurements reported in Fig. II.2. However, no delay in the corner film formation is noticeable in the channel experiments. The corner films form in the channel right from the beginning of the experiments. Why this is so remains to be explained. Perhaps this is due to wall roughness generated on the channel walls during the channel fabrication process.

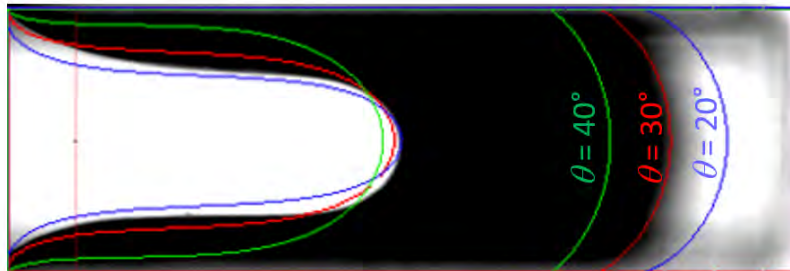


Figure II.4: Overlay of picture of the experiment with pure water with focus on the SUEX bottom wall and corresponding images obtained from Surface Evolver simulations (solid lines in color) for three values of contact angle.

3 The effect of particles

Since from previous works on evaporation in square tubes, e.g. [Chauvet *et al.*, 2009, Chauvet *et al.*, 2010], it is known that the evaporation rate, and thus the bulk meniscus

displacement speed, highly depends on the corner liquid films, it is interesting to look at the effect of particles on the corner films. The comparison of the triple line on the SUEX bottom plate for various concentrations in particles in Fig. II.5 shows that the particle presence significantly affects the corner films (as evidenced by the comparison with the shape in yellow which corresponds to the pure water case). Whereas the corner film shape is typical of a quasi-static shape in the case of pure water (the film thickness w_{film} , defined at the distance between the triple line and the nearest channel lateral wall in Fig. II.5, tends to a plateau at some distance below the channel entrance), the corner films are globally thinner and with a more complex film thickness variations along the channel in the presence of particles (Fig. II.5).

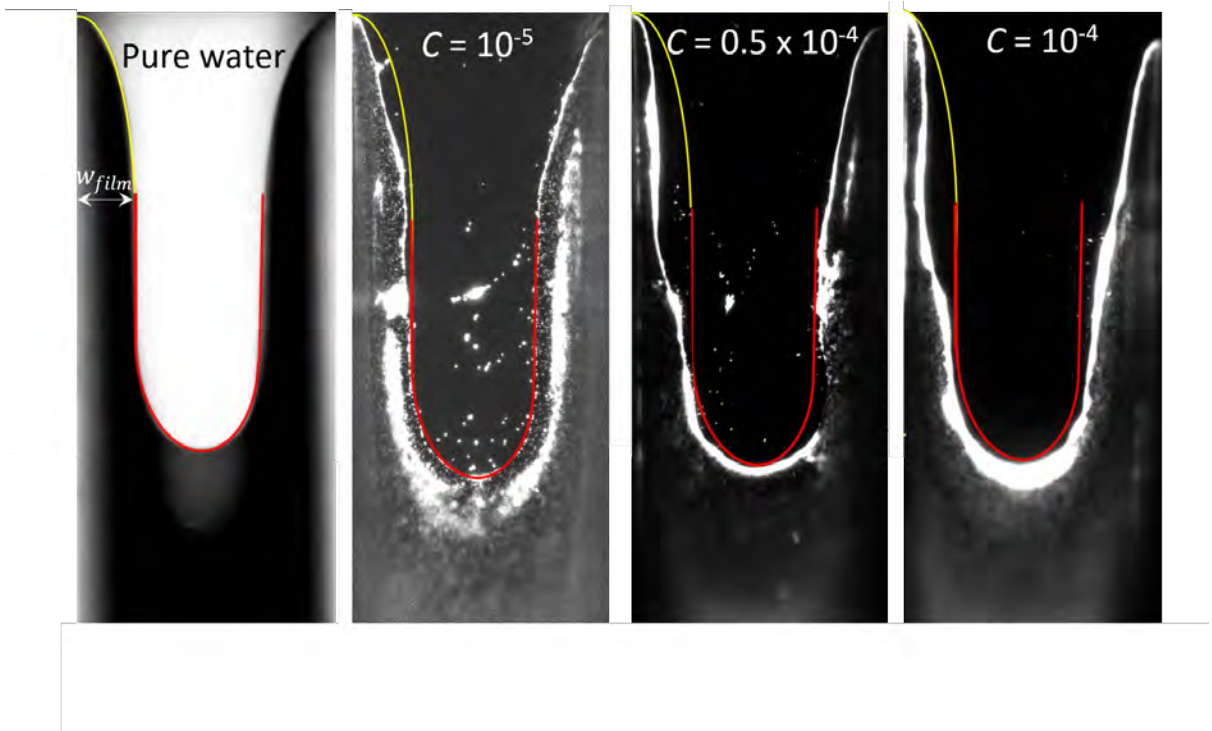


Figure II.5: Triple line shape on SUEX bottom plate for pure water and the three particle concentrations. The curve in red is the shape in the main meniscus region in the pure water experiment whereas the shape in yellow is the shape in the corner film upper region in the pure water experiment. The bright zones in the pictures with particles correspond to particle accumulation zones. The indicated times correspond to the time in Fig. II.14a

This is quantified in Fig. II.6 which shows the liquid-gas distribution over the half of the channel width along a line located at a distance of 0.3 mm from the channel open end (this line is shown in orange in Figs. II.3a, II.4 and II.6). Fig. II.5 shows also the preferential accumulation of particles along the triple line, notably in the corner film region. Nevertheless, as indicated by the shape in red in Fig. II.5, the triple line shape is somewhat similar in the four experiments in the region of the triple line most advanced points (these correspond to the positions z_{bm1} and z_{bm2} in Fig. II.3). The effect of particles

on the corner films is further discussed in Section II.7 after presentation of the evaporation kinetics (next two sections) and the particle final deposit.

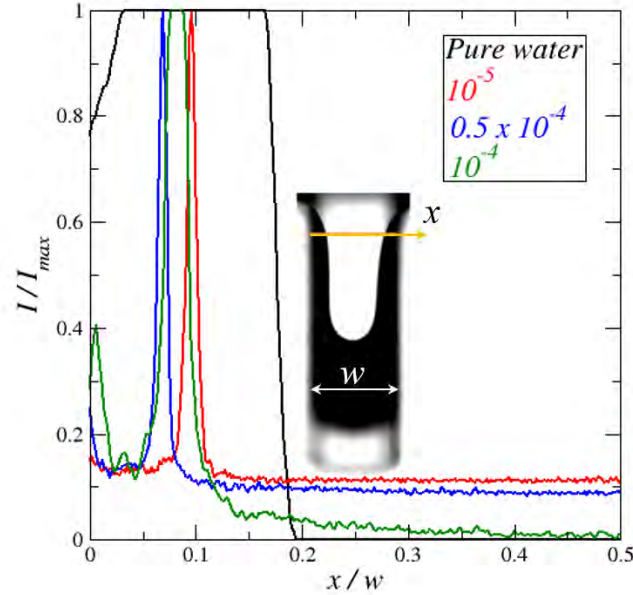


Figure II.6: Corner film thickness at time $t = 90$ min evaluated at a distance of 0.3 mm from the channel entrance (this location corresponds to the horizontal orange line in the inset); I denotes the light intensity (expressed in grey level in the images). In the images with particles, the light intensity is maximum at the triple line. Note that the plots are over the half of the channel width.

4 Evaporation kinetics in the pure water case

The evaporation kinetics in the pure water experiment is illustrated in Fig. II.11a and b showing the evolution of the triple line most advanced points z_{bm1} and z_{bm2} on the channel SUEX bottom surface and PDMS top surface, respectively and in Fig. II.12a and b showing the variation of the distance $z_{bm1} - z_{bm2}$. From a qualitative point of view, the water evolution during evaporation is illustrated in Fig. II.7, with six time steps of the experiment.

4.1 Image processing

In this experiment no dye is used since the contrast between liquid and air was already visible enough. In fact the liquid films at the bottom of the channel result dark, with respect to the top of the channel that has a lighter color.

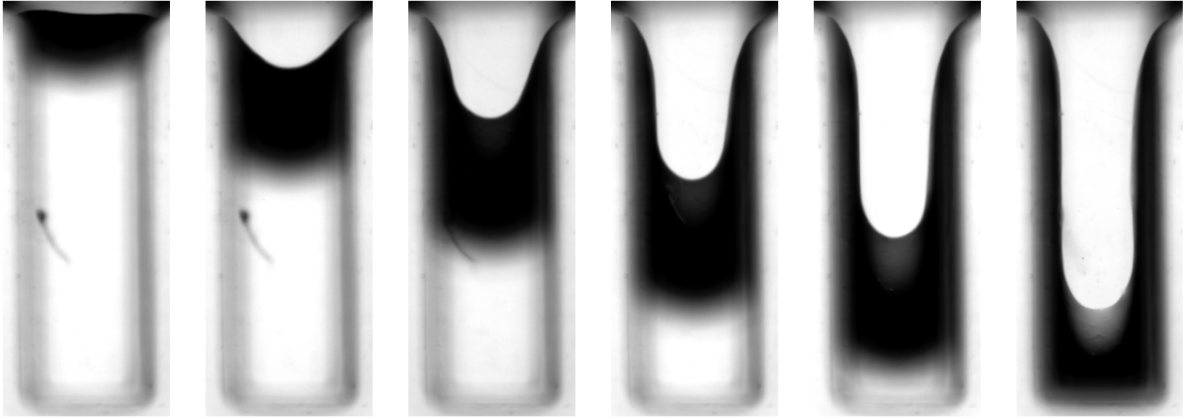


Figure II.7: Images of the evaporation experiment in the pure water case with focus at the bottom of the channel (SUEX); images are taken every 25 minutes.

The image processing procedure has the following steps, for the first three points we use ImageJ and Matlab for the last ones:

1. Images are 16bit grey-scale, Fig. II.8, therefore for a convenient analysis they are converted to 8 bit, with values ranging from 0 to 255; a pixel is black when its grey value is 0, and white if it's 255. Then, images are straightened by rotating them and cut to keep only the region we are interested in, Fig. II.8.

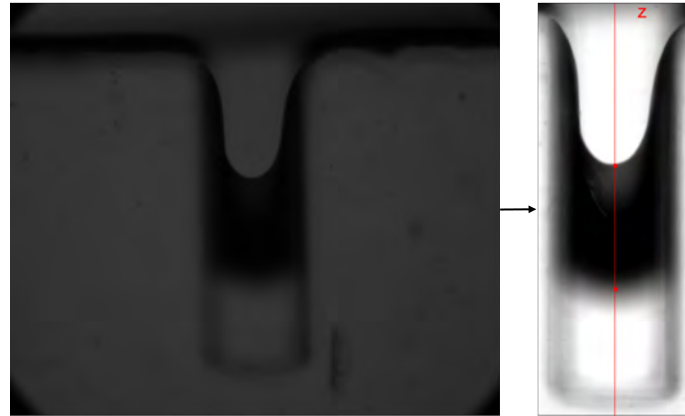


Figure II.8: From raw image to post processes in ImageJ, on the right the line for the Reslice plugin is drawn and measure 1716 pixels.

2. A line is drawn in the center of the channel, Fig. II.8, where the most advanced points at the top and bottom develop, and the Reslice plugin is applied to the stack. This reconstructs a 2D image from the image volume contained in the current stack. For example if we are reslicing a stack that contains N images on a length of L pixels, the result will be an image $N \times L$, Fig. II.9.
3. The obtained image represents the position of the front in time, since it's still in grey values, a binarization is needed to extract the information.

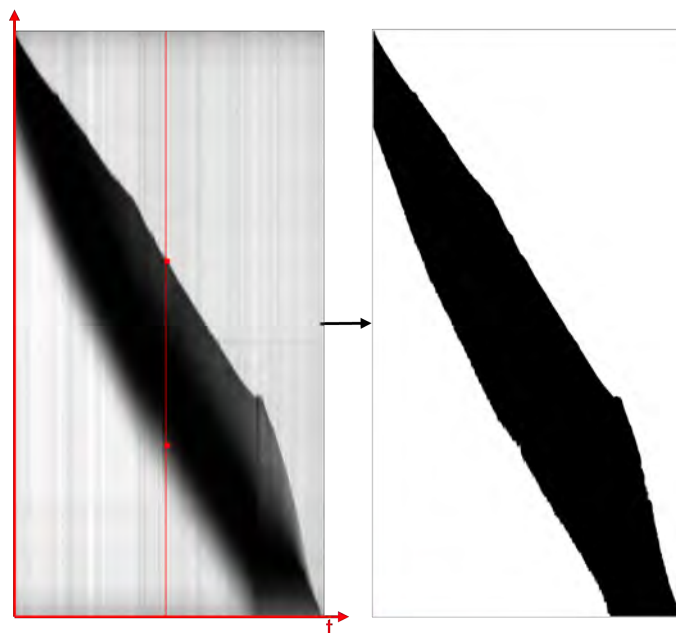


Figure II.9: Result of the Reslice plugin and consequent binarization to be treated in Matlab, the image is 850×1716 , where 850 is the number of images and 1716 is the size of the channel from Fig. II.8.

4. Once the image is black and white, we use a code in Matlab that for each column takes the position of the first and last black pixel starting from the top. This correspond to the evolution of the triple line on both the SUEX and PDMS, Fig. II.10.
5. Since the data are still computed in pixel, we use a space factor, computed from the images considering that the channel is 0.8 mm wide, and a time factor, for which we know the frequency of the images.

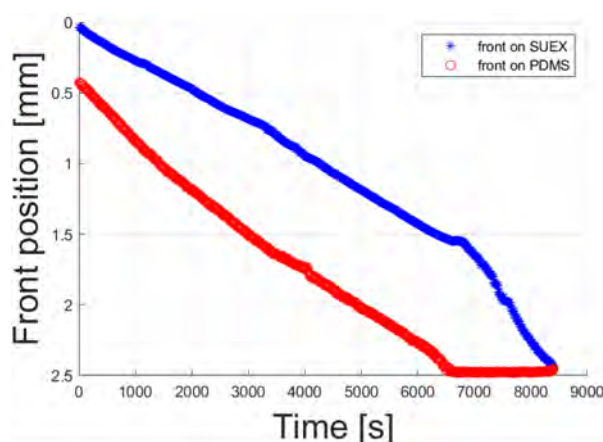


Figure II.10: Evolution of the triple line on SUEX and on PDMS resulting from the processing in Matlab of Fig.II.9

4.2 The three phases

Three main periods can be distinguished. In the first period the triple line moves faster on the PDMS wall than on the SUEX bottom wall until the quasi-static equilibrium shape illustrated in Fig. II.3b is reached. The distance between the triple line most advanced point on the PDMS wall and the SUEX bottom wall thus increases in this period (Fig. II.11b) until a plateau is reached. The plateau in Fig. II.11b corresponds to the second period where the triple lines move at the same pace on the top and bottom walls (as well as on the lateral walls). In other words, the quasistatic liquid - gas interfacial shape illustrated in Fig. II.3b moves inward at a constant speed without significant deformation in this second period. The triple line constant speed is also evidenced by the quasi-linear displacement of the triple line most advanced points z_{bm2} and z_{bm1} in Fig. II.11a. The third period starts when the triple line on the PDMS wall reaches the end wall. Then the triple line continues moving on the SUEX bottom wall as the mass of liquid confined in the end region of the channel gradually decreases. This is illustrated in Fig. II.11b, where the distance $z_{bm2} - z_{bm1}$ becomes $L - z_{bm1}$, where L is the channel length as indicated in Fig. II.3, and gradually goes to zero.

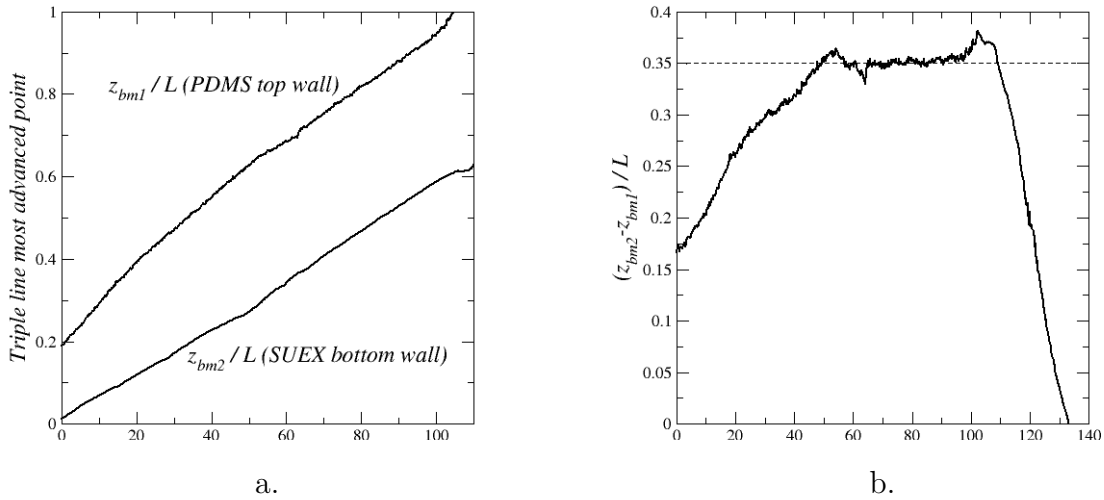


Figure II.11: (a) Experiment: Evolution of triple line most advanced point on SUEX bottom surface (z_{bm1} in Figs. II.3 or II.6) and on PDMS top surface (z_{bm2} in Figs. II.3 or II.6) for pure water, (b) Experiment: Evolution of the difference in the triple line most advanced point positions between PDMS top wall and SUEX bottom wall (i.e. $z_{bm2} - z_{bm1}$)

4.3 The evaporation rate

As discussed in previous works, e.g. [Chauvet *et al.*, 2009, Prat, 2007], the evaporation rate highly depends on the presence of the liquid corner films up to the channel entrance. The liquid is transported within the films from the main meniscus region up to the film

tip region where it evaporates. This transport induces the displacement of the bulk meniscus within the channel. Due to the so-called screening effects (see Section II.4), evaporation is significantly more important in the channel entrance region than further inside the channel when the bulk meniscus has sufficiently receded into the channel. In other words, as reported in [Chauvet *et al.*, 2010], evaporation from the main meniscus becomes rapidly negligible and evaporation actually occurs in the corner film tip region. Thus, the evaporation rate J is expected to decrease in the first period as the main meniscus recedes into the channel and to reach a constant value in the second period. The evaporation rate J and the liquid mass $m(t)$ within the channel (regardless of the liquid mass in the corner films for simplicity) are related by

$$J = -\frac{dm(t)}{dt} = \rho_\ell \frac{dV_\ell}{dt} \quad (4.1)$$

where ρ_ℓ is the liquid density and V_ℓ is the liquid volume limited by the main meniscus. The latter can be roughly expressed as

$$V_\ell \approx A(L - z_{bm2}(t)) + \frac{1}{2}A(z_{bm2}(t) - z_{bm1}(t)) \quad (4.2)$$

as long as $z_{bm2}(t) < L$, where A is the channel cross-section surface area. As shown in Fig. II.11b, $z_{bm2}(t) - z_{bm1}(t) \approx \text{constant}$ for pure water in period 2. Thus, in this period $\rho_\ell A \frac{dz_{bm2}(t)}{dt} = J$, which consistently leads to a linear variation of $z_{bm2}(t)$ with time (and thus also as regards $z_{bm1}(t)$ since $z_{bm2}(t) - z_{bm1}(t) \approx \text{constant}$) as J is expected to be constant due to the combination of the corner film and screening effects in this period. This is further discussed in Section II.7.

4.4 Surface Evolver simulations

As can be seen from Fig. II.12a and b, the simulation with Surface- Evolver leads to evolutions quite similar to those in the experiment. In the Surface Evolver simulations, there is no time scale and the parameter which is varied is the volume of gas present in the channel, or more precisely the gas saturation, i.e. the fraction S_g of the channel volume occupied by gas. As discussed before it is expected that S_g increases linearly with time since the evaporation is expected to be constant in the second period. For the sake of comparison between the experimental results and the Surface Evolver simulations (SES), the SES results have thus been plotted as a function of S_g in Fig. II.12. The comparison between the SES and the experimental result in Fig. II.11b and II.12b indicates that the capillary forces control the shape of the liquid-gas interface in the case of the pure water experiment.

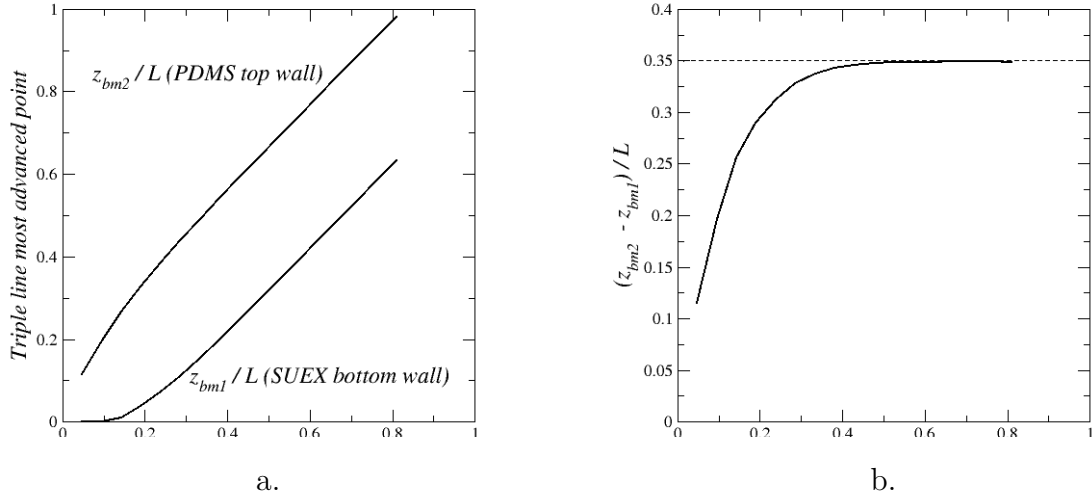


Figure II.12: (a) Surface Evolver simulation: variation of triple line most advanced point on SUEX bottom surface and on PDMS top surface as a fraction of the volume fraction of gas in the channel, (b) Surface Evolver simulation of the evolution of the difference in the triple line most advanced point positions between PDMS top wall and SUEX bottom wall (i.e. $z_{bm2} - z_{bm1}$).

5 Impact of particles on the evaporation kinetics

The evolution of triple line most advanced points on SUEX bottom wall and PDMS top wall in the presence of particles is shown in Fig. II.14. Note that the initial filling of channel by the liquid phase, i.e. the initial liquid saturation, varies from one experiment to the other. For this reason, the following procedure was used to set a common time in all the experiments. Concerning Fig. II.14a, the triple line on SUEX bottom wall observed in the first recorded image in the experiments was the most advanced inside the channel for the concentration $10^{-4}g/mL$. Let label the experiments from 1 to 4 in order of increasing concentration. This position $\max(z_{bm1-i})$ was thus selected to set a common time for the four experiments. The time when this position is reached in each experiment is denoted by t_i . Thus $t_4 = 0$ for $C = 10^{-4}g/mL$. Then the time in the other experiments was shifted as

$$t_{newi} = t + (\max(t_i) - t_i) \quad (5.1)$$

As a result of the time shift, the position $\max(z_{bm1-i})$ is reached at the same time in the four experiments. Similarly, for Fig. II.14b, the triple line on the PDMS wall observed in the first recorded image in the experiments was also the most advanced for the concentration $10^{-4}g/mL$. The corresponding position was thus selected to set a common time for the four experiments in the same way.

5.1 Image processing

The image treatment for the experiments in the presence of particles does not change drastically with respect to the one explained in section II.4.1. The main difference consists in capturing the position of the front. In fact, previously we used the contrast of the water, while in these cases we take advantage of the accumulation of particles at the triple lines. The image we obtain after the Reslice plugin is in Fig. II.13

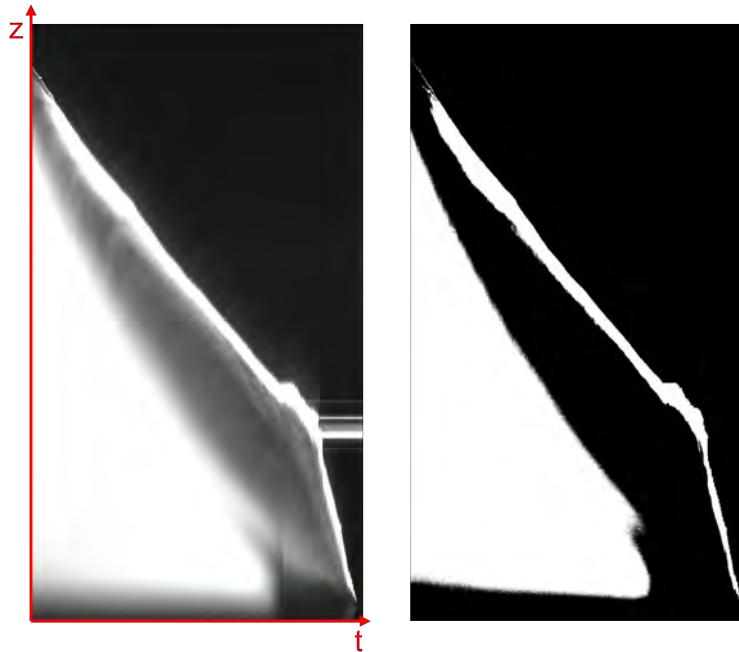


Figure II.13: Resulting image from the reslice plugin in ImageJ. The white pixels represent the accumulation of the particles, therefore the position of the two fronts.

5.2 The effects on the evaporation dynamic

As can be seen from Fig. II.14, the triple line displacement is slower in the presence of particles both on PDMS top wall and SUEX bottom wall with an impact of the particles more marked as regards the triple line displacement on the bottom SUEX wall. However, there is no clear difference on the results between the three particle concentrations. Based on a previous work on evaporation in the presence of colloidal particles from a granular porous medium [Keita *et al.*, 2013], one could expect that the higher the concentration, the slower is the evaporation. However, as discussed in Section II.7, the mechanism leading to the reduced evaporation, i.e. the film thinning, is different from the one considered in [Keita *et al.*, 2013]. Figs. II.5 and II.6 indicate that the greater the concentration, the thinner is the film. However, this impact on the film thickness is too weak to impart a noticeable variation in the evaporation rate between the three particle concentrations

tested. It can also be noticed that the evolution after $t = 130$ min in Fig. II.14a is not monotonic with the concentration.

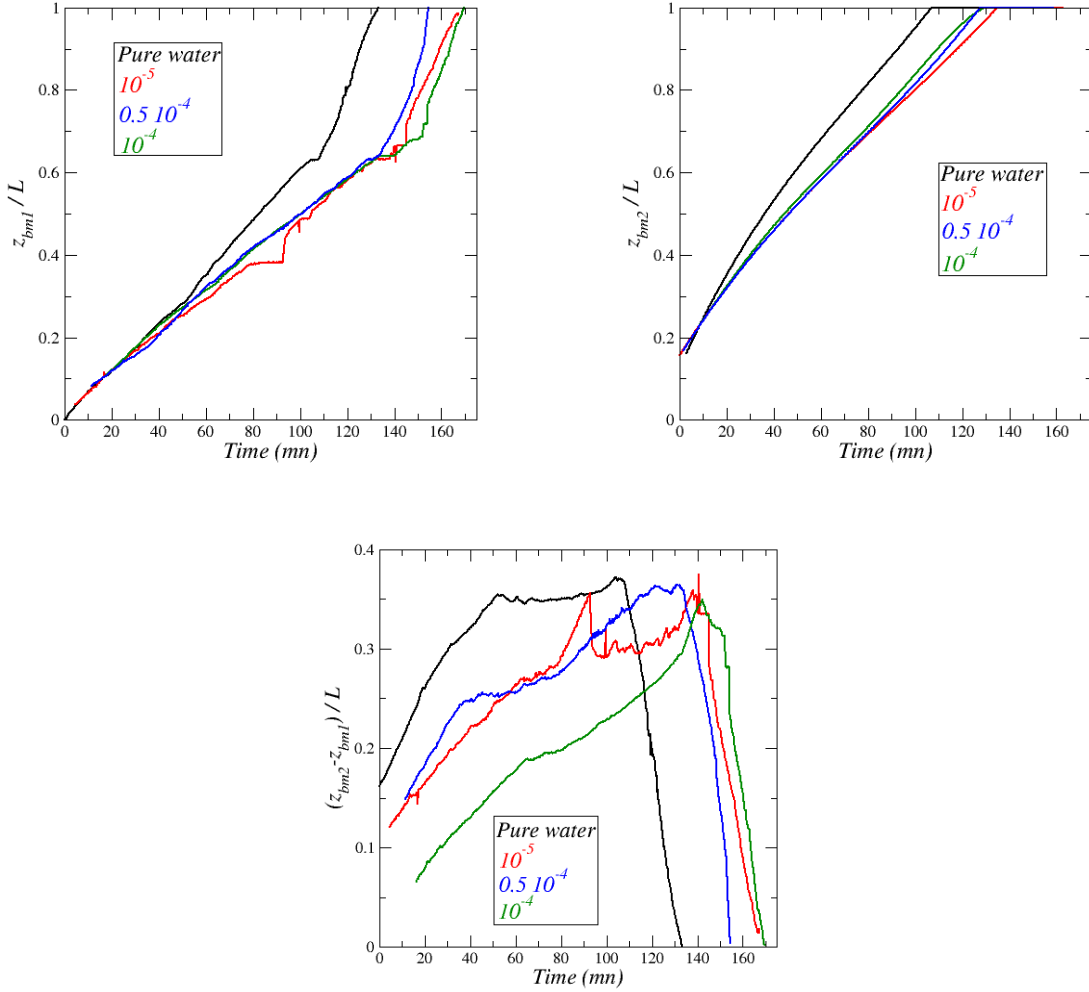


Figure II.14: (a) Evolution of triple line most advanced point on SUEx bottom surface (z_{bm1} in Fig. II.3), (b) and PDMS top surface (z_{bm2} in Fig. II.3). (c) Experiment: Evolution of the difference in the triple line most advanced point positions between PDMS top wall and SUEx bottom wall (i.e. $z_{bm2} - z_{bm1}$) for the various concentrations in particles.

As depicted in Fig. II.14c, an interesting difference can be observed between the pure water case and the case with particles when the difference $z_{bm2}(t) - z_{bm1}(t)$ between the triple line most advanced positions is plotted as a function of time (using the same procedure for setting a common time as for Fig. II.14a). Note that $z_{bm2}(t)$ is set equal to the channel length L once the triple line on the PDMS top channel wall has reached the channel end. This difference reaches a plateau in the case of the pure water experiment whereas it keeps increasing in the presence of particles. Also, this difference in the presence of particles is smaller than for pure water when the triple line on the PDMS top wall has not reached the channel end.

A peak can be observed in Fig. II.14c for the concentration $10^{-5}g/mL$ when t is the range $[80, 100]$ minutes. In fact, the triple line on the SUEX bottom gets pinned for a while due to a local accumulation of particles in the centre of the bottom wall whereas the triple line on the PDMS continues to move. As a result, the distance $z_{bm2}(t) - z_{bm1}(t)$ increases faster than for the other concentrations. When the triple line depinning occurs, the triple line on the bottom SUEX wall moves rapidly toward a new capillary equilibrium. This is an illustration of a stick-slip phenomenon [Kim *et al.*, 2018] explaining here the peak in the curve when $t \sim 80 - 100$ min. Similar stick-slip phenomena are observed for the other concentrations, but the triple line remains stuck for less time than in the case of the peak in Fig. II.14c for the concentration $10^{-5}g/mL$. Also, it can be observed from the movies that the stick-slip phenomena occur earlier for the smaller concentration ($10^{-5}g/mL$) than for the largest one ($10^{-4}g/mL$). Typically, when the main meniscus is in the last third of the channel for the concentration $10^{-4}g/mL$ whereas the phenomenon can be observed over the last two third of the channel for the concentration $10^{-5}g/mL$. The situation for the intermediate concentration ($0.5 \times 10^{-4}g/mL$) is closer to concentration $10^{-5}g/mL$ than $10^{-4}g/mL$. The fact that the stick-slip phenomenon becomes visible after a while can be explained by the fact that it takes some time for the particles to accumulate at and in the vicinity of the triple line. However, based on this argument, the stick-slip phenomenon should be expected to be observed earlier for the largest concentration whereas the contrary is observed. This remains to be explained. It can be also noticed that the stick-slip phenomenon can be observed both along the triple line region corresponding to the corner films and along the region corresponding to the main meniscus.

6 The final deposit

The final distribution of deposited particles after full evaporation is illustrated in Fig. II.15. Very limited deposition occurred on the PDMS top plate. The deposits essentially formed on the SUEX walls. As shown in Fig. II.15, two main regions of deposited particles can be distinguished. The region where corner liquid films were present and the left and right corners at the junction between the channel bottom and the end wall. The latter are fully consistent with the evolution of the liquid gas distribution toward the end of evaporation computed with Surface-Evolver (Fig. II.16), showing the formation of two liquid wedges in the corresponding corners. It is recalled that the Surface Evolver simulation corresponds to the case of pure water (no particles). The possible effect of the presence of the particles is roughly addressed in Fig. II.16 by considering two values of contact angle on the SUEX wall (the contact angle on the PDMS wall imposed in these

simulations is 104°). For both values, above and below the critical contact angle of 45° , the terminal wedge effect is obtained. The greater the concentration, the greater is the brightness of the deposits in Fig. II.15, indicating, as expected, a greater accumulation of deposited particles with an increasing initial particles concentration. More details can be seen for the highest concentration ($C = 10^{-4} g/mL$) in the image in false color in Fig. II.15. To obtain this image, the calibration curve has been used to convert the light intensity into particle concentration (considered as an indicator of particle accumulation since the particles are not in a suspension in this image whereas the calibration curve was established with particles in suspension). This image indicates a greater particle accumulation in the films compared to the end wedge region. Also, this image indicates that the particle deposit in the films is heterogeneous with more deposited particles in the upper region of the films and in the vicinity of the triple line.

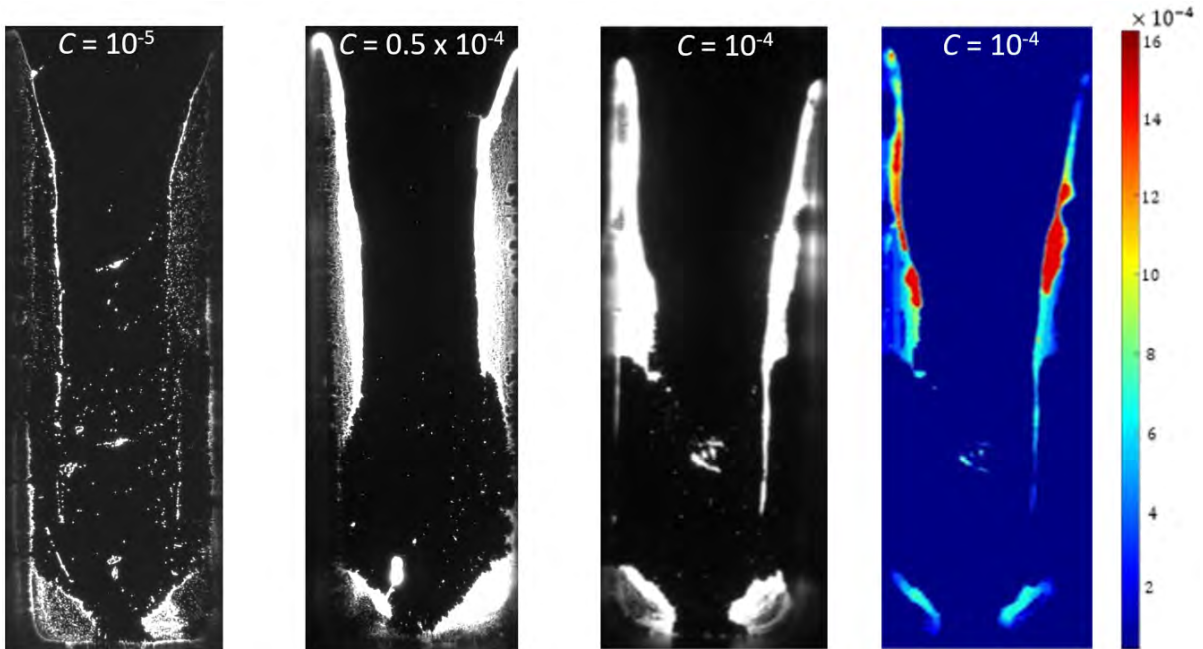


Figure II.15: Spatial distribution of deposited particles at the end of experiment after full evaporation. The preferential zones of particle deposition are in bright. The false color image on the right shows a more detailed information on the deposited particle distribution for the highest concentration tested.

7 The impact of corner film thickness on the evaporation rate

Numerical simulations are performed to evaluate the impact of film thickness on evaporation rate. The simulations correspond to the films illustrated in Fig. II.4, namely

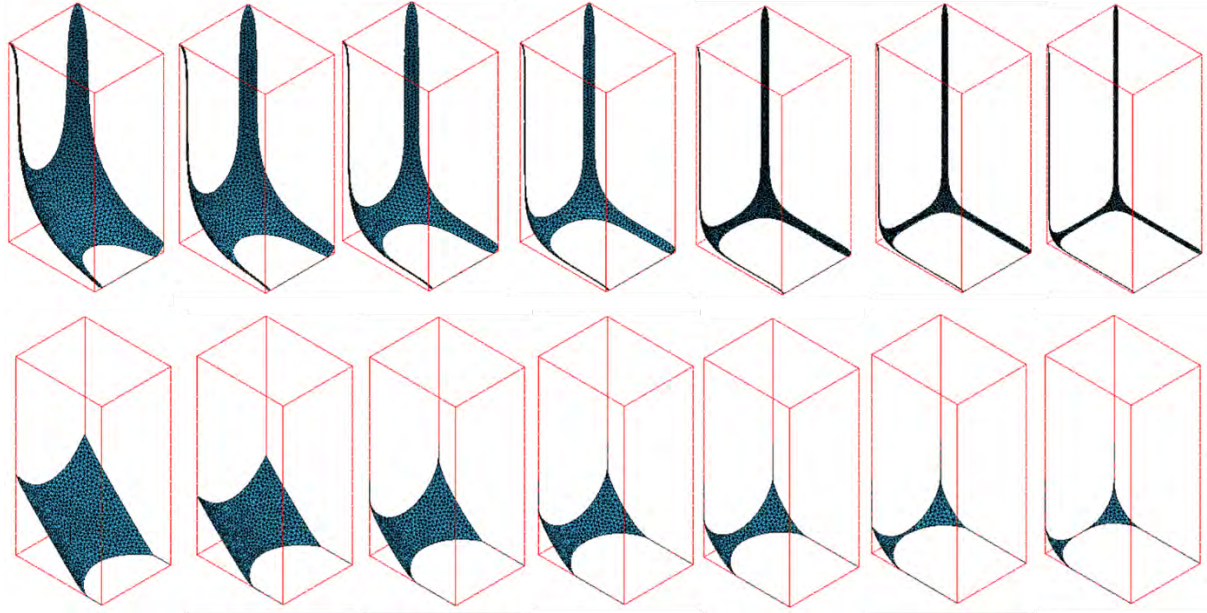


Figure II.16: Final liquid distribution in the composite channel as computed by Surface Evolver for two values of contact angle on the SUEX walls

pure water for three values of contact angle on SUEX (20° , 30° , 40°). The gas-liquid interface in the channel (as illustrated in Fig. II.4) is computed using Surface Evolver [Laurindo et Prat, 1998]. Then the result is imported in the commercial software COMSOL Multiphysics considering the computational domain illustrated in Fig. II.17. Based on a previous work [Beyhaghi *et al.*, 2014], the size of the hemisphere shown in Fig. II.17a is selected so as to be sufficiently large for the results to be independent of its size. The diffusion equation is solved in the channel (gas region) and within the gas region in the hemisphere imposing a dimensionless vapor partial pressure of 1 on the liquid-gas interface and zero on the hemisphere limiting surface. Zero flux condition is imposed on the solid walls. In fact, the vapor partial pressure gradients are significant only in a small region of the computational domain in the vicinity of the channel entrance. This is further shown in Fig. II.17c illustrating the so-called screening effect, i.e. the fact that the vapor partial pressure gradients vanish inside the channel due to the presence of the corner films. This gives the variation of the evaporation rate depicted in Fig. II.17d. As can be seen, the evaporation rate when the film is established (as depicted in Fig. II.5) is little less than half that of the full liquid channel (inset in Fig. II.17d). When the contact angle on SUEX is varied from 20° to 40° , the film thickness (defined in Fig. II.17d and made dimensionless using the channel width) varies from about 0.22 – 0.06, which is comparable to the variation depicted in Fig. II.6 between the case of pure water and that in the presence of particles. This variation corresponds to a reduction of about 20% in the evaporation rate (Fig. II.17d) and illustrates the strong impact of the corner film thickness

on the evaporation rate. From the estimate of the evaporation rate in the experiment $J \approx \rho_\ell A \frac{dz_{bm1}(t)}{dt}$, this 20% variation is fully consistent with the mean variation in the slope, i.e. $\frac{1}{L} \frac{dz_{bm1}(t)}{dt}$, in Fig. II.14 (before the position 0.6 is reached) between the case of pure water and that with particles (the slope ratio between both cases is about 0.81). In conclusion, the presence of the particles makes the corner films thinner in the channel entrance region, which is the region of most active evaporation in the channel, and this reduces the evaporation compared to the case of pure water, which corresponds to the thickest films.

8 On the accumulation of particles in the films and the film thinning effect

8.1 Particle convective transport is dominant in the films

The preferential accumulation of particles in the corner liquid films is consistent with a dominant convective transport of the particles within the films. This can be supported from the estimate of the Péclet number characterizing the competition between the diffusive and convective transports in the films [Camassel *et al.*, 2005]. The latter is expressed as

$$Pe = \frac{Ul}{D} \quad (8.1)$$

where U is a characteristic liquid velocity in the films, l is the length of the films and D is the particle diffusion coefficient. The latter can be estimated using the Stokes-Einstein law. For $1\mu m$ diameter particles, this gives $D \sim 10^{-13} m^2/s$. The velocity in the films can be estimated as

$$U = \frac{1}{A_c} \frac{J}{2\rho_\ell} \quad (8.2)$$

[Prat, 2007], where J is the evaporation rate and A_c is the cross-section surface area of a corner film. For simplicity, the latter is estimated for the case of pure water and the contact angle of 30° (Fig. II.4) from the formula given in [Prat, 2007].

As mentioned in Section II.4.3, the evaporation rate can be estimated as $J = \rho_\ell A \frac{dz_{bm2}(t)}{dt}$ application for $l = L/2$ gives $Pe \approx O(10^5)$, which corresponds to a highly dominant convective transport of the particles within the films. It is well known, e.g. [Huinink *et al.*, 2002], that a large Péclet number corresponds to the preferential accumulation of the particles at the evaporation front. Thus, here, one could expect that the particles accumulate along the film liquid-gas interface. This is roughly what can be seen from Fig. II.15. However,

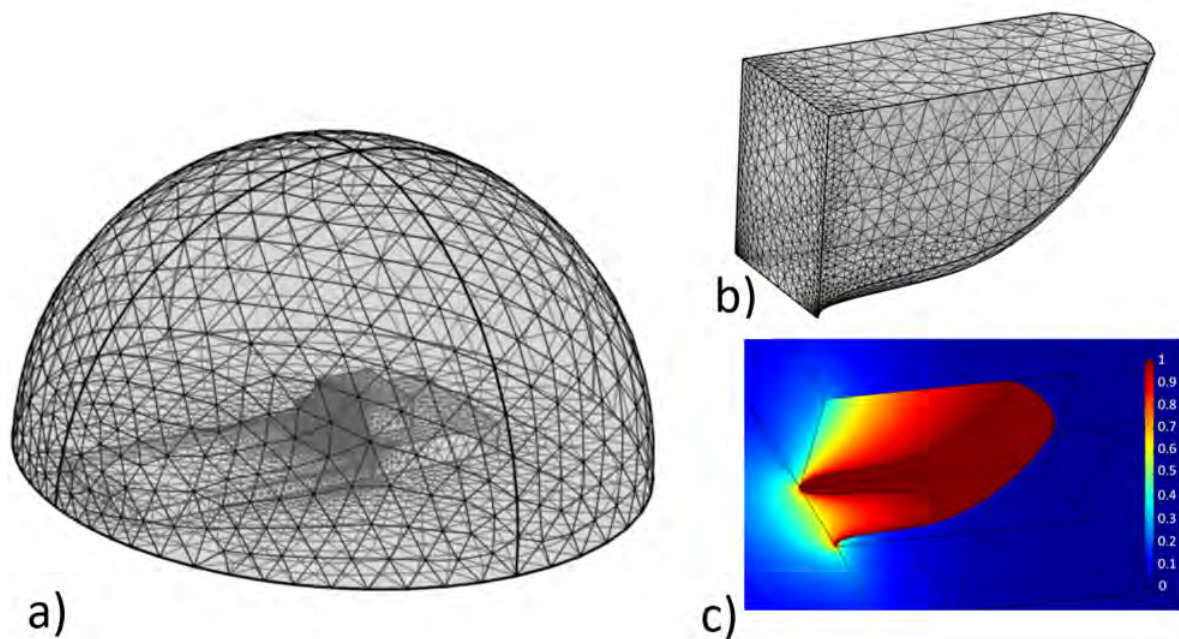


Figure II.17: Impact of film thickness on evaporation rate from the channel from numerical simulations. a) computational domain, b) computational domain in the channel (gas region), c) illustration of normalized vapor partial pressure field (dimensionless) in the channel, d) Variation of evaporation rate as a function of film thickness (in the inset the evaporation rate is normalized by the evaporation rate from the fully liquid saturated channel).

as illustrated in the image in false-color in Fig. II.15, the greater accumulation at the end of the evaporation is not at the film top but deeper inside the channel. This heterogeneous distribution is in part due to what happens in the final step when the films disconnect from the channel end and fully evaporate.

However, the inspection of the movies suggests a relatively complex particle dynamics in the films during evaporation with possible particle recirculation effects within the films. These recirculation effects should also play a role in the particle distribution within the films and would deserve to be explored in details in future works.

8.2 Accumulation of particles and particle compact packing in the corner films

In [Dufresne *et al.*, 2003] and [Keita *et al.*, 2013], the reduced evaporation rate observed in the presence of particles was attributed to the formation of a compact packing of particles and the formation of a dried zone in the accumulation zone of particles. As in a classical drying problem in porous media, e.g. [Prat, 2002], the presence of the evaporation front at the boundary of the particle packing depends on the competition between viscous and capillary effects. When the pressure drop in the liquid phase due to the viscous flow induced by the evaporation process is too large the capillary effects are not sufficient to maintain the front at the particle packing boundary and the front recedes into the packing. This leads to the formation of a dry zone introducing an additional mass transfer resistance. A similar mechanism of particle accumulation and receding front was observed in corner films in a single channel in [Seck *et al.*, 2019]. Although assuming completely dry the zone ahead of the front did not lead to results fully consistent with the experiment, the impact of the particles on the evaporation rate was quite noticeable.

Thus, the question arises as to whether a similar phenomenon can contribute to explain the reduced evaporation observed in our experiments. A simple argument indicating that the situation is different in the case of our experiments consists in evaluating the volume fraction of particles in the corner films. The total number of particles in the channel is

$$N_p = \frac{V_{ch}C}{m_p} \quad (8.3)$$

where V_{ch} is the channel volume (assuming here that the channel is fully filled by the solution initially), C is the particle concentration and m_p is the mass of one particle. Let us assume a contact angle of 30° , a film thickness of $80\mu m$ (Fig. II.6), a film extent z_{bm1} of $1mm$ and that all the particles are uniformly distributed within the two corner films. Then the particle volume fraction in the films is

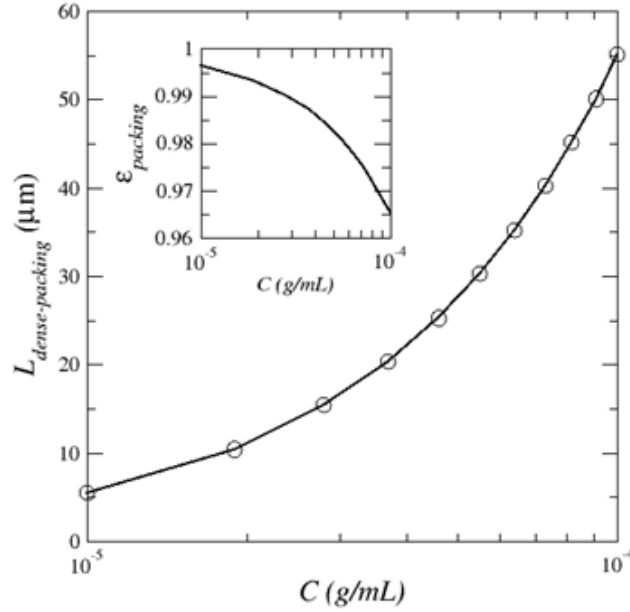


Figure II.18: Size of a compact particle packing in the corner films made of all particles introduced in the channel. The inset shows the particle volume fraction in the corner films assuming a uniform distribution of all the particles in the corner films for $z_{bm1} = 1\text{mm}$.

$$\epsilon_s = \frac{N_p}{2} \frac{V_p}{A_c z_{bm1}} \quad (8.4)$$

where V_p is the volume of one particle and A_c is the film cross-section surface area. This gives the results shown in Fig. II.18 (inset) indicating that the particle volume fraction ϵ_s is quite low. In other words, contrary to the situation analyzed in [Dufresne *et al.*, 2003] or [Seck *et al.*, 2019], a compact packing of particles (corresponding to $\epsilon = 1 - \epsilon_s \approx 0.37$) cannot form over a significant region of the corner films. To discuss further this aspect, suppose the particles are all in the tip region of the corner films and form a compact packing. The length L_{cp} of this compact zone within the corner film can be estimated from the equation

$$L_{cp}(1 - \epsilon)A_c = \frac{N_p}{2}V_p \quad (8.5)$$

where $\epsilon \approx 0.37$ (compact packing). This gives the results shown in Fig. II.18. As can be seen, the length of such a packing is on the order of a few tens of micrometers. This is too small to expect the dry zone formation to form and to affect the evaporation rate. Consistently with the observations a compact arrangement of the particles can thus be expected only in the vicinity of the triple line during the evaporation process in the

channel. Also, it can be noted that the particles are too large in our experiments to expect an impact of the Kelvin effect on the evaporation rate [Lidon et Salmon, 2014].

Consistently with the results presented in Section II.7, the conclusion is therefore that the reduced evaporation observed in our experiments in the presence of particles is due to the film thinning and not to the formation of a dry zone in the corner film region or the Kelvin effect. Then, the question remains why does the presence of the particles lead to thinner corner films compared to pure water? This is discussed in the next sub-section. Nevertheless, the comparison with the results reported in [Seck *et al.*, 2019] suggests to distinguish at least two regimes. The situation studied in [Seck *et al.*, 2019] would correspond to a “high” concentration regime where the particles are sufficiently numerous for forming a compact packing in a significant region of the corner films whereas the situation considered in our experiments would correspond to a “low” concentration regime where the number of particles in the corner films is much lower and the compact packing, if any, is limited to the vicinity of the triple lines and the liquid–gas interface.

8.3 Estimation of A_c

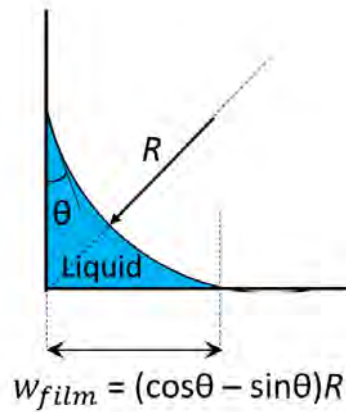


Figure II.19: Relationship between corner meniscus curvature radius, film thickness and contact angle.

The flow rate withing a corner film is expressed as

$$q_m = -\rho_l \frac{A_c R^2}{\beta \mu} \frac{dp}{dz} \quad 0 \leq z \leq z_0 \quad (8.6)$$

Where $z = 0$ is at the film tip and $z = z_0$ the position where the film merges with the main meniscus. In Eq.8.6, R is the corner film curvature radius, p is the pressure in the liquid, μ is the liquid dynamic viscosity, A_c is the corner film cross section surface area

and β is a dimensionless resistance. The latter can be expressed for a sharp corner as

$$\beta = \frac{12 \sin^2 \alpha (1 - B) 2}{(1 - \sin \alpha)^2 B^2} \frac{\psi_3^2}{(\psi_1 - B\psi_2)^2} \quad (8.7)$$

where

$$\begin{aligned} \psi_1 &= (\cos(\alpha + \theta))^2 + \cos(\alpha + \theta) \sin(\alpha + \theta) \tan \alpha \\ \psi_2 &= 1 - \frac{\theta}{\frac{\pi}{2} - \alpha} \\ \psi_3 &= \frac{\cos(\alpha + \theta)}{\cos \alpha} \end{aligned}$$

$B = \left(\frac{\pi}{2} - \alpha\right) \tan \alpha$ in which θ is the contact angle expressed in radian and $\alpha = \frac{\pi}{4}$. The corner film cross section surface area can be expressed as

$$A_c = R^2 \psi_4 \quad (8.8)$$

where $\psi_4 = \frac{\cos \theta}{\sin \alpha} \cos(\alpha + \theta) - \frac{\pi}{2} + \alpha + \theta$.

The pressure in the liquid is linked to the surface tension and R by the Young-Laplace law

$$p = p_g - \frac{\gamma}{R} \quad (8.9)$$

where p_g is the gas pressure assumed constant. The above equations are combined to obtain

$$q_m = \frac{\rho_\ell \kappa R^2}{\mu} \frac{dR}{dz} \quad (8.10)$$

where $\kappa = \frac{\psi_4}{\beta}$. This flow corresponds to half the evaporation rate J since there are two corner films in the channel. Thus

$$\frac{\rho_\ell \kappa R^2}{\mu} \frac{dR}{dz} = \frac{J}{2} \quad (8.11)$$

which is to solve with the boundary condition $R = R_{th}$ at $z = z_0$, where R_{th} is the corner film curvature radius at the junction between the corner film and the main meniscus. The solution to Eq.8.11 reads

$$R^3 = \frac{3J\mu}{2\rho_\ell \kappa \gamma} (z - z_0) + R_{th}^3 \quad (8.12)$$

The curvature radius R_{th} is determined from the pure water experiment as

$$R_{th} = \frac{w_{film}}{\cos \theta - \sin \theta} \quad (8.13)$$

where w_{film} is the film thickness shown in Fig. II.5 for pure water ($w_{film} \approx 140\mu m$). The evaporation rate can be estimated from $\rho_\ell A \frac{dz_{bm2}(t)}{dt} = J$ and Fig. II.14b. This gives $J \approx 2 \times 10^{-10} kg/s$. Computing the variation of R from Eq. 8.12 for various values of the viscosity and using the relationship $w_{film}(z) = (\cos \theta - \sin \theta)R(z)$, see Fig. II.19, leads to the film shapes depicted in Fig. II.20.

8.4 On the effect of particles on corner films

From previous works, e.g. [Chauvet *et al.*, 2009, Prat, 2007, Chauvet *et al.*, 2009], it is known that the corner film thickness depends on the contact angle and the competition between the capillary and viscous forces (gravity effects being negligible in the present experiment). As mentioned before, the contact angle must be lower than a critical value θ_c for the corner films to develop ($\theta_c = 45^\circ$ for right angle corner, [Concus et Finn, 1969]). The lower the contact angle below θ_c , the thicker the corner films are, all other factors being equal.

8.4.1 The effect on surface tension

To explain the film thinning seen in the experiments with particles, a first possibility could be the effect of particles on surface tension. As reported in [Dong et Johnson, 2003], the presence of particles can reduce the surface tension. Let us consider that the surface tension varies with the particle concentration. The quasi-static corner meniscus curvature radius distribution is given by

$$\frac{\gamma(z)}{R} = \frac{\gamma(z_0)}{R_{th}} \quad (8.14)$$

where R is the corner meniscus curvature radius see Fig. II.19 and R_{th} is the corner film curvature radius at the junction with the bulk meniscus. This leads to

$$w_{film}(z) = (\cos \theta - \sin \theta)R_{th} \frac{\gamma(z)}{\gamma(z_0)} \quad (8.15)$$

where w_{film} is the film thickness (Fig. II.5 and Fig. II.19).

The maximum surface tension variation in [Dong et Johnson, 2003] due to particles is from $71 \times 10^{-3} N/m$ to about $67 \times 10^{-3} N/m$. According to Eq.8.15

$$\frac{w_{film}(z)}{w_{film}(z_0)} = \frac{\gamma(z)}{\gamma(z_0)}. \quad (8.16)$$

Thus, the maximum film thickness variation due to this effect can be expected to be $\frac{w_{film}(z)}{w_{film}(z_0)} = \frac{\gamma(z)}{\gamma(z_0)} \approx 0.94$. Based on the results shown in Figs. II.5 and II.6, this effect is too weak to explain the corner film thinning observed in the experiment. Furthermore, it is likely that the decrease in the surface tension is partly compensated by a decrease in the contact angle.

8.4.2 The effect on the suspension viscosity

Another possibility lies in the effect of the particles on the suspension viscosity. Since evaporation induces a liquid flow in the films, this liquid flow induces a viscous pressure drop along the film. When this viscous pressure drop is negligible compared to the pressure jump, i.e. the capillary pressure, at the liquid-vapor interface, the film thickness does not vary along the channel except in the channel entrance region. This is the situation in the pure water experiment (Fig. II.3). When the viscous pressure drop is not negligible, the capillary pressure varies along the corner films. This induces the spatial variation of the film thickness, which increases along the corner from the channel entrance. Since the film thickness increases along the corners in Fig. II.5, it is tempting to consider that the effect of the particles is to increase the suspension viscosity at a sufficient level for impacting the film thickness. To evaluate the viscous pressure drop required to obtain a noticeable thinning of the film, the model presented in [Prat, 2007] is used. Consider a corner film of thickness R for the simpler case of $\theta = 0$. For simplicity, suppose that particles are present all over the film cross-section. Then, according to Darcy's law, the flow rate in the film can be expressed as

$$q_{mD} = -\rho_\ell A_c \frac{k}{\mu} \frac{dp}{dz} \quad (8.17)$$

Where k is the particle packing permeability. The latter can be estimated using the Kozeny-Carman relationship as $k = \frac{\epsilon^3 d^2}{180(1 - \epsilon^2)}$, where d is the particle diameter ($d = 1\mu m$) and ϵ is the packing porosity ($\epsilon \approx 0.36$).

The apparent viscosity μ_D of the packing is then defined using Eq.(8.6) as

$$q_{mD} = -\rho_\ell \frac{A_c}{\beta} \frac{k}{\mu_D} \frac{dp}{dz} \quad (8.18)$$

The apparent viscosity is thus the viscosity of a suspension that would lead to the same pressure drop as the Darcy's flow. From Eqs.(8.17) and (8.18), one obtains

$$\frac{\mu_D}{\mu} = \frac{R^2}{\beta k} \quad (8.19)$$

For $R \approx 100\mu m$ (an order of magnitude consistent with the corner film thicknesses in Fig. II.6), Eq.(8.19) yields $\mu_D/\mu \approx 6 \times 10^6$.

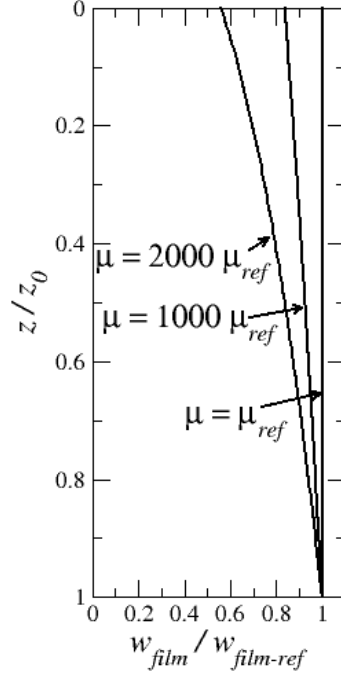


Figure II.20: Impact of suspension viscosity on film thickness variation along the channel; μ_{ref} is the dynamic viscosity for pure water, $w_{film-ref}$ is the film thickness when viscous effects are negligible.

It is found that the viscosity must be about three orders of magnitude greater than the viscosity of pure water (denoted μ_{ref} in Fig. II.20) for the corner film thickness variation along the channel to be comparable to that seen in the experiment in the presence of particle (Figs. II.5 and II.6). However, the data reported in [Thomas, 1965] indicates that the maximum increase in the viscosity due to the presence of particles is by about a factor 100, thus an order of magnitude lower than the value estimated for obtaining a film thinning comparable to the experiment. Also, the film thickness at a given location decreases with time when the film thinning is due to viscous effects. This is not what is seen in the experiments in the presence of particles since the film shape at a given location does not vary with time once formed (except at the very end of the experiment when the liquid totally disappears and on the few places where the stick-slip previously phenomenon mentioned and also discussed below occurs).

Also the particle concentration in the films is actually quite low (as discussed in Section II.8). Thus the impact of particles on the suspension viscosity is in fact negligible. The corner film thinning in the presence of the particles cannot therefore be attributed to the

increase in the suspension viscosity due to the presence of the particles.

However, the pictures of the particle distribution in Fig. II.5 suggest that the particles can agglomerate and form a dense packing, at least locally. The pressure drop due to Darcy flow through such a packing of particles can be expected to be larger than for a suspension. In order to evaluate the possible impact of such an agglomeration of particles, the impact of Darcy flow through immobile agglomerated particles is expressed in terms of equivalent apparent viscosity μ_D . This leads to an apparent equivalent suspension viscosity which is about 10^6 greater than the reference viscosity, i.e. the dynamic viscosity for pure water. Thus much larger than the viscosity required to obtain a significant film thinning according to Fig. II.20. This is a clear indication that the resistance to the flow due to the particle accumulation is sufficient to generate pressure drops compatible with the observed film thinning.

Finally, as illustrated in Fig. II.5, the conclusion is that the film shape is essentially affected by the local accumulation of particles in the vicinity of the triple line. Once the particle concentration at the triple line is sufficiently high, particles locally form a compact packing and the triple line gets pinned and this leads to the film thinning illustrated in Fig. II.5. However, the details on the complex dynamics of pinning and local packing formation leading to the corner film shapes shown in Fig. II.5 remain to be unraveled. For instance, as mentioned before, the inspection of the movies does indicate some occasional stick-slip motion of the triple line in the presence of particles. Perhaps, a detailed analysis of this stick-slip effect, e.g. [Kim *et al.*, 2018], might help better understand the capillary film thinning phenomenon in the presence of particles. Also, it has been reported that the wettability of the particles has an impact on the motion of the triple line, e.g. [Kim *et al.*, 2018]. Repeating the experiments changing the particle wettability could be insightful.

9 High concentration of particles

The previous part of this chapter corresponds to an extended version of the published article [Ghiringhelli *et al.*, 2023] where the initial concentration in particles was varied from 0 to 10^{-4} g/mL. As discussed above, the mechanism of particle compaction with formation of a receding evaporation front within the particle packing described in [Dufresne *et al.*, 2003] was not observed. The relatively low concentrations considered was shown to be not sufficient for expecting the formation of a significant compact region of particles. In this last part of the chapter, results are presented for a much larger initial concentration,

namely 0.6×10^{-2} g/mL. The corresponding experiments were actually performed several months after the ones with the lower concentrations in particles. This is also a reason why the results for this much higher concentration are presented in a dedicated section of the present chapter and not in the previous sections. The relative humidity in these additional experiments (RH \sim 60 %) was about same as in the previous experiments as well as the temperature (22°C).

9.1 Liquid - gas distribution in the channel and final deposit

The evolution of the phase distribution in the channel during the evaporation is illustrated in Fig. II.21. Even if the concentration of particles is higher than the previous experiments, the deposit on the PDMS top wall is still negligible compared to the one over the SUEX bottom wall. As depicted in Fig.II.21, corner films still form for this higher concentration. However important differences can be noted as regards the shape of the corner compared to the corresponding pictures for the lower concentrations (Fig. II.5). There is strong particle accumulation in the upper region of the films and this accumulation leads to a larger film width in the entrance region of the channel. Contrary to the previous experiments with lower concentrations, the film width in this region is larger than that for pure water (as shown in Fig. II.21c where the red curve corresponds to the triple line for pure water). Also, the variation of the film width with the distance from the channel entrance is not monotonous. The corner film width first increases in the channel entrance region, reaches a maximum and then decreases. Further away inside the channel the corner film width variation with the distance is much less important than in the channel entrance region. Contrary to the experiments with lower concentrations (Fig. II.15), the preferential accumulation of particles in the left and right corners in the region of the end wall closing the channel is not observed. The particle preferentially accumulates at and in the vicinity of the triple line on the SUEX walls. Since the triple line is initially present only near the channel open end and gradually invades the channel, a strong accumulation of particles occurs in the channel entrance region. As indicated by the red arrows in Fig.II.21, the size of the particle accumulation region in the channel entrance region increases with time. This can be interpreted as an indication that the particles form a compact accumulation in this region and that there is a flow through this growing compact region (the flow is necessary for the particles to reach this accumulation zones and to maintain a relatively high evaporation rate (= not much smaller than for pure water) as discussed later in section II.9.2).

This mechanism of preferential accumulation of particles and formation of packed particles eventually leads to a final deposit where the majority of the particles is in the upper third of the channel, i.e. the entrance region, as shown in Fig. II.21. In

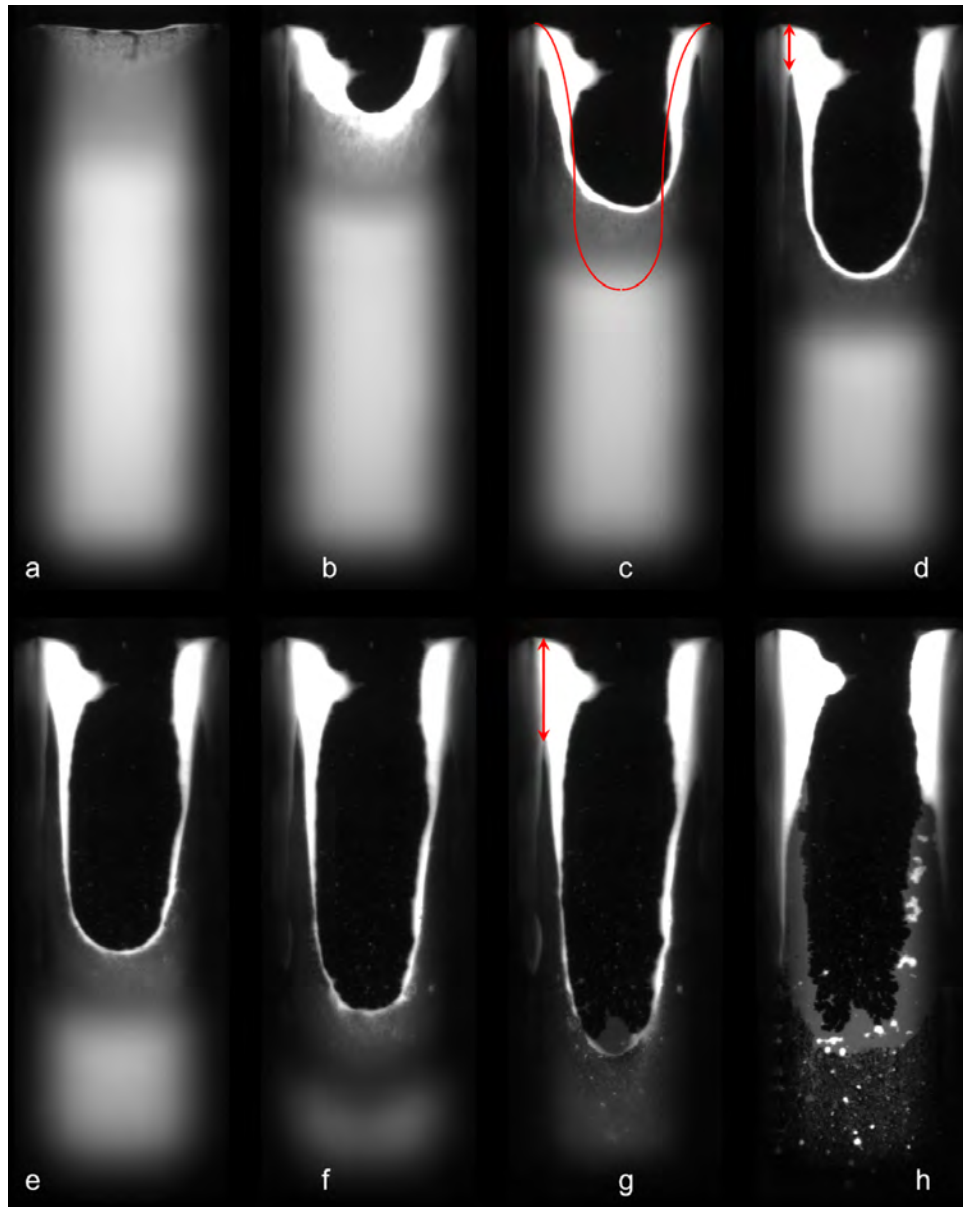


Figure II.21: a-g) Images every 25 minutes of the evaporation process with the highest concentration of particles, h) Final deposit distribution. The red arrows materialize the increase in the size of the particle deposit in the entrance region of the channel. The red line in Fig. II.21c corresponds to the triple line on the SUEX bottom wall in the pure water experiment.

other words, the images in Fig. II.7 strongly suggest the formation of a compact region of particles in the corner films, somewhat similarly to the compact particle packing reported in previous publications in experiments with channels with two open ends [Dufresne *et al.*, 2003, Dong et Johnson, 2003]. Since the corner film width is larger in the channel entrance region, it can be expected that the evaporation rate is greater than for the previous concentrations. On the other hand, if the bright region in the channel entrance region in Fig. II.21 corresponds to a zone of particle accumulation where the receding evaporation front mechanism described by Dufresne et al. [Dufresne *et al.*, 2003] takes place, the evaporation rate should be affected and lower than for the lower concentrations discussed previously. This question is discussed further in the next section.

9.2 Evaporation kinetics

As before, the evaporation kinetics is characterized by plotting the evolution of the bulk meniscus position on the SUEX bottom wall, i.e. z_{bm1} , and that of the bulk meniscus position on the PDMS top wall, i.e. z_{bm2} . The evolutions of z_{bm1} and z_{bm2} are depicted in Fig. II.22 together with the evolutions previously presented for the lower particle concentrations. Note that the experiment has been performed twice (the images depicted in Fig. II.21 correspond to the first experiment). The first experiment corresponds to the orange solid lines in Fig II.22 whereas the second experiment corresponds to the orange dashed lines. As before, a common time has been set in order to perform the comparison between the various concentrations in Fig. II.22a and II.22b (see Section II.5 and Eq.(5.1)).

As can be seen from Fig. II.22, a direct conclusion is not obvious. In a first period (20-50 min), the variation of z_{bm1} (bulk meniscus position of the SUEX bottom wall) in Fig.II.22a is consistent with a larger film width since the evolution is faster compared to the other concentrations. However, the evolution slows down in a second period and the overall time for reaching the channel end is comparable to that for the lower concentrations and thus greater than for pure water. The evolution of z_{bm2} (bulk meniscus position of the PDMS bottom wall) in Fig. II.22b is less ambiguous. This evolution is significantly slower for the higher concentration than for the lower concentrations. The most striking difference lies perhaps in the evolution of $z_{bm2} - z_{bm1}$ depicted in Fig.II.22c. Whereas this evolution is globally monotonous for the lower concentrations (except at the very end of drying when $z_{bm2} - z_{bm1}$ decreases to zero), the curve is rather different for the higher concentration with a minimum about at mid-drying (regardless again of the very last period where this distance goes to zero). Also, this distance between the two bulk meniscus positions is on average smaller for the higher concentration than for the lower ones. In other words, the average displacement velocity of the triple line on the PDMS top wall is smaller than for

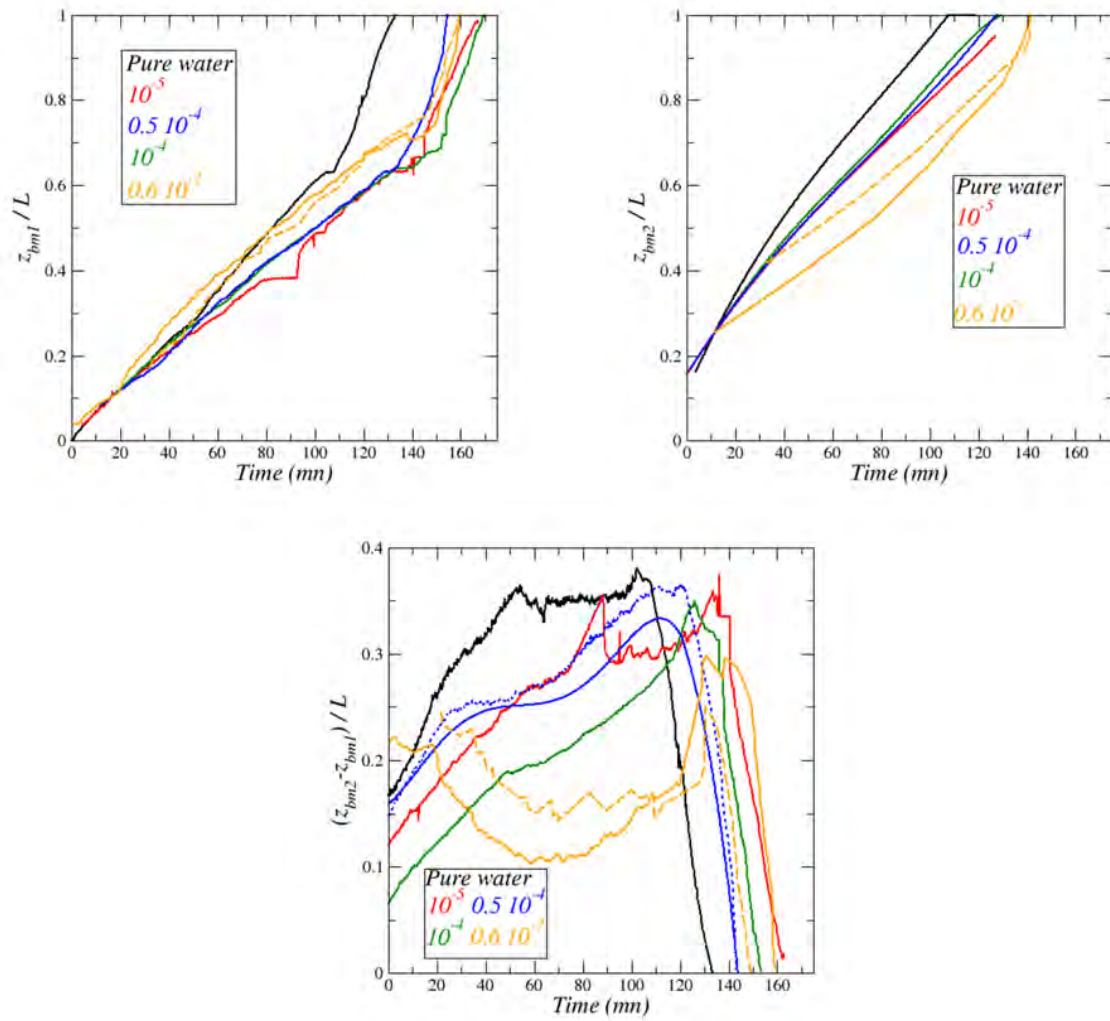


Figure II.22: (a) Evolution of triple line most advanced point on SUEx bottom surface (z_{bm1} in Fig. II.2), (b) and PDMS top surface (z_{bm2} in Fig. II.2). (c) Evolution of the difference in the triple line most advanced point positions between PDMS top wall and SUEx bottom wall (i.e. $z_{bm2} - z_{bm1}$) for the various concentrations in particles.

the lower concentrations whereas the average displacement velocity of the triple line on the SUEX bottom wall is roughly comparable. Since the apparent width of the corner films is larger in the entrance region of the channel for the higher concentration and the global evaporation kinetics is slower, a partial drying of the particle deposit in the channel entrance region, i.e. the Dufresne et al. [Dufresne *et al.*, 2003] mechanism, becomes a plausible explanation. To further analyze this possibility, let us consider again that 1) all the particles are packed in the corner films, 2) the corner film shape is comparable to the one for pure water (which is clearly a quite rough approximation based on Fig. II.21c). Then the length of the compact region of particles is given (see Section II.8 and Eq. (8.5)) by $L_{cp}(1 - \epsilon)A_c = (N_p/2)V_p$, where V_p is the volume of one particle, ϵ is the porosity of the packing (0.37), N_p is the total number of particles introduced in the channel and A_c is the film cross-section area. This gives $L_{cp} \approx 3.3$ mm, which is greater than the channel length! This too large value is interpreted as an indication that the cross-section area of the film is actually larger than for pure water, which is consistent with the larger corner film width visible in Fig. II.21. On the other hand, if we consider the whole section A of the channel instead of A_c , one obtains $L_{cp} \approx 11\mu\text{m}$, which is quite small and not consistent with the picture of the particle deposit in Fig. II.21. Thus, it is concluded here that these considerations are consistent with the consideration in Section II.9.1 that a compact region of particles forms in the corner films over a significant fraction of the channel length. To discuss further this situation, the evaporation rate is expressed using the concept of diffusive resistance length δ as

$$J = AD_v \frac{M_v}{RT} p_{vsat} \frac{(1 - RH_\infty)}{\delta} \quad (9.1)$$

where, D_v is the water vapor molecular diffusion coefficient, R is the universal gas constant, M_v is the vapor molecular weight, T is the temperature, p_{vsat} is the vapor saturated pressure and RH_∞ is the relative humidity in the surrounding air. δ represents the equivalent thickness of a gas layer of cross-section area A leading to the same evaporation rate as the one from the channel. From the computations described in section II.7, $\delta \sim 1$ mm for pure water and developed corner films corresponding to $\theta = 20^\circ$. The variation in the evaporation rate due to the presence of particles is on the order of 20% (Section II.7). This corresponds to $\delta \sim 1.2$ mm. In the case of the lower concentration, the increase in the diffusive length δ was entirely attributed to the corner film thinning in the presence of the particles. Based on the images in Fig. II.21, the mechanism leading to a reduced evaporation compared to pure water should be different for the high concentration since the film is larger than for pure water in the channel entrance region. Based on the estimate of δ , an evaporation front located about 0.2 mm (200 μm) within the packing of

particles is sufficient to reduce the evaporation rate by 20%. Such a scenario implies that the liquid flow rate within the packing is given by (considering one corner),

$$Q = J/2 = A_c \frac{k P_c}{\mu M_p} \quad (9.2)$$

Where k is the packing permeability ($k = \frac{\epsilon^3 d^2}{180(1-\epsilon)^2}$, where ϵ is the packing porosity (~ 0.37) and d is the particle diameter), μ is the liquid water dynamic viscosity, P_c is the capillary pressure (for a packing of particle, $P_c \sim \frac{6\gamma \cos\theta(1-\epsilon)}{\epsilon d}$, where the contact angle is that of water on the particles (34°)) and L_p is the length of the particle packing. Using for A_c the corner film cross section surface area corresponding to pure water (and $\theta = 30^\circ$ (Fig. II.4)), application of Eq. (9.2) gives $L_p \sim 18\mu\text{m}$. This length is small compared to the length of the particle packing, i.e. the length of the bright zone in the channel entrance region in Fig. II.21 ($400\mu\text{m}$). To obtain a comparable length ($\sim 400\mu\text{m}$), A_c must be multiplied by about 20, which corresponds to $A/A_c \sim 15$ (thus the packing of particles in one corner film region would occupy about 6.5% of the channel cross-section surface area). A firm conclusion cannot be reached from these rough computations due to the uncertainty on A_c in Eq. (9.2). Nevertheless, the above considerations indicate that the mechanism leading to the reduced evaporation in the case of the higher concentration is different from the film thinning mechanism considered for the lower concentrations. The reduced evaporation for the higher concentration is compatible with a slight retreat of the evaporation front in the particle packing forming in the corner film region. The accumulation of particles in the incipient corner films might lead to a greater particle packing zone than the zone corresponding to a liquid corner film (and thus to a greater cross-section surface area A_c). However, future work is needed to explore whether these speculations are valid or not.

10 Conclusion

From a combination of visualization experiments and numerical simulations, it has been shown in this chapter that the presence of colloidal particles reduces evaporation from a single dead-end channel compared to the situation in the absence of particles. Consistently with previous works [Chauvet *et al.*, 2009, Yiotis *et al.*, 2012] showing the strong impact of liquid corner films on evaporation, this chapter shows that the evaporation reduction effect is due to the effect of particles on the corner films. The particle accumulation in the corner liquid films modifies the dynamics of the corner films. For sufficiently low initial concentrations, the latter are thinner compared to pure water, which in turn

reduces the evaporation rate [Yiotis *et al.*, 2012]. In addition to the corner films, the experiments show that particles also tend to accumulate in the regions of the channel which are the last ones to empty. These correspond to the two hydrophilic corners at the channel closed end in the presented experiments. However, this is not observed for a much larger concentration. In complement with previous works showing an evaporation reduction effect due to the particles at the scale of a porous medium [Keita *et al.*, 2013] or a single channel [Dufresne *et al.*, 2003, Seck *et al.*, 2019, Lidon et Salmon, 2014], the present study thus sheds light on an evaporation reduction mechanism at pore scale, i.e. the corner film thinning effect, different from the ones considered in these previous works where the evaporation reduction was related to the formation of a compact packing of particles inducing the receding of the evaporation front in the porous medium or the channel. In that respect, the present study suggests to distinguish the low particle concentration regime from the higher concentration regime considered in the above-mentioned previous works. However, although the experiment performed for the most higher concentration tested did lead to the formation of a compact packing of particles in the corner film region as expected, this experiment did not lead to a significantly lower mean evaporation rate compared to the ones for the lower concentrations considered. Nevertheless, a small retreat of the evaporation front in the packing is a plausible explanation in this case since the corner films are not thinner than for pure water in the entrance region of the channel. In line with a previous work [Mata *et al.*, 2005], the study also shows that the knowledge of the “fresh” value of the contact angle is not sufficient to infer whether or not corner films can develop since the contact angle value can decrease as the result of evaporation and the pinning of the triple line. In the case of the reported experiments, the contact angle fresh value on the hydrophilic material was of on the order of 70° , thus not compatible with the formation of liquid films in right corners, whereas significant corner film effects could in fact be observed. The latter corresponded to a contact angle value of about 30° , consistent with the contact angle evolution measured in a separate droplet evaporation experiment. The next step, presented in the chapters that follow, is to investigate the effect of particles on evaporation in networks of interconnected channels [Zhao *et al.*, 2011, Vorhauer *et al.*, 2015, Wu *et al.*, 2020], seen as microfluidic tools for scale bridging between the single channel and porous media [Keita *et al.*, 2016a, Qin *et al.*, 2019].

Chapter III

Evaporation in a double channel

Contents

1	Introduction	63
2	Materials and Methods	63
3	Experiment with the SUEX system (pure water)	65
4	Experiment with the SUEX system (with particles)	69
5	Evaporation kinetics	70
5.1	The case of pure water	71
5.2	The impact of particles	72
6	The final deposit	73
7	Pre-test experiment with the Plexiglas system: the reversal of the main meniscus dynamic	75
8	Conclusions	78

1 Introduction

This chapter is dedicated to a study of evaporation in the presence of particles in a system of two interconnected channels of different sizes (Fig. III.1). The dynamics of fluorescent particles observed under a microscope during the drying process is studied as well as the displacement of the main menisci in the channels and the effect of the liquid films that form all along the evaporation.

2 Materials and Methods

Evaporation experiments are conducted in a SUEX double channel system of depth 1 mm. The two channels and the connecting one in between are 3 mm long. The larger channel

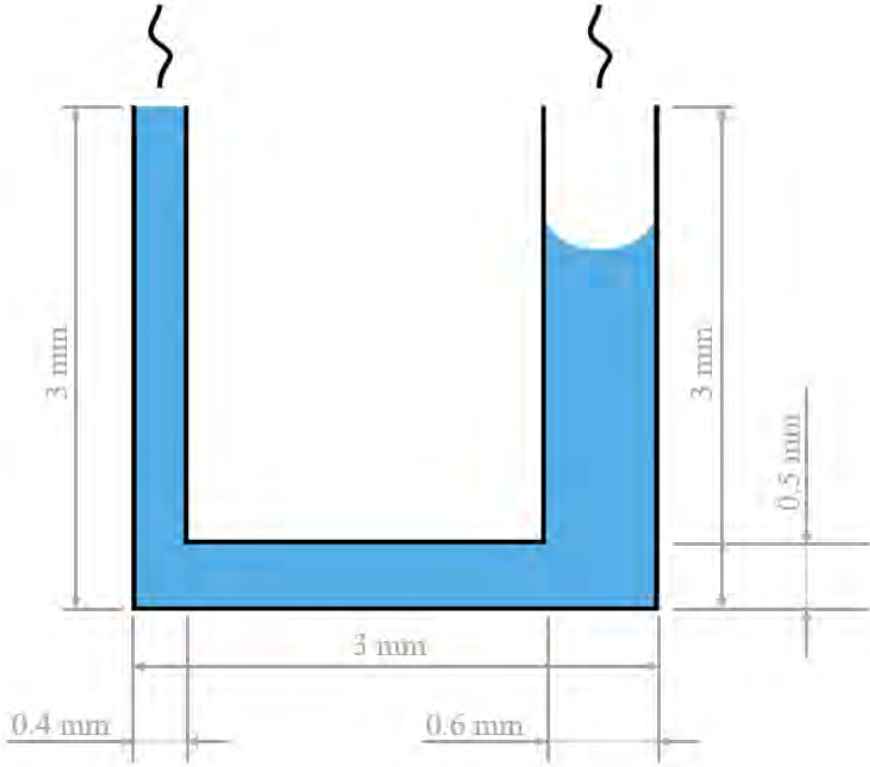


Figure III.1: Sketch of SUEx – PDMS system of interconnected channels studied in this chapter.

on the right in Fig. III.1 is 0.6 mm wide. The smaller channel on the left is 0.4 mm wide whereas the width of the interconnecting channel is 0.5 mm. As in the previous Chapter, three sides of the channel are made of SUEx while the top is closed with a PDMS layer which ensures proper sealing, avoiding leaks and facilitating the observation of the liquid and gas phases evolution and the displacement of the particles. One can refer to Chapter II for more details of the manufacturing protocol.

A pre-test experiment was also carried out with a double channel made of Plexiglas. The latter was machined thanks to a micro milling machine, ISEL CPM 4030, with a depth of 0.2 mm. The widths of the larger and smaller channels were 0.8 mm and 0.3 mm respectively. The width of the interconnecting channel was 0.8 mm. The cover plate in this system was also in PDMS. The concentration in the fluorescent 1 μm particles was 2×10^{-3} g/mL.

In the case of the SUEx/PDMS chip, a significantly smaller concentration of 0.5×10^{-4} g/mL was used. As described in Chapter II, this concentration is obtained by mixing a volume V_{part} of 2% (g/mL) solution with an appropriate volume V_{H_2O} of pure water, see equation 1.1 in Chapter II. The experimental protocol and the equipment used to carry

out these experiments are the same as the ones explained in Section II.1. The main steps of the protocol can be summarized as follows. The channel system, referred to as the “chip” in this chapter, is cleaned, closed with PDMS and the liquid is manually injected with a syringe. The chip is positioned under the microscope and images are taken every 10 seconds, using a white light for the pure water experiment and a green light for the experiments with the fluorescent particles.

3 Experiment with the SUEX system (pure water)

Fig. III.2 shows a typical picture of the chip during the evaporation experiment. Menisci are clearly visible in the smaller channel and at the junction of the larger channel and the interconnecting channel. It can be also observed that the color changes in the zone of the channels confined between the two menisci. This zone is black in the vicinity of the menisci but white further away in between the two menisci. Notice that the smaller channel is not completely full of water since the filling is realized manually with a syringe.

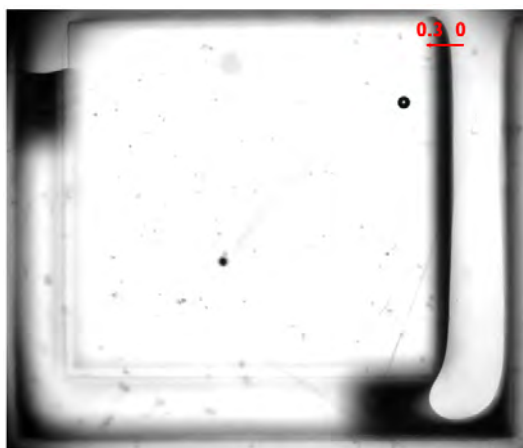


Figure III.2: The pure water experiment after 172 minutes. The red line represent the position where the corner film is characterized.

The interpretation of these various zones is given in Fig. III.3. In fact, a clean interface between a white region and black region correspond to a triple line on the SUEX channel bottom wall whereas a blurred interface between a black region and a white region correspond to the triple line on the channel PDMS top wall. As in Chapter II, the triple line moves faster in a first phase on the PDMS wall until the quasi-static interfacial shape illustrated in Fig. III.2 is reached. As discussed in Chapter II, the distortion of the liquid-gas interface is due to the difference in the wettability properties between the PDMS and the SUEX.

At the beginning of the experiment, the channels are full. Then a concave gas/liquid interface starts forming in the entrance region of the larger channel until the quasi-static

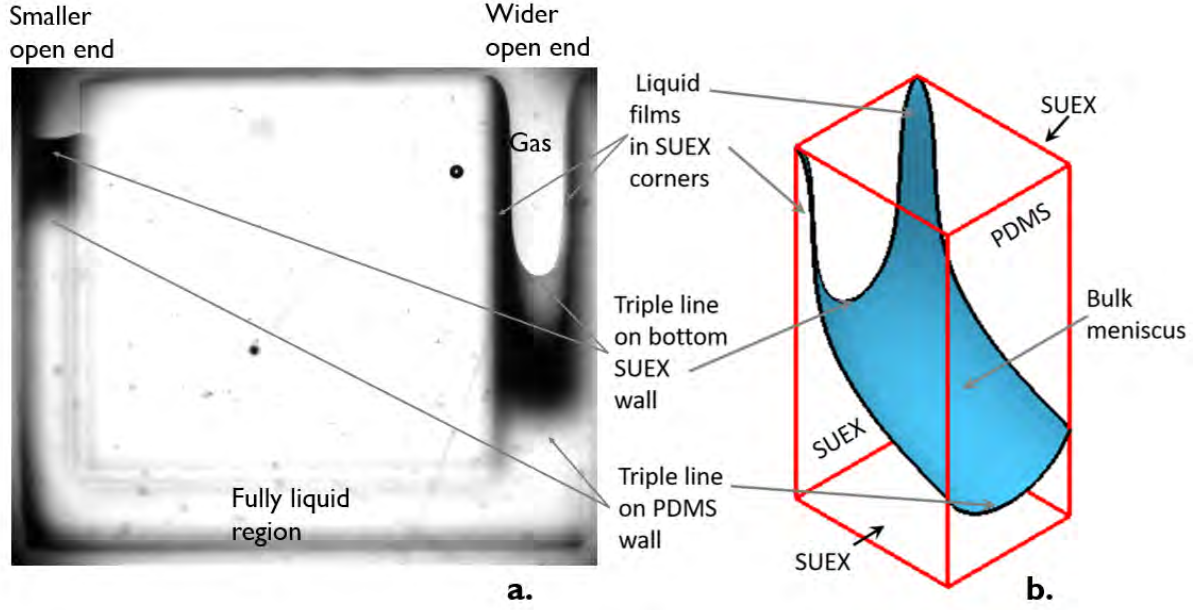


Figure III.3: Typical fluid distribution in the channel during evaporation: a) top view of the double channel in the experiment with pure water after 95 minutes, b) quasi-static shape computed with Surface Evolver for $\theta_{SUEX} = 30^\circ$ and $\theta_{PDMS} = 104^\circ$.

developed shape is reached. Afterwards, this shape (illustrated in Fig. III.3) moves into the channel and liquid films develop along the corners at the intersections between the channel SUEX bottom wall and the channel SUEX lateral walls, see Fig. III.4. The gas-liquid interface at the entrance of the smaller channel does not change significantly as the main meniscus moves in the larger channel.

This phenomenon, i.e. the fact that the main meniscus in the larger channel recedes in the larger channel while the gas/liquid interface remains stuck at the entrance of the smaller channel is referred to as “the capillary pumping effect” [Prat, 2023]. For the gas-liquid interface to remain stuck at the entrance of the small channel, the evaporation rate at this interface must be balanced by an equivalent liquid mass flow rate reaching the interface from below. This means that a liquid flow is induced between the receding meniscus in the larger channel and the gas-liquid interface pinned at the entrance of the smaller channel. This flow is induced in turn by the pressure difference in the liquid between the two menisci associated with the curvature difference between the two menisci. Since, according to Laplace law, the meniscus maximum curvature is proportional to the inverse of the channel width, the maximum curvature is less for the larger channel than for the smaller channel. As a result, the maximum curvature is reached first in the larger channel, which is therefore gradually invaded. The curvature adjusts in the smaller channel meniscus so that a liquid flow rate exactly balancing the evaporation rate at this meniscus is generated. The phase when the meniscus moves in the larger channel is referred to as “Phase 1”. Phase 2 starts when the moving main meniscus reached the

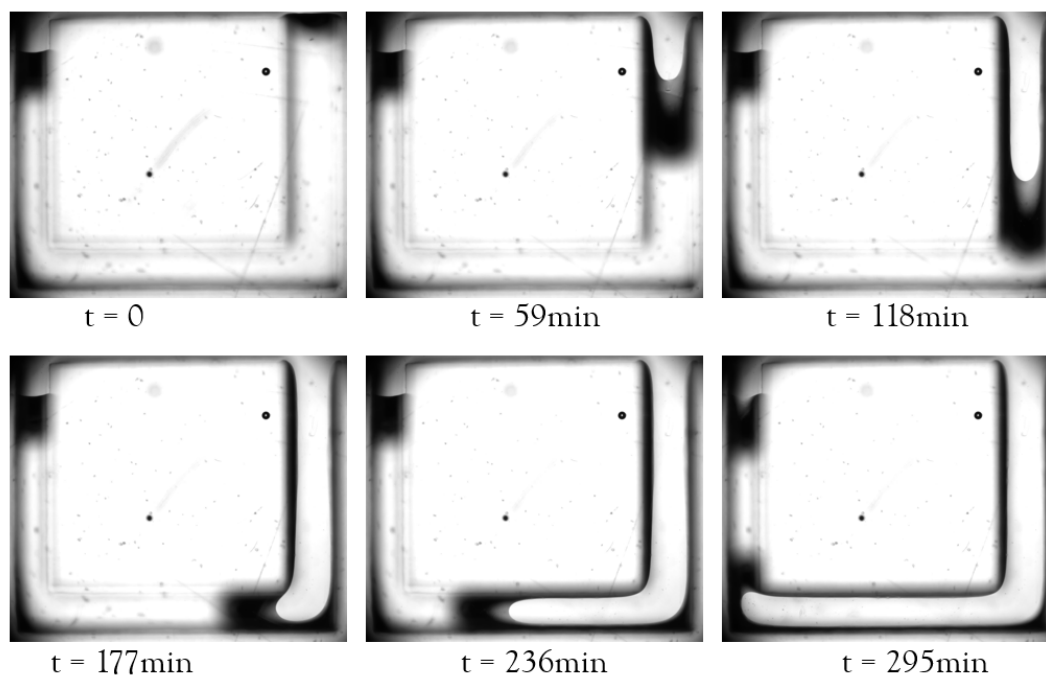


Figure III.4: Evolution of the evaporation process in the SUEX-PDMS double channel with images every 59 minutes.

junction with the interconnecting channel and lasts until it reaches the junction between the interconnecting channel and the smaller channel.

In phase 3, i.e. when both main menisci are in the smaller channel, both menisci move (upward as regards the meniscus having traveled from the larger channel, downward as regards the meniscus that was at the entrance of the smaller channel). The triple lines on the PDMS top wall, which are the most advanced in the direction of motion for both menisci, rapidly merge. This causes the detachment of the liquid from the PDMS and a redistribution of the liquid in the liquid films along the corners. As illustrated in Figs. III.2 or III.3, the phase distribution in the considered channel system as the main meniscus moves in the channels is characterized by the formation of thick liquid films in the SUEX corners (similar to the ones studied in Chapter II in a single channel). The evolution of the film thickness at the location indicated in red in Fig. III.2 is studied. The reslice tool in ImageJ is used to measure the width of the film. This tool reconstructs a 2D image from the image volume contained in the current stack. The straight-line selection tool is used to select where the reconstruction is performed, at the top of channel in the present case. Then the reconstructed image is binarized and a Matlab code is applied to extract the front between the black and white pixels, i.e. the position of the corner film triple line on the SUEX bottom wall.

The evolution of the film width in the top region of the larger channel is shown in Fig. III.5. The formation of the film starts after around 25 minutes. The film width is constant

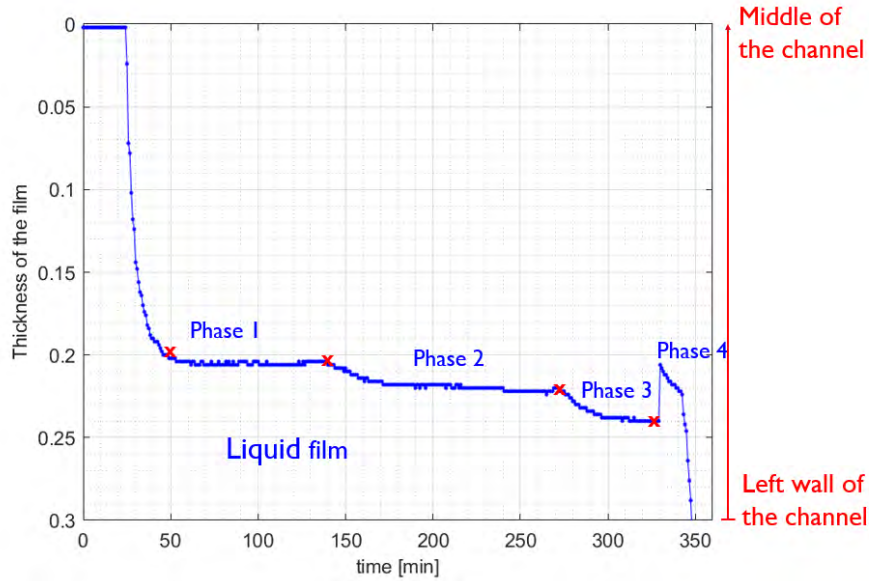


Figure III.5: Evolution of the liquid film triple line position at the position in the channel marked with the red line in Fig. III.2.

during phase 1 (when the main meniscus moves in the larger channel), which starts after about 50 minutes. As can be seen from Fig. III.5, the film remains present almost all along the drying process. The film width slightly decreases in phase 2 (i.e. when the meniscus coming from the larger channel travels in the interconnecting channel), which is qualitatively consistent with the smaller width (0.5 mm) of the interconnecting channel (the width of the larger channel is 0.6 mm). The film width decreases again when the traveling meniscus enters the smaller channel (of width 0.4 mm). This corresponds to phase 3 in Fig. III.5. As mention before, a sudden change occurs when the two main menisci merge. The liquid redistributes in the corner films. As the result the width of the film in the larger channel increases before thinning out until full drying. This corresponds to phase 4 in Fig. III.5.

The evolutions of the width of the film in the larger channel at the channel entrance and at the channel end close to the junction with the interconnecting channel are comparatively illustrated in Fig. III.6. The film near the junction with the interconnecting channel forms during phase 2 as the main meniscus starts traveling in the interconnecting channel. This is consistent with the impact of the in-plane curvature (negligible in the channel entrance region but negative in the region of the junction with the interconnecting as the result of the change of 90° in the orientation of the channel as illustrated in Fig. III.2).

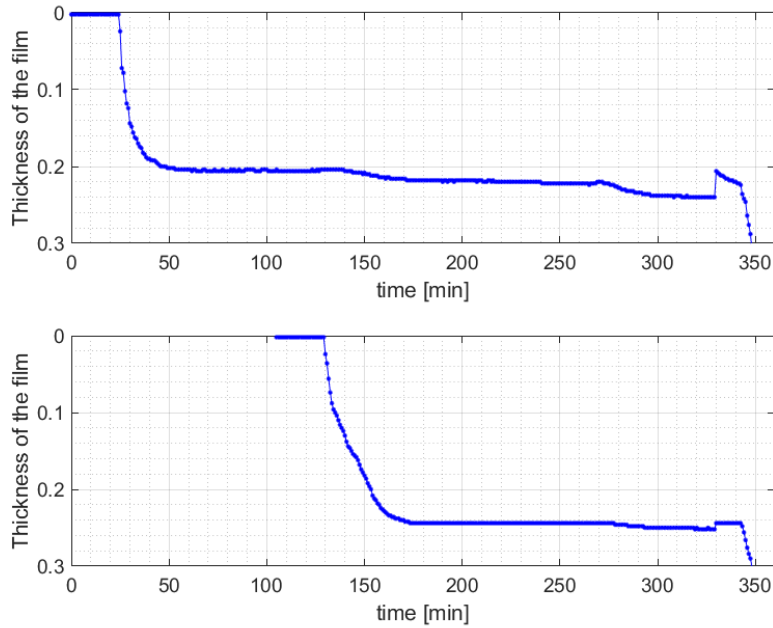


Figure III.6: Comparison of the film triple line position at the entrance (red line in Fig. III.2) of the largest channel (top plot identical to Fig. III.5) and at the end of the largest channel a bit before the junction with the interconnecting channel (bottom plot).

4 Experiment with the SUEX system (with particles)

The same experiment was carried out with the dispersion with a concentration of 0.5×10^{-5} g/mL of fluorescent particles of diameter $1 \mu\text{m}$. The phenomenology, see Fig. III.7 in terms of meniscus displacements is the same as for pure water: the main meniscus moves in the larger channel, then in the interconnecting channel while the meniscus at the entrance of the smaller channel does not move before the last phase, i.e. the phase where both menisci are in the smaller channel.

The evolution of the thick corner film in the larger channel at the position indicated in Fig. III.8 is now discussed. As illustrated in Fig. III.8, one can distinguish a bright thick line where particles accumulate in the vicinity of the triple line. In the image, one can therefore distinguish the front between the particle accumulation zone and the dry zone occupied by the gas phase from the front (interface) between the black region where liquid is present and the bright particle accumulation zone. As before, the reslice tool in ImageJ is combined with a Matlab code to measure the distance of these two fronts from the channel central line. The position evolution of both fronts is shown in Fig. III.8 with in red the distance between the bright zone position and the channel central line and in blue the distance between the bright zone inner interface and the channel central line (see Fig. III.8 for the definition of both interfaces). Therefore, the distance between the two curves in Fig. III.8 represents the thickness of the particle accumulation zone in the

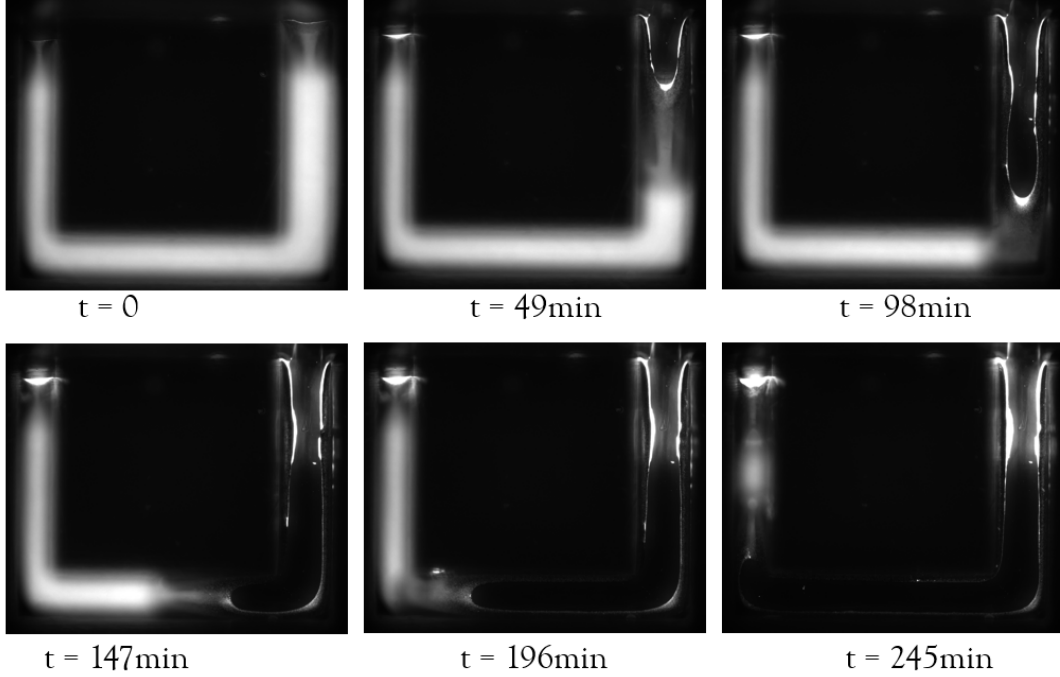


Figure III.7: Evolution of the evaporation process in the SUEX-PDMS double channel with the the 0.5×10^{-4} g/mL concentration of particles (bright spots). Images every 49 minutes.

vicinity of the liquid film triple line on the SUEX. As can be seen, the width of the particle accumulation zone increases with time, indicating that particles keep accumulating in this region. Contrary to the pure water case, the film thickness, i.e. the distance between the channel left wall and the position indicated in red in Fig. III.8, does not decrease as the main meniscus enters the interconnecting channel and moves into it. Thus, the accumulation of particle leads to the pinning of the liquid film triple line. At the end, after about 280 minutes, the abrupt increase in the red line observed in Fig. III.8 correspond to the liquid redistribution of the liquid in the corner films as for the pure water case and the final drying out but also to an optical effect leading to the increase in the luminous intensity when the channel becomes fully dry.

5 Evaporation kinetics

The evolution of the positions of the main menisci in the channel system is discussed in this section. For a given main meniscus, these positions correspond to the most advanced points of the main meniscus triple line on the SUEX bottom wall and PDMS top wall. As discussed before and illustrated in Fig. III.3b, the triple line is more advanced on the PDMS wall than on the SUEX wall due to the main meniscus distortion induced by the wettability difference between PDMS and SUEX. These positions are plotted for the three

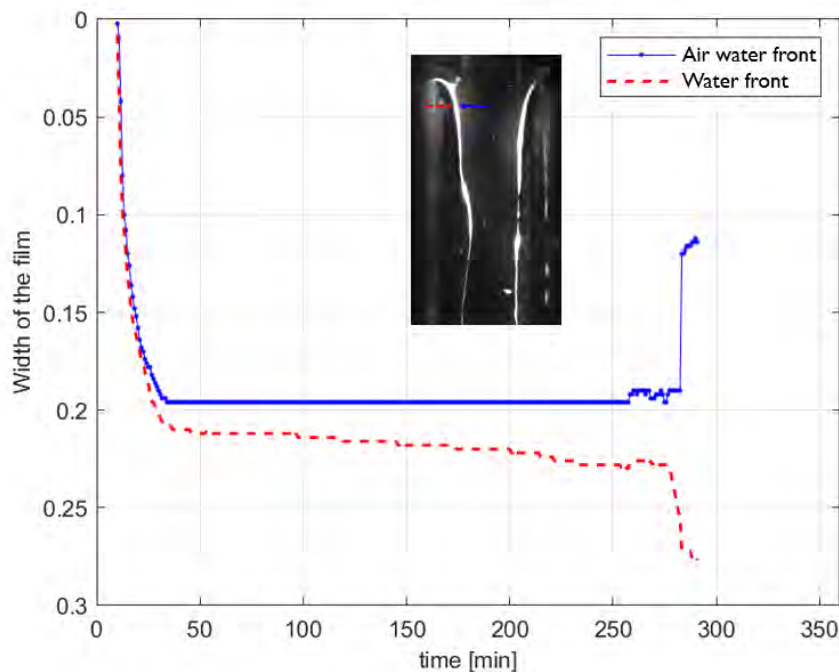


Figure III.8: Evolution of the film width, from border to triple line in blue. The distance between the two lines represents the evolution of the width of accumulated particles at the entrance of the channel.

channels (larger, interconnecting, smaller) in what follows.

5.1 The case of pure water

The evolution of the considered positions in the larger channel in Fig. III.9a is similar to that discussed in Chapter II for the single channel. The triple line starts receding on the PDMS wall sooner than on the SUEX bottom wall and it moves faster until an equilibrium is reached and the two considered points move at the same pace. The evolution is similar in the interconnecting channel Fig. III.9b). The more complex situation is when both menisci are in the smaller channel (Fig. III.9c). When the triple line on the PDMS of the meniscus coming from the larger channel enters the smaller channel one, red rectangle in Fig. III.9c, the meniscus at the entrance of the smaller channel starts moving, more precisely the triple line of this meniscus on the PDMS wall starts receding in the smaller channel. The triple line of this meniscus on the SUEX at the small channel entrance starts moving as the one of the meniscus having traveled from the larger channel reaches the smaller channel right after the junction with the interconnecting channel. The triple lines of both menisci move faster on the PDMS wall. As previously mentioned, the liquid redistributes in the liquid films in the SUEX corners when both menisci meet after 325 minutes.

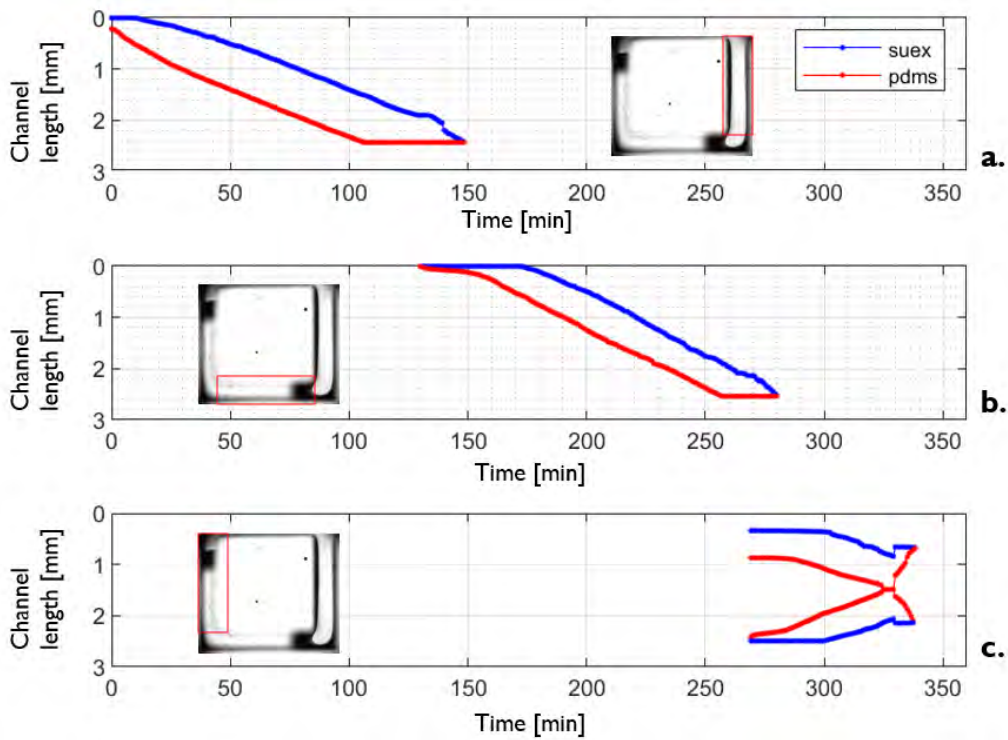


Figure III.9: Kinetics of drying in each channel of the chip, red lines refer to the position of meniscus triple line on the PDMS top wall, blue ones on the SUEX bottom wall; a) larger channel, b) interconnecting channel, c) smaller channel with occurrence of a second receding meniscus.

5.2 The impact of particles

The dynamic of the evaporation in the presence of particles for the considered low concentration in particles (10^{-4} g/mL) does not present major differences compared to pure water as regards the first two channels, Fig. III.10a and III.10b. However, the evaporation process in the larger channel and the interconnecting one is faster than in the case of pure water. This phenomenon, opposite to what could be expected from the previous chapter, can be justified by the position of the meniscus in the smaller channel. The meniscus is closer to the smaller channel open end in the presence of particles, causing a faster evaporation of the liquid. The main difference with the case of pure water lies in the dynamics in the smaller channel, see Fig. III.10c. In the pure water case, both triple lines at the smaller channel entrance start moving inside the channel as the moving meniscus reaches the smaller channel. In the presence of particles, the triple line on the SUEX wall at the open-end of the smaller channel stays pinned and does not recede. When the meniscus triple lines meet on the PDMS top wall, the liquid dispersion redistributes as in the pure water case, particles move along the films to reach the preferential zones of accumulation, while the front on the SUEX moves toward the smaller channel entrance.

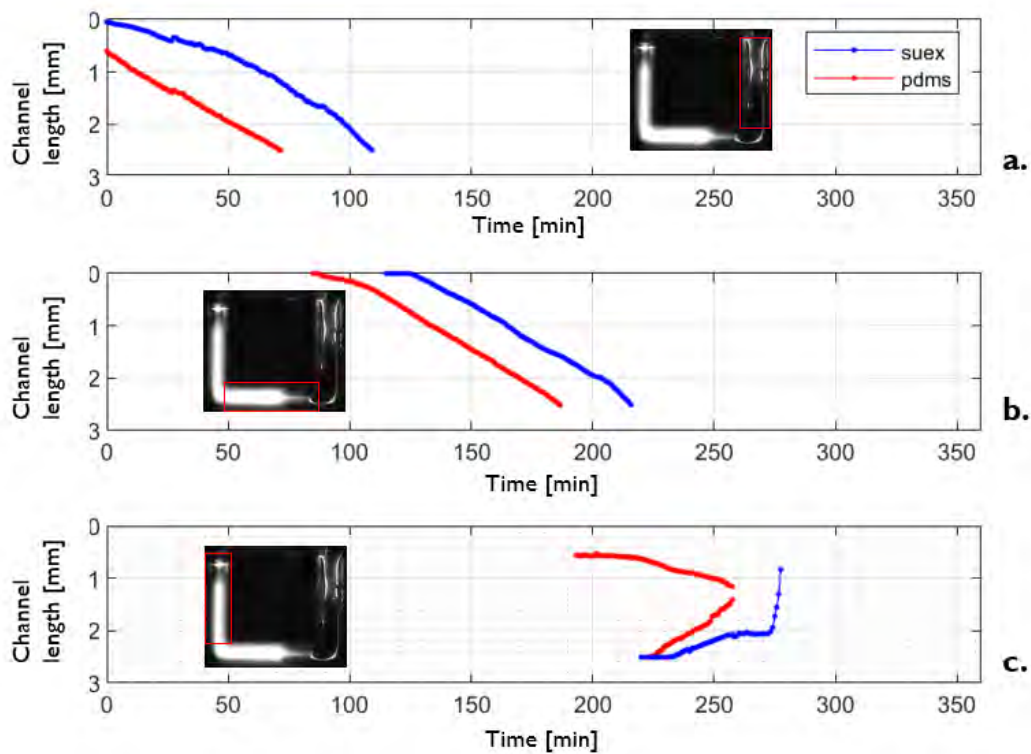
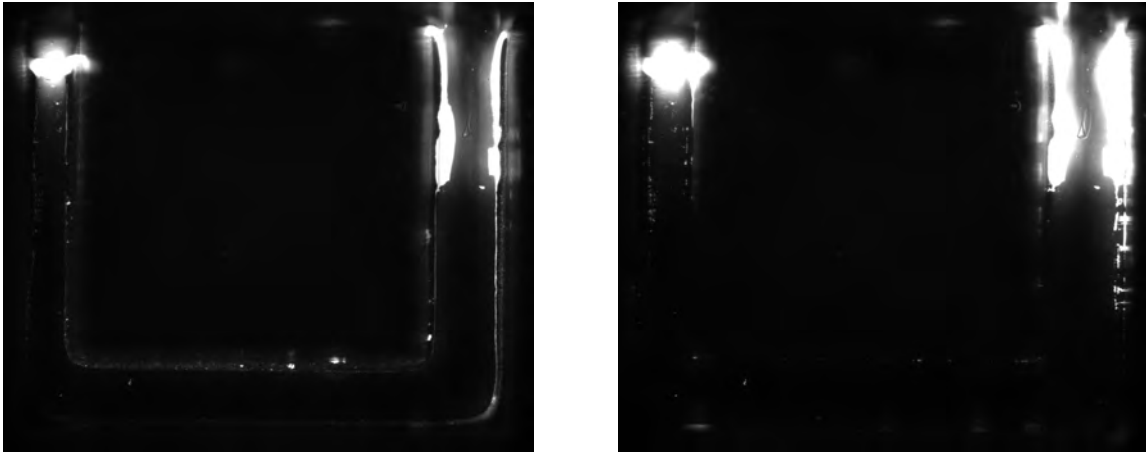


Figure III.10: Kinetics of the drying in every channel of the chip in the presence of a particles concentration of 10^{-4} , the red lines refer to the position of the front on PDMS, blue ones on the SUEX walls; a) right larger channel, b) middle channel, c) left narrower channel with the apparition of a second receding front.

6 The final deposit

The final distribution of particles is illustrated in Fig. III.11b, while the distribution 5 minutes before the drying out of the remaining corner liquid films is shown in Fig. III.11a. Notice that the deposit on the PDMS top wall is negligible compared to the one on the SUEX walls. As illustrated in Figs. III.11a and b, the preferential zones of accumulation of the particles are where the triple lines were pinned during the drying process. Due to the presence of the corner liquid films, the particles do not concentrate solely in the smaller channel as one could have expected from the consideration of the main meniscus dynamics. Actually, there are two areas of deposited particle accumulation. The first one is at the entrance of the smaller channel, consistently with the fact that the triple line on the SUEX bottom wall remains pinned (as discussed in Section III.5). The second one is the region where the liquid films were present and the evaporation rate high as in the single channel case. The flow induced in the larger channel films by evaporation as well as in the films in the interconnecting channel transports the particles up to the entrance of the larger channel where they accumulate. In short, the preferential zones of deposit results from two factors: the pinning of the triple lines and higher local evaporation rates

(as discussed for the single channel, the evaporation rate is negligible deeper inside the channels).



a.

b.

Figure III.11: The preferential zones of particle accumulation are in bright; a. after 281 min of evaporation, i.e. 5 minutes before the complete evaporation of the corner films, b. spatial distribution of deposited particles at the end of experiment after full evaporation.

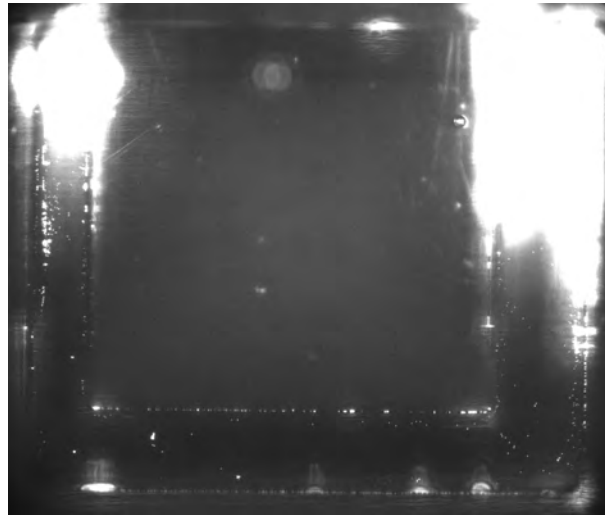


Figure III.12: Spatial distribution of deposited particles at the end of experiment after full evaporation. During the image treatment the brightness was increased to highlight the minor presence of deposited particles along the corners of all the channels.

However, some particles can deposit deeper in the system, for example in the interconnecting channel. This is illustrated in Fig. III.12 obtained by increasing the luminosity of the image. These particles perhaps deposit in phase 4, when the remaining liquid in the corner films eventually evaporates.

7 Pre-test experiment with the Plexiglas system: the reversal of the main meniscus dynamic

As mentioned in Section III.2, this experiment was carried out as the set up was developed. The micro-channels are machined in a Plexiglas plate using a micro-milling machine . As a result, the three Plexiglas walls are not as smooth as those fabricated using the lithography process and SUEX. Also, the channel depth is 0.2 mm, thus smaller than the channel depth (1 mm) in the SUEX-PDMS system. As mentioned in Section III.2, the particle concentration (2×10^{-3} g/mL) is greater (it was 0.5×10^{-4} g/mL in the case of the SUEX system). As can be seen from Fig. III.13, a remarkable difference in this experiment is the inversion in the order in which the smaller and the larger channels are invaded. Contrary to the classical case [Engøy *et al.*, 1991, Le Bray, , Scherer, 1990], the smaller channel is invaded first while the meniscus at the entrance of the larger channel stays pinned at the channel entrance. The dynamics of the main menisci is fully inverted. The moving meniscus travels in the smaller channel, then in the interconnecting channel and finally in the larger channel until it merges with the other main meniscus. The latter remains pinned at the entrance of the larger channel during the displacement of the travelling meniscus.

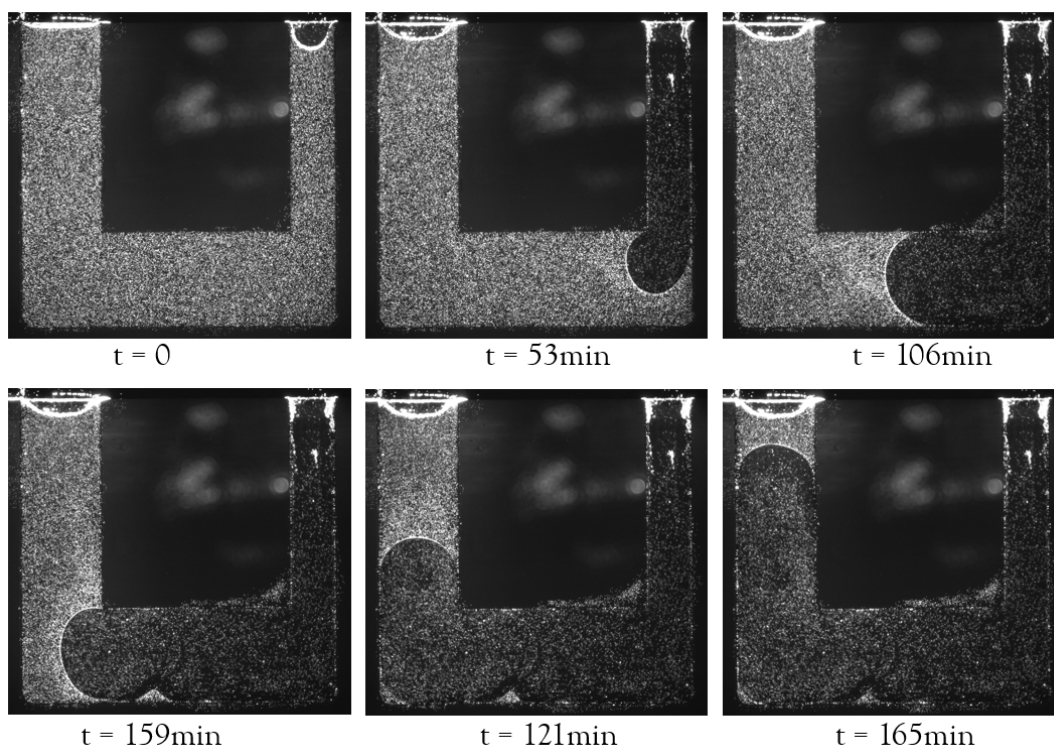


Figure III.13: Evolution of the evaporation process in a Plexiglas double channel closed with PDMS with images every 53 minutes. The bright spots represent particles.

The contact angle was not measured but the width of the liquid films forming during drying are significantly narrower than with the SUEX-PDMS system. This suggests that the contact angle is higher than the one on the SUEX. This is consistent with the measurements reported in [Osti *et al.*,] indicating a value of 70.4° for the contact angle of water on an acrylic (Plexiglas) surface. Although this value is for a smooth surface and not a rough one, it is significantly greater than the one observed on SUEX (see Chapter II). Also, contrary to the case of the SUEX-PDMS system, there is no visible shift between the main meniscus triple line on the PDMS top wall and the one on the Plexiglas bottom line. Although the Plexiglas-PDMS system is narrower (channel depth of 0.2 mm against 1 mm for the SUEX-PDMS system), the absence of the shift is an indication that the contact angle on the Plexiglas is closer to the value of the contact angle on the PDMS, which is higher than on SUEX and closer to the value of 70° as reported in Chapter II. To explain the reversal of the main meniscus dynamics, it can be first noted that the invasion capillary threshold in the two channels are comparable for both systems. This invasion threshold is the capillary pressure when the meniscus is about to move in the channel. From Laplace's law it is given by $P_{cth} \approx \gamma \cos \theta (\frac{2}{w} + \frac{2}{h})$ where w is the channel width and h is the channel depth. This of course only an approximation since here we have not considered the difference in wettability between the PDMS cover plate and the SUEX or the Plexiglas walls. The ratio between the invasion capillary thresholds in the smaller and larger channels can be therefore estimated as .

$$rat_{small-large} = \frac{(\frac{1}{w_{small}} + \frac{1}{h})}{(\frac{1}{w_{large}} + \frac{1}{h})} \quad (7.1)$$

This gives $rat_{small-large} = 1.31$ for the SUEX-PDMS system and $rat_{small-large} = 1.33$ for the Plexiglas-PDMS system.

However, it can be seen from Fig. III.14 that the curvature of the main meniscus at the entrance of the larger channel increases as the other main meniscus moves into the smaller channel. This is an indication that the accumulation of particles modifies the capillary equilibrium between the two menisci. The increase in the larger channel meniscus curvature indicates an increase in the capillary pressure. This increase is however difficult to detect on the travelling meniscus. In any case, the reversal must be attributed to the impact of the particles. It seems that particles have accumulated at the entrance of the larger channel so as to induce a greater invasion capillary pressure threshold. Since a change in the meniscus curvature is visible at the entrance of the larger channel, the invasion capillary pressure threshold is however much less than the one which can be computed for a packing of $1 \mu\text{m}$ particles (the latter is inversely proportional to the particle diameter). It is likely that more particles have accumulated at the entrance of

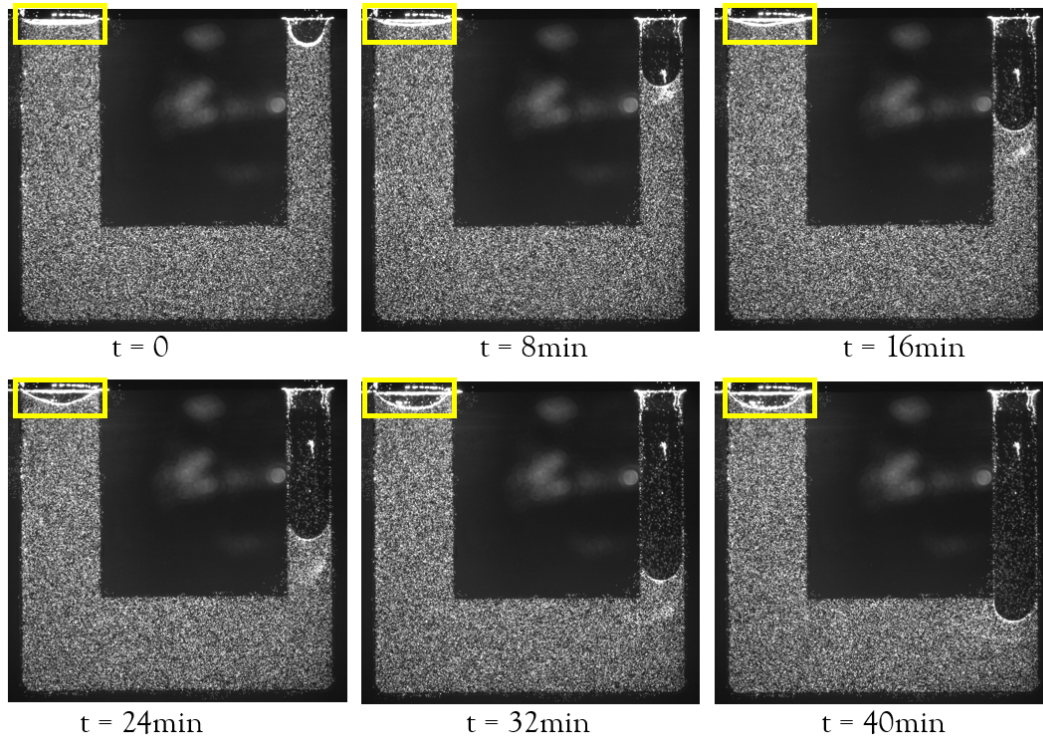


Figure III.14: Time steps, of 8 minutes, of the evolution of the evaporation process in a plexiglas double channel of width 0.2 mm closed with PDMS. The bright spots represent the particles.

the larger channel during the system filling procedure and the short drying step before the evaporation starts at the entrance of the channels. This not well controlled initial phase might have introduced a dis-symmetry in the distribution of the particles in the entrance region of the channel.

As can be seen from Fig. III.15, the final deposit in the Plexiglas-PDMS system is much more spatially uniform than in the SUEX-PDMS system (Figs. III.11 and III.12). Nevertheless, the channel entrance regions are still a preferential zone of particle accumulation. This is consistent with the fact that the main meniscus in the larger channel remains pinned at the entrance and that particles are transported by the flow directed toward this meniscus. Regarding the smaller channel, the deposit at the entrance seems to form very early (see Figs. III.11 and III.12). These figures suggest that the smaller channel entrance deposit essentially forms in the very early stage of the drying process when the curvature meniscus gradually increases before it starts moving. The image of the deposit in Fig. III.15 with more particles in the corners (i.e. along the vertical walls) also suggests that liquid films are still present during drying in this system, which is in contradiction with the classical consideration that the contact angle must be lower than 45° for a film to be present in a right corner [Prat, 2007]. This might be due to some spatial variations in the channel depth [Keita *et al.*, 2016b]. In any case, particles moving

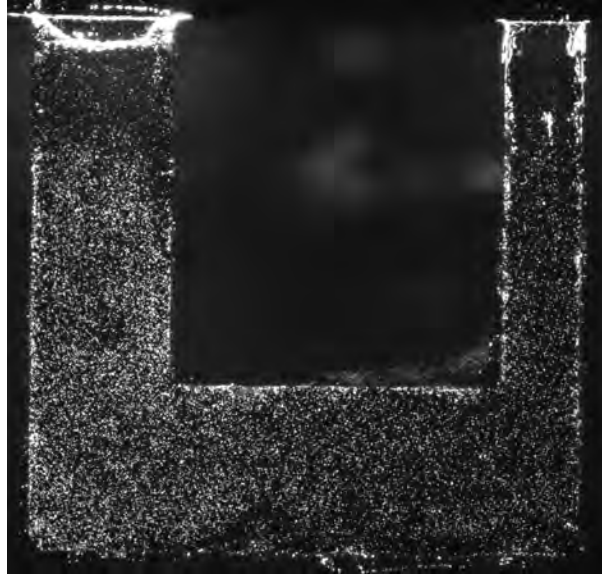


Figure III.15: Final particle deposit in the Plexiglas-PDMS system.

along the walls are visible in the movie of the experiment.

8 Conclusions

Drying of two competing interconnected channels in the presence of particles was explored in this chapter considering two systems: a SUEX-PDMS system (as in Chapter II) and a Plexiglas-PDMS system. The main meniscus dynamics in the SUEX-PDMS system was as expected, i.e. with a traveling meniscus starting in the larger channel. As for the single channel experiment, thick films formed. These films are paths for the transport of particles in direction of the evaporative zones. The final deposit in this system is spatially heterogeneous with preferential deposits in the entrance regions of both channels. The deposit is however of greater extension in the larger channel due to the film effects. The experiment with the Plexiglas-PDMS system led to an unexpected and puzzling observation: the reversal of the main meniscus dynamics with the traveling meniscus starting in the smaller channel and not in the larger one. In this system, the contact angle is greater and the corner liquid films have a much less significant impact. As a result, the deposit is much more spatially homogeneous but the channel entrance regions remain zones of preferential particle accumulation. However, the explanation of the main meniscus dynamics reversal is unclear. Due to the uncertainties associated with this experiment and the lack of clear explanation and since this experiment has not been repeated, its main interest is to show that the meniscus dynamics reversal is possible in the presence of particles.

Chapter IV

Experiments with micromodel for pure water

Contents

1	Introduction	80
2	Methods and Materials	81
2.1	Model porous medium	81
2.2	The experimental protocol	82
2.3	Drying setup (no gravity effect, $P = P_{atm}$)	83
2.4	Drying setup with gravity effects ($P_g = P_{atm}$)	85
2.5	Drying setup with partial vacuum conditions (no gravity, $P = 0.1P_{atm}$)	85
2.6	Drying setup with partial vacuum conditions and gravity effects ($P = 0.1P_{atm}$)	87
3	Image treatment (phase distribution, evaluation of evaporation rate)	88
4	Drying patterns	90
4.1	Comparing levels of saturation	91
4.2	Impact of gravity	91
4.3	Impact of partial vacuum and temperature	93
5	Evaporation kinetics	96
5.1	Impact of partial vacuum and temperature (in the absence of gravity effects)	96
5.2	Impact of gravity effects	99
6	Conclusion	100

1 Introduction

Different drying patterns are explored in this chapter for pure water (the results in the presence of particles are presented in the next chapter) varying the drying conditions. The considered conditions are summarized in Table IV.1.

Drying mode	Temperature (°C)	Relative humidity (%)	External gas pressure (mbar)	Gravity effects	Saturation pressure for experiment temperature
Capillary air drying	22	6	1000	no	2500Pa (25mbar)
Capillary-gravity air drying	22	6	1000	yes	2500Pa (25mbar)
Evaporation vacuum drying without gravity	22	6	100	no	2500Pa (25mbar)
Evaporation vacuum drying with gravity	22	18	100	yes	2500Pa (25mbar)
Vaporization vacuum drying without gravity	50-60	2	100	no	12335-19920 Pa (123.35-199.2 mbar)
Vaporization vacuum drying with gravity	50-60	2	100	yes	12335-19920 Pa (123.35-199.2 mbar)

Table IV.1: The various drying conditions explored in the chapter.

It can be first noted that the external gas pressure in the “vacuum” drying experiments is much higher than the gas pressure considered in [Ito *et al.*, 2014] (100 mbar vs 1 mbar) whereas the temperature is lower (50 – 60°C or 22°C vs 100°C). The conditions are therefore significantly less severe. Nevertheless, a situation where the external gas pressure is less than the saturation pressure is considered by increasing the temperature in the vacuum chamber to 50 – 60°C. The terminology “evaporation” vacuum drying and “vaporization” vacuum drying in Table IV.1 refers to the distinction introduced by Krisher [Krischer et Kröll, 2013] previously mentioned depending on whether the external gas pressure is greater or lower than the water vapor saturation pressure at the considered temperature.

2 Methods and Materials

2.1 Model porous medium

As depicted in Fig. IV.1, drying experiments are conducted in a model porous medium (micromodel) consisting in a 7×7 square network of interconnected channel of rectangular cross section. As sketched in Fig. IV.1 at the bottom, the depth of the channel is uniform and equal to 1 mm whereas the channel width varies between $80 \mu\text{m}$ and $910 \mu\text{m}$ according to a uniform probability density function (p.d.f.). The distance between two nodes (channel intersections) in the network is 3 mm. The channel length varies between about 2.6 and 3mm. The total dimension of the micromodel is $1.8 \text{ cm} \times 1.9 \text{ cm}$. As illustrated in Fig. IV.1, the micromodel is composed of a SUEX layer in which the channel network is located. The micromodel is closed with a PDMS layer, covered in turn by a thin glass slide. Therefore, the channels have three sides made of a hydrophilic material (SUEX), while the top wall is hydrophobic (PDMS).

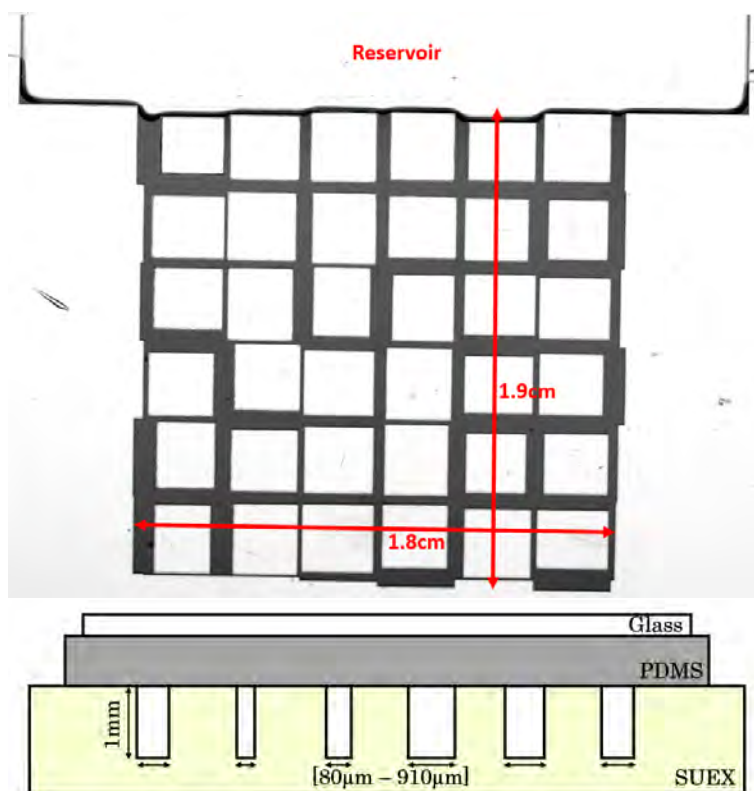


Figure IV.1: Top) Image of the micromodel with liquid (in black) in the channels. Bottom) Sketch of the cross section of the micromodel with the various layers, PDMS is colored in grey for illustration but is transparent in reality

Compared to the medium illustrated in Fig. I.17, it can be seen than the pore sizes are bigger in the micromodel (about one order of magnitude as regards the channel widths). The thickness is also significantly larger (1.8 cm vs $300 \mu\text{m}$). The number of pore

bodies over the thickness (7 in the micromodels, pore bodies correspond to the channel intersections) is comparable to the number of pores over the thickness expected in the type of fibrous components illustrated in Fig. I.17 (although this is hard to clearly see from Fig. I.17). It can be also noted that only one side of the micromodel is open to the external air top side in Fig. IV.1 whereas drying occurs from the bottom and top surfaces in the experiments corresponding to Fig. I.17.

2.2 The experimental protocol

The micromodel is cleaned with ethanol, dried with compressed air and closed with a layer of PDMS. The latter is placed on the SU-8 layer paying attention to avoid any residual bubble between the two layers. The PDMS material is chosen for its properties such as the optical transparency, flexibility, and because it sticks on other materials without any treatment. On the other hand, it is known that water can pervaporate through PDMS [Merlin *et al.*, 2012]. This was illustrated in one of the first tests during the setup of the experiment. When the micromodel was just covered by a thin layer of PDMS, the formation of air bubbles in channels far away from the micromodel entrance could be observed during drying.

To overcome this problem, the PDMS is covered with a thin glass slide that sticks to it without requiring any surface treatment. Once the setup is ready, the next step in the protocol is to fill the channel with water. We first tried the method consisting in putting the micromodel in a reservoir filled with water and set it in a vacuum bell. This was tested in a case where the micromodel was compressed between two plexiglass plates. However, this device turned out to be too heavy for the 10^{-4} g precision balance. However, when the plexiglass plates are removed, few issues arise. First, the water infiltrates between the PDMS layer and the glass, resulting in the detachment of the glass plate. Secondly, this procedure implies the use of a large number of particles resulting in a significant waste of particles for each experiment in the case of experiments with suspensions (Chapter V).

In order to avoid these drawbacks, solely the reservoir in front of the channels (Fig. IV.1a) is filled with water closing all the outlets. Then, the micromodel is placed in a vacuum jar in which the pressure is reduced down to 100 mbar for a few minutes. Next, as the pressure slowly rises back to the atmospheric pressure, the liquid fills in the channels. This process, taking the micromodel under vacuum conditions and slowly back to atmospheric pressure, is repeated two or three times, until the micromodel is completely saturated by liquid.

2.3 Drying setup (no gravity effect, $P = P_{atm}$)

Drying experiments require to control the temperature and relative humidity of the atmosphere in contact with the micromodel. Imposing constant temperature and relative humidity over the duration of the experiment (which typically lasts between about one hour and about one day) is desirable to facilitate the analyses. To this end, the liquid filled micromodel is transferred to a room where the temperature is kept constant thanks to an automatized air conditioner, set to 22°C. However, the air conditioner control system leads to some fluctuations around the selected temperature value. To damp out these fluctuations the micromodel is set in a box made of Plexiglas panels. One of these panels can be removed to set the micromodel in the box. The other panels are hermetically sealed together.

As illustrated in Fig. IV.2, the setup is also composed of a 10^{-4} g precision Sartorius balance to measure the evolution of the liquid mass. Mass data are recorded every 10 seconds. In addition, a thin support is set on the balance to hold the micromodel, which is set horizontally on the support. In between, a back light triggered by the camera (see below) is set for better visualization. The back light is set in such a way that it does not touch the balance pan, so that it does not exceed the maximum weight that can be measured.

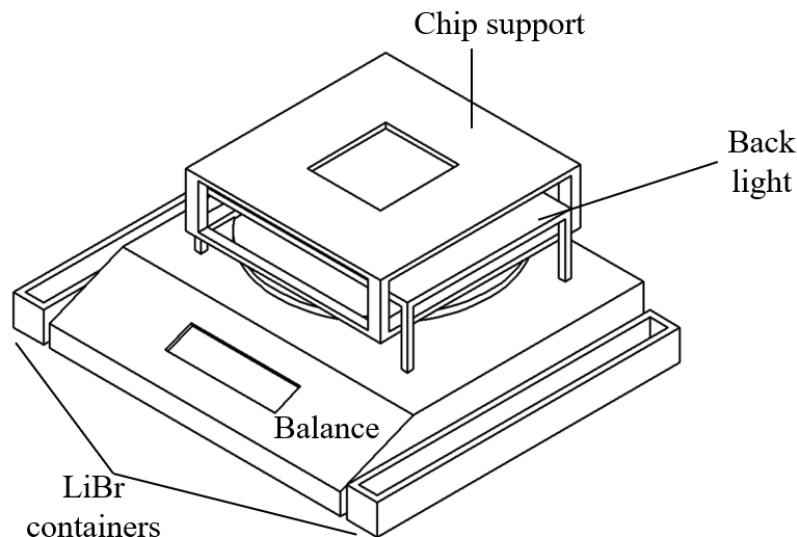


Figure IV.2: Schematic of the drying setup for experiment at the atmospheric pressure. The setup is composed of a balance, two boxes on the side for the salt solution used to control the relative humidity, a back light and a support for the micromodel. Everything is placed in a transparent box (see Fig. IV.3).

To accelerate the evaporation process, the relative humidity (RH) is kept at $6\% \pm 1\%$ thanks to the presence of a Lithium Bromide solution filling two open channels along the

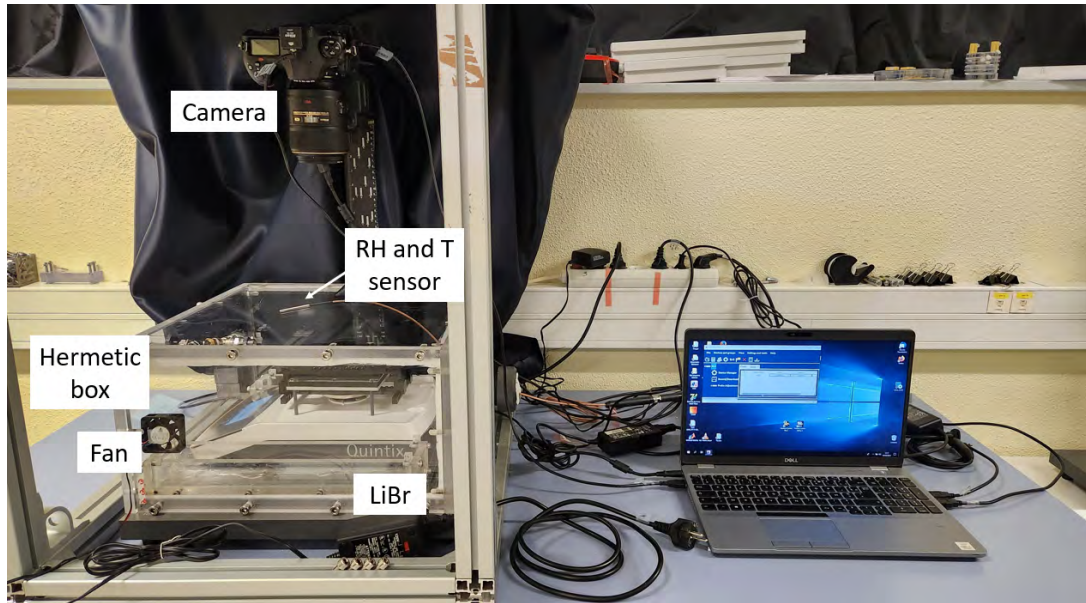


Figure IV.3: Photo of the set up of the experiment at atmospheric pressure.

sides of the balance. As soon as the box is closed a small fan is turned on for about 10 minutes, depending on the initial RH value, this speeds up the process of decreasing the humidity to about 10%. Then, the fan is turned off for two reasons: firstly, it changes the evaporation conditions imposing an air flow in the box; secondly, it prevents the balance from stabilizing. Both the temperature and the relative humidity are recorded every 5 minutes thanks to a sensor placed inside the box close to the box top panel. The whole set up is illustrated in Fig. IV.3

The evolution of the liquid distribution in the micromodel during drying is recorded by a Nikon camera D700 equipped with a macro lens. The camera is controlled by a computer via the Camera Control Pro 2 software and the images are acquired at a time interval of 2 minutes. As we shall see, drying is faster in the partial vacuum experiments. The image acquisition frequency is actually adapted to the drying conditions and can be as high as one image every 10 seconds for the conditions leading to the fastest drying. To increase the contrast between air and water, namely to perform better visualization of the fluid distribution in the micromodel, dye was added to pure water. More precisely, 0.0065g of fluorescein was added to 45g of water. This corresponds to a concentration of 0.01% which is sufficiently low for the nanoparticles, documented to be oblate ellipsoid with approximate volume of 0.4 nm^3 [Pu *et al.*, 2012], not to change the dynamics of the drying process.

2.4 Drying setup with gravity effects ($P_g = P_{atm}$)

The setup is almost identical to that described in Section IV.2.3. To impose gravity effects, the micromodel is set vertically directly on the balance pan, with the micromodel open side on top. The main modification lies in the position of the camera and the back-light. As illustrated in Fig. IV.4, the back light is set vertically behind the micromodel, along the Plexiglas back panel of the box. The camera is set on the side of the Plexiglas box as sketched in Fig. IV.4

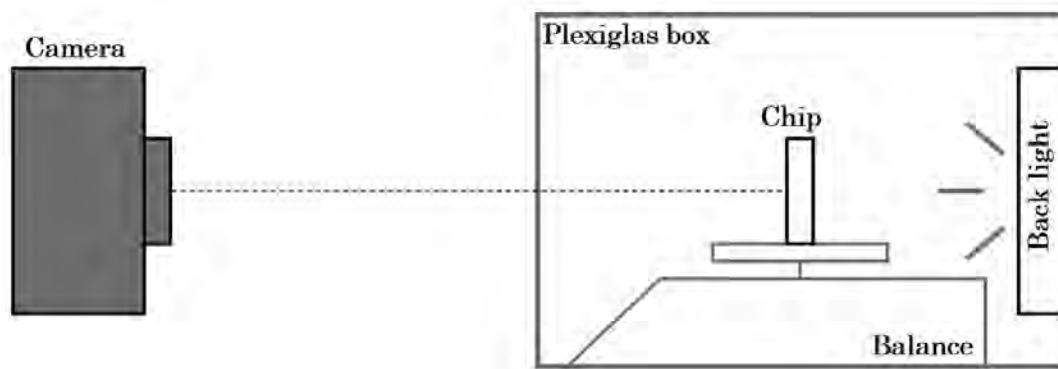


Figure IV.4: Experimental setup for the case with gravity effect.

2.5 Drying setup with partial vacuum conditions (no gravity, $P = 0.1P_{atm}$)

As sketched in Fig. IV.5, an existing oven is used to perform drying experiments under partial vacuum conditions ($P = 0.1P_{atm}$).

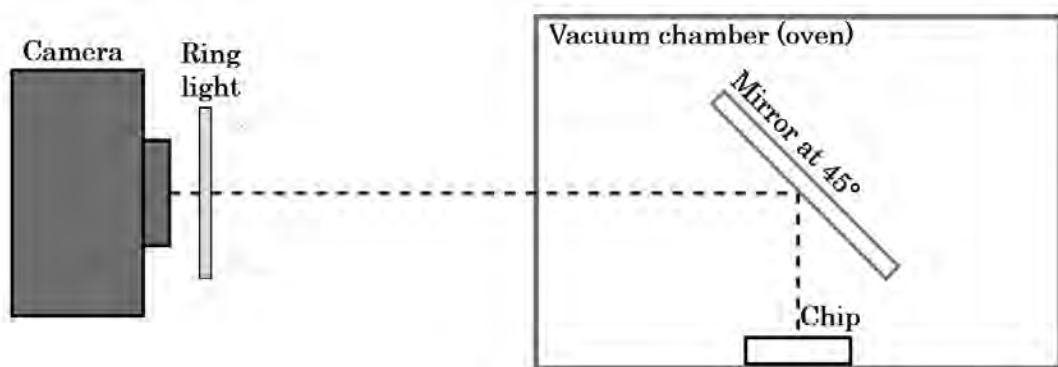


Figure IV.5: Set up of the experiment under vacuum conditions.

As also sketched in Fig. IV.5, the camera equipped with the macro lens is set outside the oven and directed in direction of the oven window. As sketched in Fig. IV.5, a mirror is set in the oven at 45 degrees, in order to reflect the horizontal micromodel. As far as the

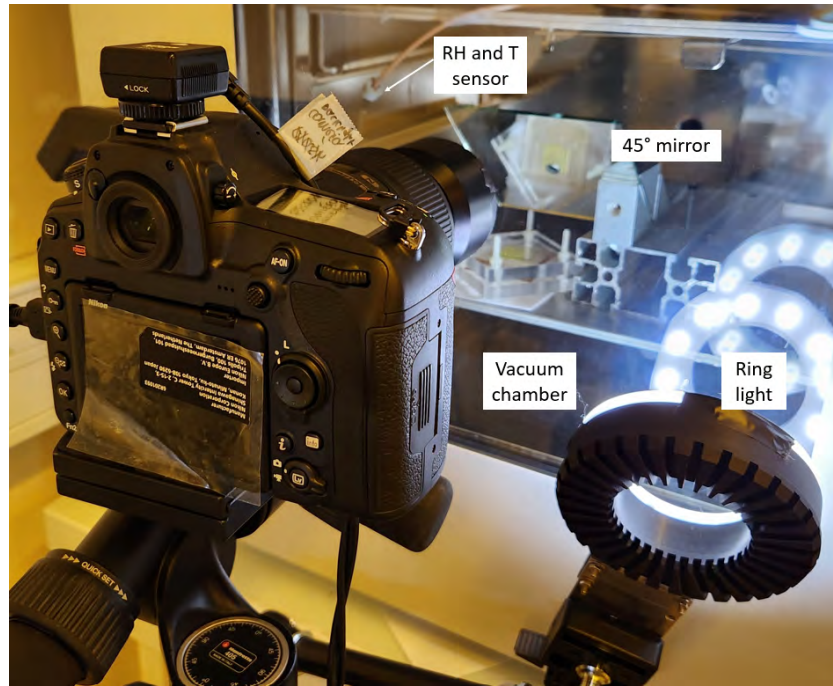


Figure IV.6: Photo of the set up of the experiment under vacuum conditions.

lightning is concerned, the back light previously employed cannot be used because there is no passage for its power cable allowing to maintain the desired reduced gas pressure in the oven. Instead, a circular light ring is used. This ring is placed firstly around the objective of the camera, Fig. IV.5, but, afterwards, it is positioned near the camera, Fig. IV.6 to diminish the reflexes on the glass of the oven. Moreover, a blue filter is added in front of the objective in order to increase the contrast in the images when fluorescein is used. A digital sensor is set in the oven to measure the temperature and the relative humidity in the oven. The probe (Rotronic HC2-HK/C Series) is connected to a Rotronic hygropalm to record the data every 2 minutes. When the vacuum system is turned on, the relative humidity in the oven drops to around 4 - 5% and stays constant during the experiment. The temperature is stable at 22°C. The pressure reaches the desired value of 100 mbar after about 1 minute.

As for the experiment at the atmospheric pressure, the micromodel is cleaned and closed with a 2-3 mm thick PDMS layer, which in turn is covered with a glass slide (as discussed in Section IV.2.1). The channels are saturated in the vacuum bell jar for a longer time than the previous experiment in order to degas the water and avoid the formation of bubbles during the evaporation in the oven. The process in the vacuum bell can be repeated more than once to reach a 100% saturation. Then, the assembly is set between two Plexiglas plates that are screwed together in the four corners. If this step is skipped, we observe the occurrence of bubbles after a few minutes at 100mbar between the surfaces

causing the leakage of water.

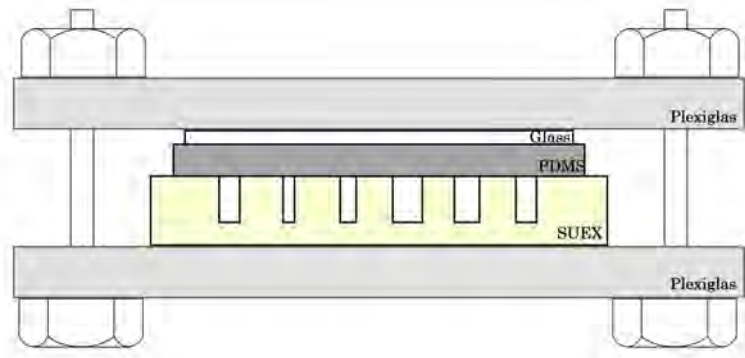


Figure IV.7: The assembly used for the partial vacuum drying experiments.

However, as sketched in Fig. IV.8, PDMS tends to fill the channels since the PDMS is squeezed on the micromodel. This reduces the channel depth and induces a channel cross section limited by a bent shape. This also results in angles lower than 90° in the two top cross-section corners.

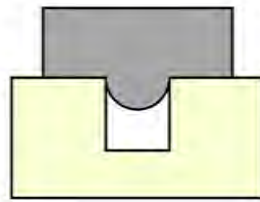


Figure IV.8: PDMS deformation created on a channel by compressing the micromodel assembly of SUEX, PDMS and glass between the two Plexiglass plates.

2.6 Drying setup with partial vacuum conditions and gravity effects ($P = 0.1P_{atm}$)

This setup for these conditions is a combination of the two setups previously described. The micromodel with PDMS and glass is compressed between the two Plexiglas plates, as illustrated in Fig. IV.7, but it is set in a vertical position in the oven with the liquid evaporating from the top. The light ring (Fig. IV.5) is still used, but without the mirror. Humidity and temperature are recorded with the help of the Rotronic hygrometer connected to a probe (Rotronic HC2-HK/C Series) set in the oven. The experiments with gravity effects and partial vacuum in the oven were performed a few months later than the ones with the micromodel held horizontally under partial vacuum conditions. Contrary to the previous experiments (micromodel held horizontally) the relative humidity does not stay stable at 5/6%, but rapidly increases up to an average value of 18/19% throughout the experiment.

3 Image treatment (phase distribution, evaluation of evaporation rate)

The drying process is typically characterized by the evolution of the drying rate and the evolution of the liquid and gas distribution within the micromodel. The evaporation rate J is typically computed from the measurement of the evolution of the liquid mass m in the micromodel: $J = -\frac{dm}{dt}$. J can be plotted as a function of time but it is also usual to plot J as a function of the saturation S , where S is the overall fraction of the pore space volume occupied by the liquid phase. The saturation S can be computed as $S = \frac{m(t)}{m(0)}$, where $m(0)$ is the mass of liquid in the micromodel when all the channels are filled by liquid. A balance is used to measure $m(t)$ in the experiments not using the oven. However, as explained before, the balance cannot be used when the micromodel is set in the oven. As a result, image processing is used to determine the saturation in the case of the experiments in the oven.

The image processing procedure has the following steps in Fiji:

1. Raw RGB images are converted to grey-scale ones by splitting the channels in the respective red, green and blue image components. The selected image is the one giving the highest contrast between air and liquid, hence the blue one as illustrated in Fig. IV.9.
2. The image is binarized by manually setting the threshold so as to only consider the liquid phase (see Fig. IV.9). Then, the "Measure" plugin is applied. The data of interest is the "Area fraction", which for thresholded images is the percentage of pixels in the image or selection that have been highlighted, i.e. the liquid phase.
3. Once the procedure is set for one image, a macro is compiled and the same actions are applied to all the images via batch processing.

This method computes for every image the number of black pixel with respect to the total area. In fact, for the experiments with basic conditions, horizontal micromodel and atmospheric pressure, and those with the gravity effects, the robustness of this procedure is verified in Fig. IV.10. In this figure, the evolution of the overall saturation obtained from the measurement of the mass with the balance is compared with that obtained from the image processing procedure for the case of the micromodel held horizontally (figure on the left) and for the case of the micromodel held vertically. Both data are normalized

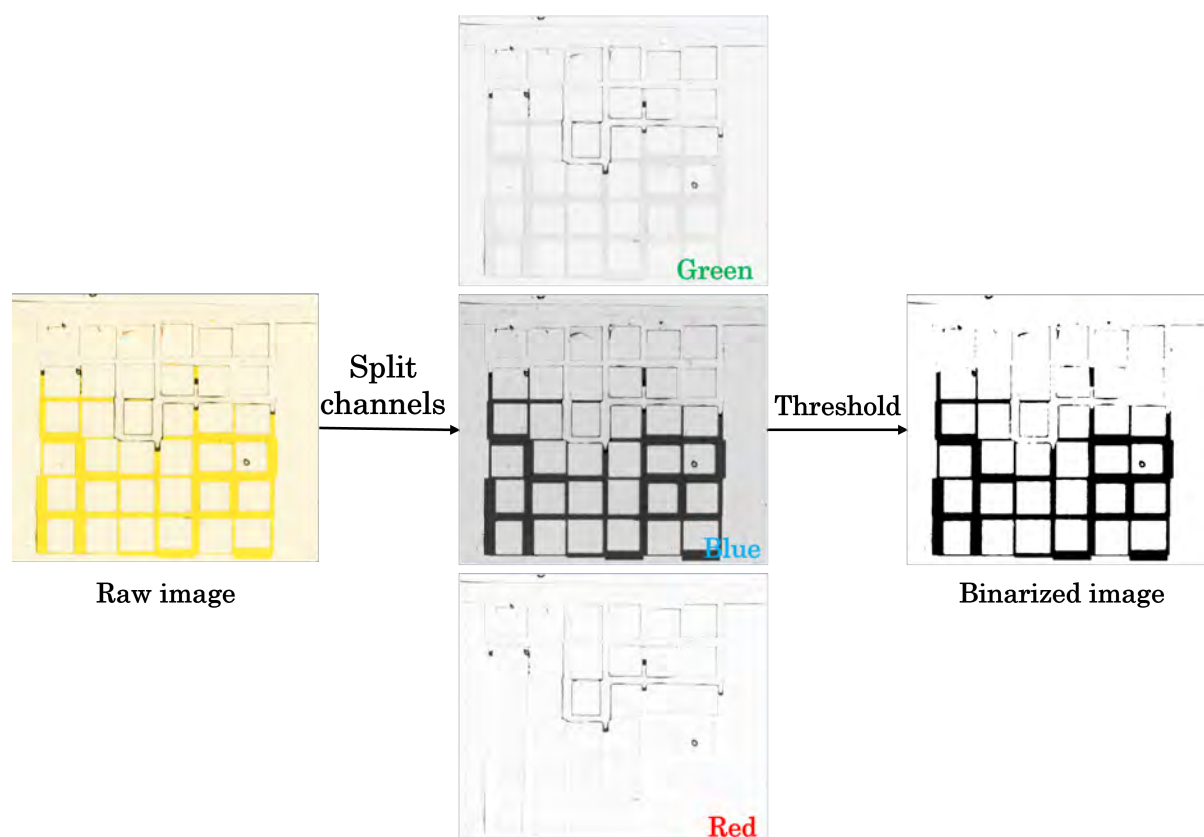


Figure IV.9: Steps of the image treatment procedure to obtain the percentage area, from the raw image, through the splitting of the channels, to the binary image.

according to

$$\Phi_{normalized} = \frac{\Phi - \Phi_{min}}{\Phi_{max} - \Phi_{min}} \quad (3.1)$$

where Φ is either the mass (balance) or the area percentage (image processing). Notice that the maximum error, defined as the absolute value of the discrepancy between two points at the same time, is about 3.3% at the end of the second curve, while it is 2.7% for the left curve.

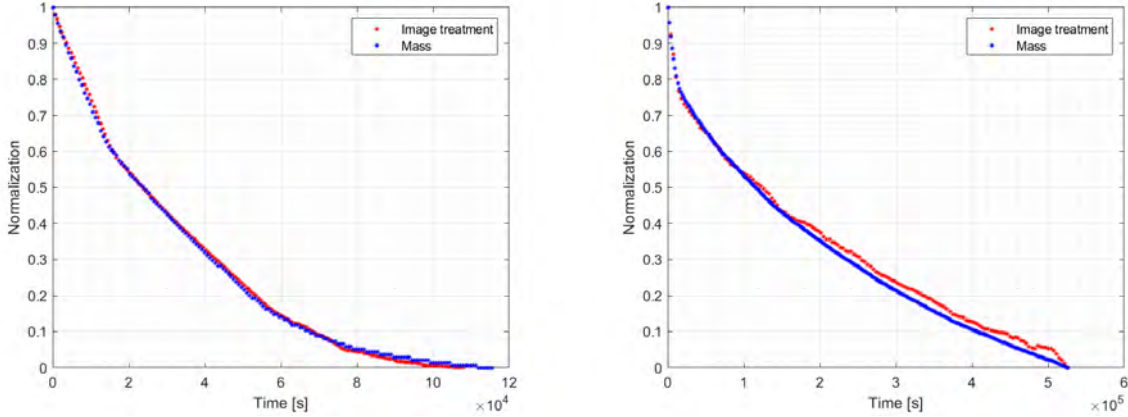


Figure IV.10: Comparison of the evolution of the dimensionless mass of liquid in the micromodel between the data of the balance and the image processing data. Drying is performed at atmospheric pressure; micromodel horizontal on the left; micromodel vertical on the right

4 Drying patterns

One of the main characteristics that can be observed is the drying pattern, i.e. the structure of the liquid and gas distribution in the micromodel channel network. Before comparing the different experimental results for these various cases, it is recalled that the gas invasion process resulting from evaporation is expected to be deterministic for a given network realization and for given boundary conditions. Nevertheless, differences can be sometimes observed between two experiments performed under the same conditions. Small changes may, in fact, occur because of slight local modifications in the wetting properties or the interfacial tension due to contamination of the network. This holds for experiments at the atmospheric pressure. As we shall see, the variation in the drying pattern can be stronger under partial vacuum conditions due to the somewhat random development of bubbles in the channels.

4.1 Comparing levels of saturation

The procedure for comparing the patterns considers the normalized mass curve evolution, for the experiments at the atmospheric pressure, and the evolution of the liquid area for the experiments at 100mbar. For a level of saturation S , we consider an epsilon $\epsilon = 0.005$ to define the interval $[S, S + \epsilon]$, where we look for the first index that represents the number of the images related to that level of saturation.

4.2 Impact of gravity

The fluid distribution in the micromodel for three values of the overall liquid saturation is shown in Fig. IV.11. The top series of pictures corresponds to the baseline case (no gravity effects, $P = P_{atm}$, $T = 22^\circ\text{C}$) whereas the bottom pictures are for the micromodel held vertically under otherwise the same conditions ($P = P_{atm}$, $T = 22^\circ\text{C}$). As can be seen from Fig. IV.11, the gravity effects tend to favor the invasion of the top region of the network. As discussed previously, gravity effects tend to limit the extension of the two phase zone (Fig. I.18b). Here, the micromodel is too small to observe an impact on the fluid distribution as strong as in Fig. I.18.

Nevertheless, Fig. IV.11 clearly illustrates the preferential invasion effect in the top region induced by the gravity effect. Physically, the impact of gravity effects can be understood from simple hydrostatic considerations. Consider the situation depicted in Fig. IV.12. From Laplace law, the hydrostatic equilibrium condition between point A and point B can be expressed as

$$2\gamma \cos(\theta_A) \left(\frac{1}{w} + \frac{1}{\ell_A} \right) - \gamma \cos(\theta_B) \left(\frac{1}{w} + \frac{1}{\ell_B} \right) \geq \rho gh \quad (4.1)$$

where γ is the surface tension, w is the channel depth (1mm), ℓ_A and ℓ_B are the widths of channel A and B respectively, θ is the contact angle, ρ is the density of the liquid, g is the acceleration of gravity and h is the vertical distance between point A and B in Fig. IV.12. For a contact angle of 50° , application of Eq.(4.1) for $\ell_A = 80\mu\text{m}$ and $\ell_B = 910\mu\text{m}$ leads to $h \approx 100\text{mm}$ which is significantly higher than the distance found through image processing (Fig. IV.12). This much larger distance explains why the invasion front is far from flat in this small micromodel. However, it can be considered that the effects of gravity affect locally the invasion when the invasion process at a given invasion step involves two channels of size less different than the lower bound and upper bound size.

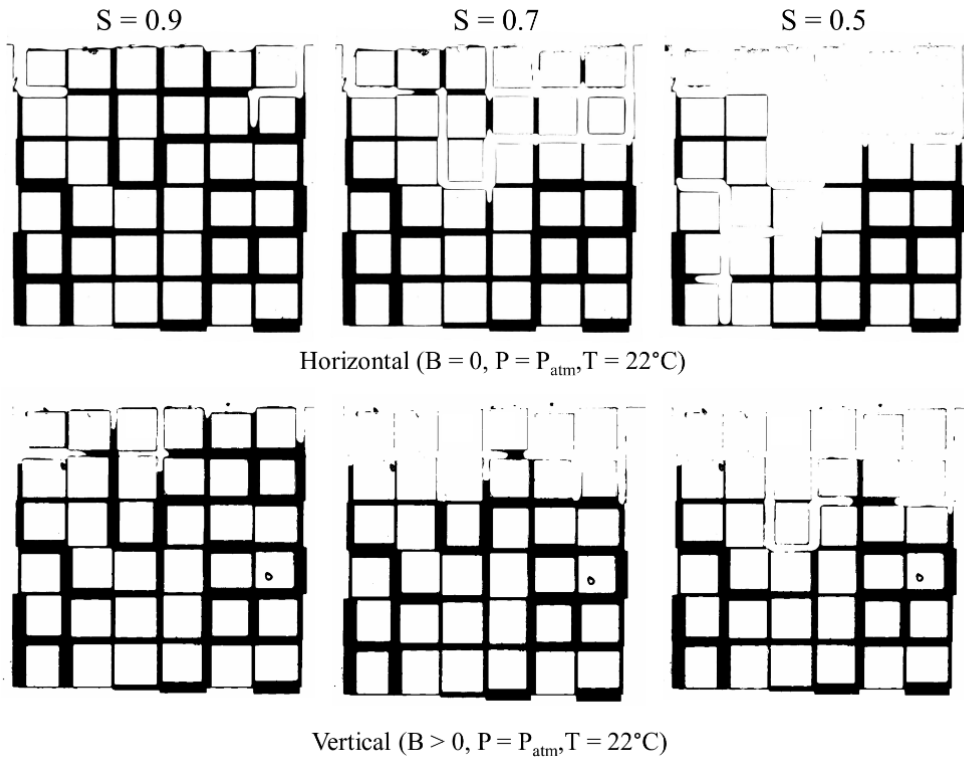


Figure IV.11: Comparison of the saturation patterns for $S = 0.9, 0.7$ and 0.5 (from left to right) between the case without gravity effects and with gravity effects. Liquid phase in black and gas phase in white, vapor escapes through top edge of micromodel. B is the Bond number ($B = \frac{\Delta\rho g a^2}{\gamma \cos \theta}$, where a is the distance between two nodes of network) characterizing the competition between gravity and capillary effects.

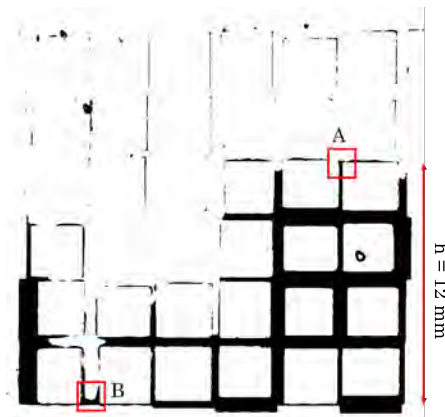


Figure IV.12: Time step $t = 50 \text{ h}$ of $B > 0$ at atmospheric pressure.

4.3 Impact of partial vacuum and temperature

The baseline patterns are compared to the ones obtained under partial vacuum conditions in Fig. IV.13. Overall the patterns are similar, i.e. look like typical invasion percolation (IP) patterns [Laurindo et Prat, 1996]. However, they are not identical. One can first notice the formation of a gas bubble in the case of the partial vacuum condition (pattern for $S = 0.9$, the bubble is in the red circle) for the experiment performed at $T = 22^\circ\text{C}$. As we shall see, the formation of such bubbles has been observed in other experiments under the partial vacuum conditions. A cavitation effect is unlikely because of the pressure level (100 mbar), which is relatively high. A possible explanation to bubble formation could be the trapping of gas during the micromodel filling process. Another possibility could be the presence of dissolved gas in the water. In other words, the exact explanation remains to be deciphered. However, it can be noticed that the occurrence of bubbles is not systematic. For instance, no bubbles formed in the experiment performed at $50\text{-}60^\circ\text{C}$.

Another difference lies in the preferential invasion in the very first row of vertical channel (compared the patterns for $S=0.9$ in Fig. IV.13 for $T = 22^\circ\text{C}$). Out of 7 channels, 5 are invaded by the gas under the partial vacuum conditions whereas only two channels are invaded under the baseline conditions for this saturation. This is perhaps due to viscous effects [Shaw, 1987]. However, it can be observed that the patterns obtained for $T = 50\text{-}60^\circ\text{C}$ are overall more similar to the baseline patterns than the ones observed at $T = 22^\circ\text{C}$ under the partial vacuum conditions. This questions the reproducibility of the experiments and does not suggest sufficient viscous effects for impacting the invasion pattern.

A similar comparison is proposed in Fig. IV.14 when the micromodel is held vertically. The comparison between the patterns for $T= 22^\circ\text{C}$ at the atmospheric pressure and under partial vacuum conditions suggests that the partial vacuum conditions enhance the preferential invasion in the top region of micromodel. This raises again the possible impact of viscous effects in conjunction here with the gravity effects. However, the experiment under partial vacuum conditions at the higher temperature ($50\text{-}60^\circ\text{C}$) does not confirm this trend. In the latter experiment, several bubbles form inside the channels (as indicated by the red circles in Fig. IV.14). The expansion of these bubbles lead to some liquid expelling from the micromodel (with partial re-invasion of the region adjacent to the micromodel top edge). This bubble expansion process modifies the pattern noticeably.

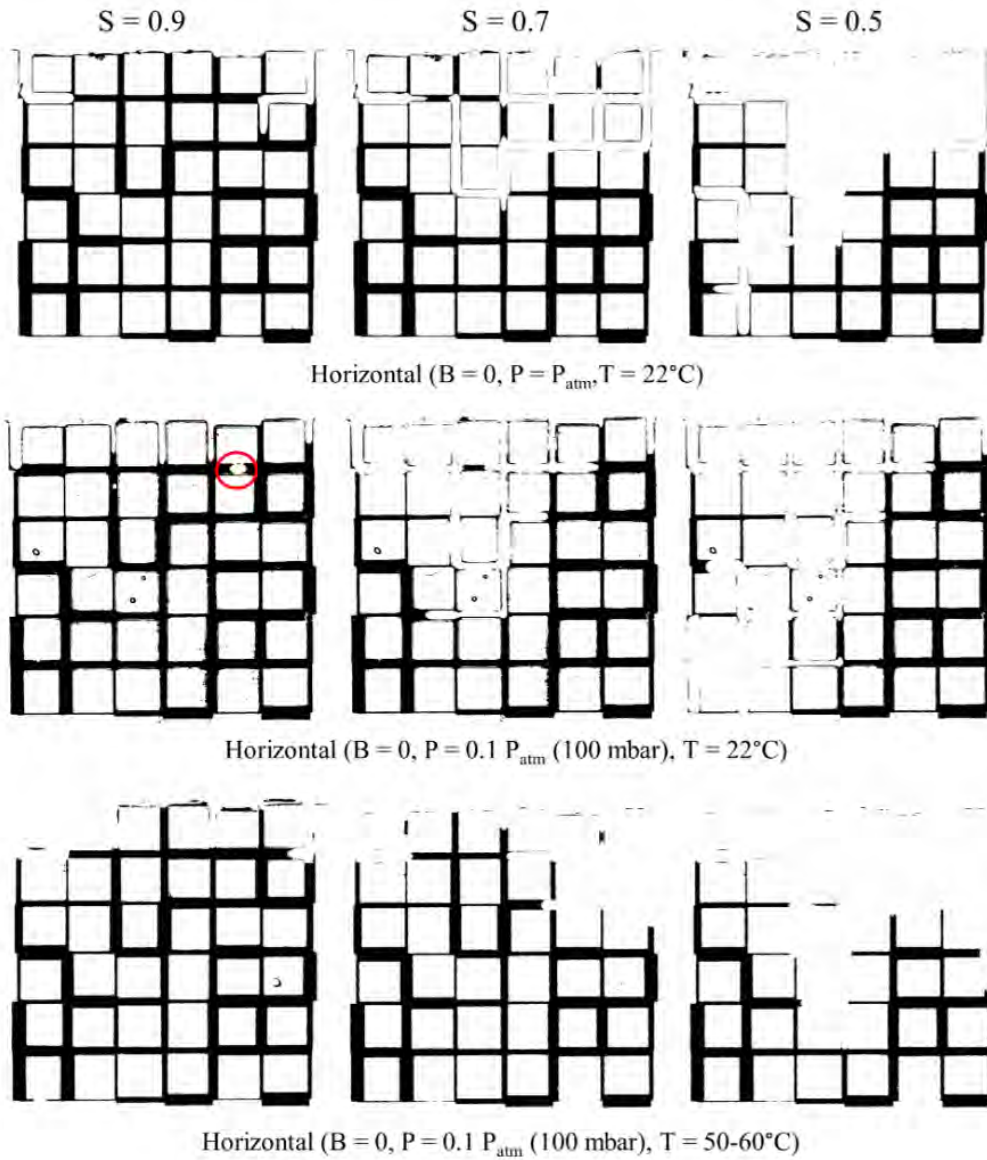


Figure IV.13: Comparison of the saturation patterns for $S = 0.9, 0.7$ and 0.5 (from left to right) between the case at normal gas pressure and the case under partial vacuum conditions for two temperature in the absence of gravity effects. Liquid phase in black and gas phase in white, vapor escapes through top edge of micromodel. A gas bubble is visible in the red circle.

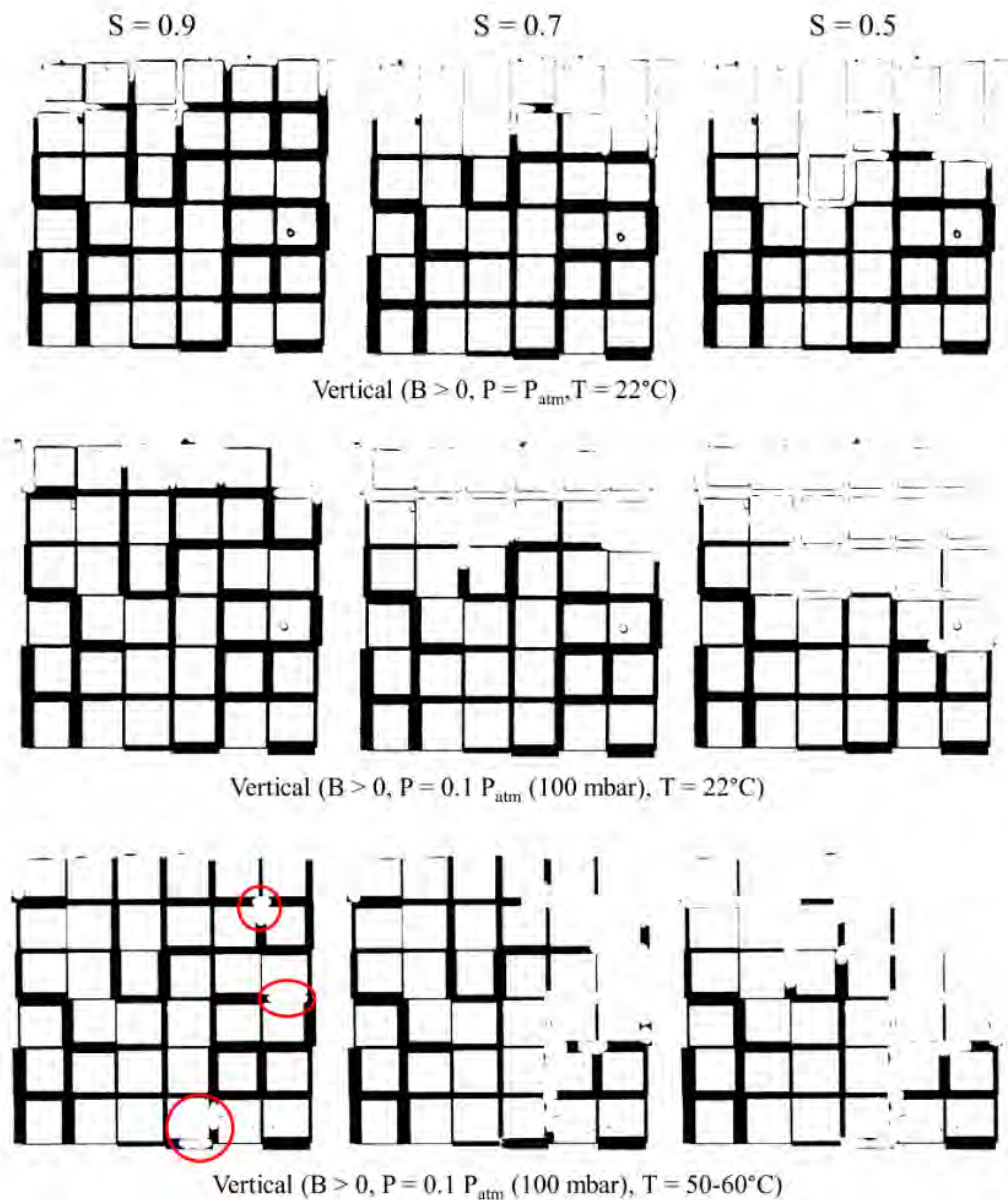


Figure IV.14: Comparison of the saturation patterns for $S = 0.9, 0.7$ and 0.5 (from left to right) between the case at normal gas pressure and the case under partial vacuum conditions for two temperature with gravity effects. Liquid phase in black and gas phase in white, vapor escapes through top edge of micromodel. Gas bubbles are visible in the red circles

5 Evaporation kinetics

The evaporation kinetics is defined here as the plot of the overall saturation as a function of time. The drying kinetics for the various cases are compared in what follows.

5.1 Impact of partial vacuum and temperature (in the absence of gravity effects)

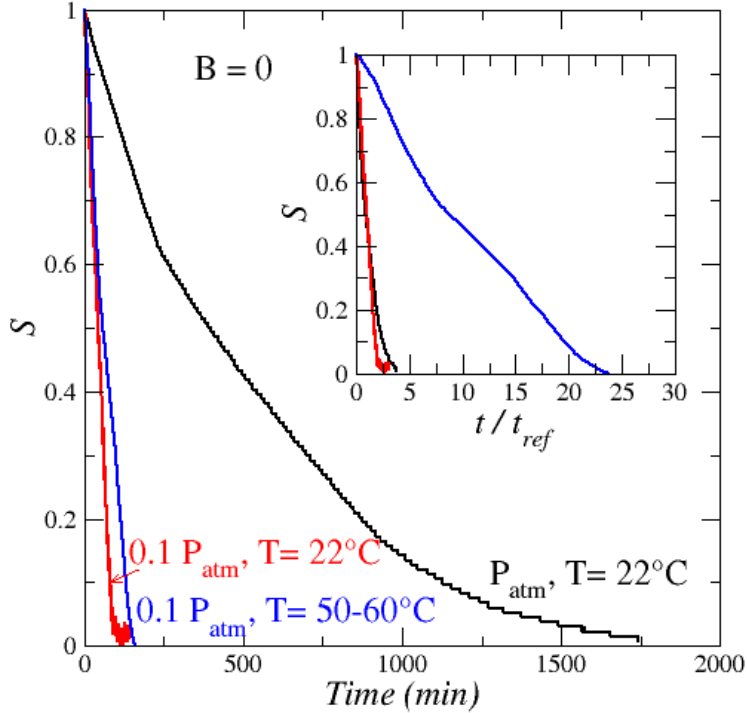


Figure IV.15: Evaporation kinetics. Impact of partial vacuum and temperature in the absence of gravity effects. The insets show the drying kinetics using the dimensionless time defined in the text.

As illustrated in Fig. IV.15, drying is much faster under partial vacuum conditions. In the literature, e.g. [Moyne, 1987, Redman *et al.*, 2017], the formation of gradients in the gas total pressure is emphasized as a specific and significant mechanism in vacuum drying. However, in our experiments this mechanism is unlikely due to the high permeability (i.e. the channel sizes) of the micromodel. In the present experiments, the mass transfer in the gas phase can be rather expected to be dominated by water vapor diffusion. It is thus interesting to look at the dependence of the vapor molecular diffusion with the total pressure and the temperature. From Chapman–Enskog theory, this coefficient can be expressed as [Cussler, 2009],

$$D = \frac{1.86 \times 10^{-3} T^{3/2} \sqrt{\frac{1}{M_1} + \frac{1}{M_2}}}{p \sigma_{12}^2 \Omega} \quad (5.1)$$

in which D is the diffusion coefficient, T the absolute temperature, p is the pressure, and M_i are the molecular weights. The quantities σ_{12} and Ω are molecular properties characteristic of the theory, the first represents the collision diameter and the second depends on an integration of the interaction between the two species.

As $D \propto \frac{T^{3/2}}{p}$, a faster drying can be expected for the partial vacuum condition since the diffusion coefficient is ten times larger for $P = 0.1P_{atm}$ than for $P = P_{atm}$. This is qualitatively consistent with the results shown in Fig. IV.15. In fact, the drying rate can be expressed more explicitly as follows,

$$J = AD \frac{M_\nu}{RT} P_{\nu S}(T) \left(\frac{RH_I - RH_\infty}{\delta} \right) = A\epsilon D_{eff} \frac{M_\nu}{RT} P_{\nu S}(T) \left(\frac{1 - RH_I}{\delta_f} \right) \quad (5.2)$$

where A is the micromodel cross-section surface area, R is the universal gas constant, M_ν is the vapor molecular weight, ϵ is the micromodel porosity, D_{eff} is the micromodel effective diffusion coefficient ($D_{eff} \sim D$ for a square network micromodel such as the one considered in this thesis), RH_∞ is the external relative humidity (in the enclosure or the oven, the values for the various experiments are reported in Table IV.1), δ is a diffusion length characterizing the external mass transfer (transfer of the vapor between the open edge of micromodel and surrounding gas), δ_f is the equivalent position of the evaporation front in the micromodel ($\delta_f = 0$ when the micromodel is full of liquid water), RH_I is the relative humidity at the open edge of micromodel. The left term in the r.h.s. of Eq.(5.2) describes the external mass transfer whereas the expression on the right describes the internal vapor transfer in the micromodel. Combining these two expressions leads to,

$$J = AD \frac{M_\nu}{RT} P_{\nu S}(T) \left(\delta + \frac{\delta_f}{\epsilon} \right)^{-1} (1 - RH_\infty) \quad (5.3)$$

which shows that the drying rate for a given phase distribution in the micromodel (i.e. given values of δ and δ_f) depends on the total pressure (via the dependence of D with the pressure), the temperature (explicitly in Eq.(5.3) and the dependence of D and $P_{\nu S}(T)$ with the temperature), and RH_∞ . In order to compare the various cases, it is therefore interesting to introduce as characteristic time,

$$t_{ref} = \frac{m_0}{J_{ref}} \quad (5.4)$$

where m_0 is the initial mass of water in the micromodel ($m_0 \approx 0.144$ g) and $J_{ref} = AD \frac{M_\nu}{RT} P_{\nu S}(T) \left(\frac{1 - RH_\infty}{\delta} \right)$, which is the evaporation rate in the absence of internal resistance (thus the evaporation rate at the beginning of the experiment when the micromodel is fully saturated with liquid water).

The evaporation rate can be also expressed as

$$\frac{dm}{dt} = -J \quad (5.5)$$

where m is the mass of liquid water in the micromodel. Introducing the reference time t_{ref} , Eq.(5.5) is expressed in dimensionless form as

$$\frac{d\left(\frac{m}{m_0}\right)}{dt^*} = \frac{J}{J_{ref}} \quad (5.6)$$

Integrating Eq.(5.6) leads to express the drying kinetics as

$$\frac{m(t^*)}{m_0} = - \int_0^{t^*} \frac{J}{J_{ref}} dt \quad (5.7)$$

Thus, if the pattern evolution is similar in two different experiments, the plots of the overall saturation (which is equal to $\frac{m}{m_0}$) as a function of the dimensionless time t^* should collapse on a single curve. The initial mass of liquid in the micromodel is 0.144 g, whereas the characteristic length δ can be estimated as $\delta \approx 1.5$ mm based on a previous work [20].

This gives the drying kinetics shown in the inset in Fig. IV.15. As can be seen, the rescaled drying kinetics are very close for the partial vacuum case and the atmospheric case at 22°C. Together with the similarity in the patterns (Fig. IV.13), this confirms that the accelerated drying with the partial vacuum conditions is due to the increase of the diffusion coefficient by the factor 10 (i.e. the ratio of the pressures). By contrast, the inset shows that the dimensionless kinetics is much slower for the higher temperature (blue curve in the inset in Fig. IV.15). The patterns are, however, relatively similar in Fig. IV.13. The overall dimensionless drying time ($\propto 24$) for this case is comparable with the overall dimensionless time in the presence of gravity effects for the case $P = P_{atm}$ and $T = 22^\circ\text{C}$ (Fig. IV.16). Thus, the internal mass transfer resistance has a more severe impact with the higher temperature. A possible explanation might lie in the effect of the corner films (see Chapter II and references therein). The higher evaporation rate for $P = 0.1P_{atm}$ and $T = 55^\circ\text{C}$ could limit the development of corner films due to the higher viscous flow in the films. However, this argument is not consistent with the results obtained for $P = 0.1P_{atm}$ and $T = 22^\circ\text{C}$ (Fig. IV.15), showing a drying rate similar to the one at $T = 50\text{-}60^\circ\text{C}$, but a much shorter dimensionless overall drying time.

5.2 Impact of gravity effects

As shown in Fig. IV.16, a faster drying than for the case at $P = P_{atm}$ is also observed under the partial vacuum condition in the presence of gravity effects. The faster drying can be also explained by the impact of the pressure on the vapor molecular diffusion. However, the dimensionless kinetics (inset in Fig. IV.16) are far from collapsing on a single curve, indicating that the evolution of the internal transfer resistance (corresponding to $\frac{\delta_f}{\epsilon}$ in Eq. (5.3)) differs between the three experiments for $B > 0$.

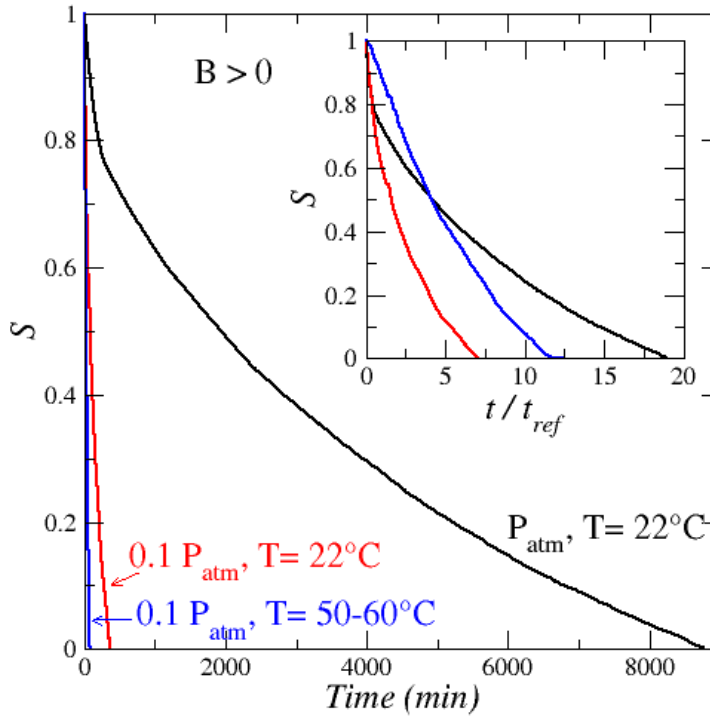


Figure IV.16: . Evaporation kinetics. Impact of partial vacuum and temperature with gravity effects. The insets show the drying kinetics using the dimensionless time defined in the text.

The patterns in Fig. IV.14 indicate a faster development of a dry zone in the upper region of the micromodel under the partial vacuum condition (at $T = 22^{\circ}C$) than for $P = P_{atm}$. This is not in agreement with the dimensionless kinetics (inset in Fig. IV.16), which is faster for $P = 0.1P_{atm}$. Also, one could expect that the formation and expansion of bubbles for $P = 0.1 P_{atm}$ and $T = 50 - 60^{\circ}C$ leads to a faster drying kinetics. This is what is obtained in the real time plots but not from the dimensionless kinetics.

The dimensionless kinetics with and without gravity effects are compared in Fig. IV.17. The comparisons for $T = 22^{\circ}C$ show a slower kinetics in the presence of gravity effects. From previous works [Laurindo et Prat, 1998], this is the expected result. The preferential invasion of the top region of micromodel due to gravity effects (illustrated in Fig. IV.11 and Fig. IV.14) induces the development of a dry zone in the top region of the

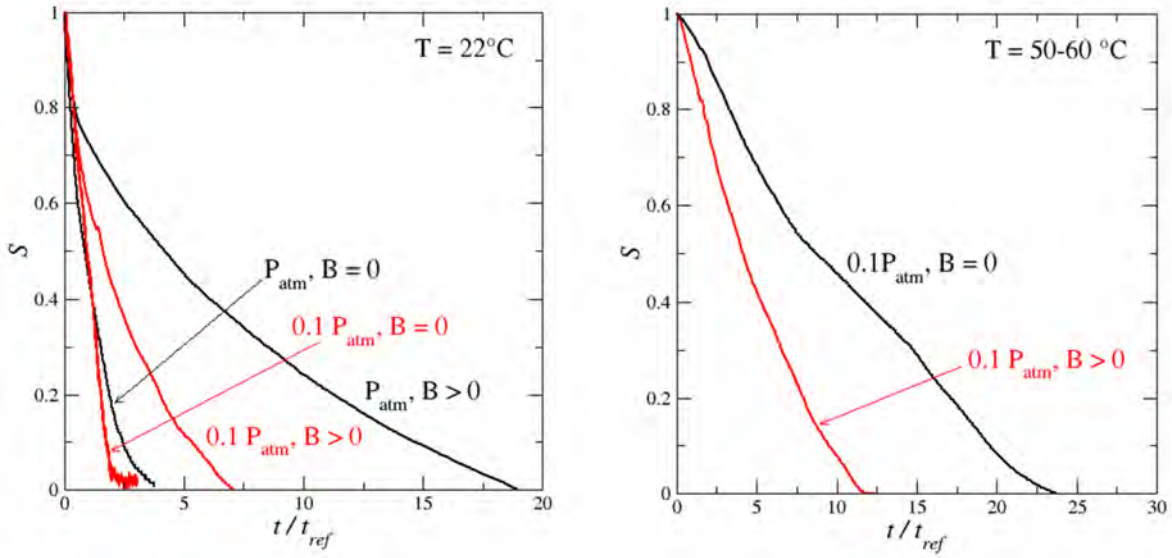


Figure IV.17: Dimensionless evaporation kinetics. Impact of gravity effects.

micromodel where the water transport is by vapor diffusion. This introduces a diffusive mass transfer resistance in addition to the external mass transfer resistance between the top edge of micromodel and the surrounding external gas. However, a quite different result is obtained for the higher temperature ($50-60^\circ\text{C}$). As shown in Fig. IV.17, drying is faster when the micromodel is vertical in this case. This can be explained by the impact of the gas bubbles mentioned in Section IV.4 and the patterns illustrated in Fig. IV.14. As can be seen from Fig. IV.14, the bubble expansion changes dramatically the pattern and hampers the formation of the dry zone in the top region of micromodel. The faster evaporation kinetics is consistent with the longer presence of liquid in the top region of micromodel. As mentioned before, the bubble expansion leads to some liquid water expelling from the micromodel and the partial filling of the large channel on top of the micromodel during the drying process. This phenomenon is consistent with a much faster dimensionless kinetics.

6 Conclusion

Drying experiments with a micromodel initially saturated with pure liquid water were reported and discussed in this chapter. The impact of gravity effects and partial vacuum conditions were explored. Regarding the patterns, the gravity effects, in spite of the small size of micromodel, favor the formation of a dry zone in the upper region of the micromodel consistently with previous works. The result is a slower kinetics compared to the corresponding case in the absence of gravity effects. However, this classical impact of gravity effects can be ineffective when gas bubbles form and expand during drying.

This was exemplified with experiments performed at $T = 50\text{-}60^\circ\text{C}$ under partial vacuum conditions ($P = 0.1P_{atm}$). Due to significant bubble formation and expansion when the micromodel was held vertically, the drying kinetics was significantly faster in the presence of gravity effects compared to the case without gravity effects under the otherwise same conditions. The origin of the bubble occurrence remains to be clarified as well as the way of controlling their occurrence. Drying is faster under partial vacuum conditions than at the atmospheric pressure. It was shown that this can be explained to a large extent by the impact of the total gas pressure on the vapor diffusion (the molecular vapor diffusion is inversely proportional to the total gas pressure). However, the consideration of the dimensionless kinetics shows that this feature is not sufficient to explain the differences observed between the various experiments. It seems difficult to clearly decipher the impact of the various parameters (beyond the impact of the pressure on the diffusion coefficient and the gravity on the pattern) that were varied owing to the interplay between drying kinetics and patterns in the relatively small micromodel used in this chapter and the limited number of experiments considered. The next step, in the Chapter that follows, is to explore whether the faster kinetics observed under the partial vacuum conditions as well as the gravity effects and change in the temperature have an impact on particles distribution during drying.

Chapter V

Experiments with micromodel in the presence of particles

Contents

1	Introduction	104
2	Methods and Materials	104
2.1	The experimental protocol	104
2.2	The plasma treatment	106
2.3	Experimental set up	108
2.4	Imaging the deposit: Particle deposit image processing	108
3	Impact of particles on drying patterns	110
3.1	$B = 0, P = P_{atm}, T = 22^{\circ}\text{C}$	110
3.2	$B > 0, P = P_{atm}, T = 22^{\circ}\text{C}$	110
3.3	$B = 0$ and $B > 0, P = 0.1P_{atm}, T = 22^{\circ}\text{C}$	112
3.4	$B = 0$ and $B > 0, P = 0.1P_{atm}, T = 50\text{-}60^{\circ}\text{C}$	114
4	Impact of particles on drying kinetics	115
4.1	$B = 0, P = P_{atm}, T = 22^{\circ}\text{C}$	115
4.2	$B > 0, P = P_{atm}, T = 22^{\circ}\text{C}$	116
4.3	$B = 0$ and $B > 0, P = 0.1P_{atm}, T = 22^{\circ}\text{C}$	116
4.4	$B = 0$ and $B > 0, P = 0.1P_{atm}, T = 50\text{-}60^{\circ}\text{C}$	119
5	Péclet number evaluation	120
6	Final deposit	121
6.1	Impact of drying conditions	121
6.2	Impact of the initial particle concentration	124
7	Impact of the plasma treatment	124
8	Attempt of final deposit statistical analysis	128
8.1	Statistical analysis by channels (procedure)	128
8.2	Correlation between mean brightness and area percentage	130

8.3	Comparison of the deposits	132
8.4	Evaporation time statistics	133
8.5	Conclusion on the "statistical" analysis	136
8.6	Conclusions	137

1 Introduction

In this chapter, drying experiments in the presence of particles in a micromodel are presented and discussed. As in the previous chapter, various conditions are explored as summarized in Table V.1 and Table V.2.

For the series of experiments summarized in Table V.1, a low initial concentration in particles, namely 0.5×10^{-4} g/mL was considered. The impact of wettability conditions (plasma treatment), gravity forces, temperature and partial vacuum conditions is explored. In addition, two experiments were performed for a higher particle concentration (0.6×10^{-2} g/mL) for the following conditions (Table V.2): $T = 22^\circ\text{C}$, no gravity effects, $P = P_{atm}$.

Before discussing the results, details on the micromodel and material and methods are given in the next section.

2 Methods and Materials

The model porous medium used for the experiments in this chapter is the same as in Chapter IV. This is a 7×7 square network of channels whose widths vary between $80 \mu\text{m}$ and $910 \mu\text{m}$ according to a uniform probability density function. The depth of the channels is 1 mm. The distance between two adjacent nodes in the network is 3 mm. The total dimension of the micromodel is $1.8 \text{ cm} \times 1.9 \text{ cm}$. As discussed in more details in Chapter IV, the micromodel is composed of a SUEX layer, in which the channel network is set, closed by a PDMS layer covered by a thin glass slide. Therefore, the channels have three sides made of a hydrophilic material (SUEX), while the PDMS top wall is hydrophobic.

2.1 The experimental protocol

After following the same cleaning protocol as in Chapter IV, the micromodel is filled with a solution of water and particles under the vacuum bell. The fluorescent particles used in the experiments of this Chapter are the same as the ones considered in Chapter II. One can therefore refer to Chapter II for further information on the particles. Here it is just

Drying mode	Initial particle concentration	Temperature (°C)	Relative humidity (%)	External gas pressure (mbar)	Gravity effects	Saturation pressure for experiment temperature
Capillary air drying without gravity	Low	22	8.7	1000	no	2500Pa (25mbar)
Capillary air drying without plasma (fresh plasma treatment)	Low	22	7.3	1000	no	2500Pa (25mbar)
Capillary air drying with gravity	Low	22	9.7	100	yes	2500Pa (25mbar)
Evaporation vacuum drying without gravity	Low	22	4.8	100	no	2500Pa (25mbar)
Evaporation vacuum drying with gravity	Low	22	15.8	100	yes	2500Pa (25mbar)
Vaporization vacuum drying without gravity	Low	50-60	1	100	no	12335-19920 Pa (123.35-199.2 mbar)
Vaporization vacuum drying with gravity	Low	50-60	1	100	yes	12335-19920 Pa (123.35-199.2 mbar)

Table V.1: The various drying conditions explored in the chapter for the low concentration in particles (0.5×10^{-4} g/mL). The red cells indicate an experiment with expanding bubbles.

Drying mode	Initial particle concentration	Temperature (°C)	Relative humidity (%)	External gas pressure (mbar)	Gravity effects	Saturation pressure for experiment temperature
Capillary air drying without gravity	High	22	7.2	1000	no	2500Pa (25mbar)

Table V.2: Conditions for the two experiments performed with a high particle concentration (0.6×10^{-2} g/mL)

recalled that the particles are of quasi-uniform diameter (equal to $1 \mu\text{m}$).

As mentioned before, two particles concentrations (in g/mL) are considered: the low concentration, namely 0.5×10^{-4} g/mL and the high concentration 0.6×10^{-2} g/mL. These concentrations are obtained by mixing a volume V_{part} of a 2% (g/mL) solution with a selected volume V_{H_2O} of water dyed with fluorescein. The fluorescein concentration is 0.01%. Thus the obtained concentration C is

$$C = \frac{V_{part}C_0}{V_{part} + V_{H_2O}} \quad (2.1)$$

where $C_0 = 0.02\text{g/mL}$. The choice of not using pure water was made to enhance the optical contrast between air and water in the micromodel because the presence of the particles is not sufficient to change significantly the liquid water grey level.

After the water has completely evaporated in the micromodel and the particles have deposited, the micromodel is opened and set under the microscope Zeiss Axio Scope.A1 with a 5x/0.16Phl lens equipped with a camera (LaVision Image sCMOS) in order to obtain images of the final particle deposit in the micromodel. To this end, the micromodel is scanned from the upper left corner row by row. For each row we select the same number of images, then, the Grid/Collection stitching plugin of Fiji is used to recompose the image of the deposit at the bottom of the whole channel network. Since the images at the microscope are taken manually, different tile overlaps, usually around 50%., have to be tested to obtain the whole image.

2.2 The plasma treatment

The need to use the plasma machine (Expanded plasma cleaner PDC-002 (230V) - harrick plasma) comes from the problem of sticking the PDMS layer to the SUEX layer. Plasma surface treatment is used to enhance adhesion to other surfaces through the modification

of the surface chemistry without altering the bulk material properties. It is also to be noticed that the treatment is performed at a temperature close to the ambient temperature. The SUEX and PDMS layers composing the micromodel are set in the plasma cleaner chamber for 7 minutes at high power and then the treated surfaces are glued together. This treatment is performed only when the adhesion of PDMS on SUEX is not good. Therefore, the plasma treatment is not systematic. Often the adhesion without plasma treatment is considered as sufficiently good for performing the experiment.

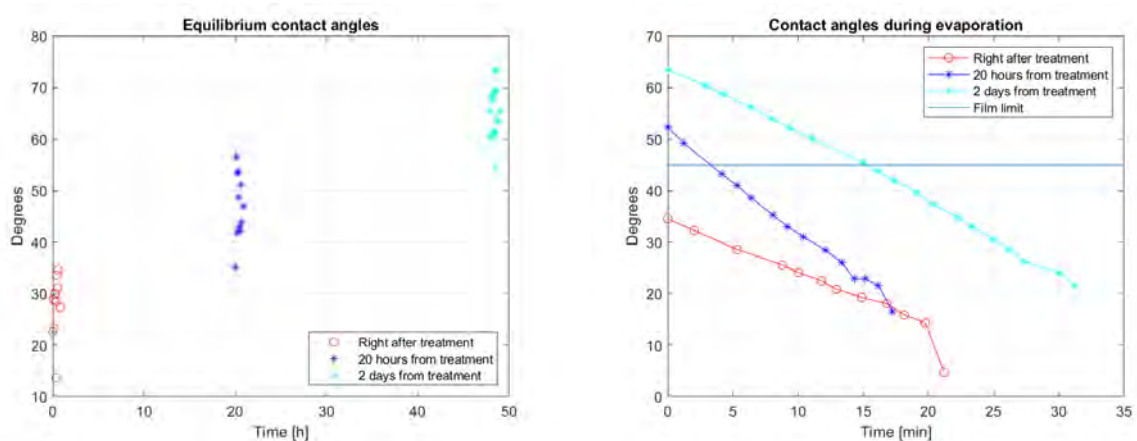


Figure V.1: On the left, equilibrium contact angles on SUEX right after the plasma treatment, after 20 hours and after 48 hours. On the right, evolution of the contact angles of an evaporating droplet of water set on a layer of SUEX treated with plasma

A consequence of the plasma treatment is the modification of the wettability properties of the materials. The SUEX becomes much more hydrophilic, with an equilibrium contact angle of 27.4° in average. The contact angle was also measured during the evaporation of a droplet right after the plasma treatment. The contact angle was found to be equal to 34.6° at the very beginning of the evaporation. Then, as shown in Fig. V.1, it dropped to 4.6° in about 20 minutes. Performing a similar measurement after leaving the SUEX at ambient temperature and atmospheric pressure for 20 hours led to the following results: the contact angle was 47° at the beginning of the experiment and decreased down to less than 20° in 20 minutes (Fig. V.1). After 48 hours of exposition to the ambient conditions the equilibrium contact angle was found to be of 65 degrees, approaching the value obtained without any treatment.

It has to be noticed that most experiments discussed in what follows were performed without plasma treatment or hours after the plasma treatment. An exception was an experiment performed right after the plasma treatment as discussed in Section V.7.

2.3 Experimental set up

The experimental set up is the same as the one employed in Chapter IV. As a quick reminder, experiments at the atmospheric pressure are run in a hermetic plexiglass box, with two containers of LiBr saturated solution to keep the relative humidity around 7%. The micromodel is set on a 10^{-4} g precision balance, Quintix Semi-Micro Sartorius Balance, to record the evolution of the mass every 10 seconds. Images are taken with a Nikon D800 camera every 2 minutes, for the longer experiments and every minute for the faster ones. A temperature and relative humidity Rotronic sensor, HC2-C04, is set at the top of the box with data recorded every 5 minutes. One can refer to Chapter IV for more details.

As described in Chapter IV, experiments under partial vacuum conditions are carried out in an oven in which the total gas pressure stabilizes at 100 mbar in about a minute. The use of a back light is not possible in the oven. As also described in Chapter IV, a ring light is used and images of the micromodel are taken through the oven door every 10 seconds. When the micromodel is held horizontally, a mirror is set at 45° to obtain the images of the micromodel through the oven door since the oven top wall is not transparent.

2.4 Imaging the deposit: Particle deposit image processing

Images of the particle final deposit on the bottom wall of the channel network are taken with the microscope equipped with a confocal green light and a 5x objective. The channel network is scanned after removal of the top glass and the underlying layer of PDMS.

The process for obtaining the deposit images follow these steps:

1. The opened micromodel is set under the microscope at the upper left corner. The green light is set at an intensity of 25% for the lower concentration in particles and the focus is done at the bottom of the channels. In the case of the higher concentration in particles, the intensity of the green light is set to 5%, so as to avoid the camera saturation..
2. The image frequency is set to 1s and the chip is manually scanned with a snake by row pattern, see Fig. V.2.

The following phase consists in choosing the images in order to have an $n \times m$ matrix, noting that the dimensions can vary from one experiment to another since the scan is manual. First doubles and images not in focus are deleted, at this point the rows can

have different numbers of images, therefore m will be the number of images in the row that has the least and we proceed by deleting images with the aim of having the same count in every row. As illustrated in Fig. V.3, the images are then stitched together via Fiji's plugin "Stitching > Grid/Collection stitching" [Preibisch *et al.*, 2009]. The used fusion method is the linear blending method, where the intensities are smoothly adjusted between the images around the overlapping area.

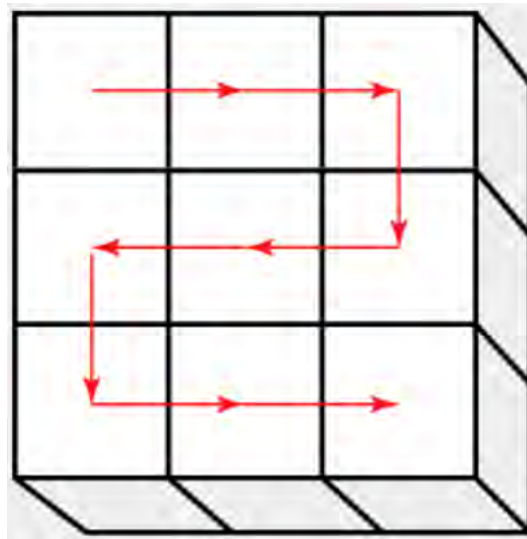


Figure V.2: Patter used for scanning the deposit in the channels of the pore network.

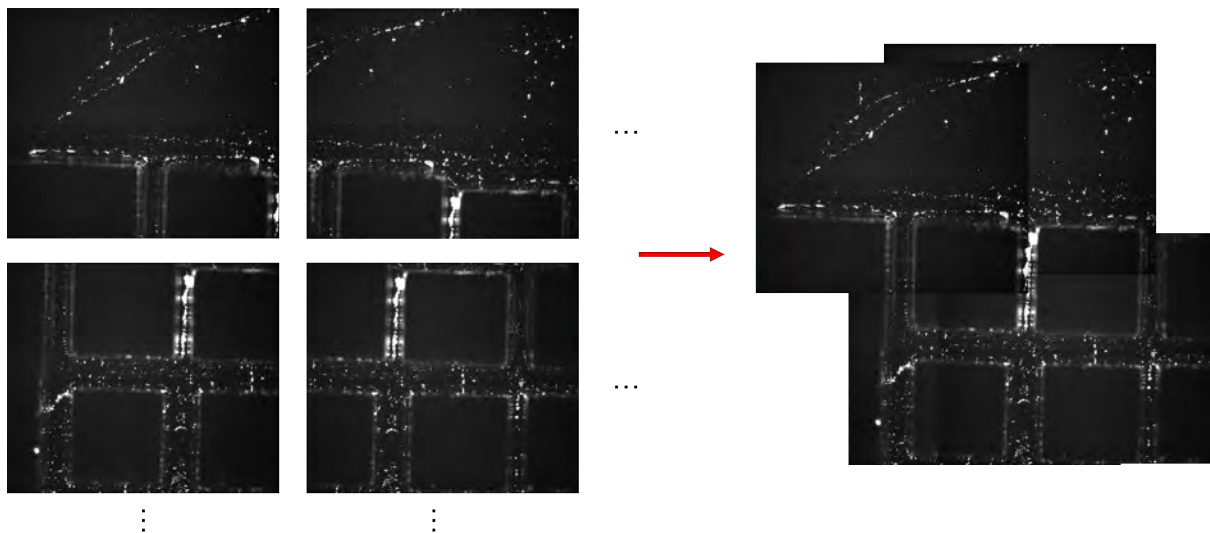


Figure V.3: Illustration of Fiji's plugin for stitching the images of the deposit. The particles correspond to the bright spots

After recombination of the images via the stitching procedure, an image of the particle deposit over the whole network is obtained as illustrated in Fig. V.4.

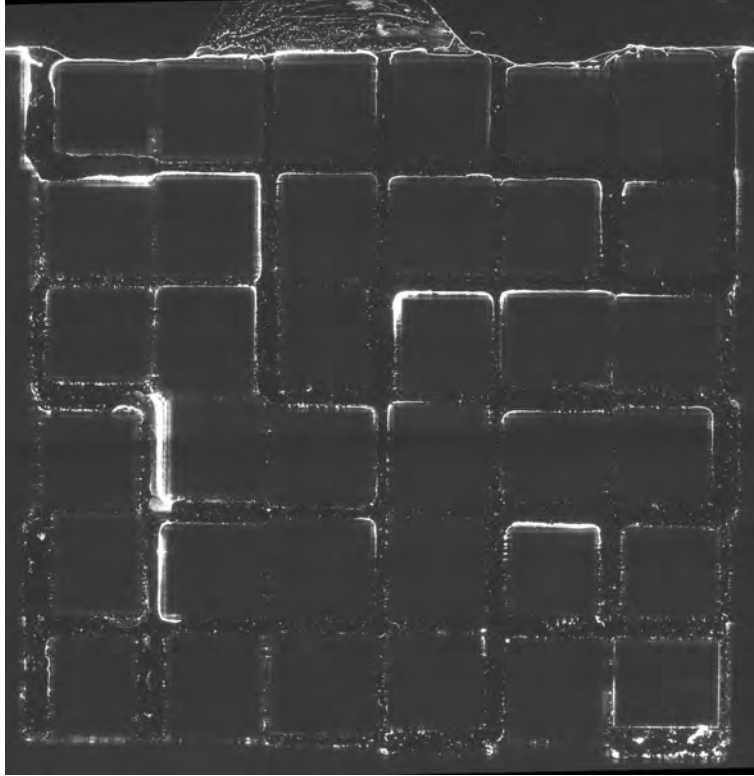


Figure V.4: Example of final image of the deposit (in bright light grey) in the micromodel after completion of the stitching procedure.

3 Impact of particles on drying patterns

This section proposes a comparison of liquid and gas distributions (patterns) during drying between the case of pure water and the case with particles.

3.1 $B = 0, P = P_{atm}, T = 22^{\circ}\text{C}$

The comparison for the situation where $B = 0, P = P_{atm}, T = 22^{\circ}\text{C}$ is presented in Fig. V.5. As can be seen, the patterns are globally similar and of invasion percolation (IP) type as expected (Chapter IV). A significant deposit of particles (shown in a red circle) can be observed on top of the images in the case of the high concentration. However, the presence of this deposit does not have an important impact on the pattern.

3.2 $B > 0, P = P_{atm}, T = 22^{\circ}\text{C}$

The comparison for the case $B > 0, P = P_{atm}, T = 22^{\circ}\text{C}$ is displayed in Fig. V.6. Some differences can be noted with a slight trend toward more invasions in the upper region of the micromodel in the presence of particles.

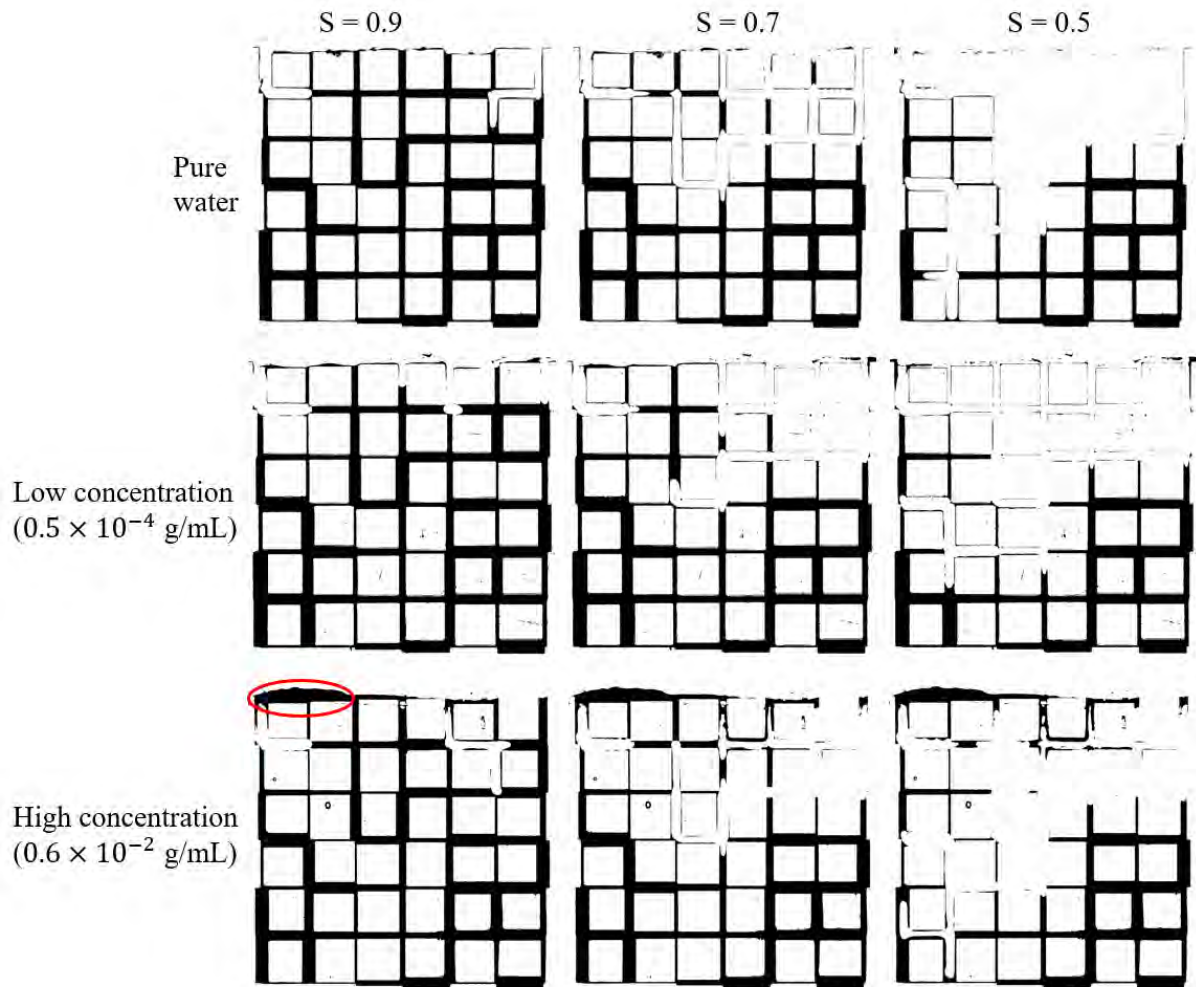


Figure V.5: Comparison of the drying patterns for $S = 0.9$, 0.7 and 0.5 (from left to right) without gravity effects at $P = P_{atm}$, $T = 22^\circ\text{C}$ in the absence of particles and with particles. Liquid phase in black and gas phase in white, vapor escapes through top edge of micromodel. The black region in the red circle for the high concentration corresponds to a deposit of particles.

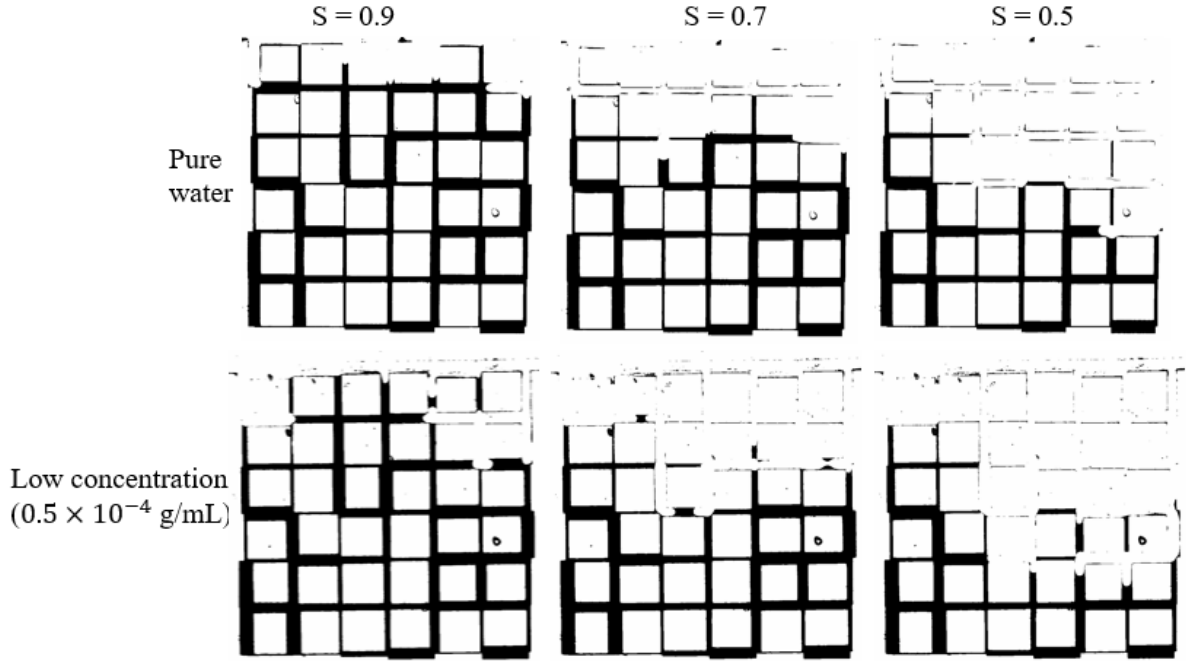


Figure V.6: Comparison of the drying patterns for $S = 0.9$, 0.7 and 0.5 (from left to right) with gravity effects at $P = P_{atm}$, $T = 22^\circ\text{C}$ in the absence of particles and with particles. Liquid phase in black and gas phase in white, vapor escapes through top edge of micromodel.

3.3 $B = 0$ and $B > 0$, $P = 0.1P_{atm}$, $T = 22^\circ\text{C}$

As can be seen from Fig. V.7, bubble forms both for pure water and in the presence of particles in the experiments under partial vacuum conditions at $T = 22^\circ\text{C}$ and in the absence of gravity effects ($B = 0$). However, the location of the bubble is different. The bubble is deeper inside the micromodel in the case of the experiment with particles (image for $S = 0.9$ in Fig. V.7). Inspection of the movie of the experiment shows a significant expansion of the bubble before it connects to the gas phase invading the micromodel from the top in Fig. V.7. This significant bubble expansion might explain the difference with the case of pure water that can be observed for the overall saturation $S = 0.5$ with invasion of the upper right region in the case of the particles whereas this region is still occupied, at least partially, with liquid water in the case of the pure water experiment.

In the presence of gravity effects (Fig. V.8), no internal bubble forms. Nevertheless, some differences are visible between the patterns for pure water and the patterns with the particles. However, the preferential invasion of the micromodel top region is observed in both cases.

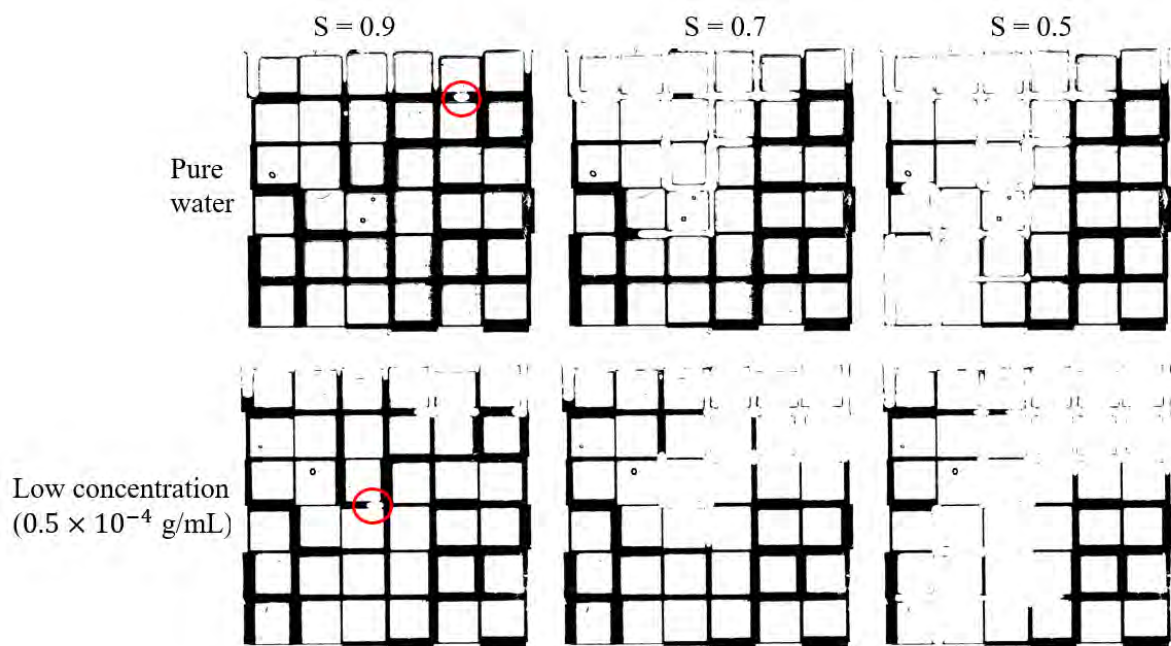


Figure V.7: Comparison of the drying patterns for $S = 0.9, 0.7$ and 0.5 (from left to right) without gravity effects ($B = 0$) under partial vacuum conditions ($P = 0.1P_{atm}$) and $T = 22^\circ\text{C}$ in the absence of particles and with particles. Liquid phase in black and gas phase in white, vapor escapes through top edge of micromodel. The red circles indicate the presence of expanding bubbles.

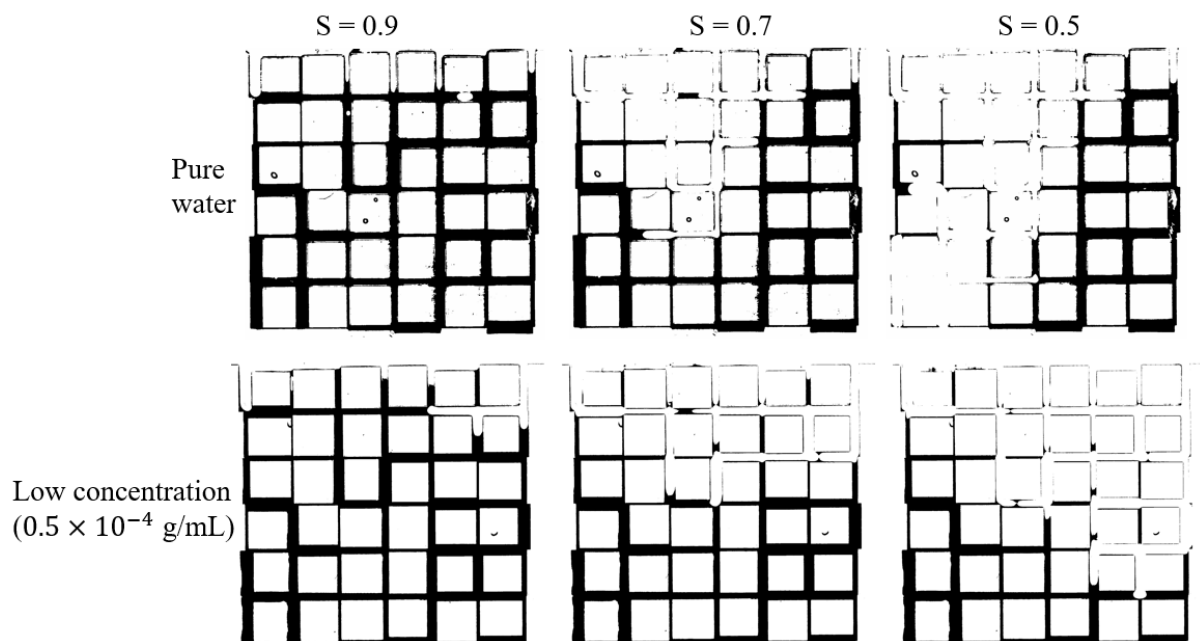


Figure V.8: Comparison of the drying patterns for $S = 0.9, 0.7$ and 0.5 (from left to right) with gravity effects ($B > 0$) under partial vacuum conditions ($P = 0.1P_{atm}$) and $T = 22^\circ\text{C}$ in the absence of particles and with particles. Liquid phase in black and gas phase in white, vapor escapes through top edge of micromodel.

3.4 $B = 0$ and $B > 0$, $P = 0.1P_{atm}$, $T = 50-60^\circ\text{C}$

The patterns are again mainly affected by the presence or not of expanding bubbles. In the case when the micromodel is held horizontally (Fig. V.9), such a bubble expansion is observed in the case with particles but not in the experiment with pure water. The impact is the expelling of the solution from the micromodel (this is materialized in Fig. V.9 by the “droplet like” zone on the right along the top edge of micromodel). Here again, the development of the bubble significantly affects the pattern compared to the case without bubble (pure water in Fig. V.9).

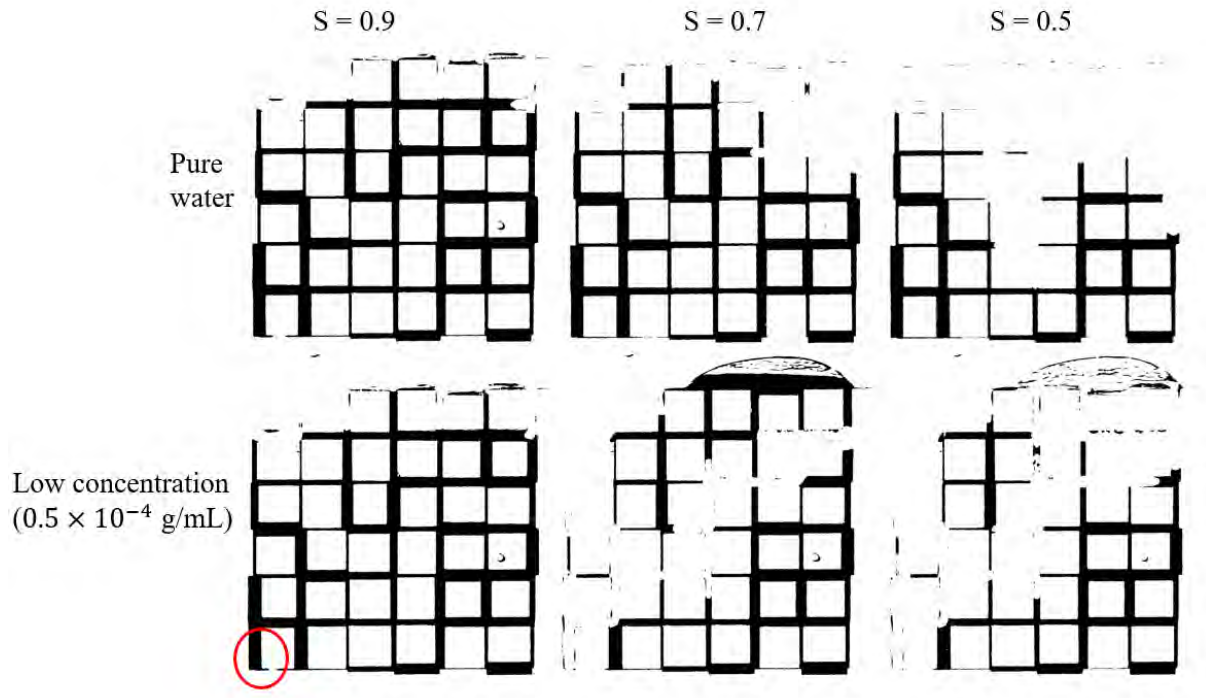


Figure V.9: Comparison of the drying patterns for $S = 0.9, 0.7$ and 0.5 (from left to right) without gravity effects ($B = 0$) under partial vacuum conditions ($P = 0.1P_{atm}$) and $T = 50-60^\circ\text{C}$ in the absence of particles and with particles. Liquid phase in black and gas phase in white, vapor escapes through top edge of micromodel. The red circle indicates the presence of an expanding bubble (visible in the movie but not in the selected images shown here)

In the case of the experiments at $T = 50-60^\circ\text{C}$ under partial vacuum conditions and with gravity effects (Fig. V.10), several expanding bubbles develop in the case of the experiment with pure water whereas such bubbles were not observed in the experiment with particles. This results again in noticeable difference in the patterns. The trend with the bubble expansions is to hamper the preferential invasion of the micromodel top region.

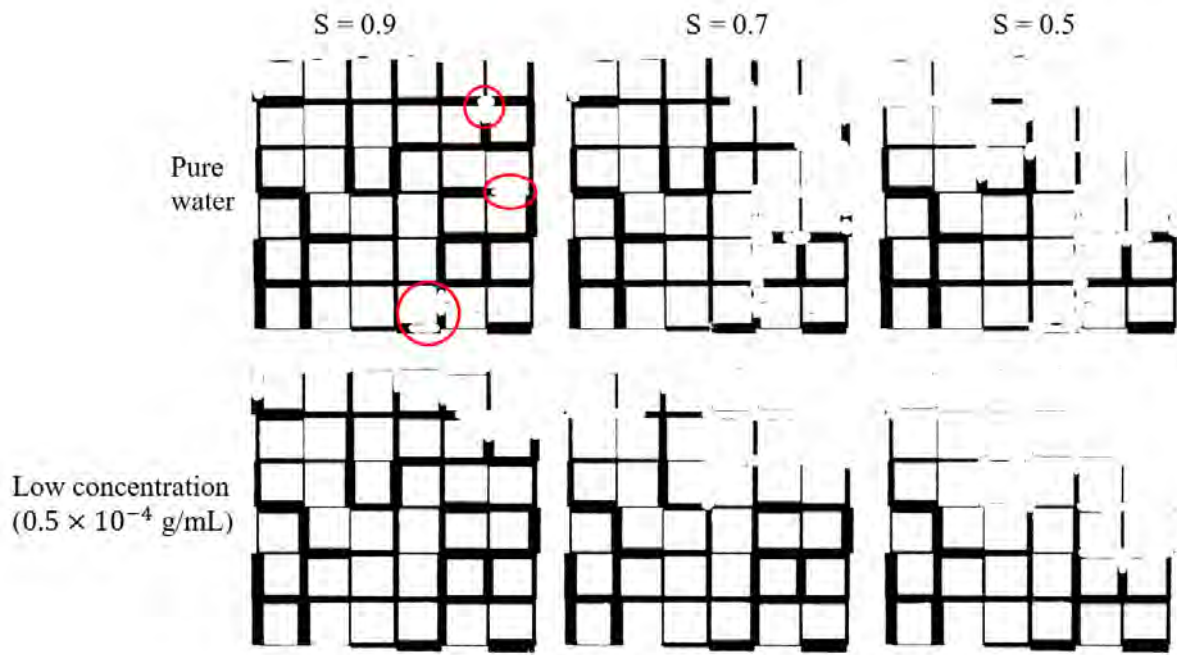


Figure V.10: Comparison of the drying patterns for $S = 0.9$, 0.7 and 0.5 (from left to right) with gravity effects ($B > 0$) under partial vacuum conditions ($P = 0.1P_{atm}$) and $T = 50-60^\circ\text{C}$ in the absence of particles and with particles. Liquid phase in black and gas phase in white, vapor escapes through top edge of micromodel.

4 Impact of particles on drying kinetics

4.1 $B = 0$, $P = P_{atm}$, $T = 22^\circ\text{C}$

The drying kinetics for three particle concentrations and the considered conditions ($B = 0$, $P = P_{atm}$, $T = 22^\circ\text{C}$) are compared in Fig. V.11. Two experiments have been performed for the higher concentration (blue curves in Fig. V.11).

As can be seen the impact of particles is negligible in the case of the low concentration in particles. This is consistent with the patterns (Fig. V.5) which are similar. By contrast, the drying kinetics is significantly slower with the higher concentration in particles. This can be explained in part by the presence of a particle deposit along the micromodel open edge (see Fig. V.12 for experiment #1 (solid line in Fig. V.5) and experiment #2 (dashed line in Fig. V.5)). The particle deposit is expected to dry out since the particles are too big ($\sim 1 \mu\text{m}$) for the Kelvin effect to have an impact). The dry deposit introduces an additional mass transfer resistance to the vapor diffusion which can explain the significantly slower drying kinetics. However, from the inspection of the top deposit in Fig. V.12, it is not obvious to explain why the kinetics is different for experiments #1 and #2. Note that the deposit is in black in Fig. V.12. Although the color is the same as for the liquid phase in Fig. V.12, there is no doubt on the nature of the black spots along

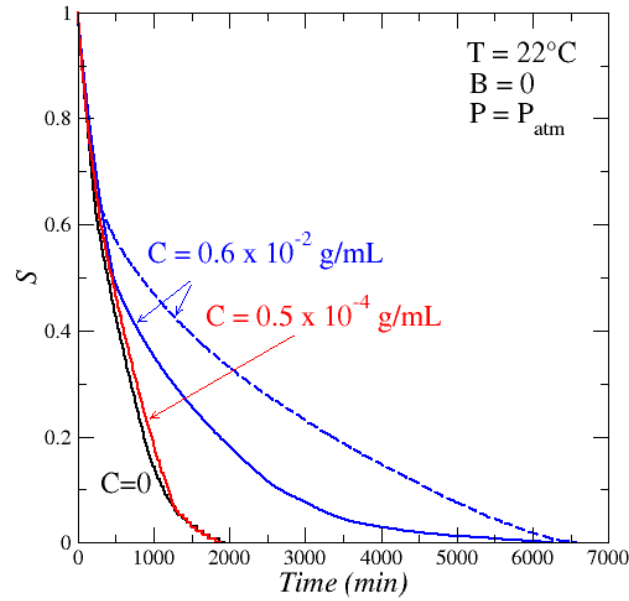


Figure V.11: Drying kinetics for various initial particle concentrations in the absence of gravity forces for $P = P_{atm}$, $T = 22^{\circ}\text{C}$

the top (open) edge of micromodel. They correspond to particle deposits.

However, the overall shape of the deposit is different in both experiments. A relatively big deposit forms on the left side of the micromodel open edge for experiment #1 whereas the top deposit is more evenly distributed in experiment #2, deposit at the outlet of the micromodel in black in Fig. V.12 and final deposit with bright particles in Fig. V.20. This can be also seen as an illustration of the difficulty for developing a procedure ensuring a good reproducibility.

4.2 $B > 0$, $P = P_{atm}$, $T = 22^{\circ}\text{C}$

As for the case $B = 0$, the impact of the particles on the drying kinetics is weak when the concentration in particles is low. This is consistent with the drying patterns depicted in Fig. V.8, which is spite of some local differences are globally similar.

4.3 $B = 0$ and $B > 0$, $P = 0.1P_{atm}$, $T = 22^{\circ}\text{C}$

As shown in Fig. V.14, the drying kinetics is much faster under the partial vacuum conditions. As discussed in Chapter IV, the faster kinetics are consistent with the increase by a factor 10 of the vapor diffusion coefficient under the partial vacuum conditions.

However, contrary to the results discussed in section V.4.1, the drying kinetics is slower in the presence of particles in the case without gravity effects. As discussed in Chapter

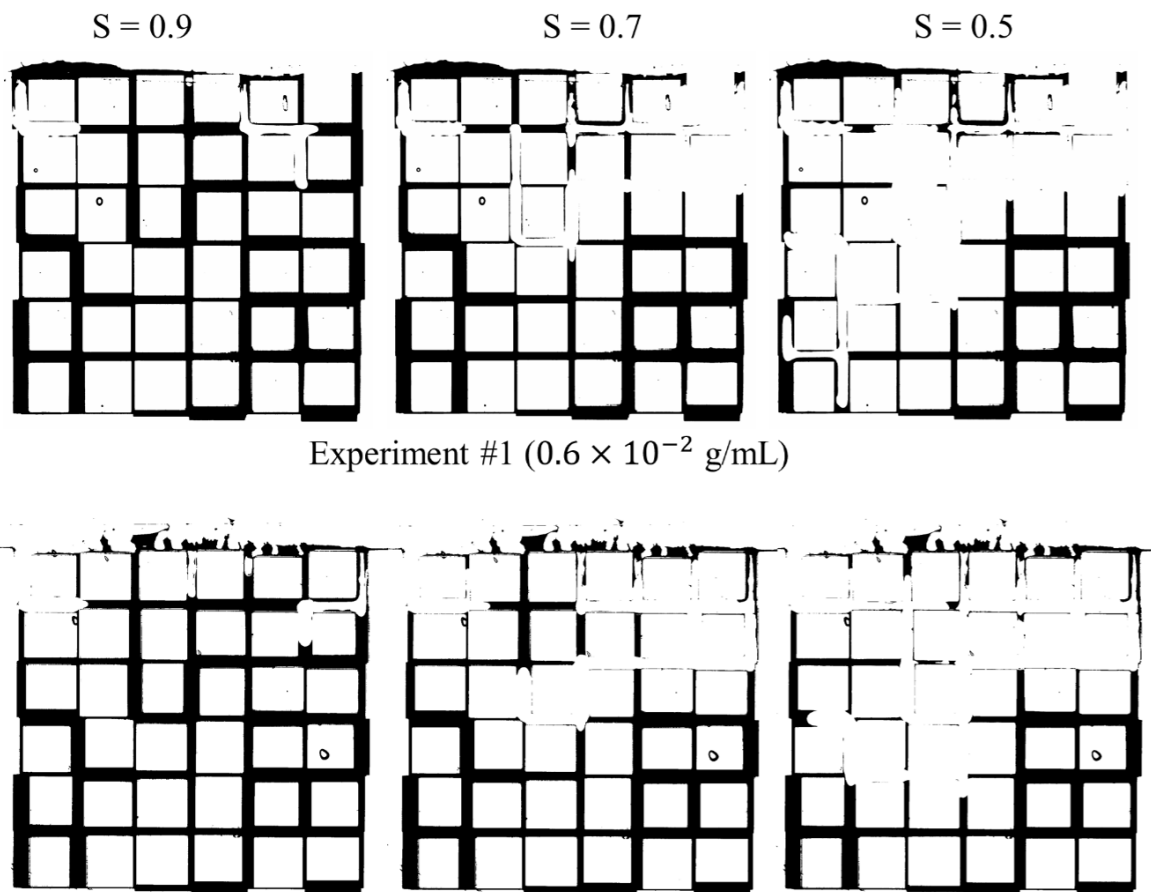


Figure V.12: Drying patterns for $S = 0.9, 0.7$ and 0.5 (from left to right) without gravity effects at $P = P_{atm}$, $T = 22^\circ\text{C}$ for the higher concentration in particles (experiments #1 and #2). Liquid phase in black and gas phase in white, vapor escapes through top edge of micromodel. Deposit of particles (unfortunately in black as for the liquid phase) is present on top of the images.

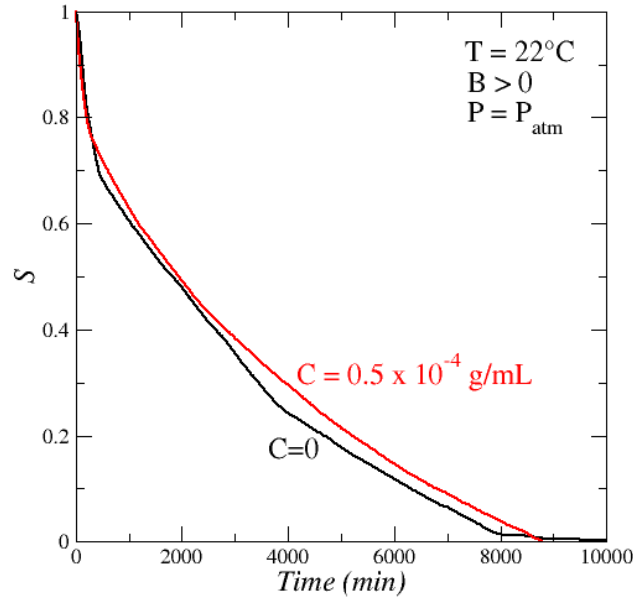


Figure V.13: Comparison of drying kinetics for pure water and the low concentration in particles in the presence of gravity forces for $P = P_{\text{atm}}$, $T = 22^\circ\text{C}$

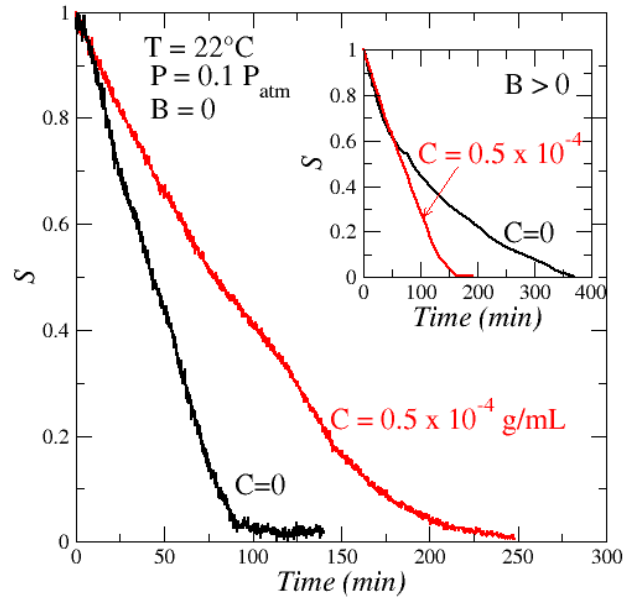


Figure V.14: Comparison of drying kinetics for pure water and the low concentration in particles in the absence and in the presence of gravity forces for $P = 0.1P_{\text{atm}}$, $T = 22^\circ\text{C}$

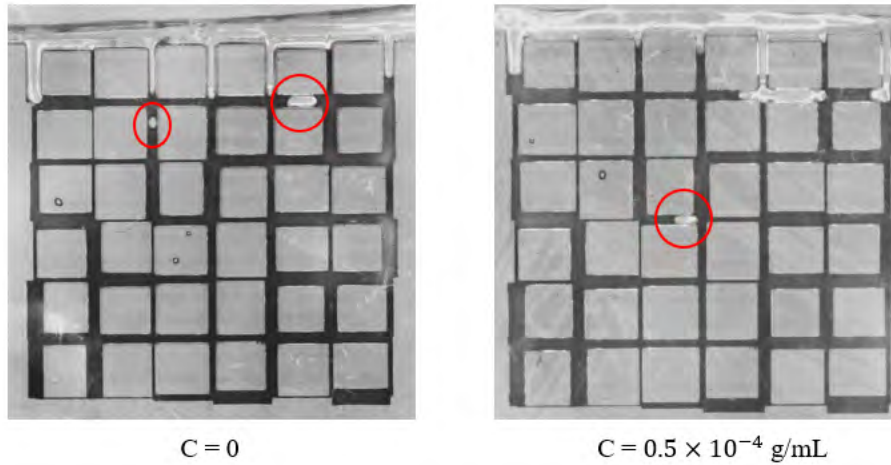


Figure V.15: Formation of bubbles for the case of pure water and the low concentration in particles in the absence of gravity forces for $P = 0.1P_{atm}$ and $T = 22^{\circ}\text{C}$, images at $t = 11\text{min}$

IV, expanding bubbles can form during drying under the partial vacuum conditions. This is the case for both experiments, i.e. with pure water and with particles, for the case $B = 0$ shown in Fig. V.14. However as recalled in Fig. V.15, the bubbles do not form at the same location in both experiments. This might be the cause of the differences in the drying kinetics.

Results for the case $B > 0$ show that the drying kinetics for pure water is significantly slower than in the presence of particles. No bubble forms in both experiments and the drying patterns are somewhat similar (Fig. V.8). However, some liquid remains longer in the upper region of the micromodel in the case of the experiment with particles (see the patterns for $S = 0.7$ and $S = 0.5$ in Fig. V.8). This is consistent with a faster kinetics in the presence of particles. The reason for this delayed evaporation in the micromodel upper region remains, however, to be explained.

4.4 $B = 0$ and $B > 0$, $P = 0.1P_{atm}$, $T = 50\text{-}60^{\circ}\text{C}$

As in Chapter IV, these conditions lead to the fastest kinetics due to both the impact of pressure on the vapor diffusion coefficient and the impact of temperature on the vapor saturation pressure (Table V.1). As can be seen from Fig. V.16, the drying kinetics is faster in the presence of particles in the absence of gravity effects for the conditions $T = 50\text{-}60^{\circ}\text{C}$. This can be attributed again to the formation and expansion of an internal bubble in the case with particles. In this experiment, the bubble expansion leads to some liquid expelling from the channel network. No bubble forms in the case of the experiment with pure water.

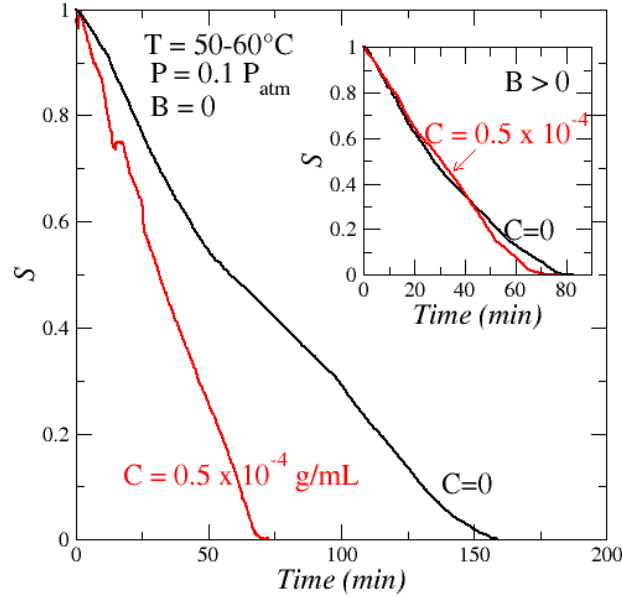


Figure V.16: Comparison of drying kinetics for pure water and the low concentration in particles in the absence and in the presence of gravity forces for $P = 0.1P_{atm}$, $T = 50-60^{\circ}\text{C}$

As shown in the inset in Fig. V.16, the drying kinetics with and without particles are comparable in the presence of gravity effects. However, the expanding bubble effect is strong in the case of the experiment with pure water whereas no bubble forms in the case of the experiment with particles. Thus, it might be considered again (i.e. as for the experiments at 22°C under partial vacuum conditions) that drying should be faster in the presence of particles if no bubble forms in both experiments (i.e. for pure water and in the presence of particles). In this respect, the situation for $T = 50-60^{\circ}\text{C}$ would be different than at the lower temperature of 22°C at the atmospheric pressure. In other words, it could be concluded that the faster drying under the partial vacuum conditions leads to a change in the impact of particles on the drying kinetics for the considered low concentration.

5 Péclet number evaluation

It is well known that colloidal particles are transported by diffusion and convection in the liquid phase during drying. Diffusion tends to uniform the particle concentration over the porous medium where the convective flow induced in the liquid by the evaporation process tends to cause the accumulation of particles toward the evaporative regions (the top surface of the micromodel at the beginning of the experiments). The competition between both transport phenomena is classically characterized by the Péclet number

[Huinink *et al.*, 2002], which can be defined as $Pe = \frac{jH}{\rho_{ell}\epsilon D_{eff}}$, where j is the evaporation flux (kg/m²/s), ρ_{ell} is the liquid density (j/ρ_{ell} is an evaporation characteristic velocity), H is the micromodel height (1.8 cm), ϵ is the porosity (~ 0.5), D_{eff} is the micromodel effective diffusion coefficient of the particles (for a square network, $D_{eff} = D_p$ (weak tortuosity) where D_p is the partial coefficient diffusion). The latter is estimated from the Einstein-Stokes law as $D_p = \frac{kT}{6\pi\mu\frac{d_p}{2}}$ where $k = 1.380649 \times 10^{-23}$ J K⁻¹ is the Boltzmann constant, d_p the particles diameter and μ is the dynamic viscosity. For our particles ($d_p = 1\mu\text{m}$) and water $\mu = 1 \times 10^{-3}$ Pa, one obtains $D_p \approx 4.3 \times 10^{-13}$ m²/s.

An estimate of j can be obtained from Fig. V.11 noting that 80% of the initial mass (0.14 g) has evaporated in about 1000 min. This gives $j \approx 10^{-4}$ kg/m²/s and $Pe \sim 9000$. This value was computed for the evaporation flux of one of the slower drying experiments ($B = 0$, $P = P_{atm}$, $T = 22^\circ\text{C}$). The conclusion is therefore that the Péclet is very high in the experiment. Based on the sole consideration of this high value, one would expect that the particles accumulate at the top surface of the micromodel. As we shall see, this is a misleading consideration. In fact, depending on the experiments, particle deposit can occur much deeper in the micromodel as discussed in the section that follows.

6 Final deposit

6.1 Impact of drying conditions

First insights on the impact of drying conditions can be obtained from the images of the final particle deposit in the micromodel depicted in Fig. V.17.

First, it can be observed that the deposit is essentially in the micromodel entrance region (top row of channels in Fig. V.17) for the conditions $B = 0$, $P = 0.1 P_{atm}$, $T = 22^\circ\text{C}$ and $T = 50\text{-}60^\circ\text{C}$, that is when the micromodel is held horizontally under the partial vacuum conditions. As discussed earlier, both cases (i.e. $T = 22^\circ\text{C}$ and $T = 50\text{-}60^\circ\text{C}$) are characterized by the formation of expanding bubbles. The expanding bubbles displace the liquid, and thus the particles, out of the micromodel or in the very first row of channels. The effect is particularly significant in the case of the higher temperature (50-60°C) with the formation of an important particle deposit (in the red ellipse in Fig. V.17) out of the micromodel.

Overall, the images in Fig. V.17 indicate that the most uniform (or perhaps more accurately the least non-uniform) deposit is obtained for the conditions $B = 0$, $P = P_{atm}$, $T = 22^\circ\text{C}$, i.e. slow drying conditions. For this case, particle deposits are visible in the upper and the lower region of the micromodel. However, the deposit is quite heterogeneous

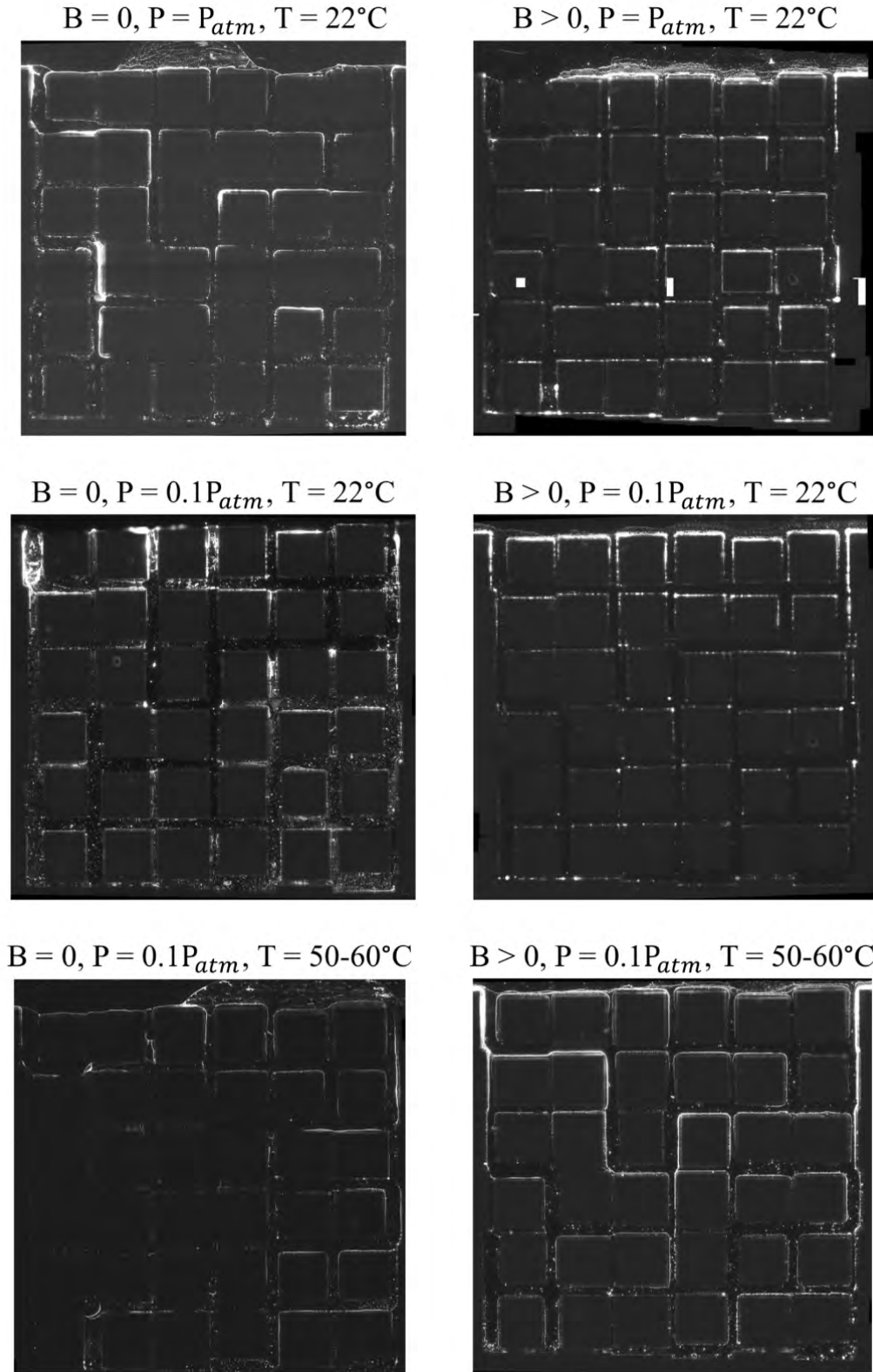


Figure V.17: Final particle deposit (in bright light grey) in the micromodel for the various drying conditions and the low initial particle concentration (0.5×10^{-4} g/mL). Note that drying with expanding bubbles as observed for the conditions $B = 0$, $P = 0.1P_{atm}$, $T = 22^\circ\text{C}$, $T = 50\text{-}60^\circ\text{C}$. The white rectangles in the image for $B > 0$, $P = 0.1P_{atm}$ and $T = 22^\circ\text{C}$ represent areas for which the superposition of images could not be satisfactorily achieved with the image stitching procedure (see Section V.2.4 for details on this image recombination procedure)

with some channels with a clear and noticeable deposit whereas the particle deposit in others seems quite weak. Also, it can be noted that the deposit in a channel is often seen along one side of channel. It is known that the considered micromodel structure favors the formation of “capillary rings” [Vorhauer *et al.*, 2015]. In [Vorhauer *et al.*, 2015], capillary rings refer to liquid trapped in the corners around the solid cube-like blocks in the micromodel (Fig. V.18). Similar secondary capillary structures are expected in our micromodel. The consideration is that the particle deposits visible in Fig. V.17 inside the micromodel for the condition $B = 0$, $P = P_{atm}$, $T = 22^\circ\text{C}$ form when these pieces of corner films eventually dry out.

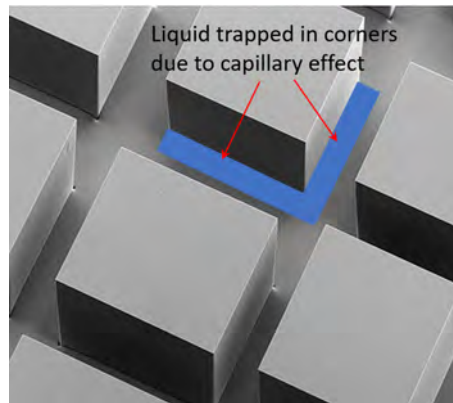


Figure V.18: Schematic of liquid trapped in corners in micromodel channels (the image with cubic blocks is adapted from [Geistlinger *et al.*, 2019])

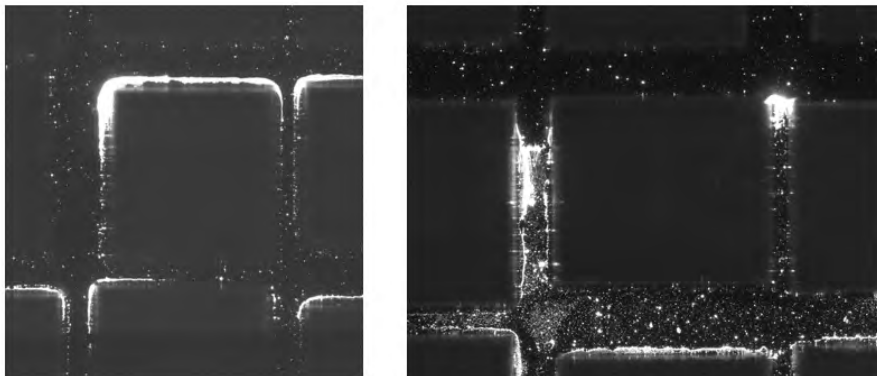


Figure V.19: Illustration of “corner deposit” (left) and “plugging deposit” (right).

This type of “corner deposit” (Fig. V.19) is visible in Fig. V.17 for the other cases as well. Although less common, another type of deposit can be distinguished in Fig. V.17: “the plugging deposit” (Fig. V.19) visible for instance for the condition $B = 0$, $P = 0.1P_{atm}$, $T = 22^\circ\text{C}$. In this case, the deposit is present across the channel width. However, this does not mean necessarily that the channel is fully occupied by particles with this type of deposit. Due to the wettability difference between SUEX and the PDMS cover

plate, it is likely that the deposit is mainly on the SUEX (as indicated by the experiment with a single channel presented in Chapter II). No obvious conclusion can be drawn from Fig. V.17 as regards the impact of gravity effects. Since the gravity effects tend to favor the invasion of the upper region of micromodel, one could expect that more particles are deposited in the lower region of the micromodel assuming here that the particle deposit preferentially occurs at the end of drying (this point is discussed in much more details in Section V.8 and turns out to be not correct). The case $B > 0$, $P = P_{atm}$, $T = 22^\circ\text{C}$ seems to be consistent with this consideration with somewhat more channels with deposit in the lower region of the micromodel compared to the case $B = 0$, $P = P_{atm}$, $T = 22^\circ\text{C}$. However, this trend is not confirmed by the experiments under partial vacuum conditions. For $T = 22^\circ\text{C}$, $P = 0.1P_{atm}$ and $B > 0$, the deposits are in the very top region of micromodel whereas for $T = 50\text{-}60^\circ\text{C}$, $P = 0.1P_{atm}$ and $B > 0$, deposits are visible mostly over the top half of micromodel.

6.2 Impact of the initial particle concentration

The impact of the particle initial concentration on the final deposit is illustrated in Fig. V.20. Corner deposits are still visible with the higher concentration but the main difference lies in the plugging deposits which are not present for the low concentration and numerous in the case of the higher concentration. As for the case of the low concentration, deposits are present a bit everywhere over the micromodel with the higher concentration but not in an uniform manner. Deposit is clearly more important in some channels. The comparison between the two experiments with the higher concentration show some common features (same channels with deposit in both experiments but also some differences in the channel occupation by the particle deposit).

The fact that there are numerous “plugging deposits” with the higher concentration should contribute to the slower drying kinetics (Fig. V.12) with the higher concentration in addition to the impact of the micromodel entrance region deposit (Fig. V.13) discussed in section V.4.1.

7 Impact of the plasma treatment

In this section, we report on an experiment performed right after the plasma treatment for the conditions $B = 0$, $P = P_{atm}$, $T = 22^\circ\text{C}$ and the low concentration in particles. This experiment is compared to the experiment performed under the same conditions and the same micromodel except for the fact that the experiment is performed about one month later after the plasma treatment. Note also that the micromodel is cleaned with ethanol

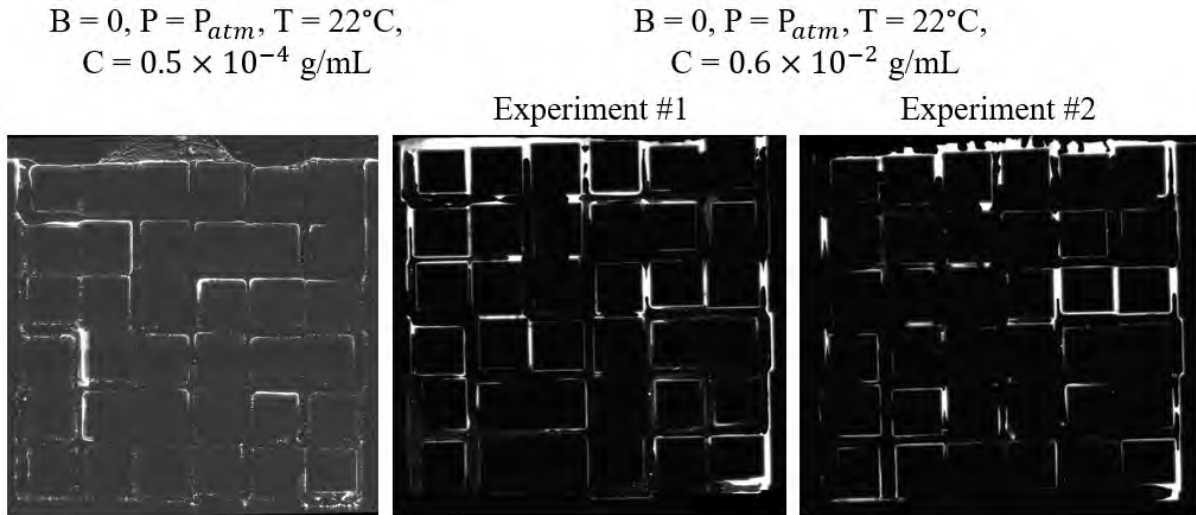


Figure V.20: Final particle deposit (in bright light whitish/grey) in the micromodel for the conditions $B=0, P = P_{atm}, T = 22^\circ\text{C}$ and the low and higher initial particle concentration.

and brushed (to remove particles) between both experiments. As discussed in section V.2.2, the contact angle on the SUEX is much lower right after the plasma treatment than hours or days later (Fig. V.1). This change in the wettability has some impact on the patterns as depicted in Fig. V.21. For instance, one can notice for $S = 0.5$ that some channels are still with liquid in the upper region of micromodel when the experiment is performed right after the plasma treatment whereas these channels have been invaded when the experiment is performed one month after the plasma treatment. However, in spite of some differences, the pattern evolution is somewhat similar in both experiments. For convenience, the experiment performed right after the plasma treatment is referred to as the “right after plasma treatment experiment” and the corresponding results labeled “right after” in the figures whereas the results of the baseline experiment, i.e. performed about one month after the plasma treatment, are labeled “one month after”.

As shown in Fig. V.22, a more marked difference lies in the drying kinetics, which is significantly faster in the “right after” experiment. The impact of contact angle on the drying kinetics in a hydrophilic network (i.e. characterized by IP patterns and not by compact pattern as in a hydrophobic network [Chapuis et Prat, 2007, Chraïbi *et al.*, 2009]) is attributed to the impact of contact angle on the corner liquid films [Prat, 2007]. The lower the contact angle, the thicker are the corner liquid films (illustrated in Fig. V.23, see also Chapter II) and the greater is the hydraulic conductivity of the corner liquid film sub-network.

This impact of the wettability on the corner liquid film network is consistent with the final particle deposit shown in Fig. V.24. Particles accumulate in the top region of the micromodel in the “right after” experiment. In this case, the corner liquid film subnetwork

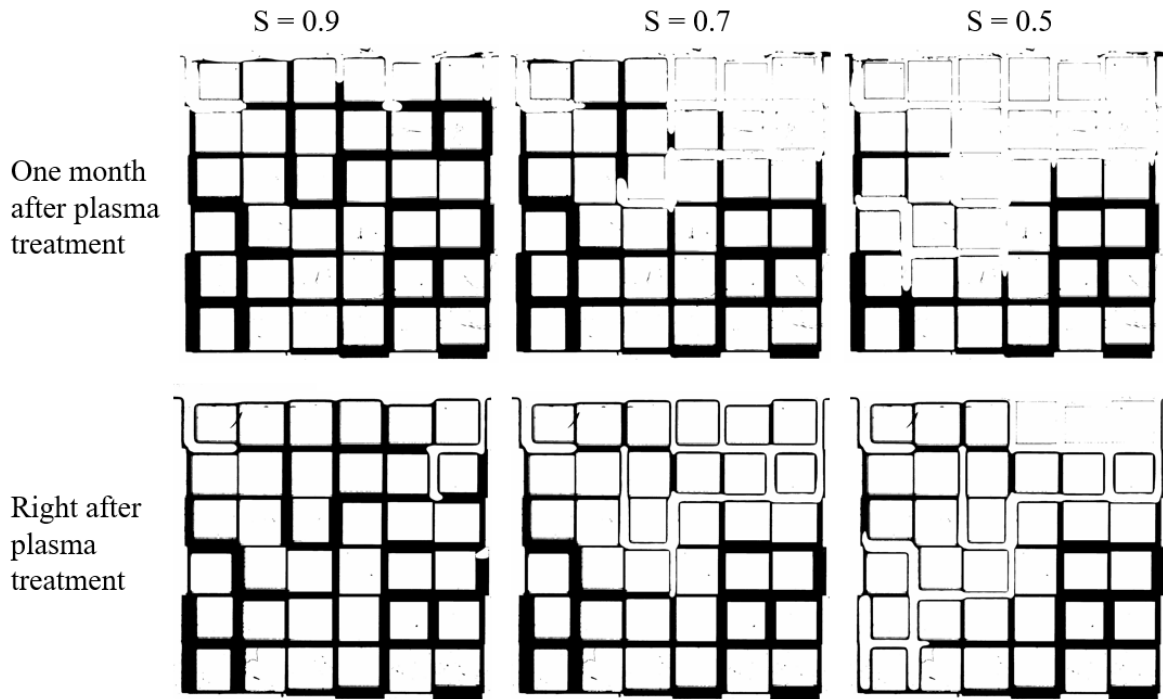


Figure V.21: Comparison of the drying patterns for $S = 0.9, 0.7$ and 0.5 (from left to right) for $B = 0, P = P_{atm}, T = 22^\circ\text{C}$ with low concentration in particles for the “right after” and “one month after” experiments. Liquid phase in black and gas phase in white, vapor escapes through top edge of micromodel.

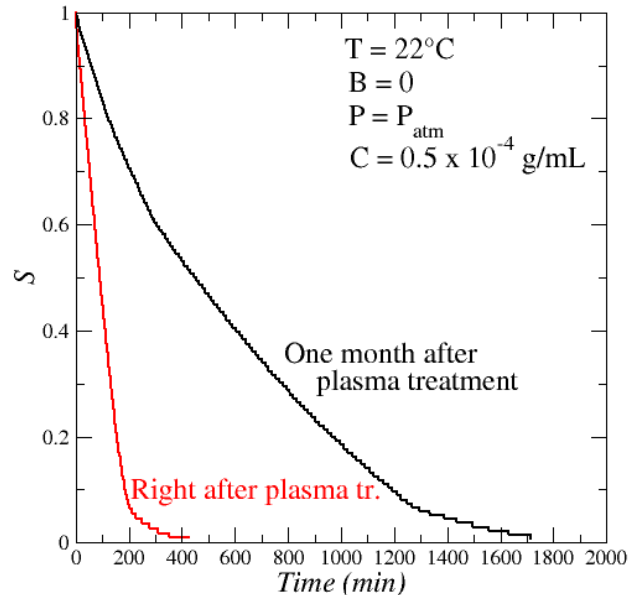


Figure V.22: Comparison of drying kinetics for the “right after” and “one month after” experiments. for the low concentration in particles in the absence of gravity forces for $P = P_{atm}, T = 22^\circ\text{C}$

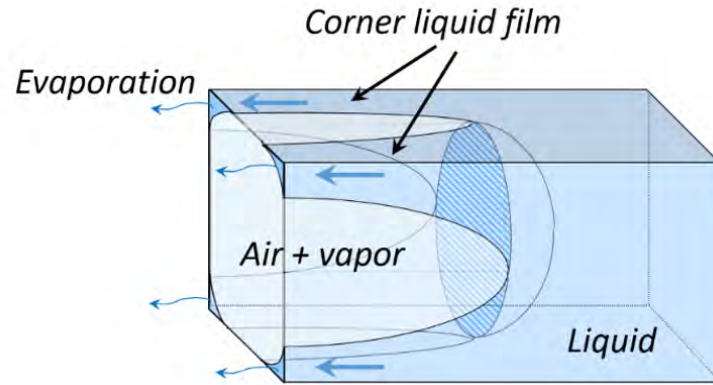


Figure V.23: Illustration of corner liquid films in a channel of square cross-section (from Chapter 1 in [Prat, 2023])

remains much longer connected and attached to the micromodel entrance region. Particles are transported in the liquid films (as in the single channel experiment of Chapter II) up to the top of micromodel. In the case of the “one month after” experiment, the contact angle is significantly greater and the corner liquid films, although still present, are not expected to form a well-connected hydraulic subnetwork. As the result, the final particle deposit is much more spread over the network.

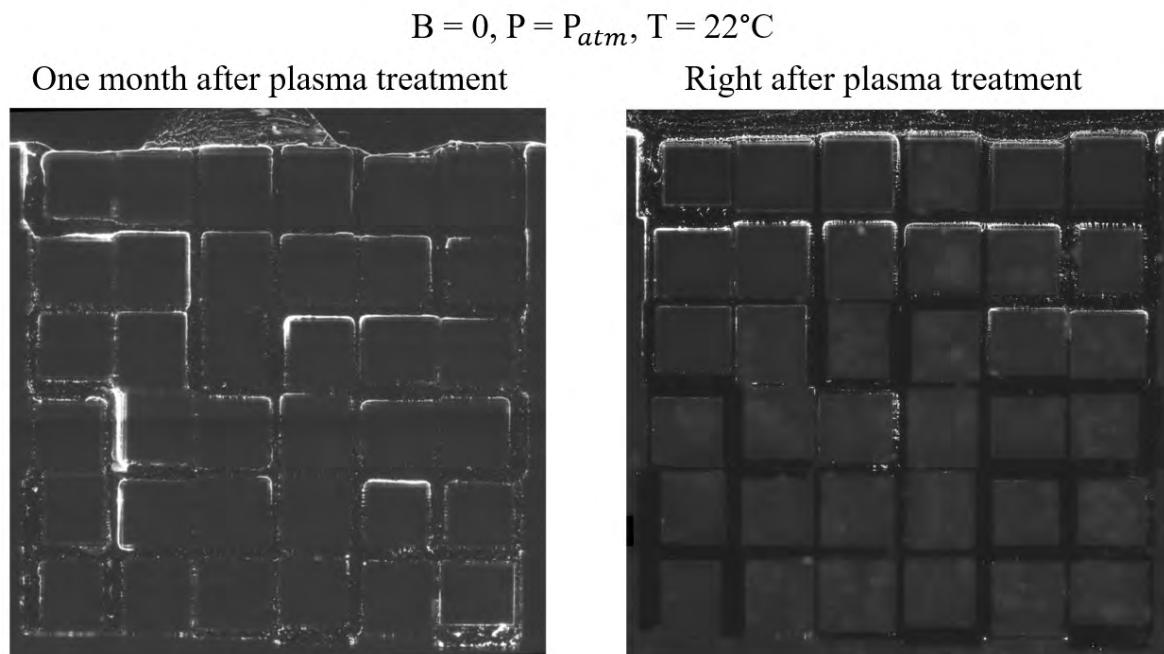


Figure V.24: Final particle deposit (in bright light whitish/grey) in the micromodel for the conditions $B = 0, P = P_{atm}, T = 22^\circ\text{C}$ and the low initial particle concentration for the “right after” and “one month after” experiments.

In other words, the comparisons presented in this section illustrates the impact of

liquid films on the distribution of particles during drying in the relatively low concentration limit considered.

8 Attempt of final deposit statistical analysis

To go further than the qualitative considerations based on the images of the final deposit, an attempt of statistical analysis is presented in this section. For instance, since the larger channels are preferentially invaded during the drying process and therefore the finer channels are presumably the last to empty, one can wonder whether there exists a clear correlation between the localization of the particle deposit in the channel network and the channel sizes, keeping, however, in mind that some fine channels can be invaded before larger channels due to some larger channel delayed access in the IP (invasion percolation) invasion process.

8.1 Statistical analysis by channels (procedure)

To perform the statistical analysis, 78 regions of interest (ROI) are defined as illustrated in Fig. V.25. These ROI correspond to the channels in the micromodel. Since the images can have various sizes, each channel region is defined for each experiment. As illustrated in Fig. V.25, the ROI are rectangles having the width of the channel and they are as long as possible while avoiding overlapping. Moreover, attention is paid to well define the limits of the channels and the regions affected by the particle reflection effect on the walls of the material.

Once the 78 regions are defined the 16bit images of the deposit are treated as follow:

1. Brightness and contrast are modified by setting an interval defined by the minimum level of grey and the maximum [230 – 900].
2. A first measurement of the mean value of grey for every channel is done.
3. A threshold for the binarization of the image is defined. In the final result the background is white while the deposit of particles is represented by black pixels as illustrated in Fig. V.26.
4. . At this point, the percentage of the area (surface fraction) corresponding to the deposit within each ROI area, i.e. each channel, can be determined. Therefore, the higher the area percentage, the higher is the number of particles in the channel.

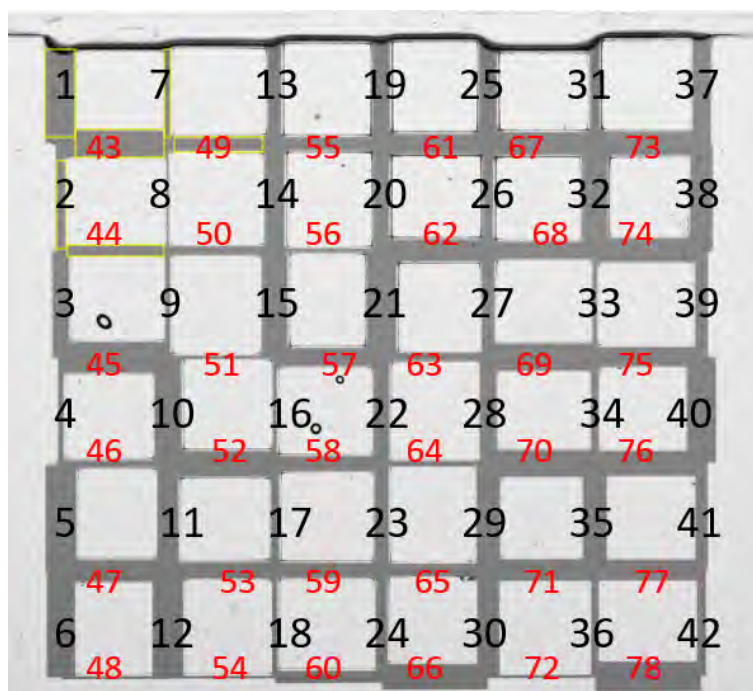


Figure V.25: Enumeration of the channels, in black the horizontal ones and in red the vertical ones. Examples of ROIs in yellow.

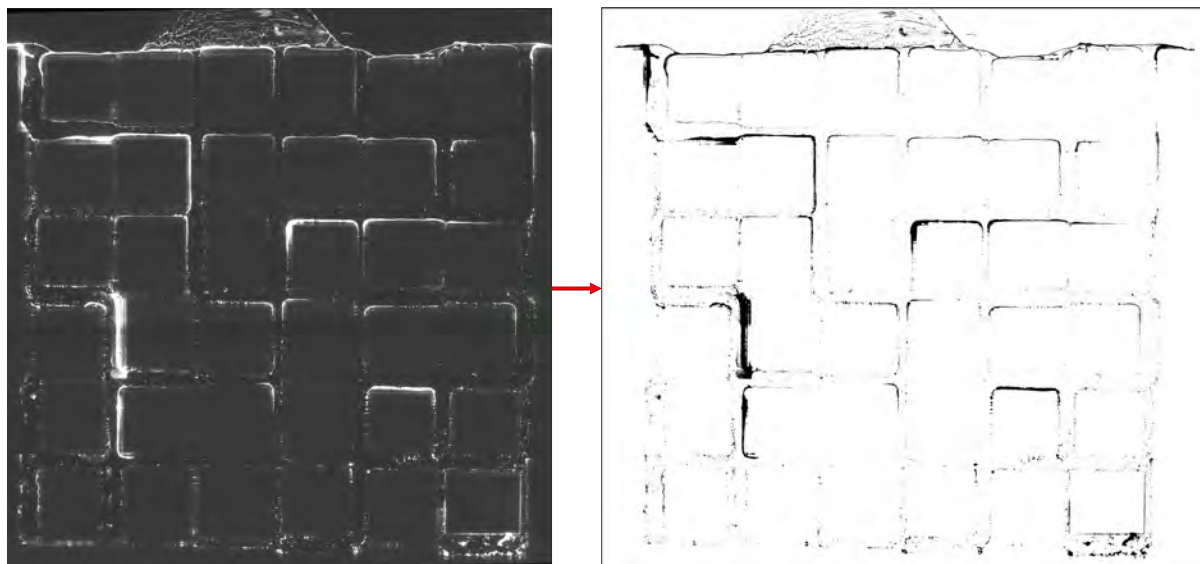


Figure V.26: On the left the final image of the deposit for the experiment with the horizontal chip at atmospheric pressure and with particle concentration 0.5×10^{-4} . On the right, the result after the binarization process, where the black pixels represent the deposited particles.

Since the qualitative discussion of the deposit suggests to distinguished sometimes the micromodel upper region from the lower region, the choice is made of dividing the micromodel in horizontal slices as illustrated in Fig. V.27. The top slice in darker blue is adjacent to the micromodel open edge, while the bottom slice in the micromodel is in lighter blue.

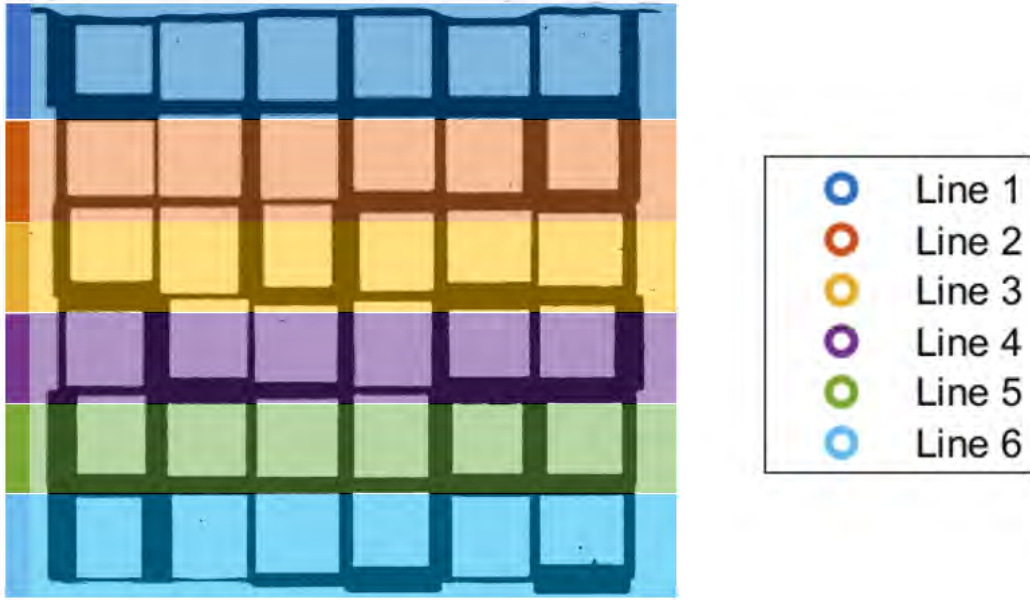


Figure V.27: Division of the micromodel in horizontal slices.

The slice color codes indicated in Fig. V.27 is used to explore the possible correlation between the channel size and the deposit localization, i.e. the mean brightness (mean level of greys) of the pixels in the channels as well as the surface fraction occupied by the deposit in each channel (area percentage).

8.2 Correlation between mean brightness and area percentage

The deposit for the case $B = 0$, $P = P_{atm}$, $T = 22^\circ\text{C}$ and the low concentration in particle is considered (Fig. V.26). The results of the statistical analysis are presented in Fig. V.28. As can be seen from Fig. V.28d, the two indicators, i.e. the mean brightness and the deposit surface fraction (area percentage), are strongly correlated. Therefore, they essentially provide the same information. As a result, the plot of the two indicators as a function of channel size in Fig. V.28 (Fig. V.28a and Fig. V.28b) are quite similar for this case. The quantity plotted in Fig. V.28c is computed as

$$\left| \frac{Mean_{brightness} - Min(Mean_{brightness})}{Max(Mean_{brightness}) - Min(Mean_{brightness})} - \frac{Area\% - Min(Area\%)}{Max(Area\%) - Min(Area\%)} \right| \quad (8.1)$$

This quantity is computed for each ROI (channel). This is an additional characterization of the equivalence between both indicators. This quantity should be zero when both indicators are strictly equivalent.

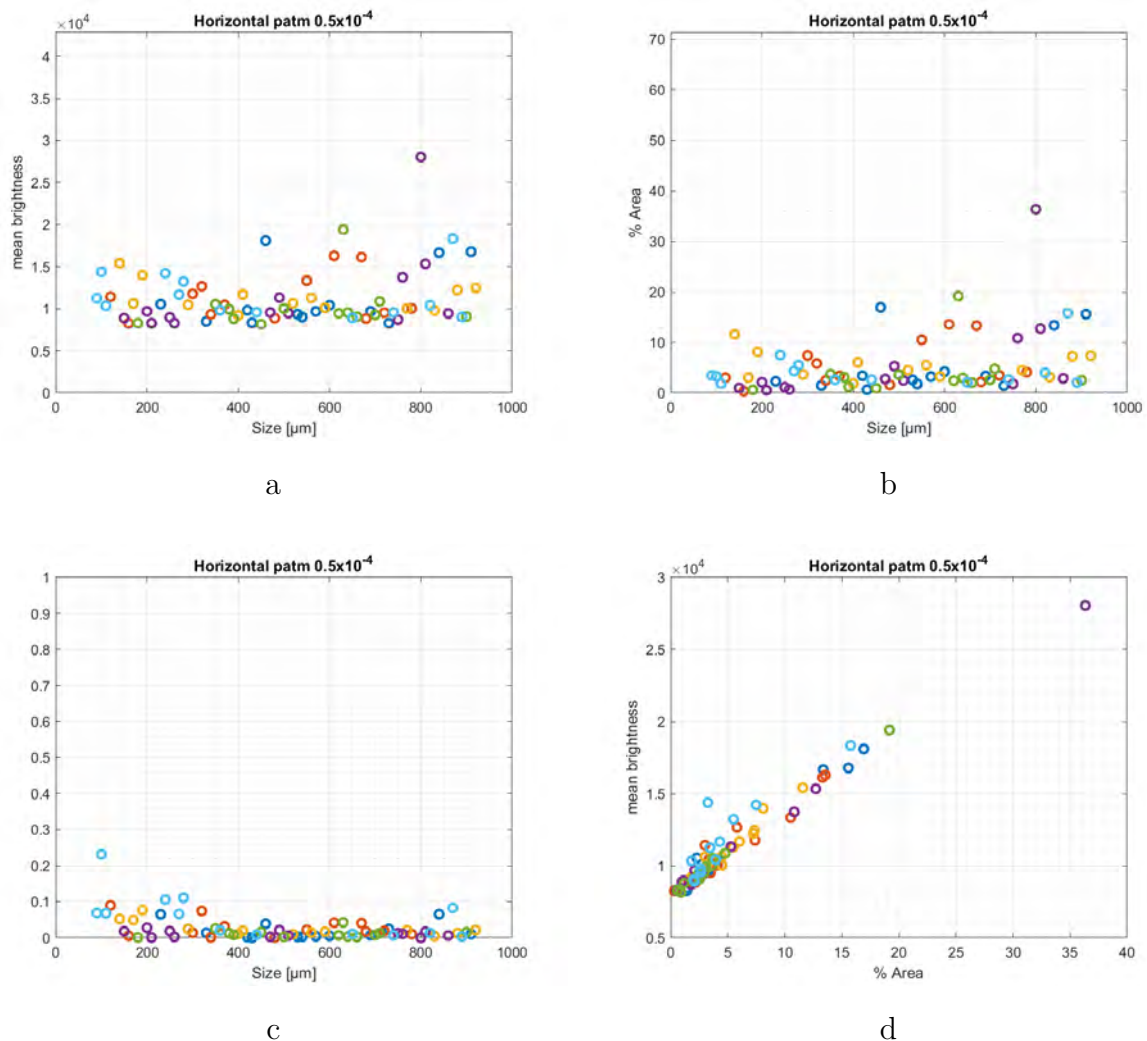


Figure V.28: Experiment for $B = 0$, $P = P_{atm}$, $T = 22^\circ\text{C}$, $C = 0.5 \times 10^{-4}$ g/mL: a. correlation between the sizes of the channels and their mean levels of grey, b. correlation between the sizes of the channels and the percentage area, c. difference in absolute value between the norms of the mean grey values and the area percentages, d. correlation between the area percentage and the brightness.

However, such a strong correlation between the two indicators (channel brightness and channel black pixel surface fraction) is not always obtained. As illustrated in Fig. V.29d and V.29c, an exception is the experiment for the drying condition $B > 0$, $P = P_{atm}$, $T = 22^\circ\text{C}$, $C = 0.5 \times 10^{-4}$ g/mL. This might be due to the fact that this is the longest experiment. The fluorescent particles tend to lose intensity over long exposure to white light. This might cause the loss of linearity shown in Fig. V.29d. For this case, the absolute difference between the norm of the two indicator values is significant (Fig.

V.29c),

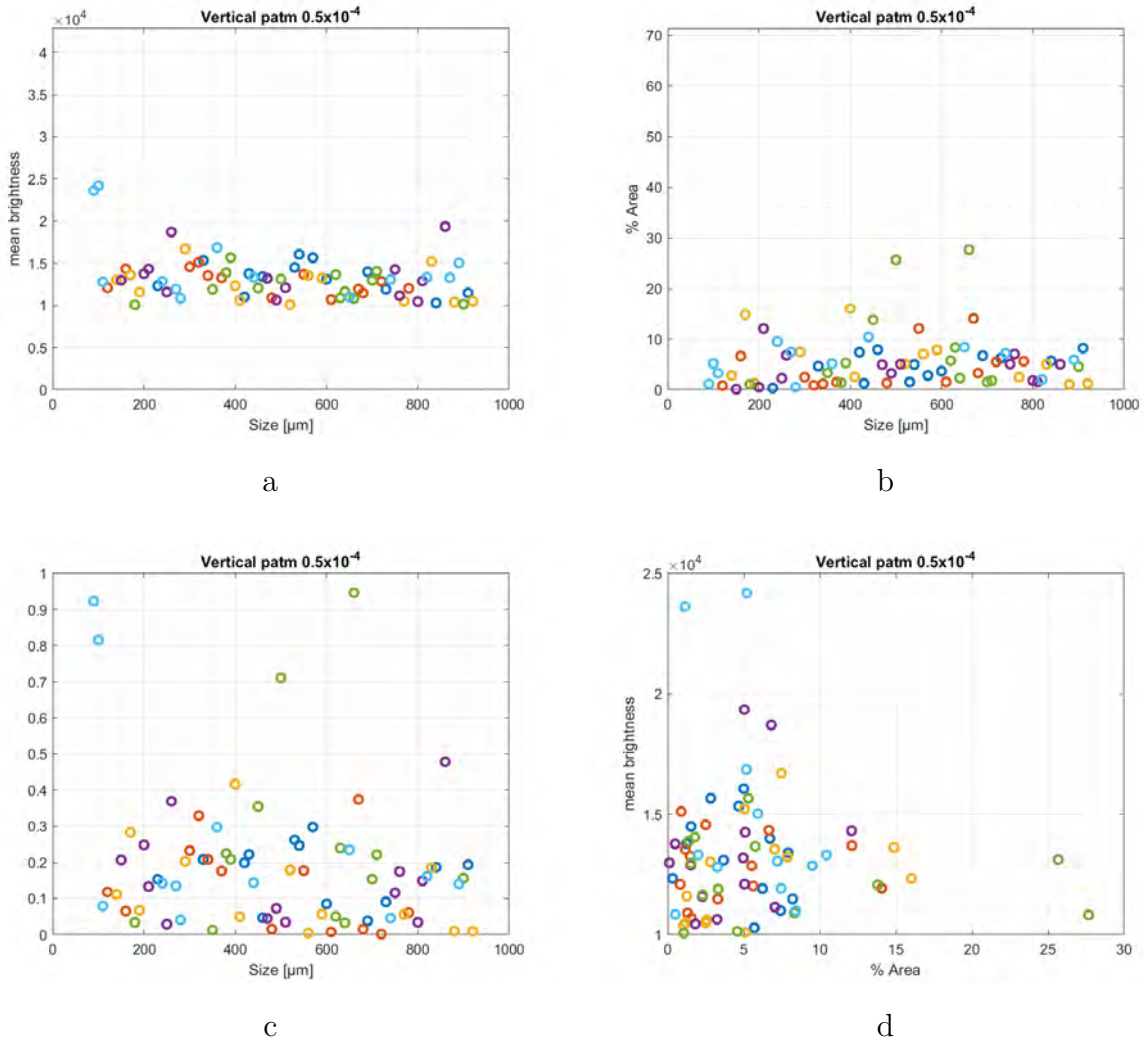


Figure V.29: Experiment for $B > 0$, $P = P_{atm}$, $T = 22^\circ\text{C}$, $C = 0.5 \times 10^{-4}$ g/mL, a. correlation between the sizes of the channels and their mean levels of grey b. correlation between the sizes of the channels and their area percentage, c. difference in absolute value between the norms of the mean grey values and the area percentage, d. correlation between the area percentage and the brightness

8.3 Comparison of the deposits

The mean brightness indicator is plotted as a function of the channel size in Fig. V.30 for the various drying conditions and the low particle initial concentration. It can be noted that the "zero brightness", which is the mean of the grey values in the channels without particle deposit varies from one experiment to the other. This is due to the fact that, even if care was taken, a surrounding light could be turned on or off depending on the experiment. Also, intensity may slightly diminish as a result of the exposure duration to

white light. A first result is that there is no obvious correlation between the brightness indicator and the channel size. Thus, the somewhat naive idea that the finer the channel the more likely is a deposit is not supported by the results shown in Fig. V.30.

The case corresponding to Fig. V.30c is perhaps somewhat different (with a more spread cloud over the vertical). It corresponds to a case with expanding bubbles leading to the expelling of the liquid out of the micromodel and stronger deposit in the top row of channel (Fig. V.17). However, the case corresponding Fig. V.30e is also a case with expanding bubbles, but the points are much less spread vertically. Overall, it might be considered from Fig. V.30 that the particles tend to accumulate more homogeneously throughout the micromodel when it is in a horizontal position whereas particles tend to accumulate more in the upper region at the micromodel when the micromodel is in the horizontal position.

8.4 Evaporation time statistics

The considerations in section V.8.1 do not take into account the fact that a fine channel located in the top region of the micromodel is more likely to be invaded before a channel of the same size located deeper in the network or even before larger channels located deeper in the network. This can be confirmed by the determination of the individual channel “evaporation” starting times. For a given channel, this time is the time when the gas phase starts to invade the considered channel for the first time. It can be noted that this invasion is not necessarily due to a local evaporation due to the capillary pumping effect (see Chapter III). The term “evaporation” starting time is thus a bit misleading (“individual channel invasion starting time” would be more correct). How this time is determined for each channel is explained in Appendix B.

The obtained results are presented in Fig. V.31. This figure first illustrates the fact that the channel in the top row (darker blue symbols) are invaded first and that the channels the last to be invaded are located in the bottom row (lighter blue symbols). The figure confirms that the consideration of the invasion percolation rule stating that the larger channels are preferentially invaded is not sufficient to infer a correlation between deposit localization and channel size since channels of a given size can be invaded at quite different times depending on their localization in the network. In other words, the channel historicity varies from one channel to the other for a given channel size. Nevertheless, it can be seen from Fig. V.31 that the IP rule is confirmed on average since the larger channel evaporation starting times are mostly in the left part of the figure (shorter evaporation starting times) whereas the finer channel evaporation starting times are mostly in the right part of the figure, which correspond to the longer evaporation starting times. This is also illustrated by the quasi-linear variation for the higher starting times.

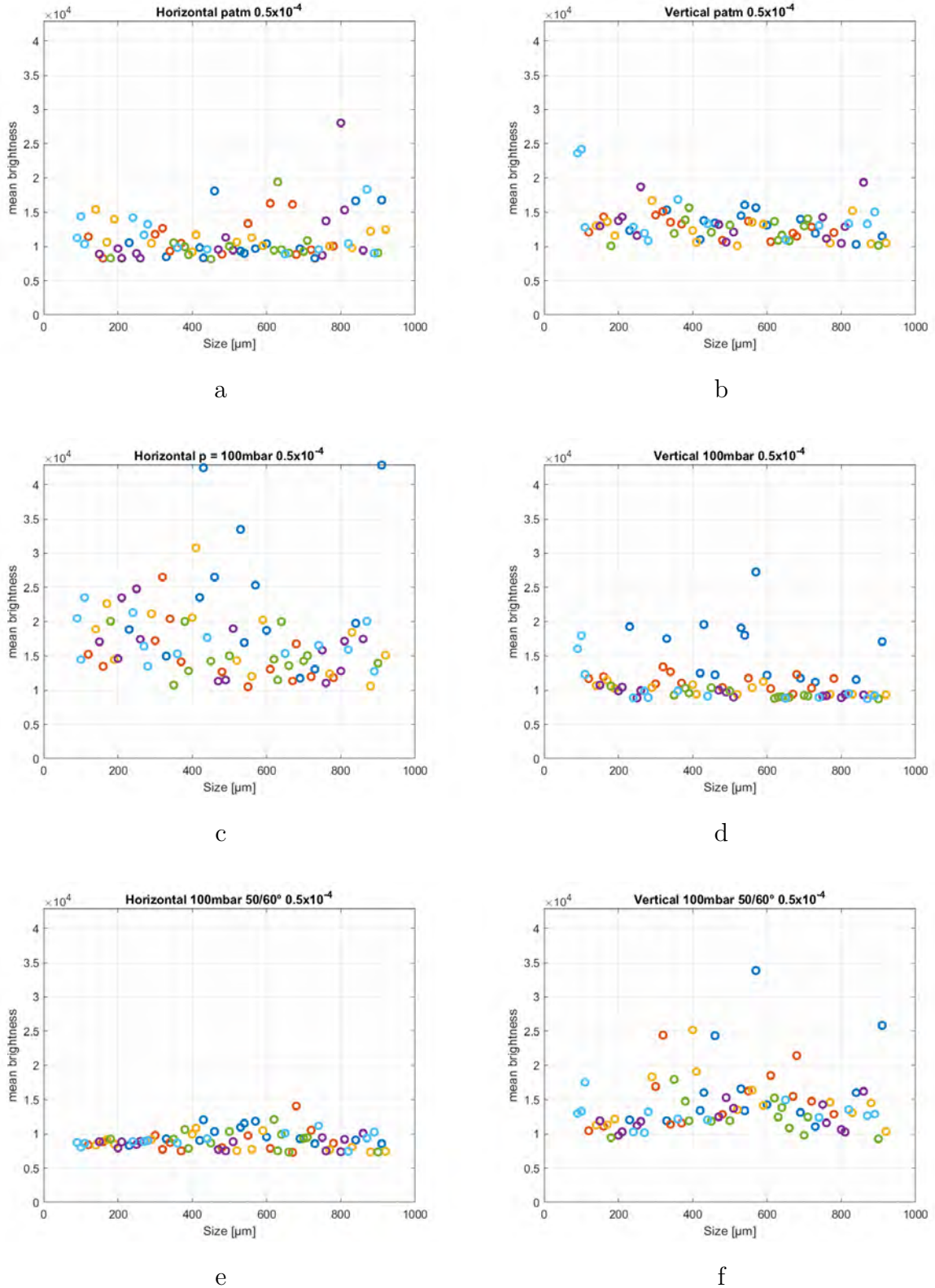


Figure V.30: Correlations between the channel size and the deposit mean level of grey for the different experiments and the low concentration in particles. The cases between the horizontal and vertical micromodel position are compared for the same pressure and temperature conditions on each horizontal row. The columns are for the same micromodel position (horizontal or vertical) but different temperatures (a. 20°, c. 20°, e. 50/60°) or pressures (b. P_{atm} , d. P_{atm} f. $P = 100mbar$.)

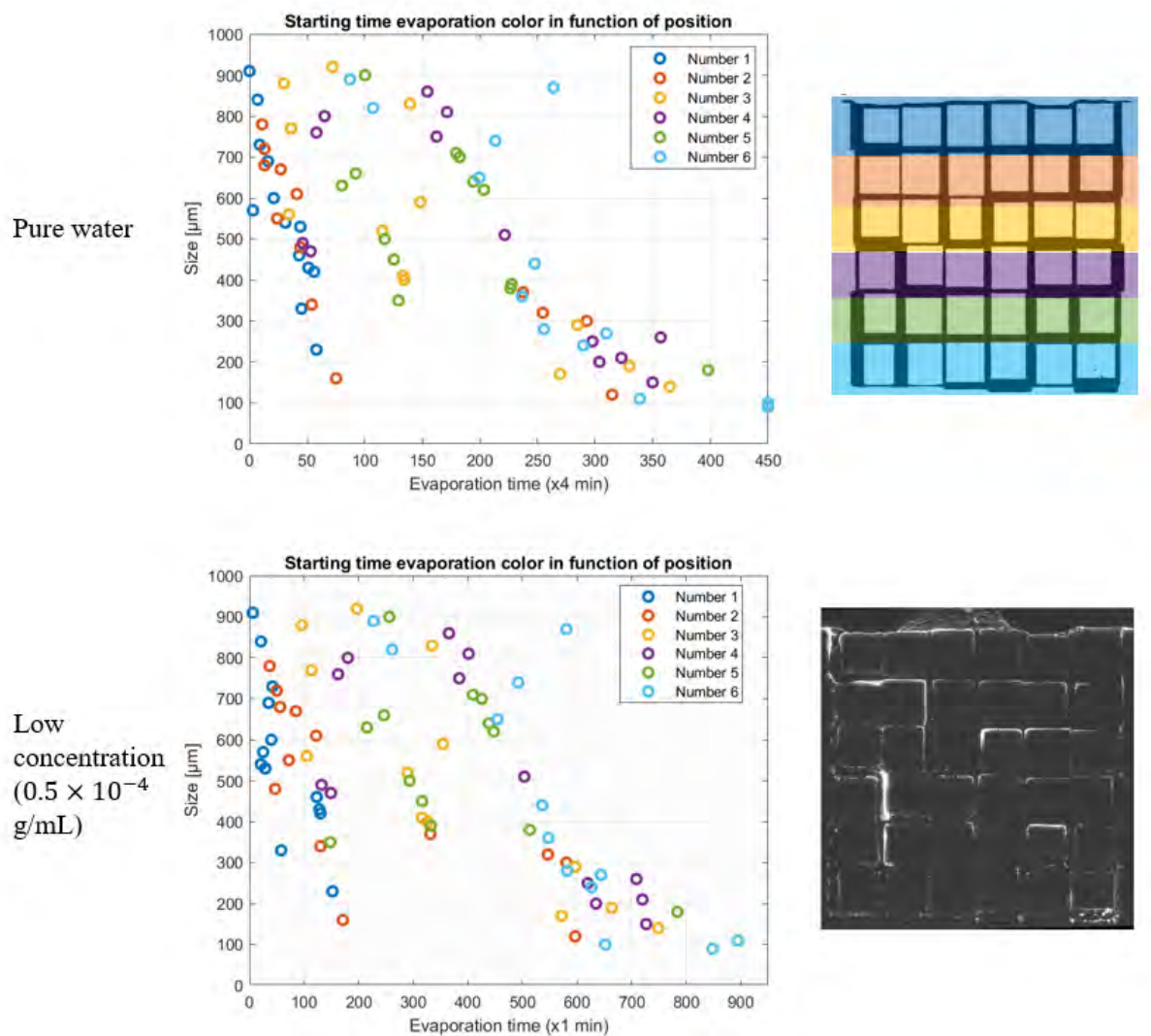


Figure V.31: Individual channel “evaporation” starting times as function of channel size and localization in the network (color code) for the conditions ($B = 0$, $P = P_{atm}$, $T = 22^\circ\text{C}$, 1 month after plasma treatment). The final deposit (bright zones) is shown in the image on the right.

It can be also noted that the particles for the considered low concentration have a quite marginal impact on the evaporation starting time distribution, which is consistent with the low impact on the drying pattern discussed in Section V.3.

Together with the final image of the deposit, these results do not indicate a simple correlation between the localization of the deposits in the network and the channel “evaporation” starting times.

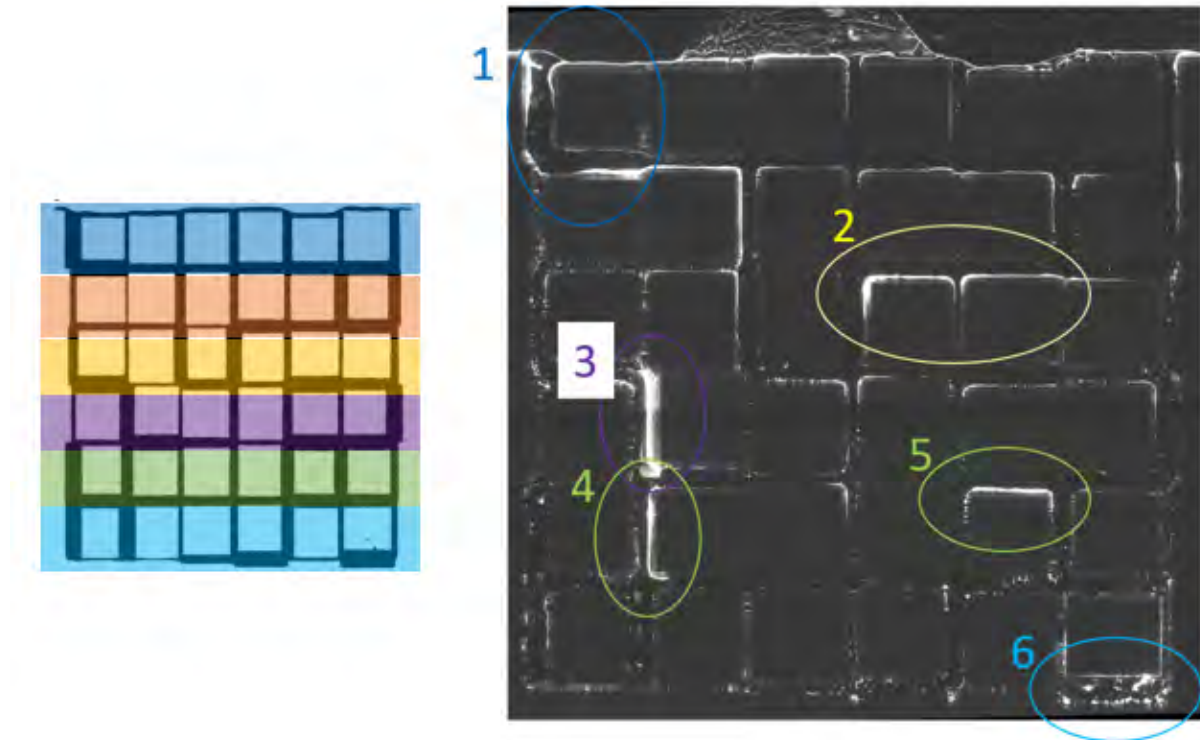


Figure V.32: Deposit channel invasion sequence for the conditions ($B = 0$, $P = P_{atm}$, $T = 22^\circ\text{C}$, 1 month after plasma treatment). The final deposit corresponds to the bright zones.

This is further illustrated in Fig. V.32. As indicated in Fig. V.32., deposit can form early in the drying process (zone #1 in Fig. V.32.) or at the end (zone #6 in in Fig. V.32.) as well at intermediate times (zones #2,3, 4, 5).

8.5 Conclusion on the "statistical" analysis

Unfortunately, the conclusion is therefore that the presented statistical analysis does not allow to go really further in the analysis of the deposit compared to the discussion based on the visual inspection of the final deposit images presented previously in the chapter. Why the deposit is noticeable in some channels in Fig. V.32 and quite negligible in others remains unexplained. This can be in part related to the impact of the corner liquid films, which play a noticeable role in the localization of the deposit as also discussed previously. The results presented in this section could be seen as an illustration that there

is no particular correlation between the localization / distribution of the corner films and the channel sizes. This, however, remains speculative. Applying the proposed statistical analysis technique to the case of the higher concentration in particles could have been a better idea since “plugging deposits” (Fig. V.19) are present in this case but quite rare for the low concentration in particles. Because of lack of time, this could not be performed.

8.6 Conclusions

In this chapter, drying experiments with a micromodel in the presence of particles were reported. Impact of particle initial concentration, ambient pressure (atmospheric pressure vs partial vacuum condition), temperature (22°C vs 50-60°C) and micromodel position (horizontal vs vertical) was explored. Overall, the obtained results are not sufficient to understand the results reported in [Ito *et al.*, 2014] showing a quite different particle distribution at the end of drying between drying at the room ambient conditions and the vacuum conditions. In this respect, it is recalled that the vacuum level in Ito *et al.* [Ito *et al.*, 2014] experiment was much higher than that considered in our experiment as well as the temperature level (100°C). In this respect, it could be interesting to consider conditions closer to the ones considered in [Ito *et al.*, 2014] in a future work.

Nevertheless, several results have been obtained. The comparison with pure water experiments shows that the drying patterns are weakly impacted by the presence of the particles in the considered experiments. This also holds for the drying kinetics except in the case of the higher concentration for which the kinetics is significantly slower, presumably mainly because of the particle deposit on top of the micromodel.

The consideration of the Péclet number is not sufficient to infer the localization of the deposit in the micromodel. The Péclet number is quite high ($O(10^4)$ at least) in the presented experiments but the particles can be distributed within the channel network at the end of drying and not only at the network very top.

The expanding bubble formation during the drying process has a strong impact not only on the drying kinetics but also on the final particle distribution. Particles are expelled from the micromodel with the liquid displaced by the bubble expansion. This has to be kept in mind when the conditions are such that the phenomenon of bubble expansion is likely, i.e. [Vincent *et al.*, 2014]. As shown by the experiments after fresh or aged plasma treatment (that is with different wettability properties), secondary capillary structures (corner liquid wedges in our case) can have a strong impact on the final deposit distribution due to the particle transport in these structures. Even when the corner liquid film subnetwork is a priori not well hydraulically connected, the corner liquid films are a privileged place for deposit, at least in the particle low concentration limit. In this respect, it would be interesting to study the evolution of these corner films during drying in relation with

the particle transport in the films. This could help understand why corner deposits are noticeable in some channels and negligible in others.

The consideration of a significantly higher concentration led to distinguish another type of channel particle deposit in addition to corner deposits observed for the low concentration: the plugging deposit. However, only one drying condition ($B = 0$, $P = P_{atm}$, $T = 22^\circ\text{C}$) was explored. It would therefore be interesting to explore the impact of the higher concentration in particles for the other drying conditions as well.

An attempt of a more detailed analysis based on the numbering of each channel was performed. However, this analysis could not explain why the deposit is heterogeneous, i.e. why deposit is noticeable in some channels and negligible in other channels. This analysis indicates that the heterogeneous nature of the deposit cannot simply be inferred from the invasion percolation rules at the core of the drying process and that deposit can form in channels invaded at quite various times during drying. As mentioned before, this situation might be due to the impact of corner films and their evolution during drying.

Conclusion and future work

This work aimed at clarifying the interplay between water evaporation and particle distribution in model porous media, from a single channel to a network of interconnected channels. To this end an experimental set up has been developed to follow the fluorescent particles in the single channel via a confocal green light microscope (Chapter II). Three different low concentrations were studied, namely 10^{-5} , 0.5×10^{-4} and 10^{-4} g/mL. The main observation is the impact of the particles on the thickness of the corner films in the channel. The corner films are thinner compared to the case of pure water, leading to a reduction of the evaporation rate. However, the thinning of the corner films is not observed for the higher concentration of particles of 0.6×10^{-2} g/mL. On the contrary, the films are even thicker than the films for pure water in the entrance region of the channel. The slower evaporation dynamics in this is attributed to the formation of a compact packing of particles inducing a slight retreat of the evaporation front. For both cases, the pinning of the triple lines due to the particle accumulation is a key mechanism. Furthermore, the transport of particles toward the pinned triple lines film leads to a preferential particle deposit in the vicinity of the triple lines, especially in the vicinity of corner film triple lines where evaporation is greater (entrance region of the channel). It has been also observed that the final deposit is highly concentrated in the areas that are last to dry out. These correspond to the corner films.

Similar outcomes are obtained in the experiments with the double channel configuration for the SUEX-PDMS system (Chapter III): the preferential areas of accumulation of the particles are the corner films forming at the beginning of the drying process in the larger channel, as well as the entrance region of the smaller channel where the triple line is pinned. The evaporation dynamics in this case follows the expected dynamics controlled by the greater invasion capillary pressure threshold in the smaller channel compared to that for the larger channel: the air invades first the larger pores as the result of evaporation from both channels. However, this expected dynamics is not observed in the case of an experiment with a Plexiglas-PDMS double channels performed with a higher concentration in particles. The dynamic is inverted, meaning that the main meniscus recedes in the

smaller channel and not in the larger one. Moreover, the deposit is more homogeneous than in the SUEX-PDMS system. This experiment, with the inverted dynamics, thus shows a spectacular impact of the presence of the particles. Since this experiment was only a single preliminary experiment performed to test various experimental systems, it would be interesting to perform more experiments with this system so as to understand the exact mechanism leading to the inverted dynamics.

The upscaling from a micro channel to a pore network was explored with a different experimental set up, using a camera instead of the microscope (Chapter IV). Drying experiments were carried out with pure water and the impact of gravity, by placing the micromodel in a vertical position, and of vacuum conditions $P = 0.1P_{atm}$ was studied. In the latter situation, it is shown that drying is faster. This is explained by the impact of the total pressure on the water vapor molecular diffusion. The latter is inversely proportional to the total gas pressure. The gravity effect induces a slower kinetics, in line with the literature, showing the formation of a dry upper region as the result of gravity effects. However, this impact of gravity on the drying pattern was not very marked in our experiments because of the small size of the pore network. Interestingly, expanding gas bubbles form during drying in the case of some experiments performed under the partial vacuum conditions. This phenomenon can accelerate the drying due to the ejection of the liquid water in direction of the micromodel top surface (or even outside the micromodel) as the result of the bubble growth. Unfortunately, the explanation of this phenomenon is unclear and remains to be elucidated.

The next step in Chapter V was to investigate the effect of particles for the same conditions: with a horizontal or vertical micromodel and at atmospheric pressure or under partial vacuum condition at ambient temperature. In addition, experiments were also performed at $P = 0.1P_{atm}$ at $T = 50-60^{\circ}\text{C}$. The impact of particles on the drying kinetics and on the saturation patterns is not very significant for the low concentration in particle of 0.5×10^{-4} g/mL. By contrast, the drying kinetics is considerably slower with a higher concentration in particles of 0.6×10^{-2} g/mL although only one condition is explored, namely $B = 0$, $P = P_{atm}$ at $T = 22^{\circ}\text{C}$. As with the single channel, the preferential zones of accumulation of particles in the micromodel are the corner liquid films when the concentration in particles is low, whereas plugging deposit over the cross-section of some channels can be observed with the higher concentration. As in the case of drying with pure water, the bubble formation during drying has a quite significant impact in the presence of particles. The formation and expansion of bubbles within the micromodel can expel the liquid out of the micromodel. This completely modifies the final deposit

since particles are transported in the expelled dispersion. The influence of wettability was examined at the atmospheric pressure and ambient temperature. The micromodel underwent a plasma treatment that decreased the contact angle from 70° to 30° . The lower contact angle improves the interconnectivity and the size of the corner films. As the result, the drying kinetics is faster. The corner films remain connected to the network outlet for a longer time compared to the case of an aged plasma treatment. This greatly affects the final particle deposit with a higher concentration in the micromodel top rows.

In summary, the experiments presented in this thesis have shed light on the evaporation process in porous media in the presence of colloidal particles. Several interesting observations on the impact of the particles on the evaporation process in model systems were reported, especially as regards the impact of particles on the development of corner films, the impact of gas bubble formations, the faster drying under partial vacuum conditions as well as the impact of the wettability properties on the corner films and the locus of the final particle deposit. However, the initial objective, which was to explain some observations in the literature indicating that a much more homogeneous final distribution of particles within a thin porous medium is obtained under vacuum conditions and not under standard convective drying conditions, is not met. A first reason is perhaps that only quasi-two-dimensional channel networks were considered in the present work. It is well known that drying in a quasi-2D network of interconnected channels is different from drying in a 3D porous medium due to different percolation properties of the liquid phase (the liquid phase forms a percolating phase much longer in 3D than in 2D). In this respect, it would be desirable to perform experiments in 3D systems, which of course makes the direct observations of the particle migration and deposit much more difficult than in the systems considered in the present work. Also, the vacuum condition and the temperature level considered in our experiments were significant less than in the experiment evoked above (these experiments are discussed in section I.5.2 in chapter I). As the result, it was not possible to observe the expected change from a capillary fingering pattern (standard drying conditions) to a compact pattern with almost flat traveling evaporation fronts (vacuum conditions). In this respect, it would be interesting to improve the experimental set-up in, at least, three directions. The first one would be to be able to perform the experiments under more important vacuum conditions (1 mbar) and for higher temperature ($\sim 100^\circ\text{C}$). The second one would be to use micromodels with smaller channels ($\sim 50\ \mu\text{m}$ for instance) so as to enhance the impact of viscous effects on the drying pattern. The third one, perhaps less important, would be to use system of homogeneous wettability and to avoid PDMS due to the parasitic pervaporation properties of PDMS. Also, the consideration of smaller channels might be interesting to

study in much more depth the migration of the particles from PIV techniques (which is possible with the florescent particles). This was not possible with the 1mm deep channel due to focus problem over the full depth of channel. This could help understand the mechanisms leading to the pinning of the triple lines due to the particles.

Appendix A

SUEX fabrication protocol

SUEX® TDFS are photo imageable epoxy sheets for plating, wafer level packaging and MEMS applications. The sheets consist of a catatonically cured modified epoxy photoresist between two throw-away layers of protective polyester film (PET). The epoxy photoresist formulation contains an antimony-free photoacid generator and is prepared under a highly controlled solvent-less process, which provides uniform coatings. The solvent developed negative working photoresist is sensitive to UV radiation in the range of $350\sim 395nm$.

The process starts with the preparation of a glass substrate, it should be free of organic contamination and metal oxides prior to lamination, therefore it is cleaned with acetone, ethanol and let dry for 5 minutes in an oven at 80° . In the meantime two Suex sheets are prepared, one of $0.5mm$ thick and the the other $1mm$, which are cut at the same size.

The lamination temperature is set at 60° and as soon as the machine is ready, the clear PET is removed from the thinner sheet. The SUEX free surface is placed on the substrate and it goes through the rolling machine. The sample is let cool down at room temperature.

Prior to exposure the second PET is removed. The composite is then placed in the UV machine xxx for 100 seconds at a 100% power. This will be bottom of the pore network.

The $1mm$ layer is now placed above the exposed $0.5mm$ thick sheet. This sample goes through lamination once again and it is let cool down before the second exposure. The pore network mask is placed on the SUEX layer and, similarly to before, it undergoes 100 seconds of exposure at 100% of power.

At this moment, the substrate with the SUEX layers receives a post exposure bake

that lasts 2 hours at 80°. This step is followed by a long and slow cooling of about 12 hours.

The pore network is ready to be developed at room temperature using a bath of PGMEA (propylene glycol methyl ether acetate), face down with mild agitation for 2 hours.

To finish the process, the wafer is washed with isopropanol and compressed air before letting it dry at 80° for about 5 minutes.

Appendix B

Evaporation time treatment

The procedure to extract the initial time of evaporation for every channel is the explained in this annex for the case of pure water $B = 0$, $P = P_{atm}$ and $T = 22^\circ\text{C}$.

As explained in Chapter V, a region of interest defines each channel, and, after the binarization of the images, the black pixels within the ROIs represent the liquid while the white ones the gas phase. Therefore the count of black pixel for each channel and for every time step is registered.

This value, F , is normalized to the maximum and minimum values as follow

$$F_{normalized}(t) = \frac{F(t) - F_{min}(t)}{F_{max}(t) - F_{min}(t)} \quad \forall \text{ channel} \quad (0.1)$$

Thus, it was possible to draw the evaporation dynamics at the pore scale.

The curves have the shape of a hyperbolic tangent, then the *lsqcurvefit* Matlab function is used to fit the data in the least-squares sense. The starting functions have the following form:

$$F_{initial} = \tanh(-x + a) + 1 + \tanh(-x + b) + 1. \quad (0.2)$$

The imposition of disparate initial conditions, allowed us to compute more than one fitting function F_{fit} , dashed lines in Fig.B.1. The best one is selected through a least residual condition, in yellow in Fig. B.1. The reason that brought us to use more than one initial function was because, looking at the data for every channel, we noticed that the step from 1 to 0, i.e. the moment of evaporation of the channel, can be sooner or later, and, for example, an initial condition with $a = 50$, $b = 100$, will not be optimal for a channel with evaporation starting at the end, the dashed red line in Fig. B.1b

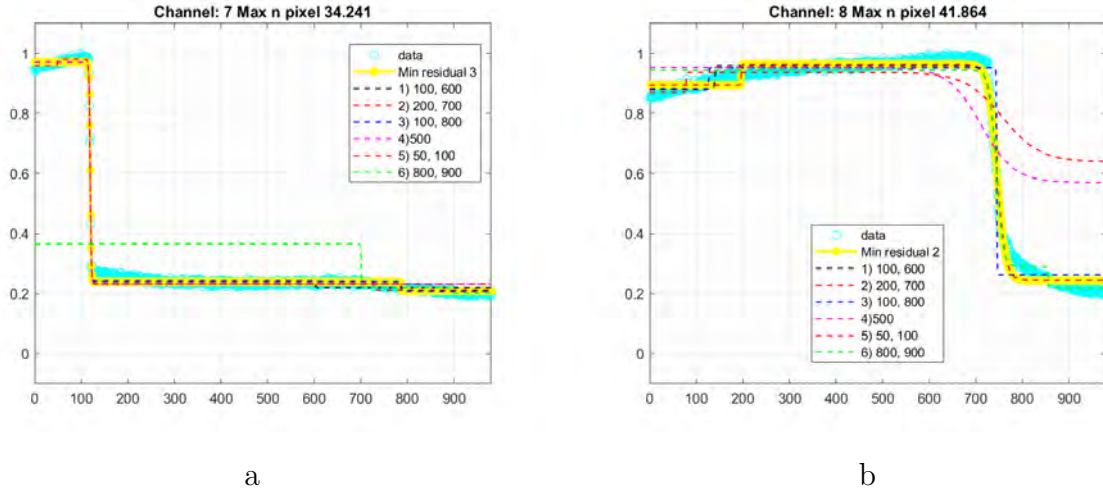


Figure B.1: In light blue the evolution of the liquid in two different channels, for the enumeration refer to Fig. V.25. The dashed lines are the different fitting function computed from different starting conditions while the yellow dots highlight the best fitting function. On the left the best fitting function is given by the starting conditions $a = 100$, $b = 800$, while on the right $a = 200$, $b = 700$.

Since all the channels have this hyperbolic tangent evolution of the liquid, meaning that, in this case, there is no refill of the channel nor bubbles growing in the middle, to obtain the moment of the beginning of the evaporation we used a gradient condition. After computing the derivative dF_{fit} , we imposed the condition to find $dF_{fit} < \epsilon$ and the first negative value would coincide to the starting evaporation point (t_{start}), the red dot in Fig. B.2, with $\epsilon = 10^{-3}$. This condition can also be used to find the first positive value higher than t_{start} , that corresponds to the end of drying in the channel (t_{end}), without considering the corner films. This value is not the most precise though since the drying can pause and restart.

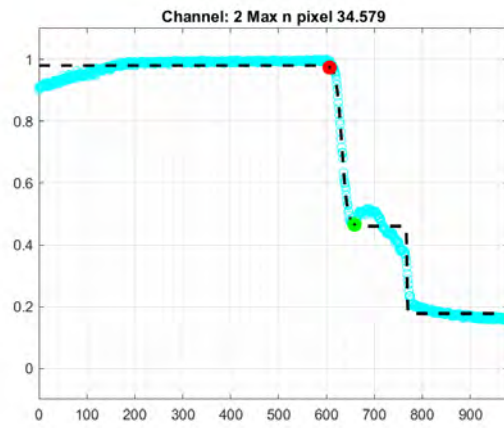


Figure B.2: The black dashed line is the best fitting function (yellow in Fig. B.1) and the red dot represent the computed starting point of the evaporation in this channel, through the gradient condition. The green point is the computed end time step of the evaporation, although you may notice that the drying is not properly finished, it may have stopped or liquid films are still present.

Bibliography

- [Abkarian *et al.*, 2004] ABKARIAN, M., NUNES, J. et STONE, H. A. (2004). Colloidal Crystallization and Banding in a Cylindrical Geometry. *J. Am. Chem. Soc.*, 126(19): 5978–5979.
- [Alramahi *et al.*, 2010] ALRAMAHI, B., ALSHIBLI, K. A. et FRATTA, D. (2010). Effect of Fine Particle Migration on the Small-Strain Stiffness of Unsaturated Soils. *Journal of Geotechnical and Geoenvironmental Engineering*, 136(4):620–628.
- [Bacchin *et al.*, 2018] BACCHIN, P., BRUTIN, D., DAVAILLE, A., DI GIUSEPPE, E., CHEN, X. D., GERGIANAKIS, I., GIORGIUTTI-DAUPHINÉ, F., GOEHRING, L., HALLEZ, Y., HEYD, R., JEANTET, R., LE FLOCH-FOUÉRÉ, C., MEIRELES, M., MITTELSTAEDT, E., NICLOUX, C., PAUCHARD, L. et SABOUNGI, M.-L. (2018). Drying colloidal systems: Laboratory models for a wide range of applications. *Eur. Phys. J. E*, 41(8):94.
- [Beyhaghi *et al.*, 2014] BEYHAGHI, S., GEOFFROY, S., PRAT, M. et PILLAI, K. M. (2014). Wicking and evaporation of liquids in porous wicks: A simple analytical approach to optimization of wick design. *AIChE J.*, 60(5):1930–1940.
- [Bird, 2002] BIRD, R. B. (2002). Transport phenomena. *Applied Mechanics Reviews*, 55(1):R1–R4.
- [Bodiguel *et al.*, 2009] BODIGUEL, H., DOUMENC, F. et GUERRIER, B. (2009). Pattern formation during the drying of a colloidal suspension. *Eur. Phys. J. Spec. Top.*, 166(1):29–32.
- [Bodiguel et Leng, 2010] BODIGUEL, H. et LENG, J. (2010). Imaging the drying of a colloidal suspension. *Soft Matter*, 6(21):5451–5460.
- [Brakke, 1992] BRAKKE, K. A. (1992). The Surface Evolver. *Experimental Mathematics*, 1(2):141–165.
- [Brunschwiler *et al.*, 2016] BRUNSCHWILER, T., ZÜRCHER, J., ZIMMERMANN, S., BURG, B. R., SCHLOTTIG, G., CHEN, X., SINHA, T., BAUM, M., HOFMANN, C., PANTOU, R., ACHEN, A., ZSCHENDERLEIN, U., KUMAR, S., WUNDERLE, B., HAUPT, M., SCHINDLER-SAEFKOW, F. et STRASSLE, R. (2016). Review of percolating and neck-based underfills with thermal conductivities up to 3 W/m-K. In *InterSociety Conference on Thermal and Thermomechanical Phenomena in Electronic Systems*. Institute of Electrical and Electronics Engineers Inc.
- [Camassel *et al.*, 2005] CAMASSEL, B., SGHAIER, N., PRAT, M. et BEN NASRALLAH, S. (2005). Evaporation in a capillary tube of square cross-section: Application to ion transport. *Chemical Engineering Science*, 60(3):815–826.

- [Chapuis et Prat, 2007] CHAPUIS, O. et PRAT, M. (2007). Influence of wettability conditions on slow evaporation in two-dimensional porous media. *Phys. Rev. E*, 75(4):046311.
- [Chauvet, 2009] CHAUVET, F. (2009). *Effet des films liquides en évaporation*. Thèse de doctorat.
- [Chauvet *et al.*, 2009] CHAUVET, F., DURU, P., GEOFFROY, S. et PRAT, M. (2009). Three Periods of Drying of a Single Square Capillary Tube. *Phys. Rev. Lett.*, 103(12):124502.
- [Chauvet *et al.*, 2010] CHAUVET, F., DURU, P. et PRAT, M. (2010). Depinning of evaporating liquid films in square capillary tubes: Influence of corners' roundedness. *Physics of Fluids*, 22(11):112113.
- [Chen *et al.*, 2004] CHEN, J., MATSUURA, T. et HORI, M. (2004). Novel gas diffusion layer with water management function for PEMFC. *Journal of Power Sources*, 131(1):155–161.
- [Chraïbi *et al.*, 2009] CHRAÏBI, H., PRAT, M. et CHAPUIS, O. (2009). Influence of contact angle on slow evaporation in two-dimensional porous media. *Phys. Rev. E*, 79(2):026313.
- [Concus et Finn, 1969] CONCUS, P. et FINN, R. (1969). ON THE BEHAVIOR OF A CAPILLARY SURFACE IN A WEDGE. *Proc. Natl. Acad. Sci. U.S.A.*, 63(2):292–299.
- [Cussler, 2009] CUSSLER, E. L. (2009). *Diffusion: Mass Transfer in Fluid Systems*. Cambridge University Press.
- [Dong et Johnson, 2003] DONG, L. et JOHNSON, D. (2003). Surface Tension of Charge-Stabilized Colloidal Suspensions at the Water-Air Interface. *Langmuir*, 19(24):10205–10209.
- [Doumenc et Guerrier, 2010] DOUMENC, F. et GUERRIER, B. (2010). Drying of a Solution in a Meniscus: A Model Coupling the Liquid and the Gas Phases. *Langmuir*, 26(17):13959–13967.
- [Dufresne *et al.*, 2003] DUFRESNE, E. R., CORWIN, E. I., GREENBLATT, N. A., ASHMORE, J., WANG, D. Y., DINSMORE, A. D., CHENG, J. X., XIE, X. S., HUTCHINSON, J. W. et WEITZ, D. A. (2003). Flow and Fracture in Drying Nanoparticle Suspensions. *Phys. Rev. Lett.*, 91(22):224501.
- [Eloukabi *et al.*, 2013] ELOUKABI, H., SGHAIER, N., BEN NASRALLAH, S. et PRAT, M. (2013). Experimental study of the effect of sodium chloride on drying of porous media: The crusty–patchy efflorescence transition. *International Journal of Heat and Mass Transfer*, 56(1):80–93.
- [Engøy *et al.*, 1991] ENGØY, T., FEDER, J. et JØSSANG, T. (1991). Counter-flow in Drying of Competing Pores. *Phys. Scr.*, 1991(T38):99.
- [Erriguible *et al.*, 2007] ERRIGUIBLE, A., BERNADA, P., COUTURE, F. et ROQUES, M. A. (2007). Simulation of vacuum drying by coupling models. *Chemical Engineering and Processing: Process Intensification*, 46(12):1274–1285.
- [Espinoza et Bond, 2016] ESPINOZA, O. et BOND, B. (2016). Vacuum Drying of Wood—State of the Art. *Curr Forestry Rep*, 2(4):223–235.

- [Fantinel *et al.*, 2017] FANTINEL, P., BORGMAN, O., HOLTZMAN, R. et GOEHRING, L. (2017). Drying in a microfluidic chip: Experiments and simulations. *Sci Rep*, 7(1):15572.
- [Friend et Yeo, 2010] FRIEND, J. et YEO, L. (2010). Fabrication of microfluidic devices using polydimethylsiloxane. *Biomicrofluidics*, 4(2):026502.
- [Fujii, 2002] FUJII, T. (2002). PDMS-based microfluidic devices for biomedical applications. *Microelectronic Engineering*, 61–62:907–914.
- [Geistlinger *et al.*, 2019] GEISTLINGER, H., DING, Y., APELT, B., SCHLÜTER, S., KÜCHLER, M., REUTER, D., VORHAUER, N. et VOGEL, H.-J. (2019). Evaporation Study Based on Micromodel Experiments: Comparison of Theory and Experiment. *Water Resources Research*, 55(8):6653–6672.
- [Geoffroy *et al.*, 2006] GEOFFROY, S., PLOURABOUÉ, F., PRAT, M. et AMYOT, O. (2006). Quasi-static liquid–air drainage in narrow channels with variations in the gap. *Journal of Colloid and Interface Science*, 294(1):165–175.
- [Ghiringhelli *et al.*, 2023] GHIRINGHELLI, E., MARCOUX, M., GEOFFROY, S. et PRAT, M. (2023). Evaporation in a single channel in the presence of particles. *Colloids and Surfaces A: Physicochemical and Engineering Aspects*, 656:130432.
- [Gostick *et al.*, 2006] GOSTICK, J. T., FOWLER, M. W., PRITZKER, M. D., IOANNIDIS, M. A. et BEHRA, L. M. (2006). In-plane and through-plane gas permeability of carbon fiber electrode backing layers. *Journal of Power Sources*, 162(1):228–238.
- [Haw *et al.*, 2002] HAW, M. D., GILLIE, M. et POON, W. C. K. (2002). Effects of Phase Behavior on the Drying of Colloidal Suspensions. *Langmuir*, 18(5):1626–1633.
- [He *et al.*, 2022] HE, M., YANG, Y., MEI, M. et QIU, H. (2022). Droplet Evaporation Dynamics on Hydrophobic Network Surfaces. *Langmuir*, 38(20):6395–6403.
- [Heinzelmann *et al.*, 1965] HEINZELMANN, F. J., WASAN, D. T. et WILKE, C. R. (1965). Concentration Profiles in Stefan Diffusion Tube. *Ind. Eng. Chem. Fund.*, 4(1):55–61.
- [Helseth et Fischer, 2003] HELSETH, L. E. et FISCHER, T. M. (2003). Particle interactions near the contact line in liquid drops. *Phys. Rev. E*, 68(4):042601.
- [Hidri *et al.*, 2013] HIDRI, F., SGHAIER, N., ELOUKABI, H., PRAT, M. et NASRALLAH, S. B. (2013). Porous medium coffee ring effect and other factors affecting the first crystallisation time of sodium chloride at the surface of a drying porous medium. *Physics of Fluids*, 25(12):127101.
- [Huber *et al.*, 2018] HUBER, R., CHEN, X. et DERBY, M. M. (2018). EVAPORATION FROM POROUS MEDIA: SINGLE HYDROPHOBIC AND HYDROPHILIC PORES. *3rd Thermal and Fluids Engineering Conference (TFEC)*.
- [Huinink *et al.*, 2002] HUININK, H. P., PEL, L. et MICHELS, M. a. J. (2002). How ions distribute in a drying porous medium: A simple model. *Physics of Fluids*, 14(4):1389–1395.
- [Incropera et Incropera, 2007] INCROPERA, F. P. et INCROPERA, F. P., éditeurs (2007). *Fundamentals of Heat and Mass Transfer*. John Wiley, Hoboken, NJ, 6th ed édition.

- [Ito *et al.*, 2014] ITO, H., ABE, K., ISHIDA, M., NAKANO, A., MAEDA, T., MUNAKATA, T., NAKAJIMA, H. et KITAHARA, T. (2014). Effect of through-plane distribution of polytetrafluoroethylene in carbon paper on in-plane gas permeability. *Journal of Power Sources*, 248:822–830.
- [Javadi *et al.*, 2013] JAVADI, A., HABIBI, M., TAHERI, F. S., MOULINET, S. et BONN, D. (2013). Effect of wetting on capillary pumping in microchannels. *Sci Rep*, 3(1):1412.
- [Jing *et al.*, 2010] JING, G., BODIGUEL, H., DOUMENC, F., SULTAN, E. et GUERRIER, B. (2010). Drying of Colloidal Suspensions and Polymer Solutions near the Contact Line: Deposit Thickness at Low Capillary Number. *Langmuir*, 26(4):2288–2293.
- [Keita, 2021] KEITA, E. (2021). Particle Deposition in Drying Porous Media. *Materials*, 14(18):5120.
- [Keita *et al.*, 2013] KEITA, E., FAURE, P., RODTS, S. et COUSSOT, P. (2013). MRI evidence for a receding-front effect in drying porous media. *Phys. Rev. E*, 87(6):062303.
- [Keita *et al.*, 2016a] KEITA, E., KODGER, T. E., FAURE, P., RODTS, S., WEITZ, D. A. et COUSSOT, P. (2016a). Water retention against drying with soft-particle suspensions in porous media. *Phys. Rev. E*, 94(3):033104.
- [Keita *et al.*, 2016b] KEITA, E., KOEHLER, S. A., FAURE, P., WEITZ, D. A. et COUSSOT, P. (2016b). Drying kinetics driven by the shape of the air/water interface in a capillary channel. *Eur. Phys. J. E*, 39(2):23.
- [Kerkhof et Geboers, 2005] KERKHOF, P. J. A. M. et GEBOERS, M. A. M. (2005). Toward a unified theory of isotropic molecular transport phenomena. *AIChE Journal*, 51(1):79–121.
- [Kim *et al.*, 2018] KIM, D.-O., PACK, M., ROKONI, A., KANEELIL, P. et SUN, Y. (2018). The effect of particle wettability on the stick-slip motion of the contact line. *Soft Matter*, 14(47):9599–9608.
- [Kim et Kang, 2003] KIM, H. Y. et KANG, B. H. (2003). Effects of hydrophilic surface treatment on evaporation heat transfer at the outside wall of horizontal tubes. *Applied Thermal Engineering*, 23(4):449–458.
- [Krischer et Kröll, 2013] KRISCHER, O. et KRÖLL, K. (2013). *Die wissenschaftlichen Grundlagen der Trocknungstechnik*. Springer-Verlag.
- [Laurindo et Prat, 1996] LAURINDO, J. B. et PRAT, M. (1996). Numerical and experimental network study of evaporation in capillary porous media. Phase distributions. *Chemical Engineering Science*, 51(23):5171–5185.
- [Laurindo et Prat, 1998] LAURINDO, J. B. et PRAT, M. (1998). Numerical and experimental network study of evaporation in capillary porous media. Drying rates. *Chemical Engineering Science*, 53(12):2257–2269.
- [Le Bray,] LE BRAY, Y. *CONTRIBUTIONS A L'ETUDE DU CHANGEMENT DE PHASE LIQUIDE-VAPEUR EN MILIEUX POREUX. SIMULATIONS NUMERIQUES SUR RESEAUX DE PORES*. Thèse de doctorat.

- [Leng, 2010] LENG, J. (2010). Drying of a colloidal suspension in confined geometry. *Phys. Rev. E*, 82(2):021405.
- [Lidon et Salmon, 2014] LIDON, P. et SALMON, J.-B. (2014). Dynamics of unidirectional drying of colloidal dispersions. *Soft Matter*, 10(23):4151.
- [Loussert *et al.*, 2016] LOUSSERT, C., BOUCHAUDY, A. et SALMON, J.-B. (2016). Drying dynamics of a charged colloidal dispersion in a confined drop. *Phys. Rev. Fluids*, 1(8):084201.
- [Mata *et al.*, 2005] MATA, A., FLEISCHMAN, A. J. et ROY, S. (2005). Characterization of Polydimethylsiloxane (PDMS) Properties for Biomedical Micro/Nanosystems. *Biomed Microdevices*, 7(4):281–293.
- [Merlin *et al.*, 2012] MERLIN, A., SALMON, J.-B. et LENG, J. (2012). Microfluidic-assisted growth of colloidal crystals. *Soft Matter*, 8(13):3526–3537.
- [Meyer et Kostin, 1975] MEYER, J. P. et KOSTIN, M. D. (1975). Circulation phenomena in stefan diffusion. *International Journal of Heat and Mass Transfer*.
- [Michel *et al.*, 2010] MICHEL, E., MAJDALANI, S. et DI-PIETRO, L. (2010). How Differential Capillary Stresses Promote Particle Mobilization in Macroporous Soils: A Novel Conceptual Model. *Vadose Zone Journal*, 9(2):307–316.
- [Mishra *et al.*, 2016] MISHRA, H., SCHRADER, A. M., LEE, D. W., GALLO, A., CHEN, S.-Y., KAUFMAN, Y., DAS, S. et ISRAELACHVILI, J. N. (2016). Time-Dependent Wetting Behavior of PDMS Surfaces with Bioinspired, Hierarchical Structures. *ACS Appl. Mater. Interfaces*, 8(12):8168–8174.
- [Mitrovic, 2012] MITROVIC, J. (2012). Josef Stefan and his evaporation–diffusion tube—the Stefan diffusion problem. *Chemical Engineering Science*, 75:279–281.
- [Mosthaf *et al.*, 2014] MOSTHAF, K., HELMIG, R. et OR, D. (2014). Modeling and analysis of evaporation processes from porous media on the REV scale. *Water Resources Research*, 50(2):1059–1079.
- [Moyne, 1987] MOYNE, C. (1987). *Transferts Couples Chaleur-Masse Lors Du Séchage : Prise En Compte Du Mouvement de La Phase Gazeuse*. These de doctorat, Vandoeuvreles-Nancy, INPL. Sous la direction de Maurice Martin. Soutenue en 1987, à Vandoeuvreles-Nancy, INPL .
- [Osti *et al.*,] OSTI, G. B. F., WOLF, F. G. et PHILIPPI, P. C. SPREADING OF LIQUID DROPS ON ACRYLIC SURFACES.
- [Pingulkar et Salmon, 2023] PINGULKAR, H. et SALMON, J.-B. (2023). Confined directional drying of a colloidal dispersion: Kinetic modeling. *Soft Matter*, 19(12):2176–2185.
- [Plötze et Niemz, 2011] PLÖTZE, M. et NIEMZ, P. (2011). Porosity and pore size distribution of different wood types as determined by mercury intrusion porosimetry. *Eur. J. Wood Prod.*, 69(4):649–657.
- [Prat, 2002] PRAT, M. (2002). Recent advances in pore-scale models for drying of porous media. *Chemical Engineering Journal*, 86(1):153–164.

- [Prat, 2007] PRAT, M. (2007). On the influence of pore shape, contact angle and film flows on drying of capillary porous media. *International Journal of Heat and Mass Transfer*, 50(7):1455–1468.
- [Prat, 2023] PRAT, W. (2023). *Mass Transfer Driven Evaporation From Capillary Porous Media*. Routledge & CRC Press.
- [Preibisch *et al.*, 2009] PREIBISCH, S., SAALFELD, S. et TOMANCAK, P. (2009). Globally optimal stitching of tiled 3D microscopic image acquisitions. *Bioinformatics*, 25(11):1463–1465.
- [Pu *et al.*, 2012] PU, Y., WANG, W., DORSHOW, R. B. et ALFANO, R. R. (2012). Picosecond polarization spectroscopy of fluorescein attached to different molecular volume polymer influenced by rotational motion. In *Organic Photonic Materials and Devices XIV*, volume 8258, pages 169–173. SPIE.
- [Qin *et al.*, 2019] QIN, F., MAZLOOMI MOQADDAM, A., KANG, Q., DEROME, D. et CARMELIET, J. (2019). LBM Simulation of Self-Assembly of Clogging Structures by Evaporation of Colloidal Suspension in 2D Porous Media. *Transp Porous Med*, 128(3):929–943.
- [Ransohoff et Radke, 1988] RANSOHOFF, T. C. et RADKE, C. J. (1988). Laminar flow of a wetting liquid along the corners of a predominantly gas-occupied noncircular pore. *Journal of Colloid and Interface Science*, 121(2):392–401.
- [Redman *et al.*, 2017] REDMAN, A. L., BAILLERES, H., PERRÉ, P., CARR, E. et TURNER, I. (2017). A relevant and robust vacuum-drying model applied to hardwoods. *Wood Sci Technol*, 51(4):701–719.
- [Richter Reis, 2014] RICHTER REIS, F., éditeur (2014). *Vacuum Drying for Extending Food Shelf-Life*. SpringerBriefs in Applied Sciences and Technology. Springer International Publishing, Cham.
- [Roman *et al.*, 2016] ROMAN, S., SOULAINÉ, C., ALSAUD, M. A., KOVSCEK, A. et TCHELEPI, H. (2016). Particle velocimetry analysis of immiscible two-phase flow in micromodels. *Advances in Water Resources*, 95:199–211.
- [Routh et Zimmerman, 2004] ROUTH, A. F. et ZIMMERMAN, W. B. (2004). Distribution of particles during solvent evaporation from films. *Chemical Engineering Science*, 59(14):2961–2968.
- [Salcedo-Díaz *et al.*, 2008] SALCEDO-DÍAZ, R., RUIZ-FEMENIA, R., KERKHOF, P. J. A. M. et PETERS, E. A. J. F. (2008). Velocity profiles and circulation in Stefan-diffusion. *Chemical Engineering Science*, 63(19):4685–4693.
- [Scherer, 1990] SCHERER, G. W. (1990). Theory of Drying. *Journal of the American Ceramic Society*, 73(1):3–14.
- [Seck *et al.*, 2019] SECK, M. D., KEITA, E. et COUSSOT, P. (2019). Some Observations on the Impact of a Low-Solubility Ionic Solution on Drying Characteristics of a Model Porous Medium. *Transp Porous Med*, 128(3):915–928.

- [Sghaier et Prat, 2009] SGHAIER, N. et PRAT, M. (2009). Effect of Efflorescence Formation on Drying Kinetics of Porous Media. *Transp Porous Med*, 80(3):441–454.
- [Shahidzadeh-Bonn et al., 2007] SHAHIDZADEH-BONN, N., AZOUNI, A. et COUSSOT, P. (2007). Effect of wetting properties on the kinetics of drying of porous media. *J. Phys.: Condens. Matter*, 19(11):112101.
- [Shaw, 1987] SHAW, T. M. (1987). Drying as an immiscible displacement process with fluid counterflow. *Phys. Rev. Lett.*, 59(15):1671–1674.
- [Shokri et al., 2008] SHOKRI, N., LEHMANN, P. et OR, D. (2008). Effects of hydrophobic layers on evaporation from porous media. *Geophysical Research Letters*, 35(19).
- [Shokri et al., 2009] SHOKRI, N., LEHMANN, P. et OR, D. (2009). Characteristics of evaporation from partially wettable porous media. *Water Resources Research*, 45(2).
- [Shokri et Or, 2013] SHOKRI, N. et OR, D. (2013). Drying patterns of porous media containing wettability contrasts. *Journal of Colloid and Interface Science*, 391:135–141.
- [Takata et al., 2004] TAKATA, Y., HIDAKA, S., YAMASHITA, A. et YAMAMOTO, H. (2004). Evaporation of water drop on a plasma-irradiated hydrophilic surface. *International Journal of Heat and Fluid Flow*, 25(2):320–328.
- [Thomas, 1965] THOMAS, D. G. (1965). Transport characteristics of suspension: VIII. A note on the viscosity of Newtonian suspensions of uniform spherical particles. *Journal of Colloid Science*, 20(3):267–277.
- [Velev et Gupta, 2009] VELEV, O. D. et GUPTA, S. (2009). Materials Fabricated by Micro- and Nanoparticle Assembly - The Challenging Path from Science to Engineering. *Adv. Mater.*, 21(19):1897–1905.
- [Vincent et al., 2014] VINCENT, O., SESSOMS, D. A., HUBER, E. J., GUIOTH, J. et STROOCK, A. D. (2014). Drying by Cavitation and Poroelastic Relaxations in Porous Media with Macroscopic Pores Connected by Nanoscale Throats. *Phys. Rev. Lett.*, 113(13):134501.
- [Vorhauer et al., 2018] VORHAUER, N., TSOTSAS, E. et PRAT, M. (2018). Temperature gradient induced double stabilization of the evaporation front within a drying porous medium. *Phys. Rev. Fluids*, 3(11):114201.
- [Vorhauer et al., 2015] VORHAUER, N., WANG, Y. J., KHARAGHANI, A., TSOTSAS, E. et PRAT, M. (2015). Drying with Formation of Capillary Rings in a Model Porous Medium. *Transp Porous Med*, 110(2):197–223.
- [Voss et al., 1995] VOSS, H. H., WILKINSON, D. P., PICKUP, P. G., JOHNSON, M. C. et BASURA, V. (1995). Anode water removal: A water management and diagnostic technique for solid polymer fuel cells. *Electrochimica Acta*, 40(3):321–328.
- [Vyawahare et al., 2006] VYAWAHARE, S., CRAIG, K. M. et SCHERER, A. (2006). Patterning Lines by Capillary Flows. *Nano Lett.*, 6(2):271–276.

- [Wan *et al.*, 2015] WAN, R., WANG, C., LEI, X., ZHOU, G. et FANG, H. (2015). Enhancement of Water Evaporation on Solid Surfaces with Nanoscale Hydrophobic-Hydrophilic Patterns. *Phys Rev Lett*, 115(19):195901.
- [Wilkinson et Willemsen, 1983] WILKINSON, D. et WILLEMSSEN, J. F. (1983). Invasion percolation: A new form of percolation theory. *J. Phys. A: Math. Gen.*, 16(14):3365.
- [Wu *et al.*, 2020] WU, R., ZHANG, T., YE, C., ZHAO, C. Y., TSOTSAS, E. et KHARAGHANI, A. (2020). Pore network model of evaporation in porous media with continuous and discontinuous corner films. *Phys. Rev. Fluids*, 5(1):014307.
- [Yiotis *et al.*, 2004] YIOTIS, A. G., BOUDOUVIS, A. G., STUBOS, A. K., TSIMPANOGLIANNIS, I. N. et YORTSOS, Y. C. (2004). Effect of liquid films on the drying of porous media. *AIChE J.*, 50(11):2721–2737.
- [Yiotis *et al.*, 2012] YIOTIS, A. G., SALIN, D., TAJER, E. S. et YORTSOS, Y. C. (2012). Drying in porous media with gravity-stabilized fronts: Experimental results. *Phys. Rev. E*, 86(2):026310.
- [Zhang *et al.*, 2014] ZHANG, Q., HASSANIZADEH, S. M., LIU, B., SCHIJVEN, J. F. et KARADIMITRIOU, N. K. (2014). Effect of hydrophobicity on colloid transport during two-phase flow in a micromodel. *Water Resources Research*, 50(10):7677–7691.
- [Zhang *et al.*, 2010] ZHANG, W., MORALES, V. L., CAKMAK, M. E., SALVUCCI, A. E., GEOHRING, L. D., HAY, A. G., PARLANGE, J.-Y. et STEENHUIS, T. S. (2010). Colloid Transport and Retention in Unsaturated Porous Media: Effect of Colloid Input Concentration. *Environ. Sci. Technol.*, 44(13):4965–4972.
- [Zhao *et al.*, 2011] ZHAO, J.-J., DUAN, Y.-Y., WANG, X.-D. et WANG, B.-X. (2011). Effect of nanofluids on thin film evaporation in microchannels. *J Nanopart Res*, 13(10):5033.